N° d'ordre : 3233

THESE

Présentée à

L'UNIVERSITE BORDEAUX I

ECOLE DOCTORALE DES SCIENCES PHYSIQUES ET DE L'INGENIEUR

Par

Ali Akbar ABBASIAN ARANI

Pour obtenir le grade de

DOCTEUR

Spécialité : Mécanique

SUR QUELQUES ASPECTS DES ECOULEMENTS INERTIELS MONO- ET DIPHASIQUE EN MILIEU POREUX

Soutenue le 24 octobre 2006

Après avis de :

MM. C. MOYNE, Directeur de Recherche CNRS, ENSEM-INPL, Nancy ……..Rapporteurs
B. NOETINGER, Ingénieur de Recherche Senior, IFP, Rueil-Malmaison

Devant la commission d'examen formée de :

MM. J.R. PUIGGALI, Professeur, Université Bordeaux I …..……..……..……..Président
B. AMAZIANE, Maître de conférences HDR, Université de Pau…….. Examinateurs
M. AZAIEZ, Professeur, ENSCPB, Bordeaux……..……..
A. AHMADI, Maître de conférences HDR, ENSAM……..……..…
D. LASSEUX, Chargé de Recherche CNRS……..…….

2006

REMERCIEMENTS

Le travail présenté ici a été réalisé au sein du groupe « Transferts & Milieux Poreux » du TREFLE, entre mai 2003 et octobre 2006, avec un soutien financer du gouvernement français et iranien. Je voudrais remercier tous ceux qui ont rendu ce travail possible, et qui, à des titres divers, ont contribué à son élaboration.

En premier lieu, mes plus vifs remerciements vont à Monsieur Didier LASSEUX, Chargé de Recherche CNRS et Madame Azita AHMADI, Maître de Conférence, HDR, de l'ENSAM de Bordeaux présents lors de toutes les étapes de ce travail. Je leur sais gré de m'avoir apporté leur extrême compétence scientifique, un grand intérêt pour mon (notre) travail, leurs sensibilité et gentillesse.

Je tiens à exprimer ma profonde gratitude à Monsieur le Professeur Jean Rodolphe PUIGGALI, Professeur à l'Université Bordeaux I, qui, après m'avoir accueilli au sein du laboratoire, m'a soutenu tout au long de mon travail. Je suis sensible à l'honneur qu'il me fait de présider ce jury.

Je tiens aussi à remercier Monsieur le Professeur Mejdi AZAEIZ, Professeur de l'Université Bordeaux I à ENCEPB pour la qualité de son encadrement administratif et ses conseils précieux. Je tiens à lui exprimer toute mon admiration.

Je remercie vivement Monsieur Christian MOYNE Directeur de Recherche, CNRS (LEMTA, ENSEM-INPL, Nancy) et Monsieur Benoît NOETINGER, Ingénieur de Recherche Senior (de l'Institut Français du Pétrole (IFP)) d'avoir bien voulu rapporté sur ce travail et accepté de participer au jury.

Je tiens à remercier Monsieur Brahim AMAZIANE Maître de conférence, HDR, à l'Université de Pau pour l'intérêt qu'il a porté à ce travail et pour avoir bien voulu prendre part au jury.

Je remercie chaleureusement ma famille, mon épousé Leila et mes enfants Fatemeh et Ali pour leur soutien tout au long de mon travail.

Mes plus vifs remerciements s'adressent enfin à tous les membres du TREFLE, Chercheurs, Techniciens et Etudiants avec lesquels j'ai passé de bien agréables moments durant ces trois dernières années.

Table des matières

Chapitre 1

Introduction générale

Chapter 1

Introduction générale

L'écoulement des fluides en milieu poreux concerne de nombreux domaines d'activité parmi lesquels on peut citer l'hydrologie, la récupération pétrolière et de gaz, l'énergie géothermique et le génie chimique. Des modèles précis sont nécessaires pour les écoulements mono et multiphasiques en milieux poreux. Alors que les modèles proposés pour les écoulements en régime visqueux à différentes échelles sont généralement acceptés, ceux pour modéliser l'écoulement monophasique en milieu poreux quand les effets d'inertie sont impliqués sont encore discutés.

Plusieurs travaux expérimentaux et théoriques ont traité des écoulements monophasique et multiphasique en milieu poreux. Après les travaux bien connus de Darcy et Forchheimer, beaucoup d'études expérimentales se sont concentrées sur la variation de la chute de pression en fonction de la vitesse du fluide. Au cours des études, une grande quantité de données expérimentales a été rendue disponible et discutée la plupart du temps sur la base d'une analyse dimensionnelle et empirique. Des travaux expérimentaux plus récents se sont concentrés principalement sur la mise en place d'une classification plus raffinée des régimes d'écoulement. Des études théoriques ont permis de développer différentes approches pour modéliser la chute de pression. Le comportement général de cette classification, (i.e, les différents régimes d'écoulement) est maintenant acceptée : le régime de Darcy, le régime laminaire d'inertie faible, le régime laminaire d'inertie forte, et le régime turbulent.

La généralisation de la loi de Darcy au cas inertiel a été le sujet de nombreuses recherches expérimentales et théoriques. Ces recherches ont porté sur la mise en place d'une base physique et/ou théorique pour la déviation à la loi de Darcy. Ces études se sont concentrées sur deux points importants : la valeur du nombre de Reynolds au delà de laquelle la loi de Darcy n'est plus valable ainsi que la prévision correcte du comportement des écoulements non-linéaires. L'analyse dimensionnelle (Ward 1964), prise de moyenne volumique (Whitaker 1996), le modèle capillaire (Azzam and Dullien 1973), et la théorie des mélanges hybrides (Hassanizadeh and Gray 1987). ont été largement utilisés

Cependant, des études théoriques et expérimentales réalisées en milieu poreux sont loin de l'écoulement inertiel (hors régime de Darcy) et ont été concentrés la plupart du temps sur les écoulements monophasiques qui concernent l'industrie du pétrole et du gaz (Swift and Kiel 1962; Tek, Coats and Katz 1962; Lee, Logan and Tek 1987). En raison de l'insuffisance d'études dans ce domaine ainsi que la difficulté mathématique pour manipuler ces écoulements fortement non-linéaires en condition mono et diphasique, notre compréhension de l'écoulement inertiel en milieu poreux est actuellement très limitée.

Avant d'entrer dans le vif du sujet, il est indispensable de présenter de manière globale un certain nombre de notions utilisées dans le traitement des écoulements multiphasiques en milieu poreux. Ce chapitre nous permet d'introduire, aussi bien, les outils de base nécessaires à la compréhension des processus régissant les écoulements multiphasiques dans des milieu poreux, que les questions posées dans ce

type de problème.

Après avoir mis en évidence l'importance de la notion d'échelles intervenant dans la description des phénomènes de transport dans un milieu poreux naturel, nous présentons la méthode de prise de moyenne volumique utilisée dans ce travail de thèse. Les écoulements inertiels monophasiques en milieux poreux sont ensuite introduits. Les différentes approches pour traiter ce type de problème, les différents régimes d'écoulements, l'origine des effets inertiels et la limite de la validité de la loi de Darcy sont ensuite discutés. Apres une brève introduction sur les écoulements diphasiques inertiels en milieux poreux, nous présentons l'objectif de cette étude.

1.1 Notion d'échelle

L'interaction des phénomènes géologiques et physiques complexes étalés dans le temps et l'espace est à l'origine de la formation de gisements pétroliers, qui sont des vastes milieux poreux au sein desquels différents fluides (eau, pétrole, gaz) coexistent et se déplacent avec une physique que l'on ne maîtrise pas totalement.

Etant donné la complexité de la structure géométriques d'un réseau poreux et l'écart entre l'échelle de taille des pores et celle du réservoir, la notion d'échelle joue un rôle primordial dans l'étude des phénomènes de transfert en milieux poreux. De plus, il n'est pas évident, du fait de cet écart de taille dans les échelle, que les phénomènes physiques régissant les écoulement à l'échelle du pore soient les mêmes à l'échelle du réservoir. Différentes échelles d'observation ont été définies pour mieux prendre en compte précisément la physique des différents processus au sien du réservoir. Celles-ci peuvent être classifiées de la manière suivante :

L'échelle de pore

Lorsque les dimensions géométriques des pores et des phases ont des valeurs largement supérieures aux dimensions moléculaires, chaque phase peut être considérée comme un milieu continu et le milieu poreux comme un ensemble de milieux continus étroitement imbriqués. Les phénomènes qui se déroulent au sein des pores sont alors parfaitement décrit par les équations dites *miroscopiques* de la thermodynamique et de la mécanique des milieux continus. Mais, une telle description ne peut être utilisée dans la pratique parce qu'elle est trop détaillée et complexe (problèmes aux limites complexes, géométrie du milieu mal connue, etc...). Cette échelle est aussi appelée *échelle du pore*. Elle permet d'observer directement les différents phénomènes se développant dans le réseau de pore proprement dit. On admet généralement comme longueur caractéristique de cette échelle celle du diamètre moyen des pores (milieux poreux consolidés) ou du diamètre moyen des grains (milieux poreux non consolidés). La description des écoulement des fluides dans les pores est généralement obtenue à cette échelle par les équations classiques de le mécanique des fluides (Navier-Stokes, conservation de la masse...).

L'échelle Local

Souvent appelée *macroscopique*, cette échelle permet une description des phénomènes pour des éléments de volume suffisamment grands par rapport au volume moyen des pores (ou des grains). Elle permet de faire la moyenne des phénomènes dans les différents pores, mais reste suffisamment faible pour que l'échantillon poreux sélectionné puisse être considéré comme homogène. Elle est généralement de l'ordre du centimètre (cm). C'est l'échelle minimale où on peut définir un volume élémentaire représentatif (V.E.R.) tenu de caractériser le milieu macroscopique. La description des phénomènes est faite en terme de milieu continu équivalent et les paramètres observés sont des valeurs moyennes. Les équations de transport peuvent être obtenues par prise de moyenne des équation de Stokes (ou Navier-Stokes) et conduisent à la loi de Darcy (ou Forchheimer) pour décrire les écoulements monophasiques (Whitaker 1986a; Whitaker 1996) et à l'extension de la loi de Darcy pour les écoulements polyphasiques en milieu poreux (Whitaker 1986b).

L'échelle Globale (ou grande échelle)

C'est l'échelle du milieu poreux hétérogène, incluant plusieurs éléments qui, localement, peuvent être considérés comme homogènes. L'écoulement est décrit par les équations de continuité et de moyenne des équations locales (Quintard and Whitaker 1987; Quintard and Whitaker 1988).

L'objectif du changement d'échelle est de produire des équations représentatives à une échelle donnée où les coefficients de transport sont déterminés par la résolution d'un problème faisant intervenir des propriétés à l'échelle inférieure. Diverses méthodologies peuvent être utilisées pour effectuer le changement d'échelle, la prise de moyenne avec fermeture, la théorie de la l'homogénéisation, les méthodes stochastiques.... On abordera dans le cadre de cette thèse essentiellement à la méthode de prise de moyenne.

1.2 La méthode de prise de moyenne

La méthode de prise de moyenne est une technique puissante qui permet d'obtenir la forme moyenne des équations de conservation à une échelle donnée, à partir des équations et des conditions aux limites à une échelle inférieure. Elle fournit également, des problèmes de fermeture reliant la petite échelle (échelle du pore par exemple) à l'échelle supérieure en proposant une représentation mathématique exacte des propriétés effectives à grande échelle (échelle local ou globale). Cette méthode est utilisée, en particulier, pour le changement d'échelle des écoulements mono et multiphasiques en milieux poreux. A titre d'exemple, la prise de moyenne volumique du problème de Stokes monophasique conduit à la loi de Darcy (Whitaker 1986a) et la même technique appliquée au problème de Navier-Stokes permet d'obtenir une équation macroscopique contenant un terme non-linéaire (Whitaker 1996).

Dans les paragraphes suivants, un bref historique de cette méthode, ainsi qu'un rappel de quelques notions de base associées à l'application de la prise de moyenne volumique sont proposés.

Historique

La méthode de prise de moyenne spatiale est une synthèse entre la méthode stochastique et la méthode de l'homogénéisation. Le concept de moyenne spatiale a été à l'origine introduit grâce à la méthode stochastique (Matheron 1965) et celui de multi-échelle par l'homogénéisation. L'utilisation de la méthode de prise de moyenne spatiale dans la modélisation des phénomènes de transfert en milieux poreux remonte à environ quarante ans (Marle 1967; Whitaker 1967). En effet, en 1967, S. Whitaker démontre le théorème de prise de moyenne et applique la méthode de prise de moyenne spatiale au problème de diffusion-dispersion en milieu poreux (Whitaker 1967). La même année, cette méthode est également utilisée pour la description des écoulements dans les lits fluidités (Anderson and Jackson 1967), ainsi que les écoulement visco-élastiques en milieu poreux (Slattery 1967).

Notions de base

La méthode de prise de moyenne spatiale permet d'aboutir, en partant d'un champ d'une grandeur microscopique, à une valeur moyenne de cette grandeur. Cette méthode est basée sur l'idée qu'à chaque point du milieu est associé un volume de prise de moyenne V, encore appelé élémentaire représentatif, (VER), de rayon r_o, Figure (1.1)

Initialement l'échelle de r_o a été intuitivement considérée très petite devant la taille macroscopique du milieu poreux L et très grande devant la taille de pores l_β (Whitaker 1969) :

$$l_\beta \ll r_o \ll L \tag{1.1}$$

Où L représente la longueur caractéristique associée à la variation des grandeurs macroscopiques.

Les valeurs moyennes de toute fonction sont définies au centre du volume de prise de moyenne. Il existe deux manières de les définir :

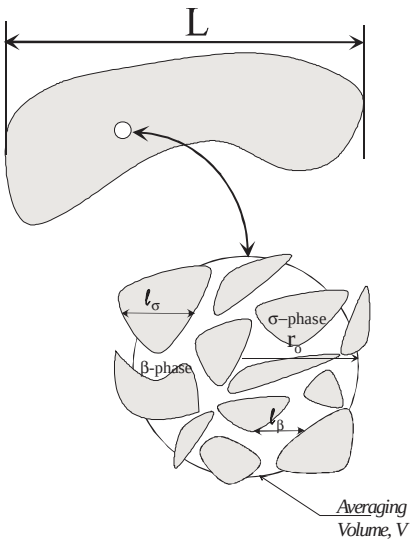

Figure 1.1: Schéma d'un volume de prise de moyenne V associé à un milieu poreux de taille L.

-moyenne volumique de phase d'une grandeur ψ_β:

$$\langle \psi_\beta \rangle = \frac{1}{V} \int_{V_\beta} \psi_\beta dV \tag{1.2}$$

Où V_β désigne le volume occupé par la phase β dans la volume de prise de moyenne,
-moyenne volumique intrinsèque de phase de la grandeur ψ_β:

$$\langle \psi_\beta \rangle^\beta = \frac{1}{V_\beta} \int_{V_\beta} \psi_\beta dV \tag{1.3}$$

Pour un grand nombre de grandeurs physiques telles que la température, la concentration, la pression, on utilise les moyennes intrinsèques de ces grandeurs puisqu'elles sont plus accessibles à la mesure expérimentale. En revanche, pour le cas de la vitesse, on utilise plutôt la moyenne volumique de phase.

La relation entre les moyennes volumiques de phase et les moyennes volumiques intrinsèques est une relation de proportionnalité :

$$\langle \psi_\beta \rangle = \varepsilon_\beta \langle \psi_\beta \rangle^\beta \tag{1.4}$$

Le coefficient de proportionnalité s'appelle porosité du milieu, c'est la fraction de volume qu'occupe la phase dans le milieu :

$$\varepsilon_\beta = \frac{V_\beta}{V} \tag{1.5}$$

La dépendance de $\langle \psi_\beta \rangle$ en fonction du volume de prise de moyenne peut être représentée sur la Figure (1.2) pour un milieu poreux quelconque, c'est-à-dire tel que la phase solide soit distribuée de façon aléatoire.

L'existence d'un volume élémentaire représentatif du milieu poreux est liée à la propriété suivante :

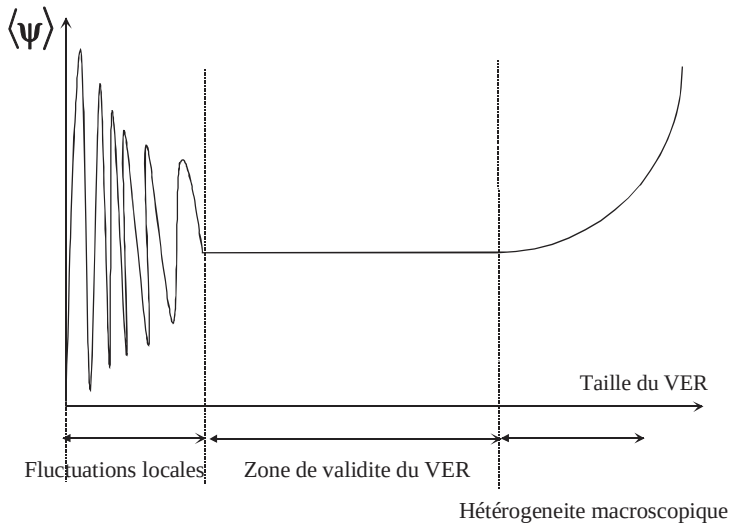

Figure 1.2: Variation d'une grandeur moyenne en fonction de la taille du volume de prise de moyenne.

$$\frac{\partial \langle \psi_\beta \rangle}{\partial r} = 0 \tag{1.6}$$

Cette équation signifie que la variation de la grandeur moyenne $\langle \psi_\beta \rangle$ avec l'augmentation de la taille du volume de prise de moyenne doit être nulle pour que ce volume soit représentatif de la structure poreuse considérée.

En dehors de l'intervalle de validité du volume élémentaire représentatif, on distingue sur la Figure (1.2) deux autres zones différentes :

- zone de fluctuations microscopique, appelée aussi zone des hétérogénéités microscopiques, la taille du volume de prise de moyenne n'est pas suffisante pour définir des grandeurs moyennes. Les variations de $\langle \psi_\beta \rangle$ sont liées aux variations locales de ψ_β à l'échelle du pore.

- l'autre partie correspond aux hétérogénéités macroscopiques, où les grandeurs moyennes varient avec l'augmentation de la taille du volume de prise de moyenne. Dans cette région, on utilise une nouvelle méthode appelée prise de moyenne à grande échelle (Quintard and Whitaker 1987; Plumb and Whitaker 1988; Quintard and Whitaker 1990a; Quintard and Whitaker 1990b). Ces hétérogénéités macroscopiques sont rencontrées dans le domaine des aquifères et des gisements où l'on assiste à une variation de la porosité en fonction de l'espace de manière discontinue.

La définition d'une grandeur moyenne est associée à l'existence d'un volume élémentaire représentatif. En d'autres termes, on ne peut définir de grandeurs macroscopiques que si la contrainte d'échelle, équation (1.1), est respectée. Cependant, dans le cas de milieux poreux périodique, Figure (1.3), la taille du volume élémentaire représentatif peut être considérée du même ordre de grandeur que celle des pores (Quintard and Whitaker 1994a; Quintard and Whitaker 1994b) et dans ces conditions la contrainte d'échelle, l'équation (1.1) devient:

$$l_\beta \sim r_o \ll L \tag{1.7}$$

La méthode de prise de moyenne est la base du travail numérique proposé au chapitre 2 et est également

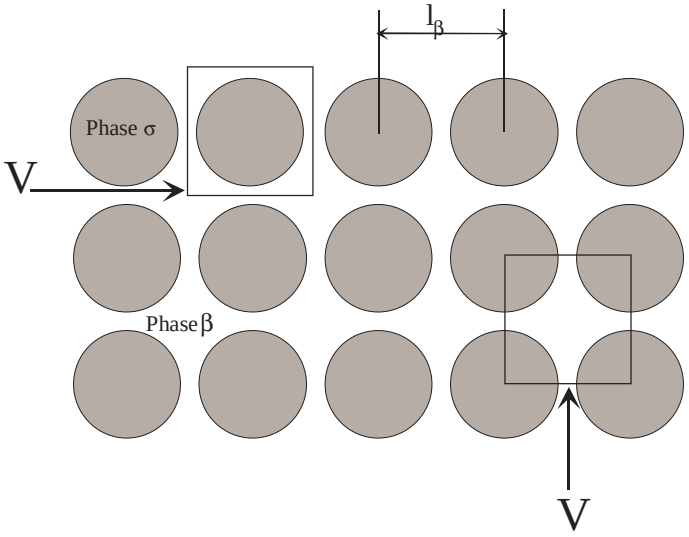

Figure 1.3: Exemple de structure poreuse périodique

utilisée pour l'obtention théorique des équations d'écoulements inertiels en condition diphasique (chapitre 3). Les notations, ainsi que les détails techniques nécessaires aux développements seront rappelés dans les chapitres correspondants.

1.3 Ecoulements inertiels monophasiques en milieux poreux

1.3.1 Les différentes approches

Plusieurs chercheurs ont développé des rapports non-linéaires entre le gradient de pression et la vitesse d'écoulement en suivant différentes approches. Diverses classes d'approches peuvent être identifiées et sont discutées dans la littérature. Pour plus d'informations sur ce sujet, référez-vous aux livres (Bear 1972; Hannoura and Barends 1981; Scheidegger 1974).

Certaines théories, développées pour expliquer des effets non-linéaires en milieu poreux, se sont basées sur les modèles descriptifs, intuitifs ou empiriques. Empirisme, enrichi avec l'analyse dimensionnelle et d'autres considérations théoriques, forme la base de ces théories (Dupuit 1863; Forchheimer 1901; Ward 1964). Des théories d'écoulement plus anciennes ont pu être classifiées dans ce groupe de modèles. En premier lieu, Forchheimer, par analogie avec l'écoulement dans les conduites, a proposé que, à fortes vitesses d'écoulement, la correction à la loi de Darcy est proportionnelle à une puissance m de la vitesse :

$$-\frac{dp}{dx} = au + bu^m \tag{1.8}$$

où m est proche de 2. Il a également proposé que la perte de pression pourrait être décrite par un polynôme d'ordre trois en vitesse :

$$-\frac{dp}{dx} = au + bu^2 + cu^3 \tag{1.9}$$

où p est la pression, u est la vitesse d'écoulement, et a, b et c sont des constantes.

Beaucoup de travail a été effectué pour obtenir des corrélations pour a, b et c en terme de propriétés à l'échelle microscopique ou macroscopique telles que la taille et la forme des grains, la porosité, la viscosité, etc. (e.g. Ergun 1952; Tek 1957; Geertsma 1974). Basé sur une analyse dimensionnelle Muskat 1937, Green and Duwez 1951 et Cornell and Katz 1953 ont constaté que le coefficient de l'équation (1.8) avec $m = 2$, peut être séparé des paramètres du fluide et de la roche, et donne l'équation suivante qui s'appelle aujourd'hui l'équation de Forchheimer :

$$-\frac{dp}{dx} = \frac{\mu}{K}u + \beta\rho u^2 \tag{1.10}$$

où β est un paramètre de roche nommé la résistante inertiel, le coefficient d'écoulement à haute vitesse, ou coefficient d'écoulement hors régime de Darcy.

Quelques autres approches sont théoriques, comme la méthode de la moyenne (Irmay 1958), les principes variationnels (Knupp and Lage 1995), la méthode de prise de moyenne (Whitaker 1986a; Whitaker 1986b; Whitaker 1996), et la technique d'homogénéisation (Sanchez-Palencia 1980; Mei and Auriault 1991; Wodie and Levy 1991; Firdaouss and Guermond 1995). Irmay 1958 fait la moyenne sur l'équation de Navier-Stokes pour un modèle de sphères de diamètres égaux représentant un milieu isotrope homogène. Il donne a, b et c en termes des propriétés du fluide et du milieu telles que la viscosité, la densité, la taille du grain, et deux facteurs de forme. Une approche semblable a été adoptée par Ahmed and Sunada 1969; Dullien and Azzam 1973 et Cvetkovic 1986.

Dans le cadre des approches théoriques, Whitaker 1996 a illustré comment la méthode de prise de moyenne peut être employée pour dériver la loi de Darcy avec la correction de Forchheimer en milieu poreux homogènes. Il partait de équation de Navier-Stokes et il a réécrit l'équation de quantité de mouvement sous la forme :

$$\langle \mathbf{v}_\beta \rangle = \frac{-\mathbf{K}}{\mu_\beta}\left[\nabla\langle p_\beta\rangle^\beta - \rho_\beta \mathbf{g} - \mu_\beta \nabla^2 \langle \mathbf{v}_\beta\rangle^\beta\right] - \mathbf{F}\cdot\langle \mathbf{v}_\beta\rangle \tag{1.11}$$

où $\mathbf{K}$, $\mathbf{F}$ sont le tenseur de perméabilité de la loi de Darcy et le tenseur de correction de Forchheimer. $\mathbf{K}$ et $\mathbf{F}$ sont solutions du problèmes de fermeture résolus en utilisant un modèle spatiale de milieu poreux périodique. Whitaker 1996 a indiqué que la correction de Forchheimer est quadratique en vitesse pour des petites valeurs du nombre de Reynolds, et l'analyse d'ordre de grandeur propose que cette dépendance fonctionnelle ne devrait pas changer considérablement avec le nombre de Reynolds.

La technique mathématique de l'homogénéisation (Dupuit 1863; Bensoussan, Lions and Papanicolaou 1978) a été exploitée pour dériver la loi de Forchheimer depuis l'équation de Navier-Stokes. Cette technique calcule la moyennes des équations de l'écoulement à l'échelle microscopiques et rend plus simples les équations macroscopiques. Ceci est réalisé par un changement d'échelle des équations microscopiques par le rapport $\varepsilon = l/L$, des longueurs liées aux phénomènes microscopiques et macroscopiques dans des milieu poreux périodiques. Ici, la micro-échelle l caractérise l'épaisseur typique de couche et la macro-échelle L caractérise la variation globale des forces et des données externes de frontière.

Le troisième groupe d'approches concerne des études numériques (Barrere 1990; Skjetne, Hansen and Gudmundsson 1995; Firdaouss and Guermond 1995, Skjetne and Auriault 1999a).

D'outres théories d'écoulement non-linéaire sont basées sur une description géométrique idéalisée assez simple des milieu poreux pour permettre aux équations les régissant d'être résolues. Un exemple de ce type de modèle est celui de Blick 1966 qui représente un milieu poreux comme un paquet de tubes capillaires parallèles remplis de fluide et d'orifices plats espacés le long de chaque tube. Un autre exemple est le travail de Barak and Bear 1981 dans lequel ils considèrent cinq différents modèles physiques avec divers degrés de complexité. En utilisant ce modèle, ils ont obtenu des rapports non-linéaires entre le gradient de pression et la vitesse d'écoulement et ont comparé ces équations aux modèles mathématiques génériques et aux résultats expérimentaux.

De la brève discussion des modèles sur l'écoulement à vitesse élevée, il ressort clairement que plusieurs approches de ce problème sont possibles. Elles sont souvent restreintes à certains matériaux et/ou à des cas spéciaux (par exemple cas d'équilibre, unidimensionnel, etc...). Ainsi, leur validité générale est incertaine et, habituellement, les étapes exigées pour prolonger les résultats à des situations plus générales sont plutôt obscures.

1.3.2 Différents régimes d'écoulement en milieu poreux

La question de la forme et la mesure exactes des effets non-linéaires a été présentée par Forchheimer en 1901 et jusqu'ici ne semble pas avoir reçu un réponse claire. Aux nombres de Reynolds élevés, l'équation empirique de Forchheimer 1901 est employée pour expliquer la déviation de la loi de Darcy:

$$-\frac{\Delta P}{L} = \frac{\mu}{K_f} u + \beta \rho u^2 \tag{1.12}$$

où K_f est la perméabilité de Fochheimer, ρ est la densité des fluides et β est le coefficient de résistance inertiel. Différents auteurs (Chauveteau and Thirriot 1967; Muskat 1937; Skjetne and Auriault 1999a) ont proposé cette forme de l'équation de Forchheimer. Ils soulignent la différence entre la perméabilité équivalente de Darcy et de Forchheimer. L'équation de Forchheimer est habituellement employée pour décrire le régime de Darcy, le régime d'inertie fort et également la transition entre eux. Cela signifie que la chute de pression est considérée comme somme de deux termes : terme visqueux et inertiel.

La nature non-linéaire et quadratique des équations de Navier-Stokes pour l'écoulement microscopique suggère que la correction moyenne à la loi de Darcy devrait être quadratique, mais une dérivation analytique générale et direct n'a pas été trouvée. Un certain nombre d'arguments apparaissent dans la littérature, mais tous exigent une certaine approximation additionnelle. Par exemple, des méthodes de prise de moyenne exigent des hypothèses pour le problème de fermeture (Ma and Ruth 1993; Whitaker 1996), tandis que dans les dérivations fondées sur "matched asymptotique expansion" (Kaneda 1986) des hypothèses phénoménologies sont nécessaires et elles donc restreintes aux milieux à grande porosité (Cheng and Papanicolaou 1997). Ainsi, à la différence de la transition soudaine de l'écoulement laminaire au turbulent dans les conduites et les canaux, où il y a une valeur critique du nombre de Reynolds séparant les deux régimes, les études expérimentales dans des milieu poreux ont prouvé que le passage du comportement linéaire au non-linéaire peut être progressif. Il a été arguée (Dullien 1992) et confirmé par la simulation numérique (Edwardes, Shapiro, Bar-Yoseph and Shapira 1990; Koch and Ladd 1997) que la contribution de l'inertie à l'écoulement dans le pore devrait également être examinée dans le cadre d'écoulement en régime laminaire avant d'assumer des effets de turbulence entièrement développés.

La simulation numérique récente a clarifié la situation considérablement, plusieurs calcul de l'écoulement traversant des cylindres circulaires trouvent une relation cubique transitoire au petit nombre de Reynolds, suivi d'une loi quadratique à plus grandes valeurs (Edwardes et al. 1990; Koch and Ladd 1997). Par ailleurs, plusieurs auteurs croient (et ont montré) que le début du comportement non linéaire peut être décrit par la loi cubique, que nous appellerons le régime d'inertie faible:

$$-\frac{\Delta P}{L} = \frac{\mu}{K_d} u + \frac{\gamma \rho^2}{\mu} u^3 \tag{1.13}$$

où γ est un paramètre sans dimensions pour le terme non linéaire. Cette équation a été obtenue par des simulations numériques dans un milieu poreux périodique bidimensionnel (Barrere 1990; Amaral Souto and Moyne 1997), et également en employant la technique d'homogénéisation pour des milieux poreux homogènes isotropes (Mei and Auriault 1991; Wodie and Levy 1991). En plus, en réexaminant les premières données (Darcy 1856; Haezn 1895; Chauveteau and Thirriot 1967), Firdaouss and Guermond 1995 ont prouvé que ces expériences sont conformes qualitativement à la loi cubique.

Les régimes d'écoulement observés dans des milieux poreux peuvent être récapitulés comme suit (Skjetne and Auriault 1999a): disparition d'inertie décrite par la loi de Darcy, inertie faible décrite par un terme de correction de troisième ordre (Mei and Auriault 1991; Wodie and Levy 1991), et inertie forte décrite par l'équation de Forchheimer. La loi de Darcy a été soutenue expérimentalement, numériquement et théoriquement. Le même appui fort n'existe pas pour les deux autres équations. L'équation d'inertie faible a un certain appui numérique. Barrere 1990 a observé le terme de troisième ordre pour des nombres de Reynolds plus grand que l'unité, tandis que la théorie est fondée sur l'hypothèse que le nombre de Reynolds est beaucoup plus petit que l'unité. Récemment, Skjetne, Thovert and Adler 1995 a constaté que l'équation d'inertie faible est valide pour les nombres de Reynolds petits en traversant un empilement cubique étroit de sphères et d'autres milieux poreux périodiques. Expérimentalement, un régime d'écoulement à inertie faible est soutenu par les premières données référencées par Muskat 1937 (Skjetne and Auriault 1999b) et également des expériences par Chauveteau and Thirriot 1967 et Rasoloarijaona and Auriault 1994. En bref l'analyse théorique prouve que la correction de la loi de Darcy est un terme cubique de vitesse, même pour des milieux poreux anisotropes pour les nombres de Reynolds (Skjetne and Auriault 1999b) :

$$\varepsilon^{1/2} \ll \mathrm{Re} \ll 1 \tag{1.14}$$

pour l'écoulement à inertie faible.

Dans cette équation le nombre de Reynolds est défini par

$$\mathrm{Re} = \frac{\rho u l}{\mu} \tag{1.15}$$

Où ρ est la masse volumique, u est la vitesse à l'échelle microscopique, l est une longueur caractéristique à l'échelle microscopique (par exemple la taille de grain) et μ est la viscosité dynamique.

Le réexamen des données expérimentales et numériques d'écoulements prouve que l'écoulement à inertie faible et le régime de Forchheimer peuvent être distingués (Skjetne and Auriault 1999a). Le régime à inertie faible se prolonge aux nombres de Reynolds bien au-dessus de l'unité. La forme de la résistance dans un croisement de l'écoulement à inertie faible et Forchheimer dépend fortement de la géométrie.

L'équation de Forchheimer est maintenant l'équation type pour décrire l'écoulement à haute vitesse dans la technologie de pétrole, et également en écoulement à basses vitesses du fait que à cette situation se réduit à la loi de Darcy (Firoozabadi and Katz 1979; Firoozabadi, Thomas and Todd 1995).

En bref l'équation de Forchheimer est une équation empirique qui a été appliquée pendant presque 100 ans dans les études des milieux poreux. Bien qu'il y ait eu plusieurs études numériques à vitesse élevée dans des milieu poreux (Coulaud, Morel and Catagirone 1988; Edwardes et al. 1990; Barrere 1990; Gipouloux 1992; Souto 1993; Ruth and Ma 1993), il y a toujours un manque de justifications théoriques. Ceci est probablement dû à une combinaison de la complexité de l'équation régissant (l'équation de Navier-Stokes) et la géométrie des milieu poreux naturels.

1.3.3 L'origine des effets inertiels

Les mécanismes microscopiques d'écoulement doivent être connus afin de comprendre les phénomènes macroscopiques d'écoulement. En effet l'information détaillée sur l'écoulement microscopique permet une analyse quantitative des causes fondamentales de l'apparition des effets non-linéaires lorsque la vitesse augmente. Malgré les nombreuses tentatives pour clarifier les raisons physiques du comportement non linéaire décrit ci-dessus, ni l'équation de Forchheimer ni l'équation d'inertie faible n'a reçu de justifications physiques.

Outre les travaux visant a fournir une base physique pour la loi de Forchheimer ou plus généralement pour l'équation non-linéaire, des chercheurs se concentrent sur la compréhension de l'origine des l'effets

inertiels. Une diversité d'opinions existent toujours sur cet origine. Actuellement, trois mécanismes sont identifiés pour les causes de la non-linéarité aux débits élevés : turbulence, inertie microscopique, et traînée microscopique. À l'origine, on a cru que les déviations de la loi de Darcy sont dues seulement de la turbulence. C'est en raison de la relation entre la vitesse élevée et le nombre de Reynolds élevé, et entre le nombre de Reynolds élevé et la turbulence. Cependant, les expériences ont indiqué que quand la vitesse de filtration augmente graduellement, les phénomènes non-linéaires apparaissent largement avant le début de la vraie turbulence dans l'écoulement en milieu poreux (Scheidegger 1974; Bear 1972; Dybbs and Edwards 1984). Ces expériences montrent que l'écoulement est non-linéaire aux vitesses où la turbulence n'est pas présente. La plupart sont convaincues que la vitesse accrue peut produire un comportement non-linéaire quand l'écoulement est encore laminaire. Ainsi, il peut être conclu fermement que les déviations de la loi de Darcy ne sont pas directement liées aux changements de régimes d'écoulement.

Hassanizadeh and Gray 1987 ont conclu que la force visqueuse microscopique est la source du début de la non-linéarité. En contradiction, Barak 1987 a discuté la formation des vortex locaux et le développement des lignes de courant tortueux à l'intérieur des pores avec l'augmentation du nombre de Reynolds et a attribué la non-linéarité aux forces d'inertie microscopiques. Cette opinion a été soutenue par plusieurs autres chercheurs (e.g. Schneebeli 1955; Bear 1972; Hubbert 1956; Scheidegger 1974; Geertsma 1974; Happel and Brenner 1983; MacDonald, El-Sayed, Mow and Dullien 1979; Cvetkovic 1986; Du Plessis and Masliyah 1988; Coulaud et al. 1988; Mei and Auriault 1991). En examinant quelques modèles d'écoulements dans des tubes en milieux poreux, Ruth et Ma Auriault 1987 ont démontré que les termes d'inertie microscopiques (moyenne) ne peuvent pas mener à une représentation complète des effets inertiels et ont recommandé que le régime d'écoulement inertiel soit décrit par un nombre de Forchheimer dans le traitement de perméabilité comme paramètre dépendant de la vitesse.

Finalement, un troisième point de vue attribue l'élévation du terme non-linéaires aux effets des forces de traînée microscopiques accrues sur les pores (e.g., Firoozabadi and Katz 1979; Slattery 1972). Bien que l'opinion sur le mécanisme responsable du début de la non-linéarité soit diverse, la littérature concorde sur le fait que les effets inertiels peuvent être entièrement compris seulement par l'analyse de l'écoulement microscopique.

1.3.4 La limite de validité de la loi de Darcy

Après l'expérience de Reynolds et sa mis en évidence des effets non-linéaires sur les écoulements, il apparaît clairement que le paramètre approprié dans l'expérience de Darcy n'est pas la vitesse de filtration mais le nombre de Reynolds, et que la déviation à la loi de Darcy est induite par des effets d'inertie.

Le nombre sans dimension de Reynolds (Re), habituellement employé pour caractériser le début du comportement non linéaire est défini comme rapport entre l'accélération et les forces visqueuses à l'échelle microscopique. Puisque le nombre de Reynolds de pore n'est pas habituellement connu, on emploie typiquement un nombre de Reynolds moyen basé sur la vitesse moyenne au lieu de la vitesse de pore. Une discussion sur l'importance du choix de la définition du nombre de Reynolds est menée au chapitre 2.

Des valeurs critiques rapportées dans la littérature sont déduites des simulations expérimentales ou numériques en analysant des équations à l'échelle macroscopiques et dépendent des caractéristiques utilisées dans la définition des Re.

De nombreuses expériences de laboratoire et études numériques ont été consacrées à la détermination du nombre de Reynolds au delà du quel la loi de Darcy n'est plus valable. En général, cette limite a été déterminée au moyen d'une valeur critique pour le nombre de Reynolds, au delà duquel le gradient de pression n'est plus proportionnel à la vitesse d'écoulement. Les valeurs critiques des Re (basés sur la vitesse moyenne et la taille de grain, équation (1.15)) correspondant au début de l'écoulement non-linéaire, selon la plupart des expériences, s'étendent entre 1 et 15. Les valeurs typiques indiquées par divers chercheurs sont 1 par Tek 1957, 2 par Wright 1968, 5 par De Vries 1979 , et entre 1 et 10 par Dybbs and Edwards

1984. En outre, les expériences numériques comprenant la solution des équations de Navier-Stokes dans un pore de milieu poreux idéalisé indiquent que le nombre de Reynolds est entre 5 et 13 (e.g., Stark 1972; Coulaud et al. 1988).

Jusque à nombre des Reynolds approximativement égaux à 100, le régime d'écoulement demeure laminaire. Cette limite, comme la limite supérieure du régime laminaire linéaire est plutôt approximative. Elle dépend fortement de la géométrie des pores, et le nombre de Reynolds seul ne peut pas définir de manière simple les paramètres d'écoulement. Pour des nombres de Reynolds plus élevés, l'écoulement devient turbulent.

1.4 Ecoulements diphasiques inertiels

Bien que la discussion sur les modèles appropriés pour le traitement de non-linéarités en écoulements monophasiques ne soit pas close, de nombreux travaux s'intéressent aux effets inertiels rencontrés lors des écoulements à deux phases.

Dans le cas des écoulements diphasiques en milieu poreux à nombre de Reynolds très faible, le modèle physique d'écoulement le plus largement admis et justifié théoriquement est celui de Darcy généralisé (Muskat 1937; Whitaker 1986b). Pour les nombres de Reynolds élevés, celui-ci est mis en défaut du fait de termes inertiels significatifs dans le modèle de base à l'échelle du pore. Cependant, il n'y a pas eu à ce jour de formalisation théorique complète d'un modèle à l'échelle du bloc de milieu poreux.

Dans ce travail, nous nous proposons d'obtenir, en utilisant la méthode prise de moyenne volumique, sous certaines contraintes précisées dans le texte, un modèle macroscopique pour les écoulements inertiels diphasiques en milieux poreux. Ce modèle comporte pour chaque phase, des termes de Darcy incluant du couplage entre phases, ainsi que des termes inertiels. Ces derniers faisant aussi intervenir du couplage.

Dans la littérature, de manière largement empirique, un modèle classiquement utilisé est celui de Darcy-Forchheimer généralisé. Il est basé d'une part sur le modèle monophasique de Darcy-Forchheimer (Forchheimer 1901) établi depuis de manière théorique (Whitaker 1996; Skjetne and Auriault 1999b) et d'autre part sur une généralisation au cas diphasique comme celle qui s'applique en régime de Darcy. Ce modèle qui fait appel à une correction quadratique en vitesse est admis dans ce travail et fait l'objet d'une étude numérique au chapitre 4.

1.4.1 Simulation numérique de l'écoulement diphasique

Nous nous intéressons, au chapitre 4, à la modélisation numérique des écoulements inertiels diphasiques en milieux poreux hétérogènes. Le modèle retenu est celui de Darcy-Forchheimer généralisé, qui, après une reformulation ad-hoc conduit à un problème similaire à de celui de Darcy. Pour cette raison, nous rappelons les principales approches utilisées dans ce dernier cas.

Historiquement, il y a deux approches principales pour modéliser l'écoulement multiphasique dans des applications hydrologiques ou dans celles liées à la récupération pétrolière. Ces deux approches, intensivement employées pour l'écriture des équations, sont l'approche à deux-pressions et l'approche en débits fractionnaires. L'approche des équations à deux-pressions a été largement répandue dans la littérature hydrologique. Dans cette approche, les équations sont écrites en termes de pression dans chacune des deux phases par une substitution directe de l'équation de Darcy dans les équations de bilan de masse pour chaque phase.

L'approche en débits fractionnaires provient de la littérature pétrolière et utilise la saturation d'une des phases et une pression comme variables indépendantes. Cette approche traite le problème d'écoulement multiphasique à travers une vitesse totale qui est la somme des vitesses de chaque phase. Cette approche mène à deux équations : l'équation de pression (elliptique), et l'équation de saturation (hyperbolique).

En écoulement unidimensionel et incompressible, en l'absence de capillarité, l'équation de saturation peut être résolue analytiquement, comme proposé par Buckley-Leverett. Dans des dimensions plus élevées, des méthodes numériques deviennent nécessaires. De nombreux méthodes et schémas numériques sont proposés. Nos choix numériques seront précisés au chapitre 4.

1.5 Objectif de l'étude

L'objet de cette étude est l'écoulement rapide (hors régime de Darcy ou inertiel) à une et deux phases en milieu poreux hétérogène dont les applications sont dans le domaine de la récupération pétrolière et du génie chimique. Le manuscrit est organisé sous forme de trois projet d'articles rédigés en Anglais. Une annexe au chapitre 4 est proposée en fin de manuscrit.

Dans le chapitre 2, on s'appuie sur le changement d'échelle pour l'écoulement inertiel monophasique en milieu poreux homogène traité du point de vue théorique à l'aide de la méthode de prise de moyenne volumique par Whitaker 1996. L'écoulement et le problème de fermeture associé sont résolus à l'aide d'un solveur pour le problème de Navier-Stokes. Le vecteur de correction à la loi de Darcy est étudié à travers des simulations numériques sur des structures modèles 2D. Pour un milieu ordonné, le comportement de cette correction en fonction du nombre de Reynolds est étudié pour différentes porosités et orientations du gradient de pression. On étudie par ailleurs, le rôle du désordre sur les régimes d'écoulement permettant d'envisager des conclusions pour des géométries de milieux poreux réalistes.

Le chapitre 3 est consacré à un travail théorique traitant le changement d'échelle de l'écoulement diphasique inertiel en milieu poreux homogène. En partant des équations de Navier-Stokes pour chaque phase, nous développons, sous certaines contraintes précisées, un modèle macroscopique pour l'écoulement inertiel diphasique en milieu poreux.

Dans le chapitre 4, nous nous somme principalement intéressés à la simulation numérique des écoulements diphasiques inertiels en milieux poreux hétérogènes. Les choix numériques sont précisés et le modèle développé est présenté et validé. Les résultats pour des configurations homogènes et hétérogènes mono et bidimensionnels sont présentés et discutés avec un accent sur les effets inertiels.

Le dernier chapitre est consacré aux conclusions et perspectives du travail.

Bibliography

Ahmed, N. and Sunada, D. K.: 1969, Nonlinear flow in porous media, *J. Hydr. Div ASCE* **95**(HY6), 1847–1857.

Amaral Souto, H. and Moyne, C.: 1997, Dispersion in two-dimensional periodic porous media, part i: Hydrodynamics, *Phys Fluids* **9**(8), 2243–2252.

Anderson, T. B. and Jackson, R.: 1967, A fluid mechanical description of fluidised beds, *Ind. Eng. Chem. Fundam.* **6**, 527–538.

Auriault, J. L.: 1987, Nonsaturated deformable porous media: Quasisatics, *Transport in porous media* **2**(1), 45–64.

Azzam, M. I. S. and Dullien, A. L.: 1973, Flow rate-pressure gradient measurements in periodically nonuniform capillary tubes, *AIChE J.* **19**, 222–229.

Barak, A. Z.: 1987, Comments on high velocity flow in porous media by hassanizadeh and gray, *Transport in Porous Media* **2**(6), 533–535.

Barak, A. Z. and Bear, J.: 1981, Flow at high reynolds numbers through anisotropic porous media, *Adv. Water Resources* **4**, 54–66.

Barrere, J.: 1990, *Modélisation Des Écoulement de Stokes et de Navier-Stokes En Milieu Poreux*, PhD thesis, Thèse de l'université Bordeaux I.

Bear, J.: 1972, *Dynamics of Fluids in Porous Media*, Dover, New York.

Bensoussan, A., Lions, J. L. and Papanicolaou, G.: 1978, Asymptotic analysis for periodic structures, *North-Holland* .

Blick, E. F.: 1966, Capillary orifice model for high speed flow through porous media, *I and EC, Process Design and Development* **5**, 90–94.

Chauveteau, G. and Thirriot, C.: 1967, Régimes d'écoulement en milieu poreux et limite de la loi de darcy, *La Houile Blanche* **1**(22), 1–8.

Cheng, H. and Papanicolaou, G.: 1997, Flow past periodic arrays at spheres at low reynolds number, *J. Fluid. Mech* **335**, 189–212.

Cornell, D. and Katz, D. L.: 1953, Flow of gases through consolidated porous media, *Ind. Eng. Chem.* **45**, 2145–2153.

Coulaud, O., Morel, P. and Catagirone, J. P.: 1988, Numerical modeling of non-linear effects in laminar flow through a porous medium, *J. Fluid. Mech.* **190**, 393–407.

Cvetkovic, V. D.: 1986, A continuum approach to high velocity flow in a porous medium, *Transport in Porous Media* **1**(1), 63–97.

Darcy, H.: 1856, Les fontaines publiques de la ville de dijon, *Librairie des corps impériaux des ponts et chaussées et des mines, Paris* .

De Vries, J.: 1979, Prediction of non-darcy flow in porous media, *J. Irrig. Drain. Div., ASCE IR2* pp. 147–162.

Du Plessis, J. P. and Masliyah, J. H.: 1988, Mathematical modelling of flow through consolidated isotropic media, *Transport in Porous Media* **3**(2), 145–161.

Dullien, A. L. and Azzam, M. I. S.: 1973, Flow rate-pressure gradient measurement in periodically nonuniform capillary tube, *AIChE J.* **19**, 222–229.

Dullien, F. A. L.: 1992, *Porous Media-Fluid Transport and Pore Structure*, Academic Press, Inc.

Dupuit, J.: 1863, Etudes théoriques et pratiques sur le mouvement des eaux, *Dunod, Paris* .

Dybbs, A. and Edwards, R. V. A.: 1984, A new look at porous media fluid mechanics darcy to turbulent, *Fundamentals of Transport Phenomena in Porous Media* **82**, 201–256. in NATO ASIE, Martinus Nijhoff Publishers, Dordrecht.

Edwardes, D. A., Shapiro, M., Bar-Yoseph, P. and Shapira, M.: 1990, The influence of reynolds number upon the apparent permeability of spatially periodic arrays of cylinders, *Phys. Fluids A* **2**(1), 45–55.

Ergun, S.: 1952, Fluid flow through packed columns, *Chem. Eng. Prog.* **48**, 89–94.

Firdaouss, M. and Guermond, J. L.: 1995, Sur l'homogénéisation des équations de navier-stokes à faible nombre de reynolds, *C. R. Acad. Sci. Paris, Série I* **320**, 245–251.

Firoozabadi, A. and Katz, D. L.: 1979, An analysis of high-velocity gas flow through porous media, *Journal of petroleum Technology* **February 1979**, 211–216.

Firoozabadi, A., Thomas, L. K. and Todd, B.: 1995, High-velocity flow in porous media, *SPE Reservoir Engineering* **10**, 149–152.

Forchheimer, P.: 1901, Wasserbewgung durch boden. z., *Vereines deutscher ingnieure* **XXXXV**(45), 1782–1788.

Geertsma, J.: 1974, Estimating the coefficient of inertial resistant in fluid flow through porous media, *Society of Petroleum Engineers Journal* **October 1974.**, 445–450.

Gipouloux, O.: 1992, *Contribution Numérique À L'homogénéisation Des Équation de Stokes et de Navier-Stokes En Milieu Poreux*, PhD thesis, Université de Bordeaux I.

Green, L. and Duwez, P. J.: 1951, Fluid flow through porous metals, *J. Appl. Mech.* **18**, 39–45.

Haezn, A.: 1895, *The Filtration of Public Water-Supplies*, Wiley.

Hannoura, A. A. and Barends, F. B. J.: 1981, Non-darcy flow, a state of art, *Proc. Euromech* **143**, 37–51. Verruiji and F. B. J. barends (eds).

Happel, J. and Brenner, H.: 1983, *Low Reynolds Number Hydrodynamics*, Prentice-Hall, Englewood Cliffs, NJ.

Hassanizadeh, S. M. and Gray, W. G.: 1987, High velocity flow in porous media, *Transport in Porous Media* **2**(3), 521–531.

Hubbert, M. K.: 1956, Darcy's law and the field equation of the flow of underground fluids, *Trans. SPE of AIME* **207**, 222– 239. (JPT).

Irmay, S.: 1958, On the theoretical derivation of darcy and forchheimer formulas, *J. Geophys. Res.* **39**, 702–707.

Kaneda, Y.: 1986, The drag on a sparse random array of fixed spheres in flow at small but finite reynolds number, *J. fluid Mech.* **167**, 455–463.

Knupp, P. M. and Lage, J. L.: 1995, Generalization of the forchheimer-extend darcy flow model to the tensor permeability case via a varitional principale, *J. Fluid Mech.* **299**, 97–107.

Koch, J. B. and Ladd, A. J. C.: 1997, Moderate reynolds number flows through periodic and random arrays of aligned cylinders, *J. fluid Mech.* **349**, 31–66.

Lee, R. L., Logan, R. W. and Tek, M. R.: 1987, Effect of turbulence on transient flow of real gas through porous media, *SPE Format, Eval.* pp. 108–120.

Ma, H. and Ruth, D. W.: 1993, The microscopic analysis of high forchheimer number flow in porous media, *Transport in Porous Media* **13**(2), 139–160.

MacDonald, I. F., El-Sayed, M. S., Mow, K. and Dullien, F. A. L.: 1979, Flow through porous media, the ergun equation revisited, *Ind. Eng. Chem. Fundm* **18**(3), 199–208.

Marle, C. M.: 1967, Ecoulement monophasique en milieu poreux, *Rev. Inst. Francais du Pétrole* pp. 1471–1509.

Matheron: 1965, *Les Variables Régionalisées et Leur Estimation: Une Application de la Théorie Des Fonctions Aléatoires Aux Science de la Nature*, Masson, Paris.

Mei, C. C. and Auriault, J. L.: 1991, The effect of weak inertia on flow through a porous medium, *J. Fluid Mech* **222**, 647–663.

Muskat, M.: 1937, The flow of homogeneous fluids through porous media, *International Human Ressources development* .

Plumb, O. A. and Whitaker, S.: 1988, Dispersion in hetrogeneous porous media, i. local volume averaging and large scale averaging, *Water Resources Research* **24**(7), 913–926.

Quintard, M. and Whitaker, S.: 1987, Ecoulement momophasique en milieu poreux: Effet des hétérogénéités locales, *J. Mech. Théor. et Appl.* **6**, 691–726.

Quintard, M. and Whitaker, S.: 1988, Two-phase flow in heterogeneous porous media: The method of large-scale averaging, *Transport in Porous Media* **3**(4), 357–413.

Quintard, M. and Whitaker, S.: 1990a, Two-phase flow in heterogeneous porous media, i. the influence of large spatial and temporal gradients, *Transport in Porous Media* **5**(4), 341–379.

Quintard, M. and Whitaker, S.: 1990b, Two phase flow in heterogenous porous media II: Numerical experiments for flow perpendicular to a stratified system, *Transport in porous media* **5**(5), 429–470.

Quintard, M. and Whitaker, S.: 1994a, Transport in ordered and disordered porous media i: The cellular average and the use of weighting functions, *Transport in Porous Media* **14**(2), 163–177.

Quintard, M. and Whitaker, S.: 1994b, Transport in ordered and disordered porous media II: Generalized volume averaging, *Transport in Porous Media* **14**(2), 179–206.

Rasoloarijaona, M. and Auriault, J. L.: 1994, Nonlinear seepage flow through a rigid porous medium, *Eur. J. Mech. B/Fluids* **13**(2), 177–195.

Ruth, D. and Ma, H.: 1993, Numerical analysis of the viscous incompressible flow in a diverging-converging RUC, *Transport in Porous Media* **13**(2), 161–177.

Sanchez-Palencia, E.: 1980, *Non Homogeneous Media and Vibration Theory, Lecture Notes in Physics*, Springer.

Scheidegger, A. E.: 1974, *The Physics of Flow Through Porous Media*, University of Toronto Press, Toronto, Canada.

Schneebeli, G.: 1955, Expériences sur la limite de validité de la loi de darcy et l'apparition de la turbulence dans un écoulement de filtration, *La Houille Blanche* **2**(10), 141–149.

Skjetne, E. and Auriault, J. L.: 1999a, High-velocity laminar and turbulent flow in porous media, *Transport in Porous Media* **36**(2), 131–147.

Skjetne, E. and Auriault, J. L.: 1999b, New insights on steady, non-linear flow in porous media, *Eur. J. Mech. B/Fluids* **18**(1), 131–145.

Skjetne, E., Hansen, A. and Gudmundsson, J. S.: 1995, High-velocity flow in a rough fracture, pp. 83–124. In Dr. Ing. Thesis by Skjetne E., High-velocity flow in porous media; analytical, numerical and experimental studies, Department of Petroleum Engineering and Applied Geophysics, Norwegian University of Science and Technology.

Skjetne, E., Thovert, J. F. and Adler, P. M.: 1995, *High-Velocity Flow in Spatially Periodic Porous Media*, PhD thesis. In Dr. Ing. Thesis by Skjetne E., High-velocity flow in porous media; analytical, numerical and experimental studies, Department of Petroleum Engineering and Applied Geophysics, Norwegian University of Science and Technology.

Slattery, J.: 1967, Flow of viscoelastic fluids through porous media, *AIChE Journal* **13**, 1066–1071.

Slattery, J.: 1972, *Momentum, Energy, and Mass Transfer in Continua*, McGraw-Hill, New York.

Souto, H. P. A.: 1993, *Diffusion-Dispersion En Milieux Poreux: Étude Numérique Du Tenseur de Dispersion Pour Quelques Arrangements Périodiques Bidimensionnels: Ordonnés et Désordonnés*, PhD thesis, Institut National de Lorraine.

Stark, K. P.: 1972, A numerical study of the nonlinear laminar regime of flow in an idealized porous medium, *IAHR, Fundamentals of transport phenomena in porous media* pp. 86–102.

Swift, G. W. and Kiel, O. G.: 1962, The prediction of gas-well performance including the effects of non-darcy flow, *J. Petrol. Technol. Trans. AIME* **222**, 791–798.

Tek, M. R.: 1957, Development of a generalized darcy equation, *Trans. AIME* **210**, 376–377.

Tek, M. R., Coats, K. H. and Katz, D. L.: 1962, The effect of turbulence on flow of natural gas through porous reservoirs, *J. Petrol. Technol. Trans. AIME* **222**, 799–806.

Ward, J. C.: 1964, Turbulent flow in porous media, *J. Hydr. Div., ASCE* **90**(HY5), 1–12.

Whitaker, S.: 1967, Diffusion and dispersion in porous media, *AIChE J.* **13**, 420–427.

Whitaker, S.: 1969, Advances in the theory of fluid motion in porous media, *Ind. Eng. Chem.* **12**(3), 14–28.

Whitaker, S.: 1986a, Flow in porous media i: A theoretical derivation of darcy's law, *Transport in Porous Media* **1**(1), 3–25.

Whitaker, S.: 1986b, Flow in porous media II: The governing equation for immiscible two-phase flow, *Transport in Porous Media* **1**(1), 105–125.

Whitaker, S.: 1996, The forchheimer equation: A theoretical development, *Transport in Porous Media* **25**(1), 27–61.

Wodie, J. C. and Levy, T.: 1991, Correction non linéaire de la loi de darcy, *C. R Acad. Sci. Paris II* pp. 157–161.

Wright, D. E.: 1968, Nonlinear flow through granular media, *J. Hydr. Div. ASCE* **4**, 851–872.

Chapitre 2

The correction to Darcy's law for inertial flow in porous media: a numerical investigation

The correction to Darcy's law for inertial flow in porous media: a numerical investigation

Abstract

The purpose of this paper is to analyze the inertial correction to Darcy's law during one-phase Newtonian incompressible flow in model 2D periodic structures over a wide range of Reynolds numbers. The analysis is based on the volume averaged form of the Navier-Stokes equation requiring the solution of both the flow and associated closure problem. Weak and strong inertia regimes as well as the transition between the two are investigated through comprehensive numerical simulations. For ordered structures, the dependence of the correction on porosity and on the orientation of the pressure gradient is studied. Further conclusive results are obtained from the introduction of structural disorder.

1 Introduction

It is now well established that the classical Darcy's law used to describe one phase flow in a homogeneous non deformable porous medium and given by

$$\langle \mathbf{v}_\beta \rangle = -\frac{\mathbf{K}}{\mu_\beta} \cdot \left(\boldsymbol{\nabla} \langle p_\beta \rangle^\beta - \rho_\beta \mathbf{g} \right) \tag{1}$$

$\langle \mathbf{v}_\beta \rangle$ being the seepage or Darcy velocity, $\boldsymbol{\nabla} \langle p_\beta \rangle^\beta$ the macroscopic pressure gradient and $\mathbf{K}$ the permeability tensor, only holds when the pore-scale flow occurs in the creeping regime. The equivalent macroscopic constraint is that the Reynolds number, usually defined as

$$\mathrm{Re} = \frac{\rho_\beta \langle v_\beta \rangle d}{\mu_\beta} \tag{2}$$

d being a typical grain size of the porous medium, remains small compared to unity. Here we have used μ_β and ρ_β to represent the dynamic viscosity and density of the β-phase and $\mathbf{g}$ for the gravitational acceleration. Originally obtained from experiments (Darcy, 1856) and later formalized using upscaling techniques (Sanchez-Palencia, 1980; Whitaker, 1986), equation (1) must be reconsidered when inertial effects become significant. Active research has been dedicated to derive adequate corrections to the linear relationship in (1) from numerical, theoretical and experimental points of view since the early work of Forchheimer (Forchheimer, 1901) where ad hoc 1D relationships of the form

$$\frac{\partial \langle p_\beta \rangle^\beta}{\partial x} = -\alpha \langle v_\beta \rangle - \rho_\beta \beta \langle v_\beta \rangle^m \tag{3}$$

or

$$\frac{\partial \langle p_\beta \rangle^\beta}{\partial x} = -\alpha \langle v_\beta \rangle - \rho_\beta \beta \langle v_\beta \rangle^2 - \rho_\beta^2 \gamma \langle v_\beta \rangle^3 \tag{4}$$

obtained on an empirical basis were proposed (see Chauveteau (1965) for a literature review on these empirical models and experimental works). While α, β and γ were considered as parameters intrinsic to the medium, the exponent m in equation (3) was identified to a value close to 2 (Lindquist, 1933; Green and Duwez, 1951; Cornell and Katz, 1953; Schneebeli, 1955). This popular form has been considered as a valid

one, either from comparison to experimental data (Ergun, 1952; Ward, 1964; Beavers and Sparrow, 1969; Dullien and Azzam, 1973; MacDonald et al., 1979), theoretical derivation (Irmay, 1958; Blick, 1966; Ahmed and Sunada, 1969; Cvetkovic, 1986; Hassanizadeh and Gray, 1987; Ruth and Ma, 1993b; Giorgi, 1997; Chen et al., 2001) or computational results (Coulaud et al., 1988; Ma and Ruth, 1993; Ruth and Ma, 1993a; Thauvin and Mohanty, 1998; Papathanasiou et al., 2001; Fourar et al., 2004). It has been extensively used in petroleum and chemical engineering applications for several decades (Bear, 1972; Scheidegger, 1974; Geertsma, 1974). Deviation to (1) starting at Re between 1 and 15 as observed by almost all authors (Tek, 1957; Wright, 1968; Dybbs and Edwards, 1984) has been attributed to turbulence (Tek et al., 1962) until the late 60's. The physical justification of the quadratic nature of the correction was supported either by intuition or dimensional analysis and the analogous turbulent kinetic energy loss in straight tubes. After a classification of flow regimes (Chauveteau and Thirriot, 1967) indicating that turbulence was not the origin of the deviation to the linearity of (1), experimental and unsteady numerical simulation evidence of the onset of turbulence for Re on the order of 100 was demonstrated (Dybbs and Edwards, 1984; Ghaddar, 1995; Koch and Ladd, 1997). During the early 90's, a careful attention to the onset of deviation to (1) was reported in both numerical and theoretical works, questioning the quadratic dependence of the correction. Numerical simulation results obtained on model structures made of regular arrays of cylinders of circular cross section lead to $m = 3$ in (3) (Barrere, 1990). This result was confirmed independently from a theoretical point of view using double scale homogenization (Wodie and Levy, 1991; Mei and Auriault, 1991; Rasoloarijaona and Auriault, 1994; Skjetne and Auriault, 1999a) in the range $\epsilon^{1/2} \lesssim \mathrm{Re} \lesssim 1$ where ϵ is the porosity (note that Re here is based on the characteristic pore dimension). This so-called *weak inertia regime* was first obtained in the case of periodic homogeneous and isotropic media but was further extended to the case of anisotropic ones with the restriction of invariance while reversing the flow direction (Firdaouss and Guermond, 1995; Firdaouss et al., 1997), although this last constraint was relaxed in Skjetne and Auriault (1999b). Further numerical simulations confirmed this result (Koch and Ladd, 1997; Amaral Souto and Moyne, 1997; Rojas and Koplik, 1998; Skjetne et al., 1999) and lead to a classification of the non-linear deviation to Darcy's law involving -at least- three different regimes separated by transitions (Skjetne and Auriault, 1999b): i) the *weak inertia regime* which appears at the onset of non-linearity and where the correction term scales as a $\langle v_\beta \rangle^3$ ($\epsilon^{1/2} \lesssim \mathrm{Re} \lesssim 1$), ii) a *strong inertia regime* where the correction is quadratic in $\langle v_\beta \rangle$, i.e. a Forchheimer type of correction ($\mathrm{Re} \gtrsim 1$ to 10), iii) turbulence which will not be discussed further in the present work ($\mathrm{Re} \gtrsim O(100)$).

Precise physical justification of these cubic and quadratic dependences are still a matter of questioning (Skjetne and Auriault, 1999a). Since macroscopic inertial forces are clearly weak compared to viscous ones (Hassanizadeh and Gray, 1987; Ma and Ruth, 1993; Whitaker, 1996), non-linearity in the drag-velocity relationship must originate from microscopic inertial and viscous forces. Invoking the former as the dominant effect (Happel and Brenner, 1983; Suekane et al., 2003) is justified by i) streamlines deformation resulting from bends in flow paths (i.e. tortuosity) (Hayes et al., 1995), and in constrictions and enlargements, ii) backflow as well as flow separation yielding form drag, iii) fluid flow channeling which gradually disappears with increasing Re leading to a strong modification of kinetic energy loss distribution within the medium (Andrade et al., 1999). Non-linearity resulting from viscous drag can be justified by the development of boundary layers at pore walls as observed experimentally (Dybbs and Edwards, 1984) giving rise to inertial core flow at the pore scale. Due to boundary layers growing with increasing Re, local velocity in the cores increases non-linearly. Coupling between inertial and viscous effects must also be considered with the dissipation in recirculation zones (Ruth and Ma, 1993a). This coupling has recently lead to propose a correction to (1) in a complex empirical exponential form rather than a polynomial one (Panfilov and Fourar, 2006).

Even if the flow classification under the Darcy, weak and strong inertia regimes has been widely admitted, the dependence of the transition between these different regimes, when they can be identified, upon structural properties of the medium such as porosity, disorder and anisotropy has not been yet documented. Moreover, as shown in many theoretical developments (Barak and Bear, 1981; Hassanizadeh and Gray, 1987; Mei and Auriault, 1991; Wodie and Levy, 1991; Whitaker, 1996; Giorgi, 1997), the non-linear correction to (1) involves a correction tensor. However, all reported numerical (and experimental) analyses of this correction are performed on the velocity magnitude in a scalar fashion. Our purpose in

this work is to shed light on these two aspects of the problem that are of pratical major importance. On the one hand, inspecting the tensorial form of the macroscopic inertial flow is not only useful to analyze the anisotropic character of the non-Darcy part of the flow but is required in the perspective of a second up-scaling over a heterogeneous medium involving different regions, each of them being characterized by its non-Darcy correction (and permeability) tensors. On the other hand analyzing the evolution of the different regimes when they can be reasonably distinguished as well as the transition between them versus structural parameters of the medium is also necessary to help understanding the physical origin of these regimes and refine the macroscopic description of the flow.

Since analytical solutions to the Navier-Stokes problem are restricted to simple geometries, at asymptotically small Reynolds numbers and in the limits of very dilute or very concentrated arrays, most of the time making use of the Oseen's approximation, we chose to perform comprehensive direct numerical simulations in the Reynolds ranges 0-150 (regular arrays) and 0-30 (disordered arrays), and for porosities between 0.3 and 0.75. The analysis is performed on the basis of a theoretical derivation of the macroscopic mass and momentum equations obtained by volume averaging the incompressible one-phase Navier-Stokes problem (Whitaker, 1996).

The paper is organized as follows. In section 2, we shortly recall the macroscopic model and the associated closure problems yielding both the permeability and correction tensors. Results are reported and discussed in section 3 after a short presentation of the numerical method used to compute the two tensors along with validation and precision tests. Computations were carried out with special attention to high accuracy in order to investigate the existence of the different regimes, the scaling laws in these regimes as well as the transition (or crossover) between them versus flow orientation and structural parameters, namely porosity and disorder. This was performed on 2D model structures of a porous medium corresponding to regular, weakly and strongly disordered arrays of parallel cylinders of square cross sections.

2 Governing equations

2.1 Microscopic boundary value problem and macroscopic model

The single-phase flow of an incompressible Newtonian fluid β is considered in a macroscopic region of a rigid porous medium as illustrated in figure 1. The boundary value problem describing the process at the microscopic (pore) scale is given by the classical mass and momentum (Navier-Stokes) balance equations

$$\rho_\beta\left(\frac{\partial \mathbf{v}_\beta}{\partial t} + \mathbf{v}_\beta \cdot \boldsymbol{\nabla}\mathbf{v}_\beta\right) = -\boldsymbol{\nabla} p_\beta + \rho_\beta \mathbf{g} + \mu_\beta \boldsymbol{\nabla}^2 \mathbf{v}_\beta \tag{5}$$

$$\boldsymbol{\nabla} \cdot \mathbf{v}_\beta = 0 \tag{6}$$

with the boundary conditions

$$\mathbf{v}_\beta = 0 \qquad \text{at } A_{\beta\sigma} \tag{7}$$

$$\mathbf{v}_\beta = \mathbf{f}(\mathbf{r}, t) \qquad \text{at } A_{\beta e} \tag{8}$$

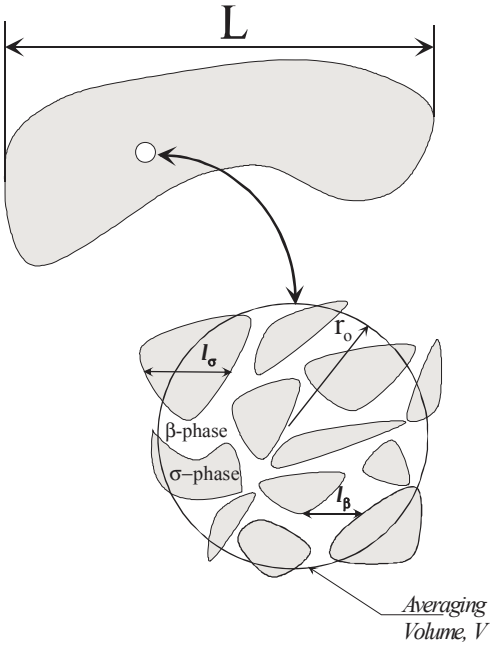

Figure 1: Macroscopic region and local averaging volume

In these equations $\mathbf{v}_\beta$ and p_β are respectively the velocity and total pressure of the β-phase; $A_{\beta\sigma}$ represents the interface area between the β-phase and the solid phase σ contained within the macroscopic region, while $A_{\beta e}$ represents the β-phase entrances and exits of the macroscopic region.

Up-scaling of this problem was proposed by Wodie and Levy (1991) and Mei and Auriault (1991) using the double scale homogenization under the restriction $\mathrm{Re} \ll 1$ and more recently by Whitaker (1996) using the volume averaging method. In this latter work, it was demonstrated that the macroscopic model is given by

$$\boldsymbol{\nabla} \cdot \langle \mathbf{v}_\beta \rangle = 0 \tag{9}$$

$$\langle \mathbf{v}_\beta \rangle = \frac{-\mathbf{K}}{\mu_\beta} \cdot \left(\boldsymbol{\nabla} \langle p_\beta \rangle^\beta - \rho_\beta \mathbf{g} \right) - \mathbf{F} \cdot \langle \mathbf{v}_\beta \rangle \tag{10}$$

where $\mathbf{K}$ (having the dimension of m^2) and $\mathbf{F}$ (dimensionless) are the permeability and Darcy's law correction tensors respectively and in which the following definitions of the superficial and intrinsic phase averages of any quantity ψ_β associated to the β-phase are respectively given by

$$\langle \psi_\beta \rangle = \frac{1}{V} \int_{V_\beta} \psi_\beta dV \tag{11}$$

and

$$\langle \psi_\beta \rangle^\beta = \varepsilon^{-1} \langle \psi_\beta \rangle = \frac{1}{V_\beta} \int_{V_\beta} \psi_\beta dV \tag{12}$$

In this last relationship, V_β represents the volume of the β-phase contained within the averaging volume, V at least as large as the Representative Elementary Volume (REV) of the structure (see figure 1) and

$$\varepsilon = \frac{V_\beta}{V} \tag{13}$$

is the porosity of the medium.

The macroscopic model in equations (9) and (10) remains valid provided two constraints are satisfied. First, scale hierarchy must be such that

$$l_\beta \ll r_0 \ll L \tag{14}$$

where l_β is the characteristic length-scale in the β-phase (pore diameter), r_0 is the radius of the averaging volume and L is the macroscopic length-scale (see figure 1). Second the characteristic time t^* at which the process is observed must satisfy

$$\frac{\mu_\beta t^*}{\rho_\beta l_\beta^2} \gg 1 \tag{15}$$

or equivalently

$$\frac{\rho_\beta \left|\langle \mathbf{v}_\beta \rangle^\beta\right| l_\beta}{\mu_\beta}(l_\beta/L) \ll 1 \tag{16}$$

for the quasi-steady nature of the macroscopic flow to hold. Under these circumstances, and within the framework of a spatially periodic model of a porous medium, $\mathbf{K}$ and $\mathbf{F}$ can be explicitly determined from the solution over the unit cell of the periodic structure (period l_i, $i = 1, 3$) of two closure problems respectively given by (Barrère et al., 1992; Whitaker, 1996; Whitaker, 1999):

$$\begin{cases} 0 = -\boldsymbol{\nabla}\mathbf{d} + \boldsymbol{\nabla}^2\mathbf{D} + \mathbf{I} \\ \boldsymbol{\nabla}\cdot\mathbf{D} = 0 \\ \mathbf{D} = 0 \qquad \text{at } A_{\beta\sigma} \\ \mathbf{d}(\mathbf{r}+l_i) = \mathbf{d}(\mathbf{r}) \qquad \mathbf{D}(\mathbf{r}+l_i) = \mathbf{D}(\mathbf{r}) \qquad i = 1,2,3 \end{cases} \tag{17}$$

$$\langle \mathbf{D} \rangle = \mathbf{K} \tag{18}$$

$$\begin{cases} \frac{\rho_\beta \mathbf{v}_\beta}{\mu_\beta}\cdot\boldsymbol{\nabla}\mathbf{M} = -\boldsymbol{\nabla}\mathbf{m} + \boldsymbol{\nabla}^2\mathbf{M} + \mathbf{I} \\ \boldsymbol{\nabla}\cdot\mathbf{M} = 0 \\ \mathbf{M} = 0 \qquad \text{at } A_{\beta\sigma} \\ \mathbf{m}(\mathbf{r}+l_i) = \mathbf{m}(\mathbf{r}) \qquad \mathbf{M}(\mathbf{r}+l_i) = \mathbf{M}(\mathbf{r}) \qquad i = 1,2,3 \end{cases} \tag{19}$$

$$\langle \mathbf{M} \rangle = \mathbf{H} \tag{20}$$

while

$$\mathbf{F} = \mathbf{K}\cdot\mathbf{H}^{-1} - \mathbf{I} \tag{21}$$

Here, $\mathbf{H}$ is a flow-dependent tensor and corresponds to the apparent permeability (Edwards et al., 1990) allowing an alternate form of equation (10)

$$\langle \mathbf{v}_\beta \rangle = \frac{-\mathbf{H}}{\mu_\beta}\cdot\left(\boldsymbol{\nabla}\langle p_\beta\rangle^\beta - \rho_\beta \mathbf{g}\right) \tag{22}$$

Important remarks must be made at this point. First, it must be emphasized that under the assumptions of well separated scales (relation (14)), steady flow (relation (15)) and for a spatially periodic medium, the determination of $\mathbf{F}$ obtained from the solution of equations (17) through (21) is exact regardless of the Reynolds number value (Whitaker, 1996). In addition, while $\mathbf{K}$ can be shown to be symmetric (and positive definite) (Ene and Sanchez-Palencia, 1975), $\mathbf{F}$ and $\mathbf{H}$ are not, as will be proved further with our numerical results. Finally, it must be stressed that, while $\mathbf{K}$ is a quantity intrinsic to the structure, $\mathbf{F}$ and $\mathbf{H}$ depend not only on the medium but also on both the Reynolds number and pressure gradient orientation. As a consequence, the macroscopic force resulting from flow in an isotropic unit cell is no longer pure drag as it would be in the Darcy regime for any orientation of the flow. Exception is when the isotropic unit cell possesses at least one symmetry axis and flow is aligned with this axis and evidence of these features is shown below.

2.2 Determination of the macroscopic properties

Without introducing any particularity, gravity is not considered in the rest of this work. While $\mathbf{K}$ can be determined either directly from the solution of the creeping flow over a periodic unit cell or equivalently from the closure problem (17), the determination of $\mathbf{H}$ (or $\mathbf{F}$) requires the solution of the stationary Navier-Stokes flow problem over the unit cell. Once dimensionless variables denoted by the superscript * given by

$$x^* = \frac{x}{l} \qquad y^* = \frac{y}{l} \qquad z^* = \frac{z}{l} \tag{23}$$

$$\mathbf{v}_\beta^* = \frac{\mathbf{v}_\beta}{\omega} \qquad p_\beta^* = \frac{p_\beta}{p_{ref}} \tag{24}$$

are used along with the decomposition (Gray, 1975; Zuzovsky et al., 1983)

$$p_\beta = \langle p_\beta \rangle^\beta + \tilde{p}_\beta \tag{25}$$

the cellular flow problem can be written

$$\mathrm{Re}^*\, \mathbf{v}_\beta^* \cdot \boldsymbol{\nabla} \mathbf{v}_\beta^* + \boldsymbol{\nabla} \tilde{p}_\beta^* - \boldsymbol{\nabla}^2 \mathbf{v}_\beta^* = -\boldsymbol{\nabla} \langle p_\beta^* \rangle^\beta \tag{26}$$

$$\boldsymbol{\nabla} \cdot \mathbf{v}_\beta^* = 0 \tag{27}$$

$$\mathbf{v}_\beta^* = 0 \qquad \text{at } A_{\beta\sigma} \tag{28}$$

$$\mathbf{v}_\beta^*(\mathbf{r}^* + l_i^*) = \mathbf{v}_\beta^*(\mathbf{r}^*) \qquad \tilde{p}_\beta^*(\mathbf{r}^* + l_i^*) = \tilde{p}_\beta^*(\mathbf{r}^*) \qquad i = 1, 2, 3 \tag{29}$$

In equation (23), l represents one of the edge sizes of either the periodic unit cell in the regular case or the random cell when disorder is introduced while in equation (26), Re^* is a Reynolds number defined by

$$\mathrm{Re}^* = \frac{\rho_\beta \omega l}{\mu_\beta} \tag{30}$$

A suitable choice of the reference velocity, ω, and pressure, p_{ref}, is

$$\omega = \frac{l^2}{\mu_\beta} \left| \boldsymbol{\nabla} \langle p_\beta \rangle^\beta \right| \qquad p_{ref} = l \left| \boldsymbol{\nabla} \langle p_\beta \rangle^\beta \right| \tag{31}$$

Since $\left| \boldsymbol{\nabla} \langle p_\beta^* \rangle^\beta \right| = 1$, the original choice of the intensity and orientation of the external force per unit volume, $\boldsymbol{\nabla} \langle p_\beta \rangle^\beta$, applied on the periodic structure is now done by selecting a Re^* and the orientation of $\boldsymbol{\nabla} \langle p_\beta^* \rangle^\beta$. As indicated above, solving the problem (26) through (29) for $\mathrm{Re}^* = 0$ and $\boldsymbol{\nabla} \langle p_\beta^* \rangle^\beta$ successively along the three directions of periodicity axes of the unit cell is equivalent to solving the closure problem (17) and yields $\mathbf{K}^* = \mathbf{K}/l^2$ since in this flow regime

$$\langle \mathbf{v}_\beta^* \rangle = -\mathbf{K}^* \cdot \boldsymbol{\nabla} \langle p_\beta^* \rangle^\beta \tag{32}$$

For a given $\mathrm{Re}^* \neq 0$ and orientation of $\boldsymbol{\nabla} \langle p_\beta^* \rangle^\beta$, the determination of $\mathbf{H}^* = \mathbf{H}/l^2$ (or $\mathbf{F}^* = \mathbf{F}$) is more computational time consuming. It is performed by solving first the periodic stationary Navier Stokes problem (26) through (29) to obtain $\mathbf{v}_\beta^*$. In a second step, this result is inserted in the dimensionless form of the closure problem (19), namely

$$\mathrm{Re}^*\, \mathbf{v}_\beta^* \cdot \boldsymbol{\nabla} \mathbf{M}^* + \boldsymbol{\nabla} \mathbf{m}^* - \boldsymbol{\nabla}^2 \mathbf{M}^* = \mathbf{I} \tag{33}$$

$$\boldsymbol{\nabla}\cdot\mathbf{M}^*=0 \tag{34}$$

$$\mathbf{M}^*=0 \qquad \text{at } A_{\beta\sigma} \tag{35}$$

$$\mathbf{m}^*(\mathbf{r}^*+l_i^*)=\mathbf{m}^*(\mathbf{r}^*) \qquad \mathbf{M}^*(\mathbf{r}^*+l_i^*)=\mathbf{M}^*(\mathbf{r}^*) \qquad i=1,2,3 \tag{36}$$

yielding $\mathbf{H}^*$ and $\mathbf{F}$ according to

$$\langle\mathbf{M}^*\rangle=\mathbf{H}^* \tag{37}$$

$$\mathbf{F}=\mathbf{K}^*\cdot\mathbf{H}^{*-1}-\mathbf{I} \tag{38}$$

This problem has again a Navier-Stokes structure and can be solved with the same procedure as the one used to solve the flow. With all these considerations, the same Navier-Stokes solver can in fact be used to determine both $\mathbf{K}^*$ and $\mathbf{F}$.

In order to investigate the deviation to Darcy's law, we consider the macroscopic force per unit volume $\mathbf{f}$ exerted on the structure ($\mathbf{f}=-\mu_\beta\mathbf{H}^{-1}\cdot\langle\mathbf{v}_\beta\rangle$) and decompose this force into a Darcy part ($\mathbf{f_d}=-\mu_\beta\mathbf{K}^{-1}\cdot\langle\mathbf{v}_\beta\rangle$) and a contribution $\mathbf{f_i}$ from inertia ($\mathbf{f_i}=-\mu_\beta\mathbf{K}^{-1}\cdot\mathbf{F}\cdot\langle\mathbf{v}_\beta\rangle$). Classically, in many references as in Koch and Ladd (1997) analysis was based on the modulus of $\frac{\mathbf{f}}{\mu_\beta|\langle\mathbf{v}_\beta\rangle|}=\frac{-\mathbf{K}^{*-1}\cdot(\mathbf{F}+\mathbf{I})\cdot\langle\mathbf{v}_\beta^*\rangle}{\left|\langle\mathbf{v}_\beta^*\rangle\right|}$, i.e. on $\frac{1}{\left|\langle\mathbf{v}_\beta^*\rangle\right|}$. An alternative would be to focus on $\mathbf{f_i}$ and, using a convenient normalization factor inspired from $\mathbf{f_d}$, analyze the flow regimes in terms the dimensionless correction vector $\mathbf{f_c}$ given by

$$\mathbf{f_c}=\frac{\mathbf{K}}{\mu_\beta\left|\langle\mathbf{v}_\beta\rangle\right|}\cdot\mathbf{f_i}=\frac{\mathbf{K}^*}{\left|\langle\mathbf{v}_\beta^*\rangle\right|}\cdot\mathbf{f_i^*}=\frac{-\mathbf{F}\cdot\langle\mathbf{v}_\beta^*\rangle}{\left|\langle\mathbf{v}_\beta^*\rangle\right|} \tag{39}$$

while $\mathbf{f_i^*}=\frac{\mathbf{f_i}}{|\boldsymbol{\nabla}\langle p_\beta\rangle^\beta|}$ and $\langle\mathbf{v}_\beta^*\rangle=-\mathbf{H}^*\cdot\boldsymbol{\nabla}\langle p_\beta^*\rangle^\beta=-\mathbf{K}^*\cdot\boldsymbol{\nabla}\langle p_\beta^*\rangle^\beta-\mathbf{F}\cdot\langle\mathbf{v}_\beta^*\rangle$. Indeed, this form is more sensitive than the traditional one proposed in the literature.

It should be noted that, if one is only interested in analyzing the correction, the resolution of the closure problem for $\mathbf{H}$ (or $\mathbf{F}$) is not required. In fact, one can solve the flow (equations (26) through (29)) and compute $\langle\mathbf{v}_\beta^*\rangle$ to get $\mathbf{f_c}$ from an equivalent form of equation (39)

$$\mathbf{f_c}=\frac{\langle\mathbf{v}_\beta^*\rangle+\mathbf{K}^*\cdot\boldsymbol{\nabla}\langle p_\beta^*\rangle^\beta}{\left|\langle\mathbf{v}_\beta^*\rangle\right|} \tag{40}$$

Since the correction is analyzed through its dependence upon the Reynolds number, attention must also be dedicated to its definition and in the following, we shall use two forms different from Re^*, namely Re_d and Re_k, respectively given by (Koch and Ladd, 1997; Papathanasiou et al., 2001; Rojas and Koplik, 1998)

$$\mathrm{Re}_d=|\langle\mathbf{v}_\beta\rangle^*|\,d^*\,\mathrm{Re}^*=\frac{\rho_\beta\langle\mathbf{v}_\beta\rangle d}{\mu_\beta} \tag{41}$$

where $d^*=d/l$ is the dimensionless grain size of the porous structure and

$$\mathrm{Re}_k=|\langle\mathbf{v}_\beta\rangle^*|\,\sqrt{k^*}\,\mathrm{Re}^*=\frac{\rho_\beta\langle\mathbf{v}_\beta\rangle\sqrt{k}}{\mu_\beta} \tag{42}$$

When the structure is isotropic, i.e. $\mathbf{K}^*=k^*\mathbf{I}$, the latter definition is preferable to the former and this is motivated by the fact that, from a practical point of view, d is not necessarily well defined for all kinds of porous media and most of the time unknown a priori whereas k is accessible by rather simple experiments. In addition, d is not universally related to the pore size.

Results obtained from the solution of equations (33) to (36) in the case of regular, weakly and strongly disordered structures are presented in the next section.

3 Results and discussion

3.1 Method of resolution and validation

As detailed above, the determination of tensors $\mathbf{K}^*$ and $\mathbf{F}$ can be obtained using the same algorithm of resolution of the Navier-Stokes problem (26) through (29) (or (33) to (36)). A 3D numerical procedure having the following features was developed. A finite volume formulation was employed over a Marker And Cell (staggered) cartesian regular grid (Patankar, 1980). This technique is known to be both accurate and easy to implement allowing to treat any kind of geometry while leading to very conservative schemes. The viscous diffusive term was discretized with a second order centered scheme while the inertial convective term was discretized with a Quadratic Upwind Interpolation for Convective Kinematics (QUICK) scheme. This scheme, initially proposed by Leonard (1979) reveals to be very stable, fast converging and highly accurate avoiding significant numerical diffusion (Leschziner, 1980; Han et al., 1981) in comparison to hybrid schemes. Alternative forms of the QUICK discretization procedure were proposed in the literature (Pollard and Siu, 1982; Freitas et al., 1985) and, in the present work, we used an improved version of this scheme (Hayase et al., 1992). Velocity and pressure fields were sought iteratively following an artificial compressibility algorithm (Peyret and Taylor, 1983). Starting from a guessed pressure field, this algorithm consists in computing the momentum equation separately from the continuity equation, this latter being substituted by a perturbed divergence equation. At each iteration of this algorithm, the linear non-symmetric system was solved using a bi-conjugate gradient (or conjugate gradient when $\mathrm{Re}^* = 0$ to compute $\mathbf{K}^*$) routine. Under- (or inertial) relaxation was used to improve convergence especially for the larger Reynolds numbers investigated in this study.

Since our goal is to analyze the evolution of the correction tensor $\mathbf{F}$ in a quantitative manner, it is important to first check the validity and the precision of the numerical procedure above described. To do so, we use the unit cell of a regular array of parallel solid cylinders of circular cross section having the same diameter and arranged on a square centered lattice as represented in figure 2. We only consider the case $\boldsymbol{\nabla}\langle p_\beta^* \rangle^\beta = \mathbf{e_x}$ which, for evident reasons of isotropy and symmetry about $\mathbf{e_x}$, leads to $\langle \mathbf{v}_\beta^* \rangle \cdot \mathbf{e_y} = 0$, a diagonal $\mathbf{F}$ tensor and a zero y component of $\mathbf{f_c}$. Consequently, this unique pressure gradient orientation yields k^* ($\mathbf{K}^* = k^*\mathbf{I}$) when $\mathrm{Re}^* = 0$ and provides the correction f_{cx} to the velocity given in (39) which reduces to the first diagonal term f_{xx} of $\mathbf{F}$. For comparison purposes, flow computations were performed with parameters used elsewhere (Fourar et al., 2004), i.e. with $\epsilon = 0.386$ yielding $d^* \cong 0.62521$.

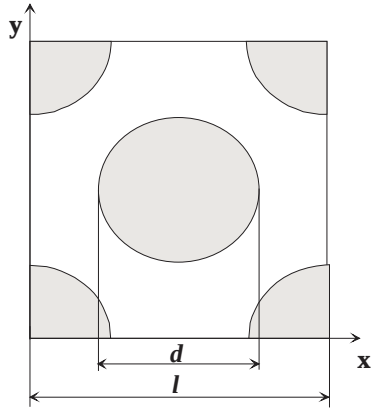

Figure 2: Unit cell used for validation tests

3.1.1 Permeability

Although some relatively precise estimations of k^* are available in this case, at least at large values of the porosity (Drumond and Tahir, 1984), no exact analytical results for the flow are available on such

a structure and comparison can only be performed with other numerical results. The Stokes flow was computed with the finite volume (FV) method detailed above. The convergence criterion of the overall algorithm was 10^{-12} on the L^2 norm of the divergence of the velocity over all grid blocks while the relative error criterion for the linear system solver was 10^{-15}. The problem was also solved with a Boundary Element Method (BEM) using constant elements which reveals to be very precise for this type of problem (Larson and Higdon, 1987). All the results on k^* are gathered in Table 1.

Method (# of grid blocks)	k^*
FEMLAB (Fourar et al., 2004) (unknown)	$2.3111\ 10^{-4}$
BEM (14700 elements)	$2.2952\ 10^{-4}$
FV (500x500)	$2.2130\ 10^{-4}$
FV (1000x1000)	$2.2505\ 10^{-4}$
FV (1500x1500)	$2.2663\ 10^{-4}$

Table 1: Permeability results obtained with the finite volumes method developed in this work. Comparison to BEM and Fourar's results. Unit cell of figure 2, $\epsilon = 0.386$

Although the numerical method of the present work seems to very slightly underestimate the permeability in this particular configuration, results are in very good agreement since the maximum relative error between all these values is less than 4.5%.

3.1.2 Non-Darcy correction

The dependence of $f_{cx} = f_{xx}$ on Re_k corresponding to Re^* ranging from 0 to 60 is compared to results reported in Fourar et al. (2004) and is represented in figure 3.

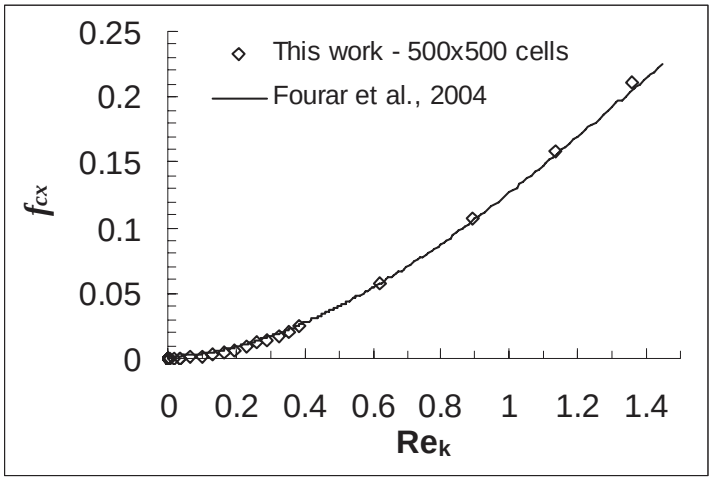

Figure 3: Evolution of f_{cx} versus Re_k for the unit cell of the model configuration in figure 2. Comparsion with results in (Fourar et al., 2004).

The agreement is excellent leading to a relative difference always less than 0.5% over the whole range of Re_k. Truncations on either ϵ or d/l are probably not identical in the present work and in the cited reference and this can possibly be part of the explanation of this difference. This validates the present numerical method. Considering however that precision of the finite volume method might suffer from geometrical representation of curved objects with cartesian grids as well as from pure grid size effect, we choose, in the rest of this work, to analyze the behaviour of $\mathbf{F}$ on 2D configurations involving square objects.

3.2 Ordered structure

We start the analysis with the case of a 2D infinite isotropic and regular square pattern of cylinders of identical square cross section for which the unit cell is represented in figure 4.

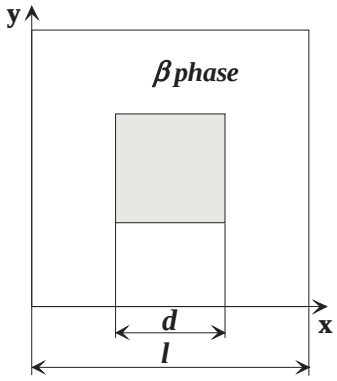

Figure 4: Unit cell of the regular array used to compute $\mathbf{F}$.

3.2.1 Precision

Precision was first investigated in the case $\boldsymbol{\nabla}\langle p_\beta^* \rangle^\beta = \mathbf{e_x}$ with $\epsilon = 0.75$. As in the test case of section 3.1, this choice of the orientation of $\boldsymbol{\nabla}\langle p_\beta^* \rangle^\beta$ allows the computation of k^* and the non-Darcy correction which reduces again to f_{xx}. Permeability was computed varying the number of grid blocks from 400 to 250000 with the same convergence criteria as those of section 3.1. Results on k^* along with the corresponding relative errors, using k^* obtained with 250000 grid blocks as the reference value, are reported in table 2. They clearly show the excellent precision achieved even with relatively coarse grids.

# of grid blocks	k^*	$\Delta k^*/k^*$ %
20x20	0.0130765	0.4089
40x40	0.0130355	0.0941
120x120	0.0130242	0.0074
200x200	0.0130235	0.0018
400x400	0.0130233	$7.8\ 10^{-5}$
500x500	0.0130232	–

Table 2: Permeability variation with the number of grid blocks. Unit cell of figure 4 with $\epsilon = 0.75$.

On this basis, $f_{cx} = f_{xx}$ was computed on the same unit cell using four different grid sizes, the convergence criterion at each value of the Reynolds number being taken as $max(10^{-7} f_{xx}, 10^{-12})$ for the overall algorithm while the convergence criterion for the linear system solver was 10^3 smaller. Computations were performed for $10^{-3} \leq \mathrm{Re}^* \leq 10^4$ (i.e. $1.5\ 10^{-6} \leq \mathrm{Re}_d \leq 60$ or $6.5\ 10^{-6} \leq \mathrm{Re}_k \leq 13.6$) assuming that the stationary laminar solution is still physically valid in the upper range of these Reynolds numbers. An example of pressure and velocity fields is depicted in figure 5 and results on the evolution of f_{cx} versus Re_k are represented in figure 6.

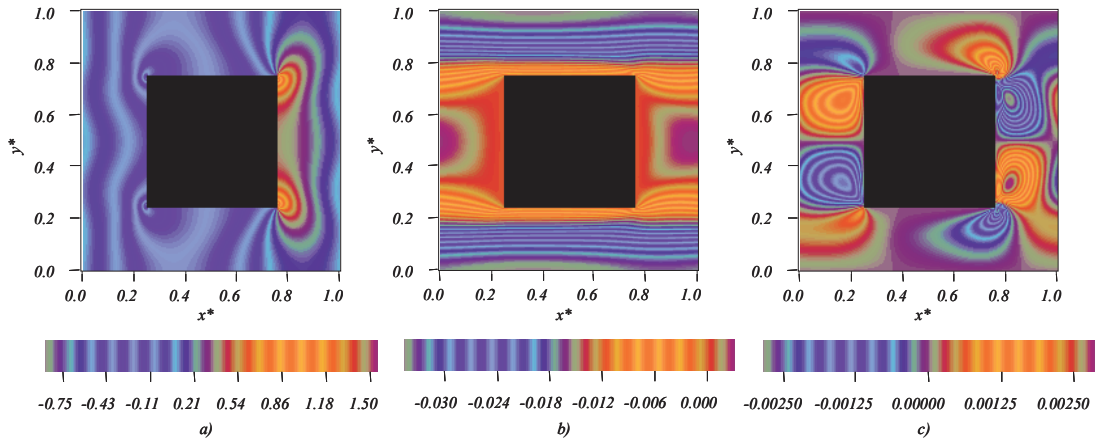

Figure 5: Numerical results obtained on the unit cell of figure 4, $\epsilon = 0.75$, $\boldsymbol{\nabla}\langle p^*_\beta\rangle^\beta = \mathbf{e}_x$, $\mathrm{Re}_k = 13.6$ ($\mathrm{Re}_d = 59.6$), *a*) $\tilde{p}^*_\beta$ (see equation 25), *b*) $\mathbf{v}_\beta.\mathbf{e_x}$, *c*) $\mathbf{v}_\beta.\mathbf{e_y}$.

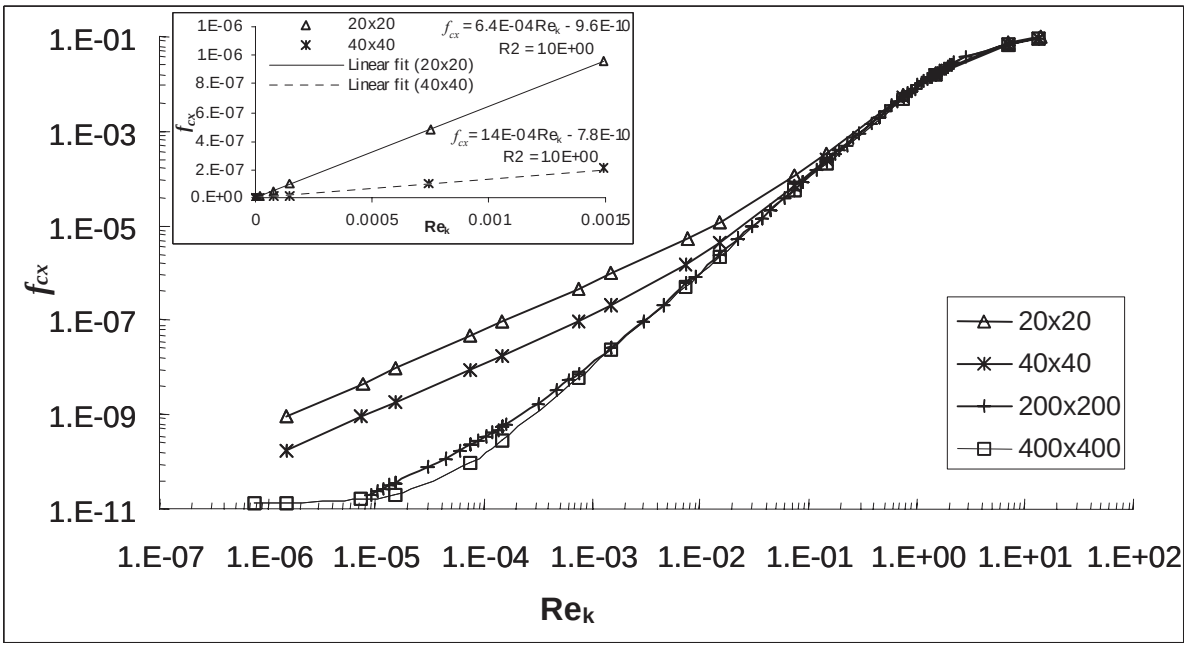

Figure 6: Evolution of $f_{cx} = f_{xx}$ with Re_k obtained on the unit cell of figure 4 with 4 different grid sizes, $\epsilon = 0.75$, and $\boldsymbol{\nabla}\langle p^*_\beta\rangle^\beta = \mathbf{e_x}$. A power law fitted on points corresponding to $7.4\ 10^{-4} \lesssim \mathrm{Re}_k \lesssim 0.4$ gives an exponent 1.97 for 200x200 or 400x400 grid blocks. *Inset*: coarse grid restitutes an artificial linear variation of f_{cx} with Re_k at low Reynolds numbers.

For the two coarser grids investigated here, the onset of Darcy's law deviation seems to vary linearly with Re_k yielding a quadratic velocity correction (see inset of figure 6) and excessive attention must be paid to this phenomenon which is a pure grid size effect.

In fact, when macroscopic properties are computed using 200x200 grid blocks, one clearly observes a *weak inertia regime* ($7.4\ 10^{-4} \lesssim \mathrm{Re}_k \lesssim 0.3$; $3.2\ 10^{-3} \lesssim \mathrm{Re}_d \lesssim 1.3$) where f_{cx} is scaled by Re_k^2 (see figures

6 and 7) and a *strong inertia regime* ($0.9 \lesssim \mathrm{Re}_k \lesssim 2.2$; $3.9 \lesssim \mathrm{Re}_d \lesssim 9.6$) where f_{cx} varies linearly with Re_k (see figure 8). In this particular configuration where the mean flow is basically 1D, this last regime would allow a relationship between the pressure gradient and seepage velocity of the form reported in equation 3 where β is the inertial resistance factor. The two regimes are separated by a transition (or crossover) region ($0.3 \lesssim \mathrm{Re}_k \lesssim 0.9$) the extent of which will be shortly discussed below. At sufficiently low Reynolds numbers (($\mathrm{Re}_k \lesssim 7\ 10^{-6}$; $\mathrm{Re}_d \lesssim 3\ 10^{-5}$) and for a finer grid size (i.e. 400x400), the Darcy regime is also recovered. This leads to a classification of the different regimes (Darcy, weak and strong inertia) in accordance with that proposed in the literature (Rojas and Koplik, 1998; Skjetne and Auriault, 1999b). For larger Reynolds numbers, assuming that the stationary Navier-Stokes model is still physically meaningful, another regime appears where f_{cx} varies again with Re_k^2 (see figure 9). However, this last regime is beyond the scope of this paper and will not be investigated further (see Koch and Ladd (1997) for some results).

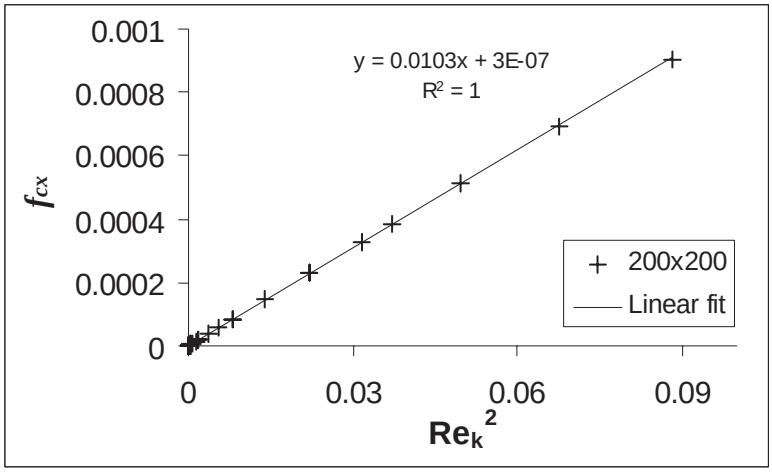

Figure 7: Weak inertia regime. Correction to Darcy's law ($f_{cx} = f_{xx}$) scales as Re_k^2 (i.e. $(\langle \mathbf{v}_\beta \rangle . \mathbf{e_x})^3$). Unit cell of figure 4, $\epsilon = 0.75$, $1.5\ 10^{-4} \lesssim \mathrm{Re}_k \lesssim 0.4$, $\boldsymbol{\nabla} \langle p_\beta^* \rangle^\beta = \mathbf{e_x}$

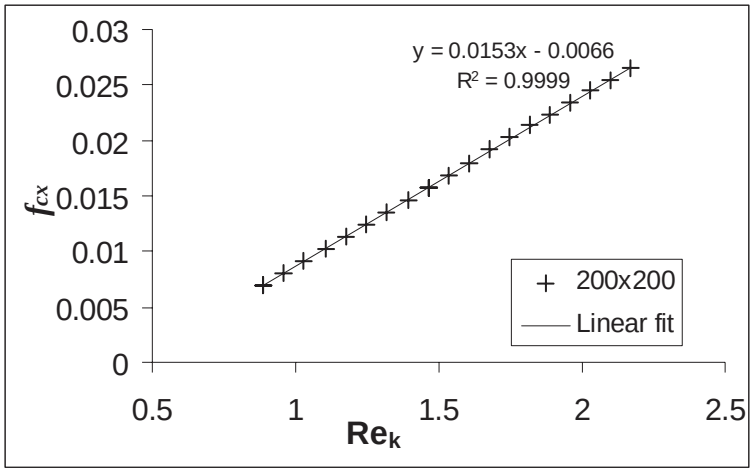

Figure 8: Strong inertia regime. Correction to Darcy's law ($f_{cx} = f_{xx}$) scales as Re_k (i.e. $(\langle \mathbf{v}_\beta \rangle . \mathbf{e_x})^2$). Unit cell of figure 4, $\epsilon = 0.75$, $0.9 \lesssim \mathrm{Re}_k \lesssim 2.2$, $\boldsymbol{\nabla} \langle p^*_\beta \rangle^\beta = \mathbf{e_x}$

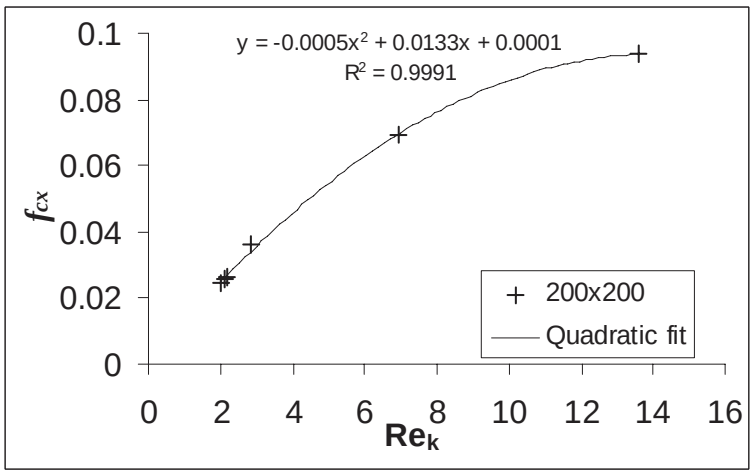

Figure 9: Regime above strong inertia. $f_{cx} = f_{xx}$ scales as Re_k^2. Unit cell of figure 4, $\epsilon = 0.75$, $\mathrm{Re}_k \gtrsim 2$, $\boldsymbol{\nabla} \langle p^*_\beta \rangle^\beta = \mathbf{e_x}$

Although these fits provide excellent estimations in restricted ranges of the Reynolds number, it must kept in mind, as discussed in the introduction, that this approach is based on *approximations*. This will be more clearly demonstrated with dependence of the correction on the pressure gradient orientation as well as on disorder later investigated in this paper.

3.2.2 Permeability and non-Darcy correction versus porosity - $\nabla \langle p^*_\beta \rangle^\beta = e_{\mathbf{x}}$

As a consequence of the precision test described above, all our computations on the model configuration of figure 4 were performed with 150x150 grid blocks which is dense enough to analyze the values of the non-Darcy correction where they are significant. We first consider the case $\boldsymbol{\nabla} \langle p^*_\beta \rangle^\beta = \mathbf{e_x}$ yielding a flow

also in the x direction. We investigated 10 porosity values ranging from 0.30 to 0.75 and Re_d up to 70 (Re_k up to around 14). Results on $f_{cx} = f_{xx}$ versus Re_k^2 and Re_k in the weak and strong inertia regimes are represented in figure 10 and 11 respectively.

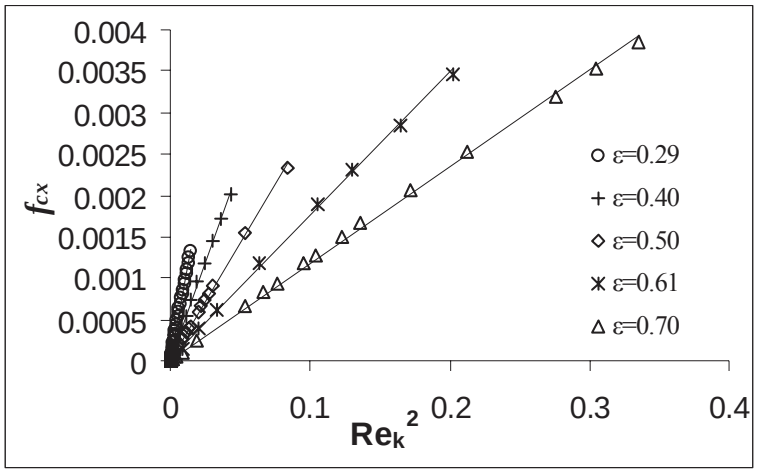

Figure 10: Evolution of f_{cx} with Re_k^2 and ϵ in the weak inertia regime; $\boldsymbol{\nabla}\langle p_\beta^* \rangle^\beta = \mathbf{e_x}$

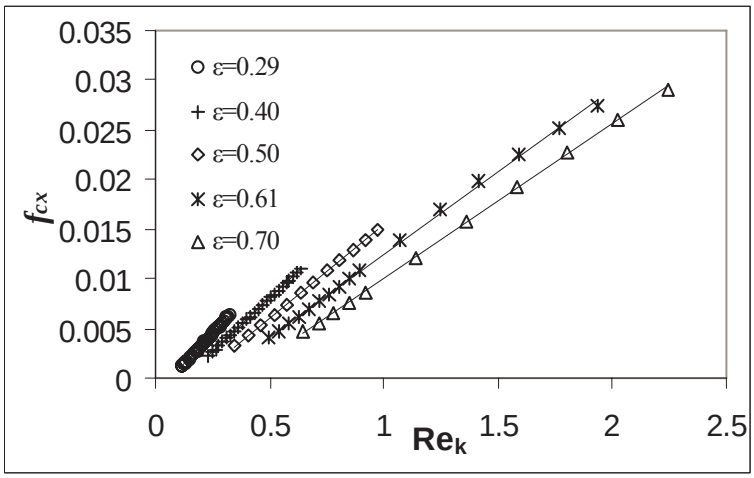

Figure 11: Evolution of f_{cx} with Re_k and ϵ in the strong inertia regime; $\boldsymbol{\nabla}\langle p_\beta^* \rangle^\beta = \mathbf{e_x}$

For the porosity range investigated here, these two regimes are well identified in restricted Reynolds number ranges. It must be pointed out that, for instance, for $\epsilon = 0.29$, f_{cx} remains linear versus Re_k only in the range $0.14 \lesssim \mathrm{Re}_k \lesssim 0.33$. The distinction between the regimes was overlooked by Amaral Souto and Moyne (1997) in the same configuration with $\epsilon = 0.64$ because these authors analyzed the quantity $\epsilon^3 \frac{1}{\mathrm{Re}_d\ k^*}(1 + f_{xx})$ proportional to the drag coefficient (or friction factor) but not enough sensitive to exhibit the expected nonlinearity which remains small in this situation. As a consequence we further analyze the weak and strong inertia regimes by using the following linear representations for f_{cx}

$$A\,\mathrm{Re}_k^2 + B \qquad \textit{(weak inertia)} \tag{43}$$

$$C\,\mathrm{Re}_k + D \qquad \textit{(strong inertia)} \tag{44}$$

and the corresponding values of the permeabilities k^* along with the coefficients A, B, C and D are reported in table 3.

ϵ	k^*	A	B	C	D
0.2944	0.0003651	0.1027	$4\ 10^{-7}$	0.0251	$-1.8\ 10^{-3}$
0.36	0.0007255	0.0649	$2\ 10^{-6}$	0.0228	$-2.3\ 10^{-3}$
0.402	0.001068	0.0506	$3\ 10^{-7}$	0.0215	$-2.7\ 10^{-3}$
0.4425	0.001509	0.0397	$7\ 10^{-7}$	0.0201	$-2.9\ 10^{-3}$
0.5006	0.002386	0.0297	$8\ 10^{-7}$	0.0190	$-3.5\ 10^{-3}$
0.5466	0.003346	0.0241	$1\ 10^{-6}$	0.0180	$-3.8\ 10^{-3}$
0.6073	0.005104	0.0187	$3\ 10^{-7}$	0.0172	$-4.6\ 10^{-3}$
0.6558	0.007059	0.0155	$1\ 10^{-7}$	0.0165	$-5.2\ 10^{-3}$
0.7012	0.009492	0.0125	$3\ 10^{-7}$	0.0157	$-5.7\ 10^{-3}$
0.75	0.013023	0.0103	$1.3\ 10^{-6}$	0.0153	$-6.7\ 10^{-3}$

Table 3: Permeabilities and coefficients in equations (43) and (44) obtained from least square linear fits. Unit cell of figure 4. Porosity range: $0.3 \leq \epsilon \leq 0.75$.

To account for the dependence of k^* on ϵ over the whole range of porosity, it is convenient to use a relationship of the form (Ergun, 1952)

$$a\epsilon^{\alpha_1}\left(1-\epsilon\right)^{\alpha_2} \tag{45}$$

rather than employing estimations from approximated solutions to the flow that are asymptotically valid at exceedingly small or large porosities. A least square fit of the form (45) performed on k^* yields

$$k^* \simeq 0.015\frac{\epsilon^{3.23}}{\left(1-\epsilon\right)^{0.57}} \qquad 0.3 \lesssim \epsilon \lesssim 0.75 \qquad Err \simeq 5\ 10^{-11} \tag{46}$$

where Err is the mean square error of the estimator of k^*

In equation (46), exponents are slightly different from those in the Kozeny relationship originally derived for sphere packs but extensively used for a wide variety of unconsolidated structures like in Ergun (1952), MacDonald et al. (1979) and Amaral Souto and Moyne (1997) and in which exponents would be $\alpha_1 = 3$ and $\alpha_2 = -1$. The pre-factor $a = 0.015$ in 46 is also different from the value 0.00667 proposed by Ergun or the value 0.00556 deduced from fits on experimental data by MacDonald et al. (1979) over a wide variety of media and used later by Amaral Souto and Moyne (1997). However, as already pointed out, sensitivity to errors on coefficients appearing in the drag coefficient to Reynolds number relationship is weak to precisely estimates these coefficients. One of the conclusions from MacDonald et al. (1979) is that their proposed fit would be precise to within $\pm 50\%$.

Turning the attention to the non Darcy correction indicates that, for the whole range of porosity, B is almost 0 confirming a cubic dependence upon velocity magnitude for the onset of the deviation to Darcy's law. For a given Re_k, the intensity of inertia increases when ϵ decreases. Moreover, the slopes of $f_{cx}\left(\mathrm{Re}_k^2\right)$ and $f_{cx}\left(\mathrm{Re}_k\right)$ decrease when ϵ increases and this is much more significant in the weak inertia regime. Here it must strongly emphasized that an analysis of this correction as a function of Re_d^2 and Re_d would lead to exactly inverse conclusions on both intensity and slopes. The importance of the choice of the Reynolds number definition must therefore be underlined .In fact, C is reduced by a factor less than 2 when ϵ increases from 0.3 to 0.75 whereas the decrease on A is one order of magnitude in the same porosity range. In this porosity interval, D decreases by a factor less than 4. It must also be emphasized that, for this particular cell and pressure gradient configuration, the values of f_{cx} in the weak inertia regime represent a quasi insignificant correction to Darcy's law.

In the strong inertia regime, where the correction to Darcy's law has a quadratic dependence on velocity, a comparison between the inertial resistance factor β in equation (3) and the coefficient C obtained from our results can be easily performed. In fact, the classical Forchheimer model implicitly assumes no weak inertia regime and $D = 0$ in equation (44). For this approximation to hold, a modified permeability -referred to as the Forchheimer permeability- which differs from the true Darcy permeability is generally introduced (see for instance Skjetne and Auriault (1999a) Skjetne and Auriault (1999b)). Under such circumstances, the relation between C and β would be

$$\frac{C}{\sqrt{k^*}} = \beta l \tag{47}$$

Carrying out again a least square fit of the form (45) on the values of $\frac{C}{\sqrt{k^*}}$ obtained on the regular structure under study yields

$$\frac{C}{\sqrt{k^*}} \simeq 0.12 \frac{(1-\epsilon)^{0.38}}{\epsilon^{2.04}} \qquad 0.3 \lesssim \epsilon \lesssim 0.75 \qquad Err \simeq 1.1\ 10^{-5} \tag{48}$$

where Err is again the mean square error of the estimator of $\frac{C}{\sqrt{k^*}}$. Exponents and pre-factor obtained from this fit are also slightly different from those appearing in widely used correlations proposed by Ergun (1952) based on an implicit model of packed spheres and where $\alpha_1 = -3$, $\alpha_2 = 0.5$, $a = 1.75$ or by MacDonald et al. (1979) and used by Amaral Souto and Moyne (1997) where $\alpha_1 = -3$, $\alpha_2 = 0.5$, $a = 1.8$. Discrepancy of these relationships with computed results obtained on square and hexagonal arrays of uniform and non uniform cylinders of circular cross section was examined by Papathanasiou et al. (2001) through the analysis again of the relationship between the drag coefficient and the Reynolds number. Using Re_k in the expression of the drag coefficient to advantageously avoid an implicit relationship between k and any other structural dimension, they concluded to a relationship implying, with our notations, $C \simeq 0.08 \frac{1-\epsilon}{\epsilon}$. Although the discrepancy of this relation with our results must be found in the difference of cylinder shape, special attention must be paid to the precision of such a correlation when extracted from the drag coefficient to Reynolds number relationship.

To avoid a complex description of the crossover region between the weak and strong inertia regimes, we define a crossover Reynolds number Re_{kc} as the value below and above which the best approximation is from equation (43) and (44) respectively (see figure 12).

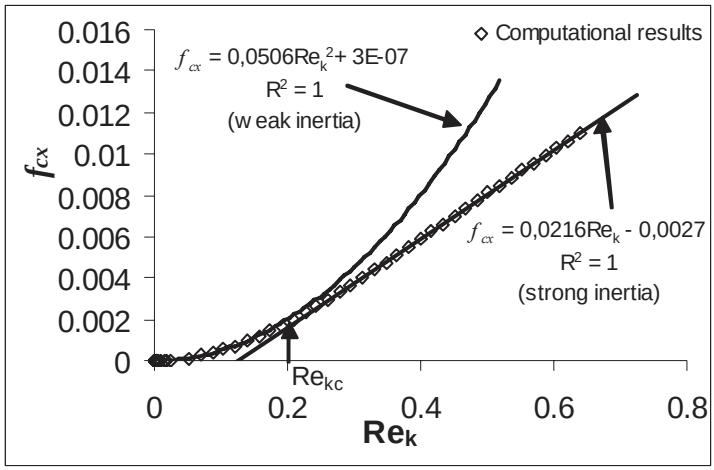

Figure 12: Fits in the weak and strong inertia regimes are used to define the crossover Reynolds number Re_{kc}. Unit cell of figure 4, $\epsilon = 0.402$; $\boldsymbol{\nabla}\langle p^*_\beta \rangle^\beta = \mathbf{e_x}$

This value is the one minimizing the difference between the weak and strong inertia models and is hence given by

$$\mathrm{Re}_{kc} = \frac{C}{2A} \tag{49}$$

Similarly, we define the upper bound of Re_k at which f_{cx} deviates by 5% from the strong inertia model in equation (44) allowing the estimation of the Reynolds range $\Delta\,\mathrm{Re}_k$ over which this model remains a reasonable approximation.

Results on Re_{kc} and the corresponding values of Re_{dc} simply given by

$$\mathrm{Re}_{dc} = \left(\frac{1-\epsilon}{k^*}\right)^{0.5} \mathrm{Re}_{kc} \tag{50}$$

are represented versus ϵ in figure 13. Clearly, these results show that the larger the porosity, the larger (respectively the smaller) the value of Re_k (respectively Re_d) above which the correction depends linearly upon the Reynolds number. Moreover, as indicated in figure 14, the range of Reynolds numbers $\Delta\,\mathrm{Re}_k$ where this correction is a relevant approximation is increasing with ϵ while the corresponding range $\Delta\,\mathrm{Re}_d$ decreases. As for k^* and C, it is appealing to correlate Re_{kc}, Re_{dc} and $\Delta\,\mathrm{Re}_k$ in the form reported in (45) where porosity limits are involved. For the structure under concern and the range of porosity investigated here, we find

$$\mathrm{Re}_{kc} \simeq 0.69\ \frac{\epsilon^{1.49}}{(1-\epsilon)^{0.36}} \qquad 0.3 \lesssim \epsilon \lesssim 0.75 \qquad Err \simeq 1.0\ 10^{-5} \tag{51}$$

$$\mathrm{Re}_{dc} \simeq 6.96\ \epsilon^{0.05}\,(1-\epsilon)^{0.55} \qquad 0.3 \lesssim \epsilon \lesssim 0.75 \qquad Err \simeq 1.4\ 10^{-3} \tag{52}$$

and

$$\Delta\,\mathrm{Re}_k \simeq 4.09\ \epsilon^{1.94}\,(1-\epsilon)^{0.01} \qquad 0.3 \lesssim \epsilon \lesssim 0.75 \qquad Err \simeq 1.6\ 10^{-4} \tag{53}$$

As shown by equations (52) and (53), it is remarkable to notice that Re_{dc} has a quasi square-root dependence on $(1-\epsilon)$ while $\Delta\,\mathrm{Re}_k$ mainly depends on the square of ϵ.

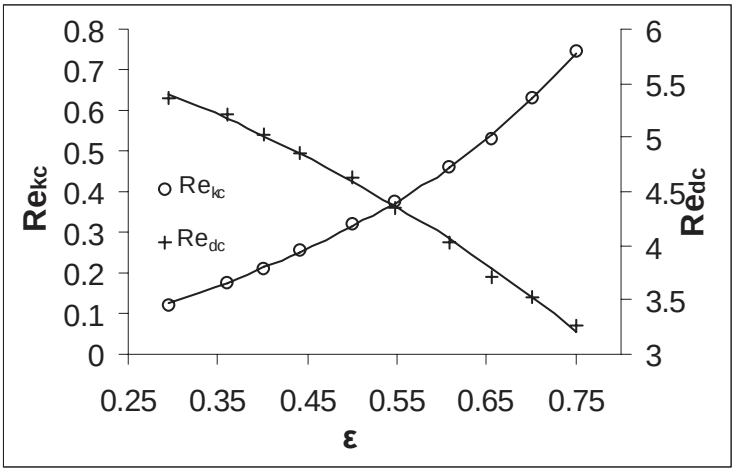

Figure 13: Evolution of the crossover Reynolds number versus ϵ. Continuous lines are correlations of equations (51) and (52).Unit cell of figure 4; $\boldsymbol{\nabla}\langle p^*_\beta\rangle^\beta = \mathbf{e_x}$

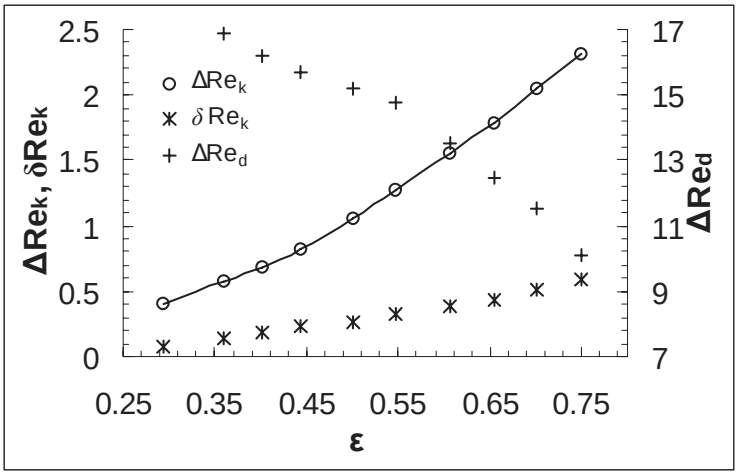

Figure 14: Evolution of the Reynolds intervals $\Delta\,\mathrm{Re}_k$ and $\Delta\,\mathrm{Re}_d$ over which f_{cx} varies linearly with Re_k (or Re_d) versus ϵ. Continuous line corresponds to the correlation of equation (53). $\delta\,\mathrm{Re}_k$ is the Reynolds interval of the transition between the weak and strong inertia regimes. Unit cell of figure 4; $\boldsymbol{\nabla}\langle p^*_\beta\rangle^\beta = \mathbf{e_x}$

In figure 14, we have also reported the Reynolds interval $\delta\,\mathrm{Re}_k$ of the transition region between the weak and strong inertia regimes versus ϵ. Although $\Delta\,\mathrm{Re}_k$ is 4 to 5 larger than $\delta\,\mathrm{Re}_k$, it must be noticed that the latter interval remains of significant extent.

In the next paragraph, we investigate the case of pressure gradients not aligned with one of the periodicity axis of the unit cell for $\epsilon = 0.75$.

3.2.3 Non-Darcy correction versus $\nabla\langle p^*_\beta\rangle^\beta$ orientation - $\epsilon = 0.75$

F tensor structure analysis

When $\boldsymbol{\nabla}\langle p^*_\beta\rangle^\beta$ is not aligned with $\mathbf{e_x}$ or $\mathbf{e_y}$, the computation of the tensor $\mathbf{F}$ requires the use of the full algorithm described in section 2.2. This was performed for $\epsilon = 0.75$ in the range $0 \leqslant \mathrm{Re}_d \leqslant 30$ (Re_k up to 10) and $0 \leqslant \theta \leqslant 45°$, where θ designates the angle $\boldsymbol{\nabla}\langle p^*_\beta\rangle^\beta$ makes with $\mathbf{e_x}$. Results in the range $45° \leqslant \theta \leqslant 90°$ can be inferred from evident symmetry considerations according to $f_{xx}\,(90° - \theta) = f_{yy}\,(\theta)$ and $f_{xy}\,(90° - \theta) = f_{yx}\,(\theta)$, $0° \leqslant \theta \leqslant 90°$. In figure 15, we have represented the components of $\mathbf{F}$ versus θ and Re_k. As expected, $\mathbf{F}$ is not symmetric (see figure 16 representing $f_{xy} - f_{yx}$ versus θ and Re_k) except for $\theta = 0°$, $\theta = 90°$ and $\theta = 45°$ all the three corresponding to a symmetry axis while for the latter value we have in addition $f_{xx} = f_{yy}$. This can be explained in the following manner. When, for an isotropic structure, the pressure gradient is along a symmetry axis of the cell and leads to a flow for which the principal axes of $\mathbf{H}$ and $\mathbf{F}$ are not the periodicity axes $\mathbf{e_x}$ and $\mathbf{e_y}$, then $\mathbf{H}$ and $\mathbf{F}$ are symmetric and $h_{xx} = h_{yy}$ and $f_{xx} = f_{yy}$. The non symmetric character of $\mathbf{F}$ increases with Re_k while the values of θ corresponding to $f_{xy} - f_{yx}$ extrema vary from $\theta \sim 22.5°$ and $\theta \sim 67.5°$ at very low Reynolds numbers to $\theta \sim 31°$ and $\theta \sim 59°$ at $\mathrm{Re}_k \simeq 6.7$ ($\mathrm{Re}_d \simeq 30$).

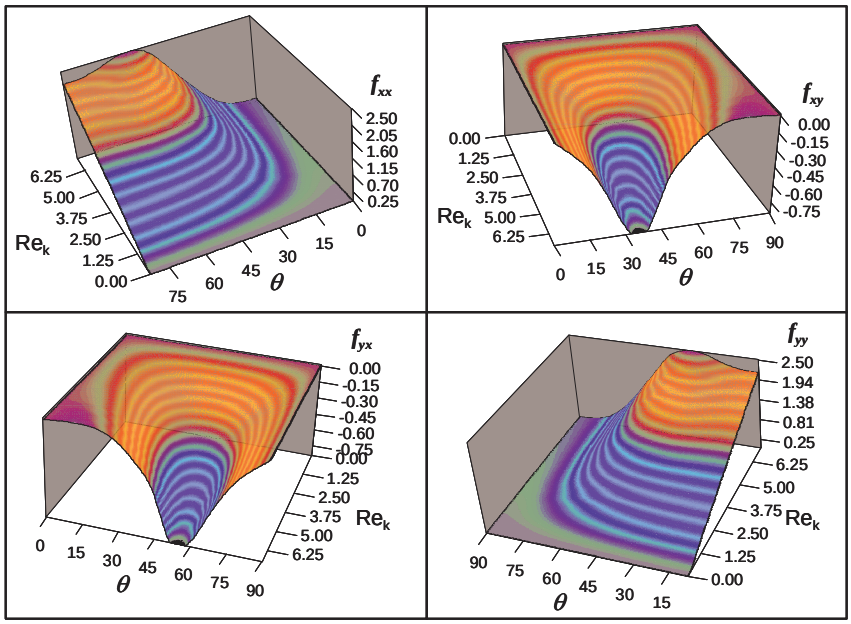

Figure 15: Components of the tensor $\mathbf{F}$ versus θ and Re_k. Unit cell of figure 4; $\varepsilon = 0.75$

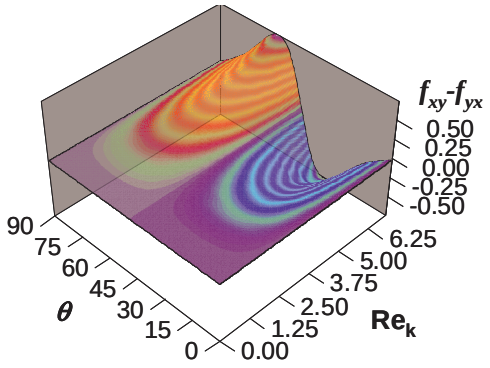

Figure 16: Difference between the off-diagonal terms of $\mathbf{F}$ versus θ and Re_k. Unit cell of figure 4; $\varepsilon = 0.75$

This suggests that, except when the flow is along one of the symmetry axes, the mean velocity $\langle \mathbf{v}_\beta^* \rangle$ is not in the direction of $\boldsymbol{\nabla} \langle p_\beta^* \rangle^\beta$, i.e. that the macroscopic force exerted on the structure is not pure drag. It must be noted that this property might be inherent to the ordered structure of the medium as mentioned in Edwards et al. (1990). This is confirmed by the results on the angle $\langle \mathbf{v}_\beta^* \rangle$ makes with $\boldsymbol{\nabla} \langle p_\beta^* \rangle^\beta$ discussed below.

Mean flow direction versus $\boldsymbol{\nabla} \langle p_\beta^* \rangle^\beta$ direction

In figure 17, we have represented the evolution of the angle θ_v versus θ and Re_k, θ_v being the angle $\langle \mathbf{v}_\beta^* \rangle$ makes with $\boldsymbol{\nabla} \langle p_\beta^* \rangle^\beta$. This angle features complex dependence on θ and Re_k. From figure 17 it can be observed that, globally, for $0 < \theta < 45°$, the flow tends to be more aligned with the x direction than $\boldsymbol{\nabla} \langle p_\beta^* \rangle^\beta$ (θ_v is positive), whereas for $45° < \theta < 90°$, $\langle \mathbf{v}_\beta^* \rangle$ tends to align with the y direction. For

instance, the maximum value of θ_v is obtained for θ decreasing from 22.5° at very small values of Re_k to a minimum value $\theta \simeq 16°$ at $\mathrm{Re}_k \simeq 3$ and increases from this value on for larger Reynolds numbers. This maximum value of θ_v always increases with Re_k. We shall now examine the consequences on the non-Darcy correction.

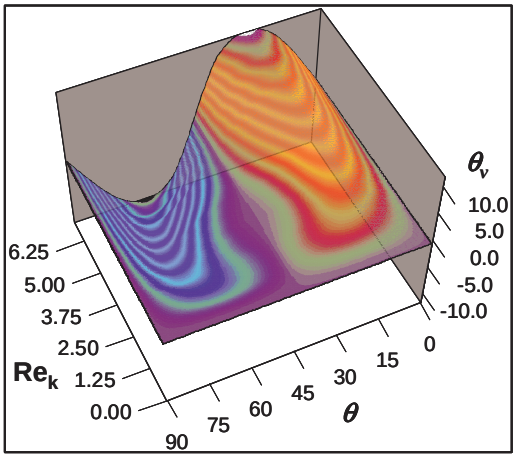

Figure 17: Angle θ_v between $\langle \mathbf{v}^*_\beta \rangle$ and $\boldsymbol{\nabla} \langle p^*_\beta \rangle^\beta$ versus Re_k for different $\boldsymbol{\nabla} \langle p^*_\beta \rangle^\beta$ orientations θ. Pure drag only exists for $\theta = 0°$, 45°, and 90° and $\theta_v(\theta) = -\theta_v(90 - \theta)$ for $0° \leqslant \theta \leqslant 90°$. *Inset*: same quantity as a function of θ and Re_k. Unit cell of figure 4; $\varepsilon = 0.75$.

Analysis of the non-Darcy correction versus $\boldsymbol{\nabla} \langle p^*_\beta \rangle^\beta$ direction

For evident symmetry reasons, $f_{cy}(\theta) = f_{cx}(90° - \theta)$ and $|\mathbf{f_c}(\theta)| = |\mathbf{f_c}(90° - \theta)|$, $0° \leqslant \theta \leqslant 90°$. Consequently, our conclusions will only be drawn on f_{cx} and $|\mathbf{f_c}|$ in the rest of this paragraph. In figures 18 and 19, we have reported the evolution of these two quantities respectively versus θ and Re_k. Due to symmetry, the maximum of $|\mathbf{f_c}|$ is for $\theta = 45°$ whatever the value of Re_k. However, this is not the case for f_{cx} since the orientation of $\boldsymbol{\nabla} \langle p^*_\beta \rangle^\beta$ leading to the maximum value of this component depends on the Reynolds number. For instance the value of θ corresponding to the maximum of f_{cx} decreases from $\theta \simeq 54°$ at very small Re_k to a minimum value $\theta \simeq 36°$ when $\mathrm{Re}_k \simeq 3.3$ (see inset of figure 18). It increases (asymptotically) to $\theta = 45°$ at large Re_k. The correction is always minimum for $\theta = 0°$ (or $\theta = 90°$) whatever the Reynolds number.

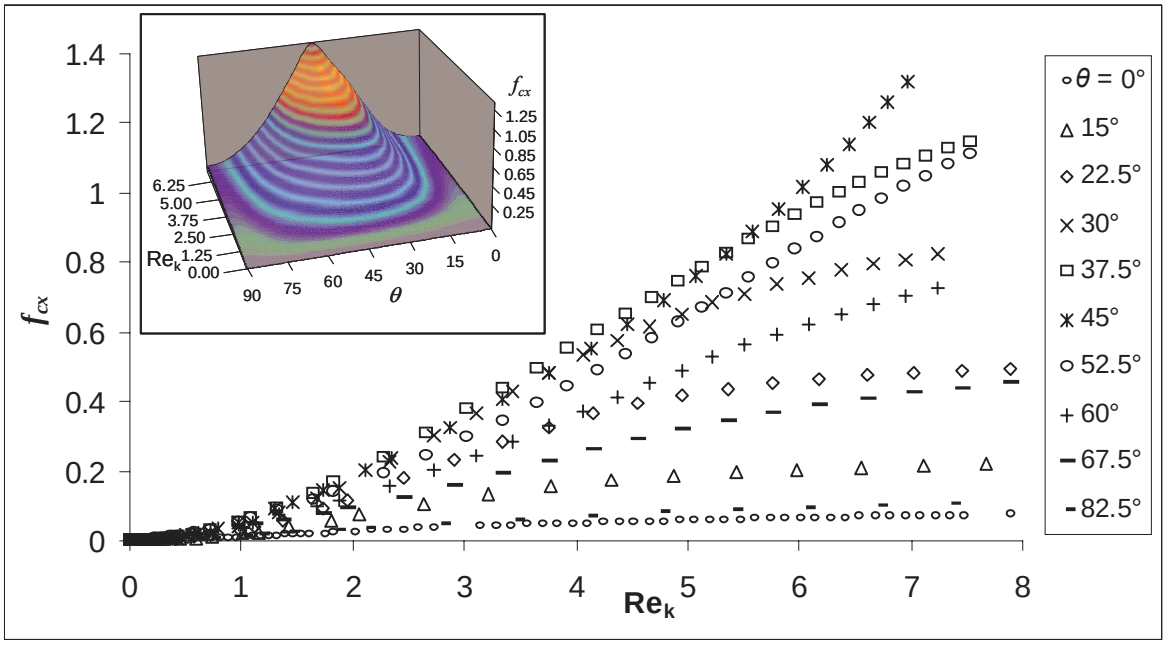

Figure 18: Variation of the x component, f_{cx}, of $\mathbf{f_c}$ with Re_k for different values of θ. *Inset*: same quantity versus θ and Re_k. Unit cell of figure 4; $\varepsilon = 0.75$

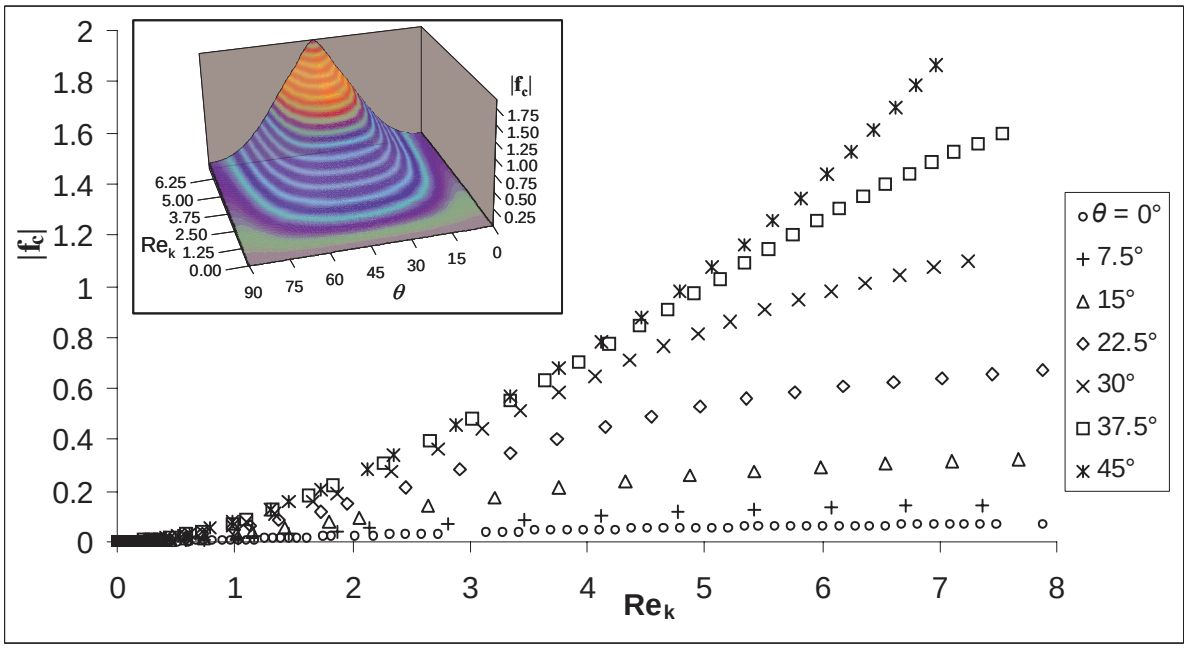

Figure 19: Variation of the modulus of $\mathbf{f_c}$ with Re_k for different values of θ. *Inset*: same quantity versus θ and Re_k. Unit cell of figure 4; $\varepsilon = 0.75$

Both f_{cx} and $|\mathbf{f_c}|$ scale as Re_k^2 for small enough values of Re_k at any orientation θ of $\boldsymbol{\nabla}\langle p_\beta^* \rangle^\beta$. As shown in figures 20 and 21 where the x component and the modulus of $\mathbf{f_c}$ are respectively represented versus Re_k^2 for Re_k up to 0.15, excellent linear dependence and the clear existence of the weak inertia regime are both confirmed.

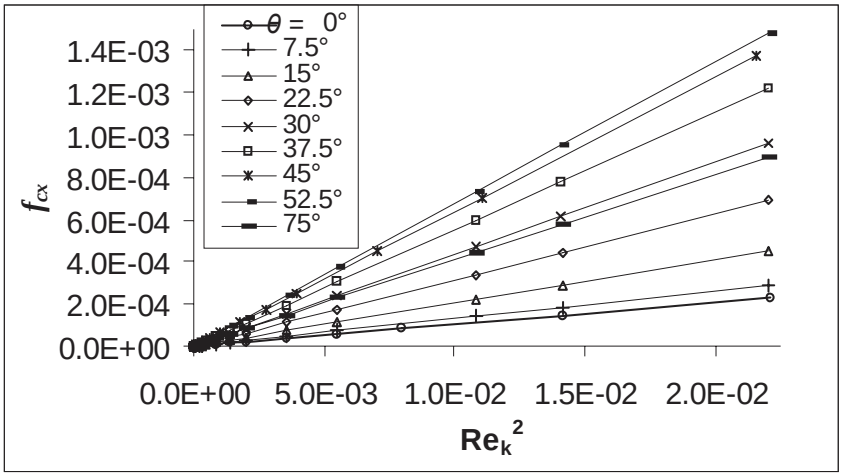

Figure 20: Variation of the x component, f_{cx}, of $\mathbf{f_c}$ with Re_k^2 for different values of θ. Unit cell of figure 4; $\varepsilon = 0.75$

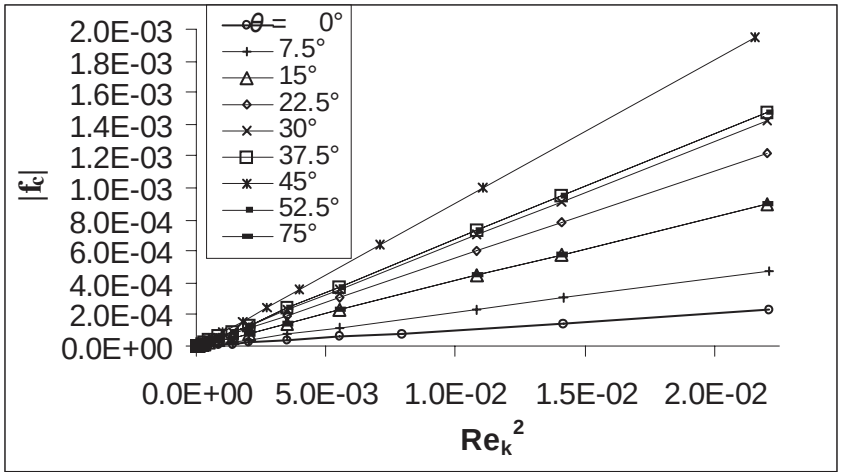

Figure 21: Variation of the modulus of $\mathbf{f_c}$ with Re_k^2 for different values of θ. Unit cell of figure 4; $\varepsilon = 0.75$

However, inspecting the behavior of f_{cx} and $|\mathbf{f_c}|$ for larger Reynolds numbers indicates that the existence of a linear evolution with Re_k in a strong inertia regime, when it can be identified, is only an approximation. This is obvious when the derivatives of these quantities are represented versus Re_k as reported in figures 22 and 23 respectively. Evidently, the relationship between f_{cx} (or $|\mathbf{f_c}|$) and Re_k is reasonably linear over a Reynolds number interval centered on the inflexion point of this relationship

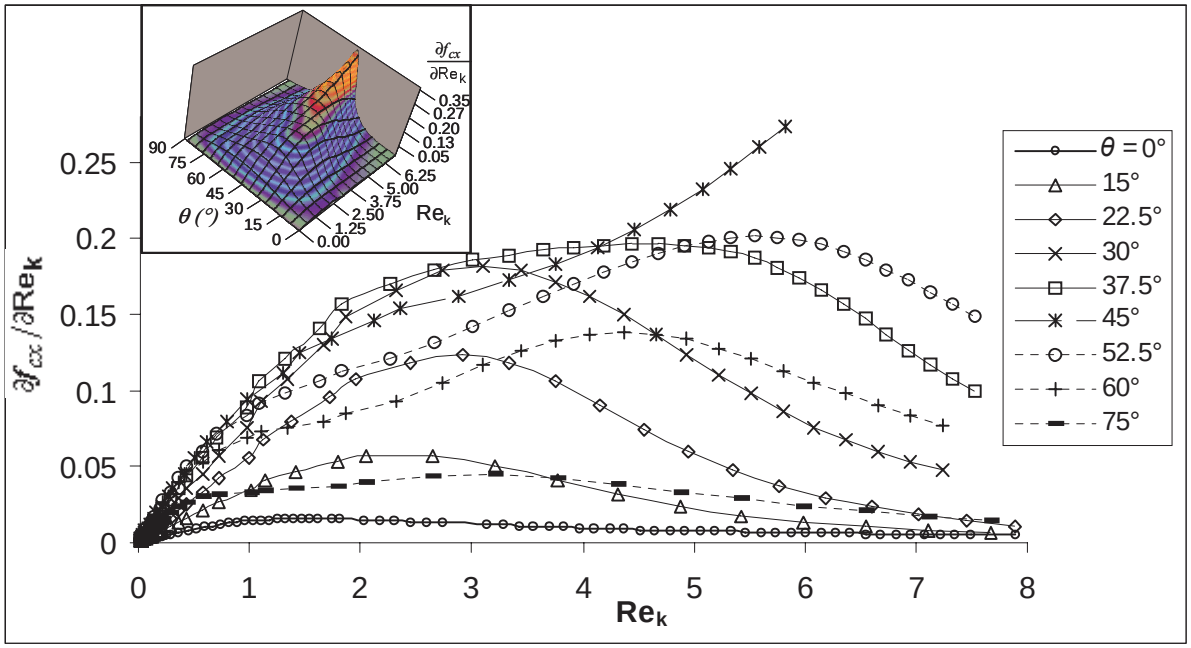

Figure 22: Variation of $\frac{\partial f_{cx}}{\partial \mathrm{Re}_k}$ with Re_k for different values of θ. *Inset*: same quantity versus θ and Re_k. Unit cell of figure 4; $\varepsilon = 0.75$

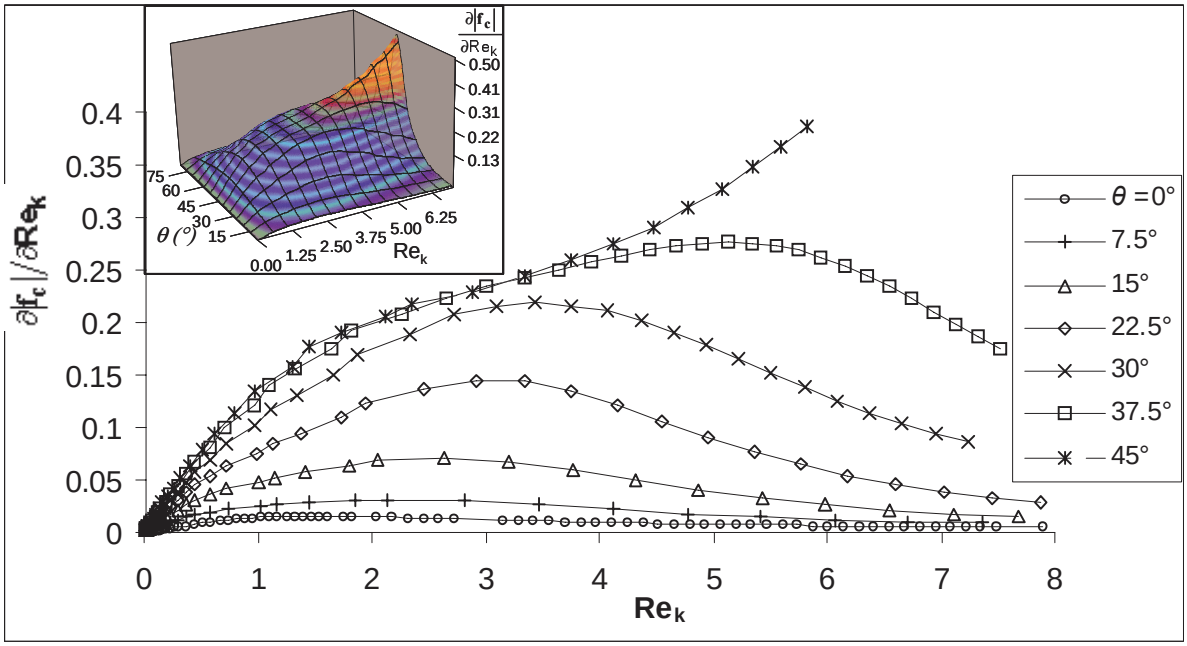

Figure 23: Variation of $\frac{\partial |\mathbf{f_c}|}{\partial \mathrm{Re}_k}$ with Re_k for different values of θ. *Inset*: same quantity versus θ and Re_k. Unit cell of figure 4; $\varepsilon = 0.75$

The case $\theta = 45°$ is a singular situation for which no inflexion point is obtained for Re_k up to ~ 7 ($\mathrm{Re}_d \sim 30$) whereas a quadratic law fits very well the data in the whole range of Reynolds numbers investigated here as demonstrated in figure 24. The existence of linear dependence of the correction on Re_k for higher values of the Reynolds number, although plausible, is however questionable regarding the non-stationary character of the flow that may occur in a higher velocity range.

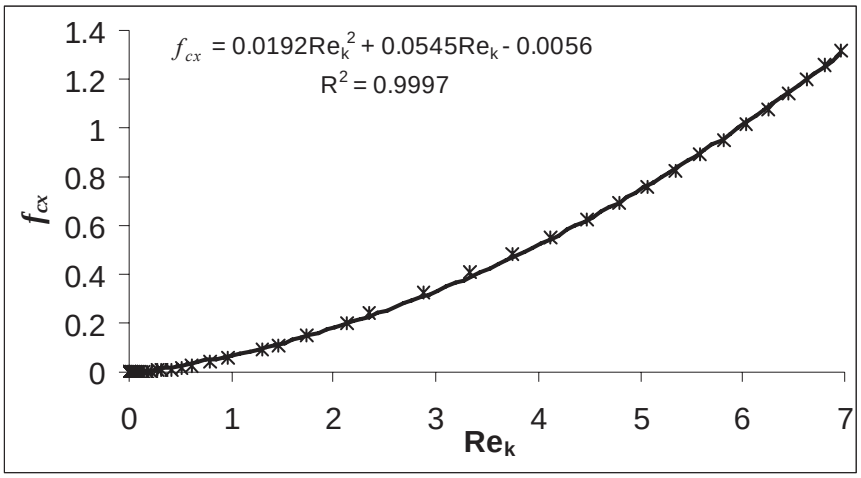

Figure 24: Quadratic law fit peformed on f_{cx} as a function of Re_k for $\theta = 45°$ and $0 \leqslant \mathrm{Re}_k \leqslant 7$. Unit cell of figure 4; $\varepsilon = 0.75$

When θ increases from 0° to values close to 45°, the inflexion zone shifts to higher Reynolds numbers (see figure 22). For instance, linearity on f_{cx} starts at $\mathrm{Re}_k \sim 0.9$ for $\theta = 0°$ and at $\mathrm{Re}_k \sim 2.5$ for $\theta = 37.5°$. On the contrary , when θ increases from 45° to 90°, the inflexion zone shifts to lower Reynolds numbers. For example, linearity for f_{cx} starts at $\mathrm{Re}_k \sim 4$ for $\theta = 52.5°$ and at $\mathrm{Re}_k \sim 1.7$ for $\theta = 82.5°$. A similar behavior is observed on $|\mathbf{f_c}|$ (see figure 23).

Identification of weak and strong inertia regimes for both f_{cx} and $|\mathbf{f_c}|$ and all angles (except for strong inertia at $\theta = 45°$), allows the determination of the coefficients A, B, C and D in correlations (43) and (44) that are represented in figures 25 and 26 . Results in the weak inertia regime indicate that

i) B is always extremely small (less than 10^{-5}) confirming that the onset of Darcy's law deviation scales as Re_k^2, i.e. $|\langle \mathbf{v}_\beta \rangle|^3$.

ii) Intensity of inertial effects strongly depends on θ. To illustrate that, the maximum ($\theta \simeq 54°$ for f_{cx}, see discussion above) to minimum ratio of A is roughly 6.5 for f_{cx} and 8.6 for $|\mathbf{f_c}|$.

iii) The correction can be significant and, for instance, reaches ~ 0.17 (f_{cx}) and ~ 0.22 ($|\mathbf{f_c}|$) for $\theta = 37.5°$.

In the strong inertia regime, it can be concluded that

i) D increases in magnitude with θ in the range $0 \leqslant \theta < 45°$ and decreases in the range $45° < \theta \leqslant 90°$

ii) D in the correlation (44) is not negligible confirming that the Forchheimer type of correction is an approximation (see the discussion above while analyzing the dependence of C on ϵ). In fact the use of a pure quadratic velocity correction requires the contribution of D to be lumped in a Forchheimer permeability different from the intrinsic one.

iii) Inertial effects strongly increase with θ in the range $0 \leqslant \theta < 45°$ and decrease in the range $45° < \theta \leqslant 90°$ This can be illustrated by the variation of C (see figure 25). For instance, the ratio of C obtained at $\theta = 37.5°$ to that obtained at $\theta = 0°$ is roughly 13 (respectively 18) when estimated on f_{cx} (respectively on $|\mathbf{f_c}|$).

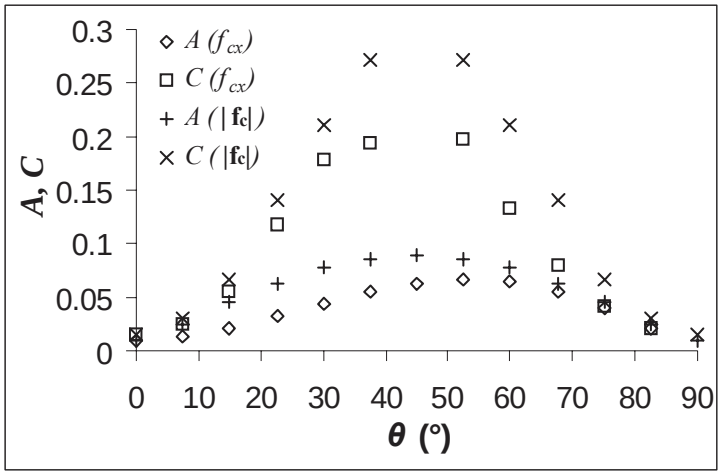

Figure 25: Coefficients A and C of correlations (43) and (44) versus $\boldsymbol{\nabla}\langle p_\beta^* \rangle^\beta$ orientation θ. Unit cell of figure 4; $\varepsilon = 0.75$

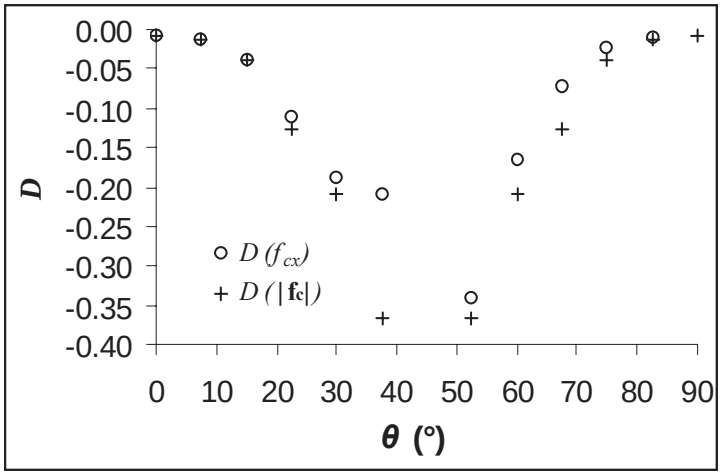

Figure 26: Coefficients D of correlation (44) versus $\boldsymbol{\nabla}\langle p_\beta^* \rangle^\beta$ orientation θ. Unit cell of figure 4; $\varepsilon = 0.75$

From these coefficients, the crossover Reynolds number Re_{kc} can be determined using the definition in equation (49). According to the relationship (50), Re_{dc} is directly proportional to Re_{kc} and results are presented only on this last quantity in figure 27. The orientation of $\boldsymbol{\nabla}\langle p_\beta^* \rangle^\beta$ has a significant influence on the crossover Reynolds value. When estimated from f_{cx}, Re_{kc} increases by a factor ~ 3 when θ is increased from $0°$ to $\sim 30°$ and decreases from this value on (note that it is not defined for $\theta = 90°$). The evolution of Re_{kc} estimated from $|\mathbf{f_c}|$ presents a minimum for θ close to $8°$, increases with θ while approaching $45°$ and is symmetric with respect to $\theta = 45°$. For instance Re_{kc} is multiplied by a factor close to 3 when θ is increased from $7.5°$ to $37.5°$. The corresponding values of Re_{dc} are at most close to 9 but might be larger for θ values closer to $45°$. These variations are in agreement with the fact that the interval of Reynolds numbers where $\mathbf{f_c}$ is approximately linear with Re_k is shifted to higher values of Re_k.

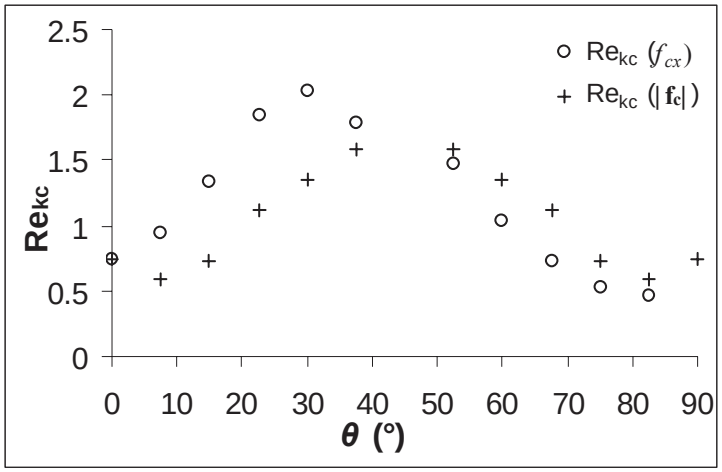

Figure 27: Crossover Reynolds numbers Re_{kc} versus $\boldsymbol{\nabla}\langle p_\beta^*\rangle^\beta$ orientation θ. This quantity is not defined here for $\theta = 45°$. Unit cell of figure 4; $\varepsilon = 0.75$

Intervals $\Delta\,\mathrm{Re}_k$ where strong inertia corrections are approximately linear functions of Re_k were estimated from Re_{kc} and the upper bound of Re_k at which deviation from linearity is equal to 5%. The variation of $\Delta\,\mathrm{Re}_k$ with θ is represented in figure 28 where we have also reported the intervals $\delta\,\mathrm{Re}_k$ corresponding to the transition between this regime and weak inertia.

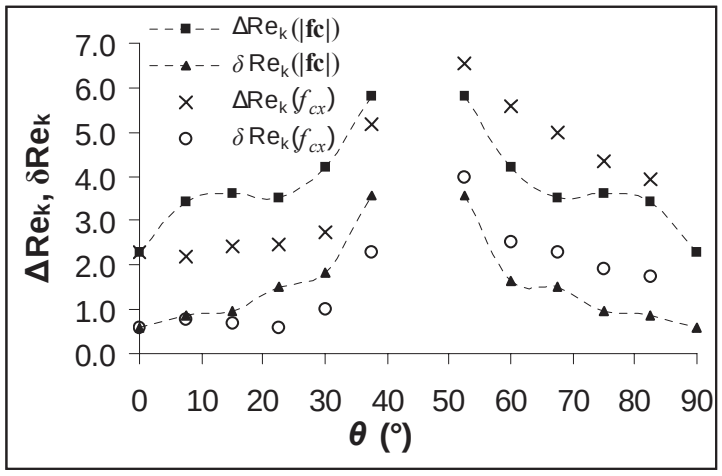

Figure 28: Evolution of the Reynolds number intervals $\Delta\,\mathrm{Re}_k$ over which f_{cx} and $|\mathbf{f_c}|$ variations with Re_k (or Re_d) are linearly approximated versus $\boldsymbol{\nabla}\langle p_\beta^*\rangle^\beta$ orientation θ. $\delta\,\mathrm{Re}_k$ is the Reynolds number interval of the transition between the weak and strong inertia regimes. Unit cell of figure 4; $\varepsilon = 0.75$

These intervals globally increase for $0° < \theta < 45°$ and decrease for $45° < \theta < 90°$. They are not defined for $\theta = 45°$. Emphasis must be put on the ratio of $\Delta\,\mathrm{Re}_k$ to $\delta\,\mathrm{Re}_k$. When f_{cx} is considered, this ratio decreases from ~ 4 at small values of θ to ~ 2 for θ approaching 45° and for $\theta > 45°$. Considering $|\mathbf{f_c}|$, this ratio decreases from ~ 4 at small values of θ to only ~ 1.5 when $\theta = 37.5°$. This indicates that the transition zone between weak and strong inertia regimes is not generally negligible. In addition, the Reynolds interval over which the generally admitted quadratic velocity correction is applicable is not

significantly larger than $\delta\,\mathrm{Re}_k$ and could even be inexistent in some particular cases.

At this point, it is interesting to investigate more realistic disordered structures restricted to two dimensions for tractable numerical simulations.

3.3 Structural disorder

In this section we shall compare the features of $\mathbf{f_c}$ in the regular case to that when disorder is introduced both on the position and the size of the solid inclusions for a given porosity ($\epsilon = 0.75$). We only consider the case $\theta = 0°$, i.e. $\boldsymbol{\nabla}\langle p^*_\beta\rangle^\beta = \mathbf{e_x}$.

3.3.1 Structure generation

In order to investigate the effect of disorder on the non-Darcy correction, weakly and strongly disordered structures were generated on the basis of the regular unit cell studied so far.

Weak disorder

Weak structural disorder is understood here as the result of random placement of the square solid inclusion in the cell of figure 4, keeping all dimensions (l and d) the same. The final structure (i.e. the unit cell of the periodic weakly disordered porous structure) is obtained by reassembling $n \times n$ random cells of edge size l resulting from this process. An example is depicted in figure 29.

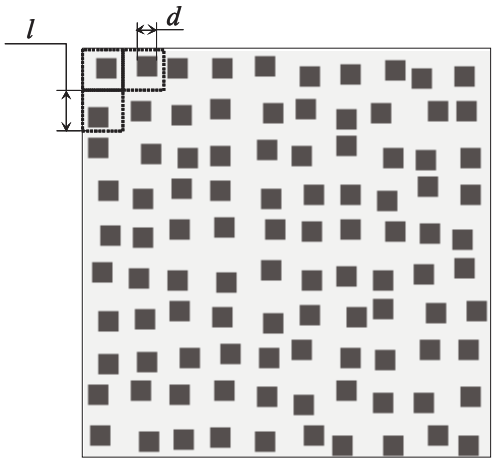

Figure 29: Weakly disordered (WD) unit cell containing 10×10 randomly placed solid inclusions. $\epsilon = 0.75$.

Random placement was obtained from generation of uniformly distributed random numbers. To avoid extremely narrow channels requiring a large number of grid blocks, random placement was constrained within a centered sub-domain of size $0.85l$ in each cell.

Strong disorder

Strong disorder was obtained by a random choice of the size of the solid square inclusions superimposed to their random placement in the cell of size l as described above using the same random generator for both random processes and constraining the porosity to a fixed value. The inclusion edge size was chosen in the range $[0.125l,\ 0.75l]$ and the final periodic unit cell was obtained as before by reassembling $n \times n$ random cells. A realization is represented in figure 30.

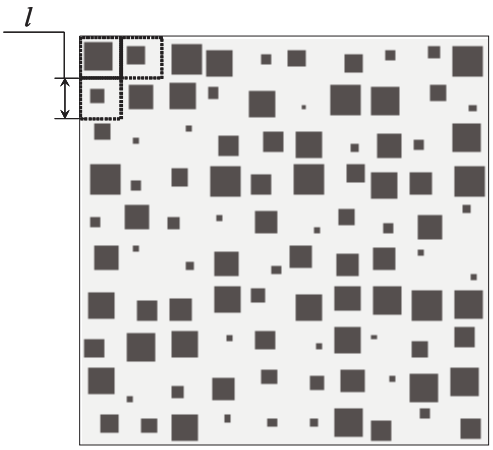

Figure 30: Unit cell of a strongly disordered (SD) structure containing 10×10 square solid inclusions. $\epsilon = 0.75$.

Unit cells of weakly and strongly disordered structures, respectively referred to as WD and SD in the following, were generated to obtain a constant porosity $\epsilon = 0.75$. When representative, these unit cells should reproduce the expected isotropic character of the infinite porous structure having the same random properties as the realization and this can be easily understood since the random generator is not direction dependent. To meet this feature, ergodicity hypothesis can be invoked so that the expected values of $\mathbf{K}^*$ and $\mathbf{F}$ are those obtained by averaging the corresponding quantities obtained on a large enough number of unit cells smaller than a representative one. To do so, $\mathbf{K}^*$ and $\mathbf{F}$ were computed over ten different realizations of x and y periodic unit cells for both WD and SD structures. We chose $n = 10$ and 400×400 grid blocks, allowing a good compromise between computational resources and precision requirements. Tests were also performed on WD unit cells with $n = 10$ and 800×800 grid blocks as well as $n = 20$ and 800×800 grid blocks. Precision criteria were those afore mentioned. Simulations were carried out for Re_k up to ~ 7 (i.e. Re_d up to ~ 31). For each SD realization, Re_d was calculated from the average value of d. An example of a flow simulation result on a WD structure is depicted in figure 31 where we have represented a velocity magnitude contour map. This figure clearly highlights channeling through less resistance flow paths resulting from disorder.

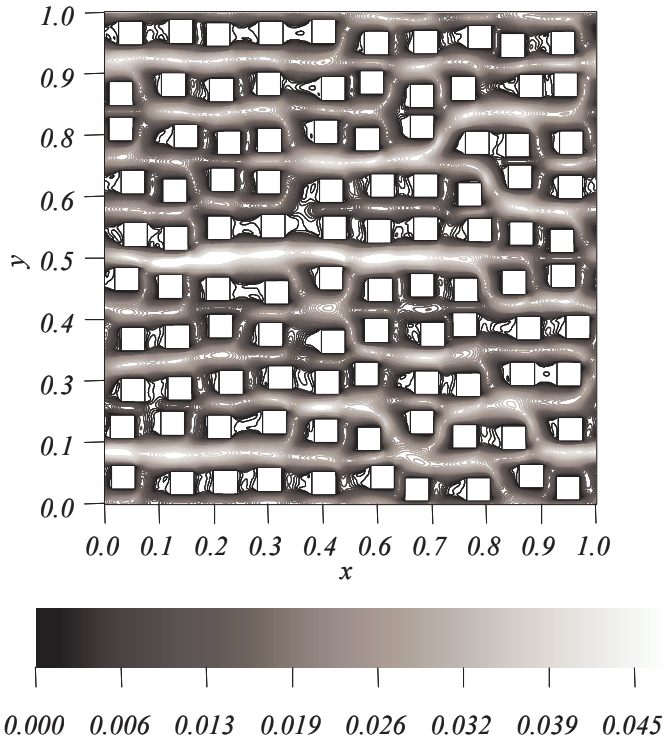

Figure 31: Velocity magnitude contour map obtained on unit cell of figure 29. $\nabla\langle p_\beta\rangle^\beta = \mathbf{e}_x$, $\mathrm{Re}_k = 2.48$, ($\mathrm{Re}_d = 10.80$)

3.3.2 Permeability

Average values of the diagonal ($\overline{k^*} = 0.5\left(\overline{k^*_{xx}} + \overline{k^*_{yy}}\right)$) and off diagonal ($\overline{k^*_{xy}}$) terms computed on the ten realizations of each structure as well as corresponding standard deviations, σ, are gathered in table 4. In both cases, $\overline{k^*}$ is very close to the value obtained on the regular structure for the same grid size ($k^* = 1.304$ 10^{-2}) with a slight increase while increasing disorder. In comparison, the standard deviations are very small showing the narrow distribution of k^*_{xx} and k^*_{yy}. The off-diagonal term k^*_{xy} has almost the same standard deviation but a mean value $\overline{k^*_{xy}}$ roughly two orders of magnitude smaller than $\overline{k^*}$ indicating that the set of realizations reasonably restores isotropy. The precision test performed on the same WD unit cells with $n = 10$ and 400×400 grid blocks on the one hand and 800×800 grid blocks on the other hand leads to a relative error of $\sim 6\ 10^{-2}\%$ and $\sim 7\ 10^{-2}\%$ on the diagonal and off-diagonal terms respectively. Moreover, the permeability tensor computed on WD unit cells with $n = 20$ and 800×800 grid blocks yields average values of $1.319\ 10^{-2}$ on the diagonal terms (i.e. a relative error of 0.8%) and $7.83\ 10^{-5}$ on the off-diagonal terms. This confirms the expected isotropic character of the cell in the Darcy regime and validates the ensemble average approach used here.

3.3.3 Non-Darcy correction

Due to disorder and since solid inclusions are kept oriented, for an infinite structure the angle θ_v that $\langle \mathbf{v}^*_\beta \rangle$ makes with $\boldsymbol{\nabla}\langle p^*_\beta\rangle^\beta = \mathbf{e_x}$ is expected to be zero whatever the Reynolds number corresponding to diagonal

Structure	$\overline{k^*}$ (σ)	$\overline{k^*_{xy}}$ (σ)
WD	$1.308\ 10^{-2}$ $(3.82\ 10^{-4})$	$-1.01\ 10^{-4}$ $(4.75\ 10^{-4})$
SD	$1.350\ 10^{-2}$ $(7.72\ 10^{-4})$	$-3.43\ 10^{-4}$ $(6.69\ 10^{-4})$
Regular	$1.304\ 10^{-2}$	–

Table 4: Average values of the components of $\mathbf{K}^*$ obtained on ten different unit cell realisations of WD and SD structures (see figures 29 and 30). $\epsilon = 0.75$, $n = 10$, 400×400 grid blocks

.

$\mathbf{H}^*$ and $\mathbf{F}$ tensors. As mentioned in the above discussion on the properties of $\mathbf{K}^*$, this feature is recovered on average in the Darcy regime. Note that since $\boldsymbol{\nabla}\langle p^*_\beta\rangle^\beta = \mathbf{e_x}$, $\tan(\theta_v) = \frac{h^*_{yx}}{h^*_{xx}}$ whereas $\mathbf{H}^* \to \mathbf{K}^*$ when $\mathrm{Re} \to 0$. However, for each realization, this is directly conditioned by the representative character of the periodic unit cell. When the Reynolds number increases, the amplitude of θ_v (i.e. the magnitude of the velocity component orthogonal to $\boldsymbol{\nabla}\langle p^*_\beta\rangle^\beta$relative to that along $\boldsymbol{\nabla}\langle p^*_\beta\rangle^\beta$) is expected to decrease as a result of the modification of the flow structure within the medium. In fact, increasing the Reynolds number leads to an increasing channeling effect coupled to an increasing number of vortices that cancel out the average y velocity component. This behavior suggested by Edwards et al. (1990) is confirmed for both WD and SD structures as shown in figures 32 and 33 representing the variation of h^*_{xx} and h^*_{yx} with Re_k and in figures 34 and 35 where the corresponding values of θ_v are reported versus Re_k. It can be clearly seen that h^*_{yx} and θ_v are decreasing in magnitude for increasing Re_k (h^*_{yx} is decreasing more rapidly than h^*_{xx}) for all the realizations. Here, Re_k was estimated with $\sqrt{(k_{xx} + k_{yy})/2}$ as the characteristic dimension.

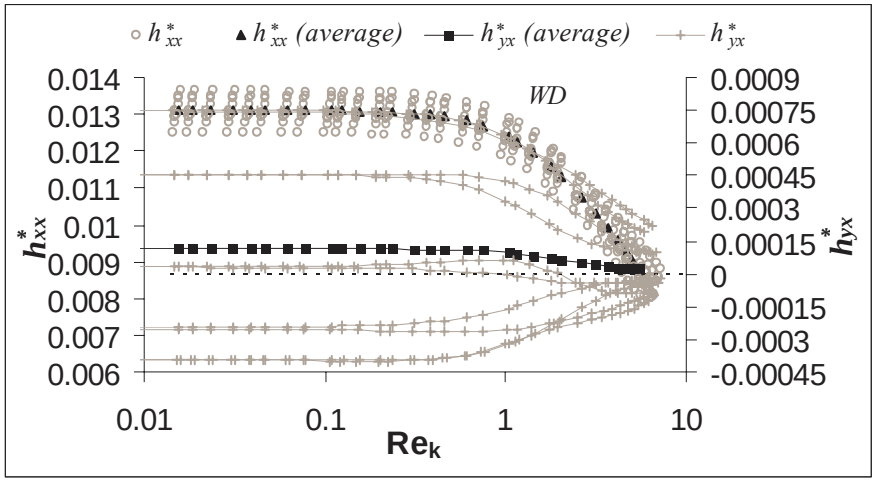

Figure 32: Variation of h^*_{xx} and h^*_{yx} versus Re_k for ten different realizations of the WD unit cell. $\boldsymbol{\nabla}\langle p^*_\beta\rangle^\beta = \mathbf{e_x}$

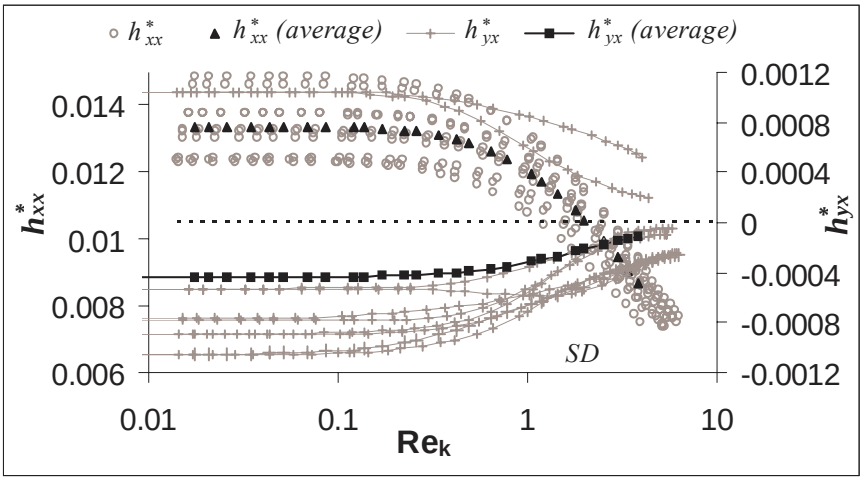

Figure 33: Varation of h^*_{xx} and h^*_{yx} versus Re_k for ten different realizations of the SD unit cell. $\boldsymbol{\nabla}\langle p^*_\beta\rangle^\beta = \mathbf{e_x}$

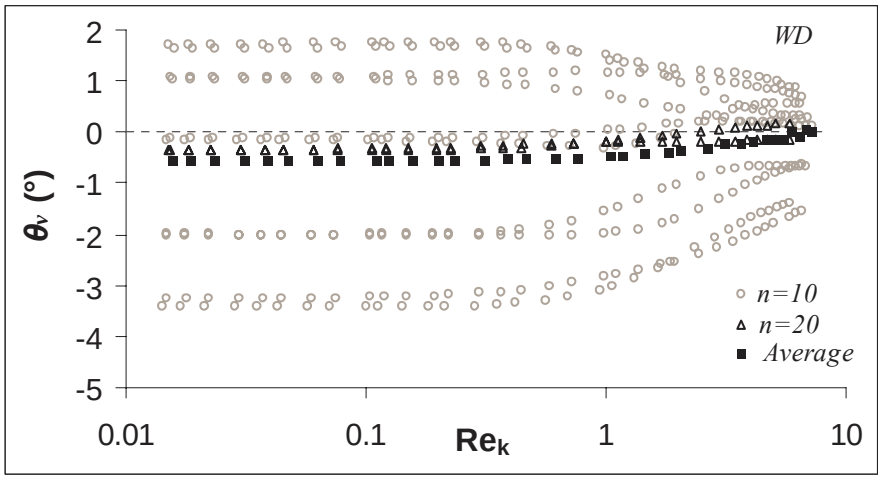

Figure 34: Angle θ_v between $\langle \mathbf{v}^*_\beta\rangle$ and $\boldsymbol{\nabla}\langle p^*_\beta\rangle^\beta$ versus Re_k for ten different realizations of the WD unit cell containing 10×10 inclusions, average of these values and results for two realizations with 20×20 inclusions. $\boldsymbol{\nabla}\langle p^*_\beta\rangle^\beta = \mathbf{e_x}$

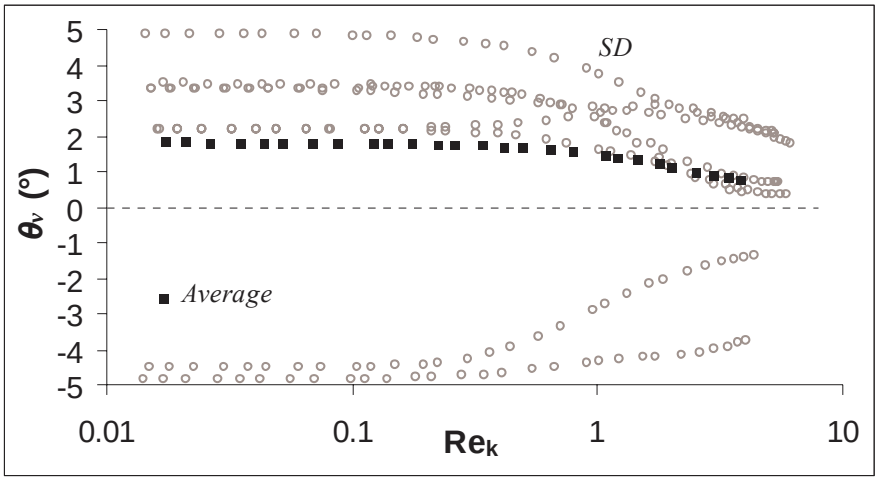

Figure 35: Angle θ_v between $\langle \mathbf{v}_\beta^* \rangle$ and $\boldsymbol{\nabla} \langle p_\beta^* \rangle^\beta$ versus Re_k for ten different realizations of the SD unit cell. $\boldsymbol{\nabla} \langle p_\beta^* \rangle^\beta = \mathbf{e_x}$

As expected, f_{xx} (and f_{yy}) are increasing with Re_k (see figures 36 and 37). It must also be noted however that off-diagonal terms of $\mathbf{F}$ are also significantly increasing in magnitude with Re_k and this suggests to investigate more thoroughly the evolution of the standard deviations of the $\mathbf{H}^*$ and $\mathbf{F}$ components with Re_k represented in figures 38 and 39.

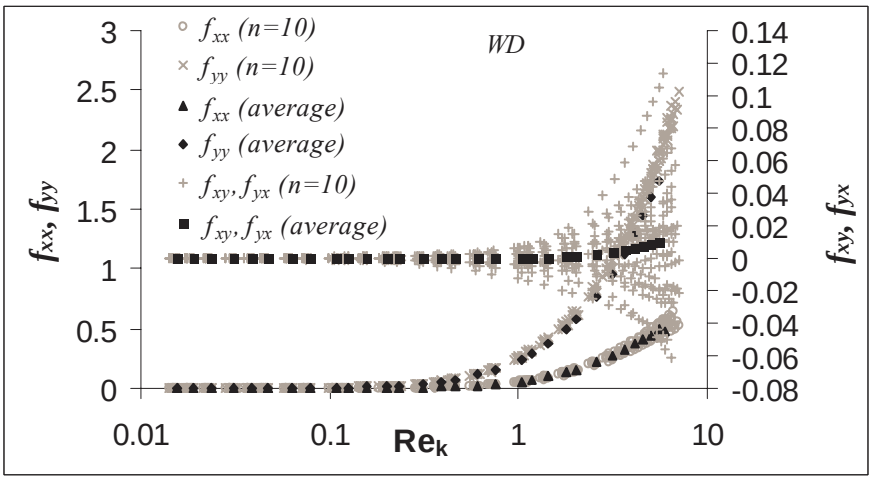

Figure 36: Variation of the terms of $\mathbf{F}$ versus Re_k for ten different realizations of the WD unit cell. $\boldsymbol{\nabla} \langle p_\beta^* \rangle^\beta = \mathbf{e_x}$

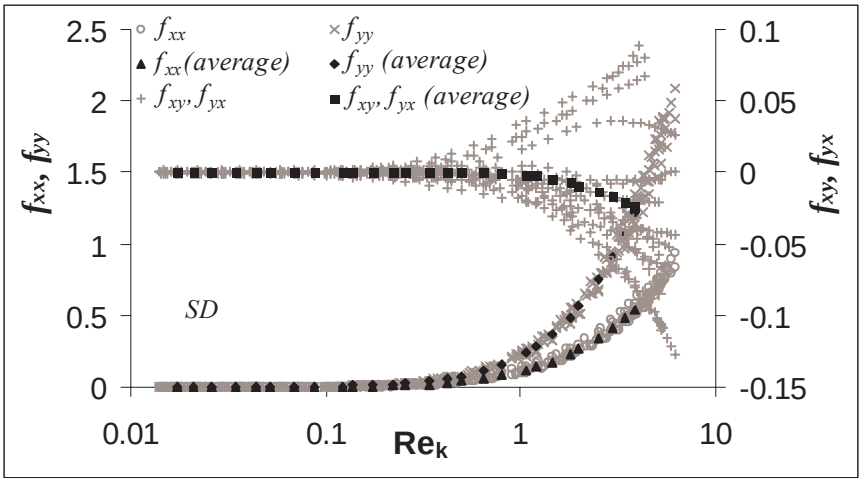

Figure 37: Variation of the terms of $\mathbf{F}$ versus Re_k for ten different realizations of the SD unit cell. $\boldsymbol{\nabla}\langle p^*_\beta \rangle^\beta = \mathbf{e_x}$

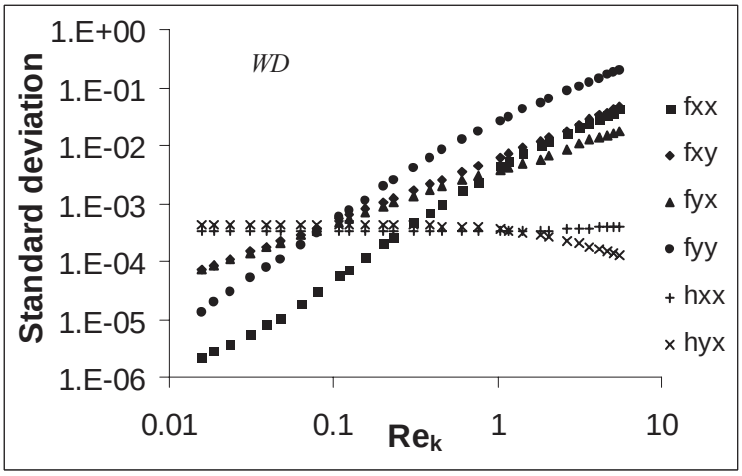

Figure 38: Variation of the standard deviations on the components of $\mathbf{H}^*$and $\mathbf{F}$ tensors calculated from ten different realizations of the WD unit cell. $\boldsymbol{\nabla}\langle p^*_\beta \rangle^\beta = \mathbf{e_x}$

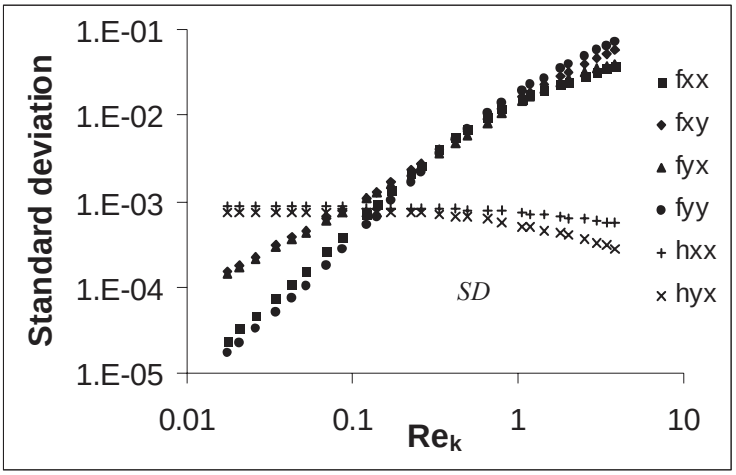

Figure 39: Variation of the standard deviations on the components of $\mathbf{H}^*$and $\mathbf{F}$ tensors calculated from ten different realizations of the SD unit cell. $\boldsymbol{\nabla}\langle p_\beta^* \rangle^\beta = \mathbf{e_x}$

The dispersion on the two components h_{xx}^* and h_{yx}^* of interest decrease for increasing Reynolds numbers, except that for h_{xx}^* for the WD structure which remains quasi constant. However, the standard deviation on all the components of $\mathbf{F}$ are strongly increasing with Re_k. This latter behavior can be easily understood recalling the direct dependence of $\mathbf{F}$ upon $\mathbf{H}^{*-1}$ (see equation (38)), the fact that components of $\mathbf{H}^*$ decrease with increasing Re_k. These facts combined with the initial lack of representativeness at $\mathrm{Re}_k \rightarrow 0$ contained in $\mathbf{K}^*$ leads to the behavior described above. The important consequence of this is a decreasing (respectively increasing) size of the REV with respect to $\mathbf{H}^*$ (respectively $\mathbf{F}$) when Re_k increases. All the results observed on average over the ten realizations are fully consistent with those obtained on two WD unit cells with $n = 20$ and the same grid size (i.e.800×800 grid blocks) (see figures 34, 40 and 41) confirming again the validity of the ensemble average approach. Tests performed on one WD structure with $n = 10$ and $800x800$ grid blocks indicate that the maximum relative error on f_{xx} or f_{yy} is less than 0.7% over the whole range of Re_k confirming the very good precision on our results.

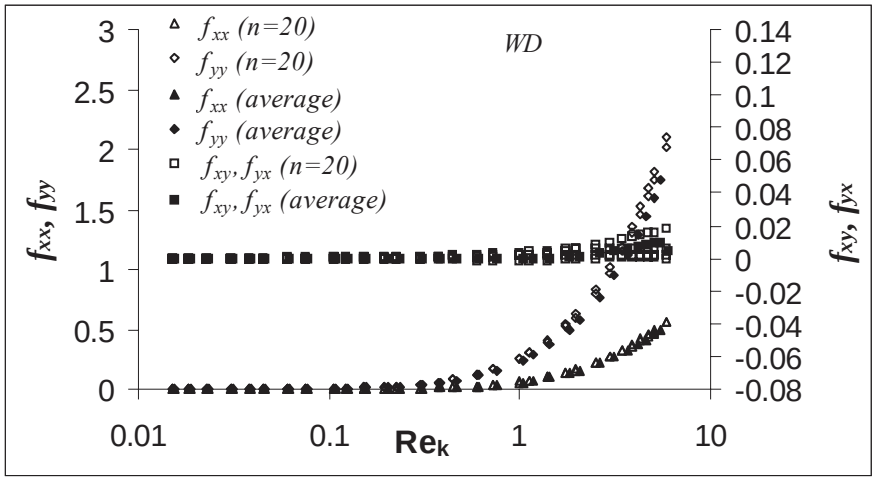

Figure 40: Variation with Re_k of the average values of the components of $\mathbf{F}$ over ten realizations with $n = 10$ and values of the same components for two realizations with $n = 20$. WD unit cell; $\boldsymbol{\nabla}\langle p^*_\beta\rangle^\beta = \mathbf{e_x}$

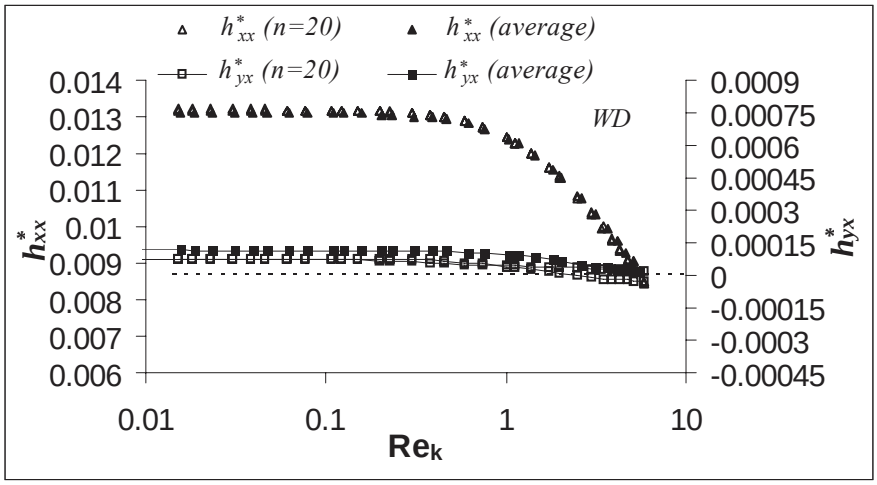

Figure 41: Variation with Re_k of the average values of h^*_{xx} and h^*_{yx} over ten realizations with $n = 10$ and values of the same components for two realizations with $n = 20$. WD unit cell; $\boldsymbol{\nabla}\langle p^*_\beta\rangle^\beta = \mathbf{e_x}$

Because off-diagonal terms of $\mathbf{F}$ cancel over the whole range of Reynolds numbers investigated here and since $\langle \mathbf{v}^*_\beta\rangle \cdot \mathbf{e_y}$ is much smaller (at least 30 and 300 times for the SD and WD structures respectively) than $\langle \mathbf{v}^*_\beta\rangle \cdot \mathbf{e_x}$, the y component, f_{cy}, of $\mathbf{f_c}$ can be disregarded in the analysis of the non Darcy correction. Hence, the non-Darcy correction is investigated only from the dependence of f_{cx} ($\simeq f_{xx}$) on Re_k in the following. The justification of that can be seen in figures 42 and 43 where the two components of $\mathbf{f_c}$ are represented versus Re_k for the WD and SD realizations.

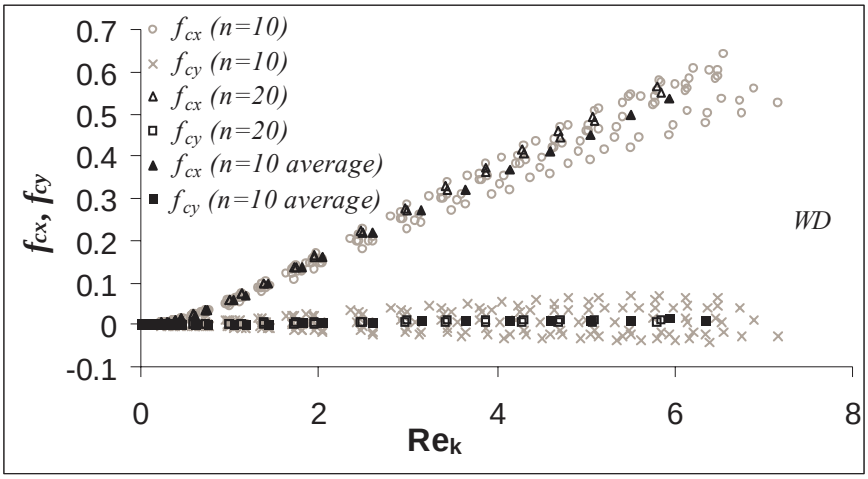

Figure 42: Variation of the components of the $\mathbf{f_c}$ vector with Re_k for ten different realizations of the WD unit cell with $n = 10$, average of these values and results for two realizations with $n = 20$. $\boldsymbol{\nabla}\langle p^*_\beta\rangle^\beta = \mathbf{e_x}$

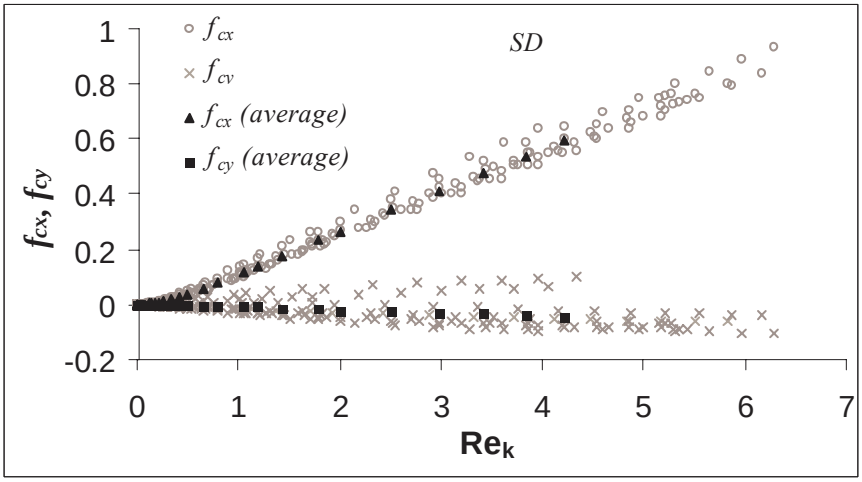

Figure 43: Variation of the components of the $\mathbf{f_c}$ vector with Re_k for ten different realizations of the SD unit cell with $n = 10$ and averages of these values. $\boldsymbol{\nabla}\langle p^*_\beta\rangle^\beta = \mathbf{e_x}$

Clearly, the onset of Darcy's law deviation scales again as Re_k^2 in the weak inertia regime that is followed by a transition regime. For larger Reynolds numbers, strong inertia regimes corresponding to excellent linear correlations with Re_k are obtained. The range over which this correlation holds are very wide indicating that this approximation becomes much more precise and robust when disorder is introduced. This is illustrated in figure 44 where $\frac{d\overline{f_{cx}}}{d\,\mathrm{Re}_k}$, normalized by its respective maximum value, is represented versus Re_k for WD and SD structures and compared to $\frac{df_{cx}}{d\,\mathrm{Re}_k}$ obtained for the regular structure with $\theta = 0°$ and $\varepsilon = 0.75$. This figure shows that $\frac{d\overline{f_{cx}}}{d\,\mathrm{Re}_k}$ tends to a constant plateau for disordered media.

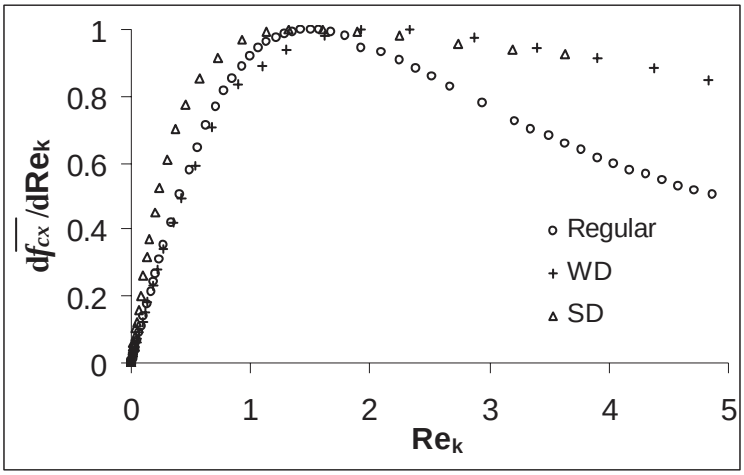

Figure 44: Variation of $\frac{d\overline{f_{cx}}}{d\,\mathrm{Re}_k}$ normalized by its maximum value versus Re_k for the WD and SD structures. Comparison to $\frac{df_{cx}}{d\,\mathrm{Re}_k}$ obtained for the regular structure with $\theta = 0°$ and $\varepsilon = 0.75$

Again, using correlations in equations (43) and (44) leads to the determination of the coefficients A, B, C and D as well as the crossover Reynolds number Re_{kc} defined in equation (49) on each realization. When possible (see discussion below), the Reynolds range $\Delta\,\mathrm{Re}_k$ where the linear relationship $f_{cx}(\mathrm{Re}_k)$ remains valid was also determined from the upper bound of Re_k at which f_{cx} deviates by 5% from the strong inertia model. The Reynolds interval, $\delta\,\mathrm{Re}_k$, of the transition region was also estimated on each realization. Averaged values $\overline{A}$, $\overline{C}$, $\overline{D}$, $\overline{\mathrm{Re}_{kc}}$, $\overline{\mathrm{Re}_{dc}}$, $\overline{\Delta\,\mathrm{Re}_k}$, and $\overline{\Delta\,\mathrm{Re}_d}$ along with their corresponding standard deviations are reported in table 5.

Structure	*Regular*	*WD*	*SD*
$\overline{A}$ (σ_A)	$1.03\ 10^{-2}$	$7.0\ 10^{-2}$ ($6.4\ 10^{-3}$)	0.20 ($4.9\ 10^{-2}$)
$\overline{C}$ (σ_C)	$1.54\ 10^{-2}$	0.10 ($8.0\ 10^{-3}$)	0.15 ($1.2\ 10^{-2}$)
$\overline{D}$ (σ_D)	$-6.7\ 10^{-3}$	$-4.8\ 10^{-2}$ ($5.9\ 10^{-3}$)	$-4.1\ 10^{-2}$ ($6.6\ 10^{-3}$)
$\overline{\mathrm{Re}_{kc}}$ ($\sigma_{\mathrm{Re}_{kc}}$)	0.74	0.73 (6.6 10^{-2})	0.40 (6.8 10^{-2})
$\overline{\Delta\,\mathrm{Re}_k}$ ($\sigma_{\Delta\,\mathrm{Re}_k}$)	2.31	5.34 (0.66)	–
$\overline{\mathrm{Re}_{dc}}$ (σ_{Re_c})	3.25	3.19 (0.28)	1.57 (0.27)
$\overline{\Delta\,\mathrm{Re}_d}$ ($\sigma_{\Delta\,\mathrm{Re}}$)	10.11	23.37 (2.98)	–

Table 5: Average values of A and C (see equations 43 and 44), Re_{kc}, $\Delta\,\mathrm{Re}_k$ and corresponding standard deviations for the WD, SD and regular structures. $\epsilon = 0.75$, $n = 10$, 400×400 grid blocks.

.

On all the realizations, B is less than 10^{-5} confirming again the pure velocity cubic dependence of the onset of deviation to Darcy's law. In addition, values of D are much larger in magnitude when disorder is introduced, leading to Forchheimer permeabilities markedly different from the intrinsic ones if a pure quadratic velocity dependence is to be used in the strong inertia regime.

These results call the following important conclusions. First, intensity of inertial effects increases with disorder as indicated by the variations of A and C both being roughly one order of magnitude greater for the SD structure in comparison to the regular one. As in the regular case for $\theta = 0°$, the non-Darcy correction remains extremely small compared to unity (around 0.03 at the crossover on the SD structure) in the weak inertia regime. Second, the decreasing value of Re_{kc} and Re_{dc} with increasing disorder must

be emphasized. This effect is much more significant when strong disorder is introduced. One should note that for the SD structure, Re_{dc} is close to unity which is the usual admitted value at which Darcy regime is lost on real porous media . Third, the Reynolds range ($\Delta\,\mathrm{Re}_k$ and $\Delta\,\mathrm{Re}_d$) where the Forchheimer type of correction can be considered as a reasonable one increases significantly when disorder is introduced. In particular, for the SD structure, $\Delta\,\mathrm{Re}_k$ and $\Delta\,\mathrm{Re}_d$ could not be estimated. Indeed, for the whole range of Re_k over which computations were carried out (up to $\mathrm{Re}_k \sim 6$, $\mathrm{Re}_d \sim 24$), the linear relationship persists with less than 5% error. These results are a strong indication that the robustness of the quadratic dependence of the correction upon the velocity can be attributed to the disorder inherent to natural porous structures. This must moderate a conclusion put forth in the literature according to which the validity of the Forchheimer correction might be attributed to the 3D nature of the flow (Fourar et al., 2004). Finally, we shall remark that the extent of the transition zone between the weak and strong inertia regimes is not noticeably modified by the introduction of disorder.

4 Conclusion

In this work we have examined the deviation to Darcy's law for one-phase incompressible flow in homogeneous porous media when significant inertial effects are to be taken into account. Our analysis is based on an exact macroscopic model valid in the framework of stationary flow over periodic structures and more general than the classical Forchheimer model involving a scalar inertial resistance factor. It includes a correction vector to Darcy's law involving a correction tensor $\mathbf{F}$. In the general case, this tensor is given by an exact closure problem, the solution of which requires that of the microscopic flow. Both solutions can be obtained from the same Navier-Stokes solver. On this basis, a second upscaling could be envisaged to take into account inertial effects in heterogeneous media.

Through a tremendous amount of comprehensive results obtained from computations performed on model 2D structures, the different mean flow regimes have been analyzed versus the Reynolds number, pressure gradient orientation, and structural parameters such as porosity and disorder. These regimes were examined making use of a dimensionless form of the excess macroscopic force exerted on the structure relative to the flow in the Darcy regime. Major conclusions emerge from these results and can be listed as follows.

For ordered structures, in general, the correction tensor $\mathbf{F}$ is a full-populated non-symmetric tensor even if the structure is geometrically isotropic. This is in accordance with the fact that the force is not pure drag, i.e. is not aligned with the mean flow. The exception is when the applied pressure gradient is along a symmetry axis of the representative unit cell. For disordered isotropic media, $\mathbf{F}$ should be diagonal when estimated over a Representative Elementary Volume, the size of which increases with increasing Reynolds numbers.

Intensity of inertial effects always increase with increasing Reynolds numbers. Special attention must be however dedicated to the definition of the Reynolds number. For an isotropic ordered structure, intensity of inertial effects is a decreasing function of the porosity when the Reynolds number is defined with the square root of the permeability. The opposite holds when the Reynolds number is defined in the classical manner using the grain size as the characteristic length.

In all cases studied here, a weak inertia regime characterized by a square dependence of the correction on the Reynolds number, i.e. a cubic dependence on the velocity, is always recovered as the onset of the deviation to Darcy's law in accordance with theoretical results reported in the literature. In most cases under study, the intensity of the correction in this regime is insignificant except on ordered structures with particular pressure gradient orientations.

For higher Reynolds numbers, the strong inertia regime where the correction is expected to linearly depend upon the Reynolds number (i.e. a quadratic dependence on the velocity) is generally a valid approximation. It corresponds to an interval of Reynolds numbers of variable extent centered on an inflexion point of the correction as a function of the Reynolds number. Moreover, since it is not purely quadratic, this would lead to the introduction of a so-called "Forchheimer permeability" different from the intrinsic one if a Forchheimer correction is to be used.

The behavior of the correction in the transition region between the weak and strong inertia regimes was not detailed. Instead, a crossover Reynolds number minimizing the difference between the weak and strong inertia models was introduced. When based on the square root of the permeability, the crossover Reynolds number is an increasing function of the porosity while the opposite holds when the definition of the Reynolds number is based on the grain size. This crossover Reynolds number significantly decreases when strong disorder is introduced. The extent of the transition zone is not markedly affected by disorder.

On disordered structures, the velocity quadratic dependence of the correction is a robust approximation in a very large interval of Reynolds numbers. Moreover, the crossover Reynolds number and the magnitude of the weak inertia correction are both small and therefore this regime is generally overlooked during experiments.

Although disorder was investigated in two dimensions only, these results provide indication that the same conclusions might be safely extended to 3D real porous structures.

References

Ahmed, N. and Sunada, D. K.: 1969, Nonlinear flow in porous media, *J. Hydr. Div ASCE* **95**(HY6), 1847–1857.

Amaral Souto, H. and Moyne, C.: 1997, Dispersion in two-dimensional periodic porous media, part i: Hydrodynamics, *Phys Fluids* **9**(8), 2243–2252.

Andrade, J. S., Costa, U. M. S., Almeida, M. P., Makse, H. A. and Stanley, H. E.: 1999, Inertial effects on fluid flow through disordered porous media, *Phys. Rev. Lett.* **82**(26), 5249–5252.

Barak, A. Z. and Bear, J.: 1981, Flow at high reynolds numbers through anisotropic porous media, *Adv. Water Resources* **4**, 54–66.

Barrere, J.: 1990, *Modélisation Des Écoulement de Stokes et de Navier-Stokes En Milieu Poreux*, PhD thesis, Thèse de l'université Bordeaux I.

Barrère, J., Gipouloux, O. and Whitaker, S.: 1992, On the closure problem for darcy's law, *Transport in Porous Media* **7**, 209–222.

Bear, J.: 1972, *Dynamics of Fluids in Porous Media*, Dover, New York.

Beavers, G. S. and Sparrow, E. M.: 1969, Non-darcy flow through fibrous porous media, *J. Appl. Mech. Trans. ASME* **December**, 711–714.

Blick, E. F.: 1966, Capillary orifice model for high speed flow through porous media, *I and EC, Process Design and Development* **5**, 90–94.

Chauveteau, G.: 1965, *Essai sur la Loi de Darcy et Les Écoulements Laminaires À Perte de Charge Non Linéaire*, PhD thesis, University of Toulouse.

Chauveteau, G. and Thirriot, C.: 1967, Régimes d'écoulement en milieu poreux et limite de la loi de darcy, *La Houile Blanche* **1**(22), 1–8.

Chen, Z., Lyons, S. L. and G., Q.: 2001, Derivation of the forchheimer law via homogenization, *Transport in Porous Media* **44**(2), 325–335.

Cornell, D. and Katz, D. L.: 1953, Flow of gases through consolidated porous media, *Ind. Eng. Chem.* **45**, 2145–2153.

Coulaud, O., Morel, P. and Catagirone, J. P.: 1988, Numerical modeling of non-linear effects in laminar flow through a porous medium, *J. Fluid. Mech.* **190**, 393–407.

Cvetkovic, V. D.: 1986, A continuum approach to high velocity flow in a porous medium, *Transport in Porous Media* **1**(1), 63–97.

Darcy, H.: 1856, Les fontaines publiques de la ville de dijon, *Librairie des corps impériaux des ponts et chaussées et des mines, Paris* .

Drumond, J. E. and Tahir, M. I.: 1984, Laminar viscous flow through regular arrays of parallel solid cylinders, *Int. J. Multiphase Flow* **10(5)**, 515–540.

Dullien, A. L. and Azzam, M. I. S.: 1973, Flow rate-pressure gradient measurement in periodically nonuniform capillary tube, *AIChE J.* **19**, 222–229.

Dybbs, A. and Edwards, R. V. A.: 1984, A new look at porous media fluid mechanics darcy to turbulent, *Fundamentals of Transport Phenomena in Porous Media* **82**, 201–256. in NATO ASIE, Martinus Nijhoff Publishers, Dordrecht.

Edwards, D. A., Shapiro, M., Bar-Yoseph, P. and Shapira, M.: 1990, The influence of reynolds number upon the apparent permeability of spatially periodic arrays of cylinders, *Phys. Fluids* **2**(1), 45–55.

Ene, H. I. and Sanchez-Palencia, E.: 1975, Equations et phénomènes de surface pour l'écoulement dans un modèle de milieu poreux, *J. Méc.* **14**, 73–108.

Ergun, S.: 1952, Fluid flow through packed columns, *Chem. Eng. Prog.* **48**, 89–94.

Firdaouss, M. and Guermond, J. L.: 1995, Sur l'homogénéisation des équations de navier-stokes à faible nombre de reynolds, *C. R. Acad. Sci. Paris, Série I* **320**, 245–251.

Firdaouss, M., Guermond, J. L. and Le Quéré, P.: 1997, Nonlinear corrections to darcy's law at low reynolds numbers, *J. Fluid Mech.* **343**, 331–350.

Forchheimer, P.: 1901, Wasserbewgung durch boden. z., *Vereines deutscher ingnieure* **XXXXV**(45), 1782–1788.

Fourar, M., Radilla, G., Lenormand, R. and Moyne, C.: 2004, On the non-linear behavior of a laminar single-phase flow through two and three-dimensional porous media, *Advanced in Water Resources,* **27**, 669–677.

Freitas, C. J., Street, R. L., Findikakis, A. N. and Koseff, J. R.: 1985, Numerical simulation of three-dimensional flow in cavity, *International Journal for Numerical Methods in Fluids* **5**, 561–575.

Geertsma, J.: 1974, Estimating the coefficient of inertial resistant in fluid flow through porous media, *Society of Petroleum Engineers Journal* **October 1974.**, 445–450.

Ghaddar, C. K.: 1995, On the permeability of unidirectional fibrous media: A parallel computational approach, *Phys. Fluids* **7**(11), 2563–2586.

Giorgi, T.: 1997, Derivation of the forchheimer law via matched asymptotic expansions, *Transport in Porous Media* **29**(2), 191–206.

Gray, W. G.: 1975, A derivation of the equations for multi-phase transport, *Chem. Eng. sci.* **30**, 229–233.

Green, L. and Duwez, P. J.: 1951, Fluid flow through porous metals, *J. Appl. Mech.* **18**, 39–45.

Han, T., Humphrey, J. A. C. and Launder, B. E.: 1981, A comparison of hybrid and quadratic-upstream differencing in high reynolds number elliptic flows, *Computer Methods in Applied Mechanics and Engineering* **29(1)**, 81–95.

Happel, J. and Brenner, H.: 1983, *Low Reynolds Number Hydrodynamics*, Prentice-Hall, Englewood Cliffs, NJ.

Hassanizadeh, S. M. and Gray, W. G.: 1987, High velocity flow in porous media, *Transport in Porous Media* **2**(3), 521–531.

Hayase, T., Humphrey, J. A. C. and Greif, R.: 1992, A consistently formulated QUICK scheme for fast and stable convergence using finite-volume iterative calculation procedures, *Journal of Computational Physics* **98(1)**, 108–118.

Hayes, R. E., Afacan, A. and Boulanger, B.: 1995, An equation of motion for an incompressible newtonian fluid in a packed bed, *Transport in Porous Media* **18**, 185–198.

Irmay, S.: 1958, On the theoretical derivation of darcy and forchheimer formulas, *J. Geophys. Res.* **39**, 702–707.

Koch, J. B. and Ladd, A. J. C.: 1997, Moderate reynolds number flows through periodic and random arrays of aligned cylinders, *J. fluid Mech.* **349**, 31–66.

Larson, R. E. and Higdon, J. J. L.: 1987, Microscopic flow near the surface of two-dimensional porous media. part 2. transverse flow, *J. Fluid Mech.* **178**, 119–136.

Leonard, B. P.: 1979, A stable and accurate convective modelling procedure based on quadratic upstream interpolation, *Computer Methods in Applied Mechanics and Engineering* **19**(1), 59–98.

Leschziner, M. A.: 1980, Practical evaluation of three finite difference schemes for the computation of steady-state recirculating flows, *Computer Methods in Applied Mechanics and Engineering* **23(3)**, 293–312.

Lindquist, E.: 1933, On the flow of water through porous soil, *Premier congéres des grands barrages, Stockholm* **5**, 81–101.

Ma, H. and Ruth, D. W.: 1993, The microscopic analysis of high forchheimer number flow in porous media, *Transport in Porous Media* **13**(2), 139–160.

MacDonald, I. F., El-Sayed, M. S., Mow, K. and Dullien, F. A. L.: 1979, Flow through porous media, the ergun equation revisited, *Ind. Eng. Chem. Fundm* **18**(3), 199–208.

Mei, C. C. and Auriault, J. L.: 1991, The effect of weak inertia on flow through a porous medium, *J. Fluid Mech* **222**, 647–663.

Panfilov, M. and Fourar, M.: 2006, Physical splitting of non linear effects in high-velocity stable flow through porous media, *Advances in Water Ressources* **29**, 30–41.

Papathanasiou, T. D., Markicevic, B. and Dendy, E. D.: 2001, A computational evaluation of the ergun and forchheimer equations for fibrous porous media, *Phys. Fluids* **13**(10), 2795–2804.

Patankar, S. V.: 1980, *Numerical Heat Transfer and Fluid Flow*, Hemisphere Publishing Corporation.

Peyret, R. and Taylor, T. D.: 1983, *Computational Methods for Fluid Flow*, Springer-Verlag, New York.

Pollard, A. and Siu, A. L. W.: 1982, The calculation of some laminar flows using various discretization schemes, *Comput. Methods Appl. Mech. Eng.* **35**, 293–313.

Rasoloarijaona, M. and Auriault, J. L.: 1994, Nonlinear seepage flow through a rigid porous medium, *Eur. J. Mech. B/Fluids* **13**(2), 177–195.

Rojas, S. and Koplik, J.: 1998, Nonlinear flow in porous media, *Phys. Rev. E* **58(4)**, 4476–4782.

Ruth, D. and Ma, H.: 1993a, Numerical analysis of the viscous incompressible flow in a diverging-converging RUC, *Transport in Porous Media* **13**(2), 161–177.

Ruth, D. W. and Ma, H.: 1993b, On the derivation of the forchheimer equation by means of the averaging theorem, *Transport in Porous Media* **7**, 255–264.

Sanchez-Palencia, E.: 1980, *Non Homogeneous Media and Vibration Theory, Lecture Notes in Physics*, Springer.

Scheidegger, A. E.: 1974, *The Physics of Flow Through Porous Media*, University of Toronto Press, Toronto, Canada.

Schneebeli, G.: 1955, Expériences sur la limite de validité de la loi de darcy et l'apparition de la turbulence dans un écoulement de filtration, *La Houille Blanche* **2**(10), 141–149.

Skjetne, E. and Auriault, J. L.: 1999a, High-velocity laminar and turbulent flow in porous media, *Transport in Porous Media* **36**, 131–147.

Skjetne, E. and Auriault, J. L.: 1999b, New insights on steady, non-linear flow in porous media, *Eur. J. Mech. B/Fluids* **18**(1), 131–145.

Skjetne, E., Hansen, A. and Gudmundsson, J. S.: 1999, High velocity flow in a rough fracture, *J. Fluid Mech.* **383**, 1–28.

Suekane, T., Yokouchi, Y. and S., H.: 2003, Inertial flow structures in a simple-packed bed of spheres, *AIChE Journal* **49**(1), 10–17.

Tek, M. R.: 1957, Development of a generalized darcy equation, *Trans. AIME* **210**, 376–377.

Tek, M. R., Coats, K. H. and Katz, D. L.: 1962, The effect of turbulence on flow of natural gas through porous reservoirs, *J. Petrol. Technol. Trans. AIME* **222**, 799–806.

Thauvin, F. and Mohanty, K. K.: 1998, Network modeling of non-darcy flow through porous media, *Transport in Porous Media* **31**(1), 19–37.

Ward, J. C.: 1964, Turbulent flow in porous media, *J. Hydr. Div., ASCE* **90**(HY5), 1–12.

Whitaker, S.: 1986, Flow in porous media i: A theoretical derivation of darcy's law, *Transport in Porous Media* **1**(1), 3–25.

Whitaker, S.: 1996, The forchheimer equation: A theoretical development, *Transport in Porous Media* **25**(1), 27–61.

Whitaker, S.: 1999, *The Method of Volume Averaging*, Theory and Applications of Transport in Porous Media, Kluwer Academic, Dordrecht, The Netherlands.

Wodie, J. C. and Levy, T.: 1991, Correction non linéaire de la loi de darcy, *C. R Acad. Sci. Paris II* pp. 157–161.

Wright, D. E.: 1968, Nonlinear flow through granular media, *J. Hydr. Div. ASCE* **4**, 851–872.

Zuzovsky, M., Adler, P. M. and Brenner, H.: 1983, Spatially periodic suspensions of convex particles in linear shear flows. III. dilute arrays of spheres suspended in newtonian fluids, *Phys. Fluids* **26**(7), 1714–1723.

Chapitre 3

Two-phase inertial flow in homogeneous porous media: A macroscopic model obtained from the volume averaging method

Two-phase inertial flow in homogeneous porous media: A macroscopic model obtained from the volume averaging method

Abstract

The purpose of this paper is to derive a macroscopic model of inertial two-phase, incompressible, Newtonian fluid flow through homogenous porous media using the method of volume averaging. Starting from the contnuity and Navier-Stokes equations in each phase β and γ, it is shown that under some constraints on the length- and time-scales that are explicitly provided, the macroscopic model is given by

$$\frac{\partial \varepsilon_\alpha}{\partial t} + \nabla \cdot \langle \mathbf{v}_\alpha \rangle = 0 \qquad \alpha = \beta,\ \gamma$$

and

$$\begin{aligned} \langle \mathbf{v}_\alpha \rangle &= -\frac{\mathbf{K}^*_{\alpha\alpha}}{\mu_\alpha}(\nabla \langle p_\alpha \rangle^\alpha - \rho_\alpha \mathbf{g}) - \mathbf{F}_\alpha \cdot \langle \mathbf{v}_\alpha \rangle \\ &\quad -\frac{\mathbf{K}^*_{\alpha\kappa}}{\mu_\kappa}(\nabla \langle p_\kappa \rangle^\kappa - \rho_\kappa \mathbf{g}) - \mathbf{F}_{\alpha\kappa} \cdot \langle \mathbf{v}_\kappa \rangle \qquad \alpha,\ \kappa = \beta,\ \gamma \qquad \alpha \neq \kappa \end{aligned}$$

or equivalently for the latter

$$\begin{aligned} \langle \mathbf{v}_\alpha \rangle &= -\frac{\mathbf{K}_\alpha}{\mu_\alpha}(\nabla \langle p_\alpha \rangle^\alpha - \rho_\alpha \mathbf{g}) - \mathbf{F}_\alpha \cdot \langle \mathbf{v}_\alpha \rangle \\ &\quad +\mathbf{K}_{\alpha\kappa} \cdot \langle \mathbf{v}_\kappa \rangle - \mathbf{F}_{\alpha\kappa} \cdot \langle \mathbf{v}_\kappa \rangle \qquad \alpha,\ \kappa = \beta,\ \gamma \qquad \alpha \neq \kappa \end{aligned}$$

In these equations, $\mathbf{F}_\alpha$ and $\mathbf{F}_{\alpha\kappa}$ are the *inertial* and *coupling inertial correction tensors*. The dominant and coupling permeability tensors $\mathbf{K}^*_{\alpha\alpha}$ and $\mathbf{K}^*_{\alpha\kappa}$ and the permeability and viscous drag tensors $\mathbf{K}_\alpha$ and $\mathbf{K}_{\alpha\kappa}$ are those defined in the traditional manner as in Whitaker (1994) and Lasseux et al. (1996). All these tensors are determined by closure problems that must be solved using a spatially periodic model of a porous medium. The procedure to compute these tensors is provided.

1 Introduction

Fluid flow through porous media is of interest in several domains, such as petroleum recovery, chemical and environmental engineering. Although Darcy's law (Darcy, 1856) and its generalized form for two-phase flow (Muskat, 1937; Raats and Klute, 1968) remain physically relevant for a wide range of applications, problems for which these models fail to correctly represent flow rate to pressure drop relationships are of considerable practical importance. Pertaining to this class of problems are flows occuring in packed beds of reactors and in many subsurface systems such as flow near wells of oil or gas production, water pumping and soil remediation to cite some but a few. Within this context, flow combining both inertial and multiphase conditions represent challenging issues that still deserve special attention.

While the initial empirical one- and two-phase versions of Darcy's law have been supported experimentally, numerically and theoretically (Whitaker, 1986a; Whitaker, 1986b; Auriault, 1987), and while studies of one-phase inertial flow has also received significant efforts, the same strong support is still lacking for the inertial two-phase flow. In studies of non-Darcy flow through porous media, the Forchheimer equation involving a quadratic velocity correction is generally used to describe single phase inertial flow. Originally put forth on an empirical basis (Forchheimer, 1901), this equation has been extensively employed

to interpret experimental data (Ergun, 1952; Ward, 1964; Beavers and Sparrow, 1969; Dullien and Azzam, 1973; MacDonald et al., 1979), or numerical results (Coulaud et al., 1988; Ma and Ruth, 1993; Ruth and Ma, 1993; Thauvin and Mohanty, 1998; Papathanasiou et al., 2001) and found some theoretical justifications (Irmay, 1958; Blick, 1966; Ahmed and Sunada, 1969; Cvetkovic, 1986; Giorgi, 1997; Chen et al., 2001). More refinements demonstrating the existence of different regimes (weak and strong inertia) were however reported both from numerical (Firdaouss and Guermond, 1995; Firdaouss et al., 1997; Koch and Ladd, 1997; Amaral Souto and Moyne, 1997; Rojas and Koplik, 1998; Skjetne et al., 1999) and theoretical (Wodie and Levy, 1991; Mei and Auriault, 1991; Rasoloarijaona and Auriault, 1994; Skjetne and Auriault, 1999) points of view. A more general form of the inertial flow of a single β-phase in a homogeneous porous medium given by

$$\langle \mathbf{v}_\beta \rangle = \frac{-\mathbf{K}}{\mu_\beta} \left[\nabla \langle p_\beta \rangle^\beta - \rho_\beta \mathbf{g} \right] - \mathbf{F} \cdot \langle \mathbf{v}_\beta \rangle \tag{1}$$

was recently proposed (Whitaker, 1996) where $\mathbf{K}$ and $\mathbf{F}$ are respectively the Darcy's law (intrinsic) permeability and non-Darcy (Forchheimer) correction tensors determined by closure problems that must be solved using a spatially periodic model of a porous medium.

Several studies reported in the literature extend the Forchheimer equation to multiphase flow and provide relationships for correlating non-Darcy flow coefficients under multiphasic conditions (Evans et al., 1987; Evans and Evans, 1988; Liu et al., 1995). Similar models were also considered in nuclear safety applications (Buchlin and Stubos, 1987; Lipinski, 1980; Lipinski, 1982) while some attempt was made to extend to porous media the Lockhart-Martinelli model (Lockhart and Martinelli, 1949) initially derived for two-phase flow in pipes (Fourar and Lenormand, 2000). Nevertheless, the Forchheimer model and its generalized form, the degeneration of which at vanishing Reynolds number correctly restores Darcy's law, have now become some standard models to describe high-velocity flow in petroleum engineering (Bear, 1972; Scheidegger, 1974; Geertsma, 1974; Firoozabadi and Katz, 1979; Firoozabadi et al., 1995). Thorough theoretical analysis still leaves much to be desired in order to fully understand inertial flow through porous media and overcome mathematical difficulties in handling highly nonlinear multiphase flow equations out of the Darcy regime.

The objective of the present study is to analyze the possibility of deriving a macroscopic model describing inertial two-phase, incompressible, Newtonian fluid flow through homogenous porous media using the method of volume averaging. Starting from the two-phase Navier-Stokes boundary value problem and following lines developed in previous works (Whitaker, 1986b; Whitaker, 1994; Lasseux et al., 1996; Whitaker, 1996), the theoretical derivation of the averaged form of the mass and momentum balance equations is achieved under the restriction of length- and time-scales constraints that are explicitly provided during the course of the development.

2 Microscopic boundary value problem

The process under consideration is the simultaneous flow in a rigid porous medium, in which the solid phase is designated by the σ-phase, of two immiscible phases β and γ both incompressible and Newtonian. The macroscopic region with the characteristic length, L, illustrated in Figure (1) represents a homogeneous porous medium with respect to the two-phase flow process.

The boundary-value problem describing the flow at the pore-scale in the macroscopic region is given by the following set of equations

$$\rho_\beta(\frac{\partial \mathbf{v}_\beta}{\partial t} + \mathbf{v}_\beta \cdot \nabla \mathbf{v}_\beta) = -\nabla p_\beta + \rho_\beta \mathbf{g} + \mu_\beta \nabla^2 \mathbf{v}_\beta \quad \text{in the } \beta\text{-phase} \tag{2a}$$

$$\nabla \cdot \mathbf{v}_\beta = 0 \quad \text{in the } \beta\text{-phase} \tag{2b}$$

$$\text{BC1} \quad \mathbf{v}_\beta = 0 \quad \text{at } A_{\beta\sigma} \tag{2c}$$

$$\text{BC2} \quad \mathbf{v}_\beta = \mathbf{v}_\gamma \quad \text{at } A_{\beta\gamma} \tag{2d}$$

$$\text{BC3} \quad -\mathbf{n}_{\beta\gamma} p_\beta + \mathbf{n}_{\beta\gamma} \cdot \boldsymbol{\Upsilon}_\beta = -\mathbf{n}_{\beta\gamma} p_\gamma + \mathbf{n}_{\beta\gamma} \cdot \boldsymbol{\Upsilon}_\gamma + 2\sigma H \mathbf{n}_{\beta\gamma} \quad \text{at } A_{\beta\gamma} \tag{2e}$$

$$\text{BC4} \quad \mathbf{v}_\gamma = 0 \quad \text{at } A_{\gamma\sigma} \tag{2f}$$

$$\rho_\gamma(\frac{\partial \mathbf{v}_\gamma}{\partial t} + \mathbf{v}_\gamma \cdot \nabla \mathbf{v}_\gamma) = -\nabla p_\gamma + \rho_\gamma \mathbf{g} + \mu_\gamma \nabla^2 \mathbf{v}_\gamma \quad \text{in the } \gamma\text{-phase} \tag{2g}$$

$$\nabla \cdot \mathbf{v}_\gamma = 0 \quad \text{in the } \gamma\text{-phase} \tag{2h}$$

$$\text{BC5} \quad \mathbf{v}_\beta = \mathbf{f}(t) \quad \text{at } A_{\beta e} \tag{2i}$$

$$\text{BC6} \quad \mathbf{v}_\gamma = \mathbf{g}(t) \quad \text{at } A_{\gamma e} \tag{2j}$$

In these equations $A_{\beta\gamma}$ represents the $\beta - \gamma$ interface contained in the macroscopic region (see Figure 1) and $A_{\beta e}$ and $A_{\gamma e}$ represent the β- and γ-phases entrances and exits of that region.

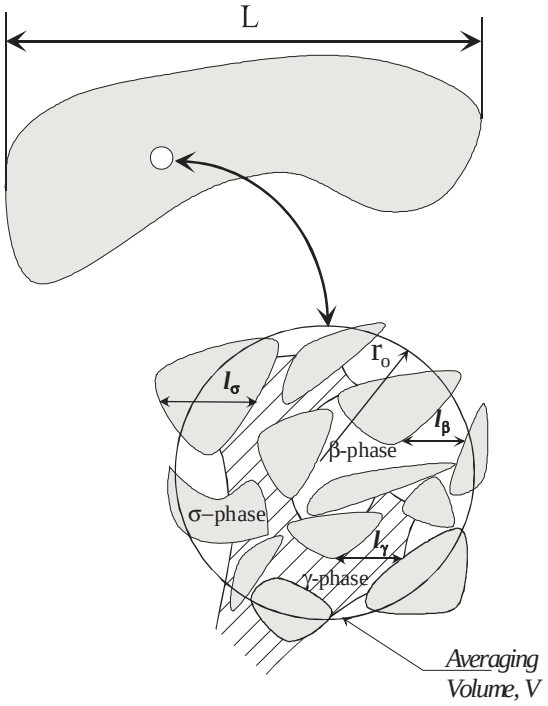

Figure 1: Macroscopic region and averaging volume

Equation (2e), in which the interfacial tension is represented by σ and the mean curvature of the interface by H, expresses the balance of the normal stress jump by capillary effects. In the presentation of this condition, we have used the assumption which ignores effects of surface-active agents that are always present in real two-phase flow systems, (Slattery, 1990). The total stress tensor, $\mathbf{T}_{\boldsymbol{\alpha}}$, α representing one of the β- or γ-phase, has been decomposed according to

$$\mathbf{T}_{\boldsymbol{\alpha}} = -p_{\boldsymbol{\alpha}} \mathbf{I} + \boldsymbol{\Upsilon}_{\boldsymbol{\alpha}} \tag{3}$$

and the viscous stress tensor Υ_α as

$$\boldsymbol{\Upsilon_\alpha} = \mu_{\boldsymbol{\alpha}}(\nabla \mathbf{v_\alpha} + \nabla \mathbf{v}_{\boldsymbol{\alpha}}^T) \tag{4}$$

In order to arrive at equations (2a) and (2g) we have used

$$\nabla \cdot (\nabla \mathbf{v}_{\boldsymbol{\alpha}}^T) = 0 \tag{5}$$

as a consequence of incompressibility.The above system of equations must be closed by specifying either p_β or p_γ at some point

$$\text{BC7} \qquad p_\beta = p_\beta^0 \qquad \mathbf{r} = \mathbf{r}^0 \tag{6}$$

3 Volume averaging

Averaging of the above boundary value problem is performed over a volume V represented in Figure 1 including the volumes V_β and V_γ of the β- and γ-phase of respective volume fractions ε_β and ε_γ given by

$$\varepsilon_\beta = \frac{V_\beta}{V} \qquad \varepsilon_\gamma = \frac{V_\gamma}{V} \tag{7}$$

In the course of the averaging process, we shall use the superficial and intrinsic averages which, for any quantity ψ_α defined in V_α, are respectively given by

$$\langle \psi_\alpha \rangle = \frac{1}{V} \int\limits_{V_\alpha} \psi_\alpha dV \qquad \alpha = \beta, \gamma \tag{8}$$

$$\langle \psi_\alpha \rangle^\alpha = \frac{1}{V_\alpha} \int\limits_{V_\alpha} \psi_\alpha dV \qquad \alpha = \beta, \gamma \tag{9}$$

with the evident relationship

$$\langle \psi_\alpha \rangle = \varepsilon_\alpha \langle \psi_\alpha \rangle^\alpha \qquad \alpha = \beta, \gamma \tag{10}$$

Derivation of the averaged form of the mass and momentum equations requires the use of the averaging theorem for a three-phase system (Howes and Whitaker, 1985). For some scalar quantity ψ_β associated with the β-phase, this theorem takes the form

$$\langle \nabla \psi_\beta \rangle = \nabla \langle \psi_\beta \rangle + \frac{1}{V} \int\limits_{A_{\beta\sigma}} \mathbf{n}_{\beta\sigma} \psi_\beta dA + \frac{1}{V} \int\limits_{A_{\beta\gamma}} \mathbf{n}_{\beta\gamma} \psi_\beta dA \tag{11}$$

in which $A_{\beta\sigma}$ and $A_{\beta\gamma}$ respectively represent the interfacial areas between the β and σ and β and γ phases contained within the averaging volume V. We will also make use of the general transport theorem (Truesdell and Toupin, 1960) that can be written as

$$\frac{\partial}{\partial t} \int\limits_{\mathcal{V}(t)} \psi_\alpha \, dV = \int\limits_{\mathcal{V}(t)} \frac{\partial \psi \alpha}{\partial t} \, dV + \int\limits_{A(t)} \psi_\alpha \, \mathbf{n} \cdot \mathbf{w} \, dA \tag{12}$$

where $A(t)$ is the surface enclosing $\mathcal{V}(t)$, $\mathbf{w}$ the velocity of a material point attached to $A(t)$ and $\mathbf{n}$ the unit vector normal to $A(t)$ pointing outside $\mathcal{V}(t)$.

Throughout the paper and as in all up-scaling procedures, a constraint on scale hierarchy is assumed, namely

$$l_\beta, l_\gamma \ll r_0 \ll L \tag{13}$$

In this relation, l_β and l_γ represent the characteristic length within each of the β and γ phases at the pore-scale and r_0 is the radius of the averaging volume, V.

3.1 Continuity equation

We start the development with the volume averaged form of the continuity equation (2b) and we write

$$\langle \nabla \cdot \mathbf{v}_\beta \rangle = 0 \tag{14}$$

Making use of the averaging theorem along with the no-slip boundary condition in equation (2c) leads to

$$\nabla \cdot \langle \mathbf{v}_\beta \rangle + \frac{1}{V} \int\limits_{A_{\beta\gamma}} \mathbf{n}_{\beta\gamma} \cdot \mathbf{v}_\beta dA = 0 \tag{15}$$

When the transport theorem is used with a constant for ψ_β and $\mathcal{V}(t) = V_\beta(t)$ (see appendix 1), this finally yields the classical form

$$\frac{\partial \varepsilon_\beta}{\partial t} + \nabla \cdot \langle \mathbf{v}_\beta \rangle = 0 \tag{16}$$

Performing the same development on the mass balance equation in the γ-phase leads to a similar result that can be simply listed as

$$\frac{\partial \varepsilon_\gamma}{\partial t} + \nabla \cdot \langle \mathbf{v}_\gamma \rangle = 0 \tag{17}$$

It shall be noted that these two continuity equations are closed and do not require any special link with the microscopic scale. As will be seen below, this is not the case with the momentum balance equations.

3.2 Momentum balance equation

The next step is the volume averaging of the momentum balance equations and we begin with the average of the left hand side ($L.H.S.$) of equation (2a). Making use again of the vector form of the transport theorem with $\mathcal{V}(t) = V_\beta(t)$ leads to (see appendix 1)

$$\langle L.H.S \rangle = \rho_\beta \left(\frac{\partial \langle \mathbf{v}_\beta \rangle}{\partial t} - \frac{1}{V} \int\limits_{A_{\beta\gamma}} \mathbf{n} \cdot \mathbf{v}_\beta \ \mathbf{v}_\beta \ dA \right) + \rho_\beta \langle \nabla \cdot (\mathbf{v}_\beta \mathbf{v}_\beta) \rangle \tag{18}$$

The averaging theorem can be used in order to express the convective inertial term as

$$\rho_\beta \langle \nabla \cdot (\mathbf{v}_\beta \mathbf{v}_\beta) \rangle = \rho_\beta \nabla \cdot \langle \mathbf{v}_\beta \mathbf{v}_\beta \rangle + \frac{\rho_\beta}{V} \int\limits_{A_{\beta\gamma}} \mathbf{n}_{\beta\gamma} \cdot \mathbf{v}_\beta \ \mathbf{v}_\beta dA \tag{19}$$

in which the no slip boundary condition in equation (2c) was employed. At this stage, it is necessary to eliminate the average of a product and to do so, we make use of the velocity decomposition given by (Gray, 1975)

$$\mathbf{v}_\beta = \langle \mathbf{v}_\beta \rangle^\beta + \tilde{\mathbf{v}}_\beta \tag{20}$$

When the intrinsic average of such a decomposition is considered and on the basis of the scale hierarchy given in equation (13), it can be shown (Carbonell and Whitaker, 1984; Whitaker, 1999) that the variations of $\langle \mathbf{v}_\beta \rangle^\beta$ are negligible within the averaging volume i.e.

$$\left\langle \langle \mathbf{v}_\beta \rangle^\beta \right\rangle^\beta = \langle \mathbf{v}_\beta \rangle^\beta \tag{21}$$

and that accordingly

$$\langle \tilde{\mathbf{v}}_\beta \rangle^\beta = 0 \tag{22}$$

Making use of these two results allows to write

$$\langle \mathbf{v}_\beta \mathbf{v}_\beta \rangle = \varepsilon_\beta \langle \mathbf{v}_\beta \rangle^\beta \langle \mathbf{v}_\beta \rangle^\beta + \langle \tilde{\mathbf{v}}_\beta \tilde{\mathbf{v}}_\beta \rangle \tag{23}$$

and hence

$$\rho_\beta \langle \nabla \cdot (\mathbf{v}_\beta \mathbf{v}_\beta) \rangle = \rho_\beta \left(\nabla \cdot \left(\varepsilon_\beta \langle \mathbf{v}_\beta \rangle^\beta \langle \mathbf{v}_\beta \rangle^\beta \right) + \nabla \cdot \langle \tilde{\mathbf{v}}_\beta \tilde{\mathbf{v}}_\beta \rangle + \frac{1}{V} \int\limits_{A_{\beta\gamma}} \mathbf{n}_{\beta\gamma} \cdot \mathbf{v}_\beta \ \mathbf{v}_\beta dA \right) \tag{24}$$

When this result is inserted in equation (18) and when $\langle \mathbf{v}_\beta \rangle^\beta$ is employed instead of $\langle \mathbf{v}_\beta \rangle$ we obtain

$$\begin{aligned} \langle L.H.S \rangle \quad = \quad & \rho_\beta \varepsilon_\beta \frac{\partial \langle \mathbf{v}_\beta \rangle^\beta}{\partial t} + \rho_\beta \frac{\partial \varepsilon_\beta}{\partial t} \langle \mathbf{v}_\beta \rangle^\beta \\ & + \rho_\beta \nabla \cdot \left(\varepsilon_\beta \langle \mathbf{v}_\beta \rangle^\beta \right) \langle \mathbf{v}_\beta \rangle^\beta + \rho_\beta \varepsilon_\beta \langle \mathbf{v}_\beta \rangle^\beta \cdot \nabla \langle \mathbf{v}_\beta \rangle^\beta \\ & + \rho_\beta \nabla \cdot \langle \tilde{\mathbf{v}}_\beta \tilde{\mathbf{v}}_\beta \rangle \end{aligned} \tag{25}$$

Making use of the average mass balance equation allows to write the above equation as

$$\langle L.H.S \rangle = \rho_\beta \varepsilon_\beta \frac{\partial \langle \mathbf{v}_\beta \rangle^\beta}{\partial t} + \rho_\beta \varepsilon_\beta \langle \mathbf{v}_\beta \rangle^\beta \cdot \nabla \langle \mathbf{v}_\beta \rangle^\beta + \rho_\beta \nabla \cdot \langle \tilde{\mathbf{v}}_\beta \tilde{\mathbf{v}}_\beta \rangle \tag{26}$$

At this point, we continue with the superficial average of the right-hand side ($R.H.S.$) of equation (2a). Applying the averaging theorem and using the no slip boundary condition at the solid-fluid interface leads to

$$\begin{aligned} \langle R.H.S \rangle = & -\nabla \langle p_\beta \rangle + \varepsilon_\beta \rho_\beta \mathbf{g} + \mu_\beta \nabla^2 \langle \mathbf{v}_\beta \rangle + \mu_\beta \nabla \cdot \left[\frac{1}{V} \int\limits_{A_{\beta\gamma}} \mathbf{n}_{\beta\gamma} \mathbf{v}_\beta dA \right] \\ & + \frac{1}{V} \int\limits_{A_{\beta\sigma}} \mathbf{n}_{\beta\sigma} \cdot (-\mathbf{I} p_\beta + \mu_\beta \nabla \mathbf{v}_\beta) dA \\ & + \frac{1}{V} \int\limits_{A_{\beta\gamma}} \mathbf{n}_{\beta\gamma} \cdot (-\mathbf{I} p_\beta + \mu_\beta \nabla \mathbf{v}_\beta) dA \end{aligned} \tag{27}$$

This form can be further simplified on the basis of an order of magnitude analysis. In fact, because the divergence operating on the area average has a characteristic length of L while the gradient operator inside the integral of the last term of equation (27) has a characteristic length scale of l_β, one readily obtains

$$\mu_\beta \nabla \cdot \left[\frac{1}{V} \int\limits_{A_{\beta\gamma}} \mathbf{n}_{\beta\gamma} \mathbf{v}_\beta dA \right] \ll \frac{1}{V} \int\limits_{A_{\beta\gamma}} \mathbf{n}_{\beta\gamma} \cdot (\mu_\beta \nabla \mathbf{v}_\beta) dA \tag{28}$$

so that the average of the right hand side of the momentum balance equation in the β-phase is

$$\langle R.H.S\rangle = -\nabla\langle p_\beta\rangle + \varepsilon_\beta\rho_\beta\mathbf{g} + \mu_\beta\nabla^2\langle\mathbf{v}_\beta\rangle + \frac{1}{V}\int\limits_{A_{\beta\sigma}+A_{\beta\gamma}} \mathbf{n}_\beta\cdot(-p_\beta\mathbf{I}+\mu_\beta\nabla\mathbf{v}_\beta)dA \tag{29}$$

In the area integral in equation (29), we have used $\mathbf{n}_\beta$ to represent either $\mathbf{n}_{\beta\sigma}$ or $\mathbf{n}_{\beta\gamma}$.

In order to obtain a closed form involving average quantities only, we use spatial decompositions of the velocity and pressure. With the analogue of equation (20) for the pressure , i.e.

$$p_\beta = \langle p_\beta\rangle^\beta + \tilde{p}_\beta \tag{30}$$

equation (29) takes the form

$$\langle R.H.S\rangle = -\nabla\langle p_\beta\rangle + \varepsilon_\beta\rho_\beta\mathbf{g} + \mu_\beta\nabla^2\langle\mathbf{v}_\beta\rangle + \frac{1}{V}\int\limits_{A_{\beta\sigma}+A_{\beta\gamma}} \mathbf{n}_\beta\cdot(-\tilde{p}_\beta\mathbf{I}+\mu_\beta\nabla\tilde{\mathbf{v}}_\beta)dA - \nabla\varepsilon_\beta\cdot\left(-\langle p_\beta\rangle^\beta\mathbf{I}+\mu_\beta\nabla\langle\mathbf{v}_\beta\rangle^\beta\right) \tag{31}$$

Here again, we have used the fact that, provided the length scale constraint in equation (13) is fulfilled, average quantities can be treated as constants in the area integral (Carbonell and Whitaker, 1984; Quintard and Whitaker, 1994). Moreover, we have made use of the averaging theorem with a constant in order to arrive at

$$\frac{1}{V}\int\limits_{A_{\beta\sigma+\beta\gamma}} \mathbf{n}_\beta dA = -\nabla\varepsilon_\beta \tag{32}$$

Reassembling equations (26) and (31), replacing the pressure superficial average by its corresponding intrinsic form and dividing the result by ε_β allows us to express the average momentum balance equation in the β -phase under the form

$$\begin{aligned}\rho_\beta\frac{\partial\langle\mathbf{v}_\beta\rangle^\beta}{\partial t} + \rho_\beta\langle\mathbf{v}_\beta\rangle^\beta\cdot\nabla\langle\mathbf{v}_\beta\rangle^\beta + \rho_\beta\varepsilon_\beta^{-1}\nabla\cdot\langle\tilde{\mathbf{v}}_\beta\tilde{\mathbf{v}}_\beta\rangle \\ = -\nabla\langle p_\beta\rangle^\beta + \rho_\beta\mathbf{g}\underbrace{+\varepsilon_\beta^{-1}\mu_\beta\nabla^2\langle\mathbf{v}_\beta\rangle - \mu_\beta\varepsilon_\beta^{-1}\nabla\varepsilon_\beta\cdot\nabla\langle\mathbf{v}_\beta\rangle^\beta}_{Brinkman\ correction} \\ + \frac{1}{V_\beta}\int\limits_{A_{\beta\sigma}+A_{\beta\gamma}} \mathbf{n}_\beta\cdot(-\mathbf{I}\tilde{p}_\beta+\mu_\beta\nabla\tilde{\mathbf{v}}_\beta)dA\end{aligned} \tag{33}$$

In this last form, the three terms in the left hand side correspond to the macroscopic acceleration and convective inertia while we can identify the two terms involving gradients of the average velocity in the right hand side as the Brinkman correction terms. A simple order of magnitude analysis will indicate that these two terms are negligible. In fact, the order of magnitude of these Brinkman terms can be estimated to be

$$\varepsilon_\beta^{-1}\mu_\beta\nabla^2\langle\mathbf{v}_\beta\rangle = \mathbf{O}\left(\frac{\mu_\beta\langle\mathbf{v}_\beta\rangle^\beta}{L^2}\right) \tag{34}$$

$$\mu_\beta\varepsilon_\beta^{-1}\nabla\varepsilon_\beta\cdot\nabla\langle\mathbf{v}_\beta\rangle^\beta = \mathbf{O}\left(\frac{\mu_\beta\langle\mathbf{v}_\beta\rangle^\beta}{L^2}\right) \tag{35}$$

In the latter of these two estimates, we have used the fact that ε_β does not exhibit significant variations on length scales shorter than L. Turning our attention to the term $\frac{\mu_\beta}{V_\beta}\int\limits_{A_{\beta\sigma}+A_{\beta\gamma}} \mathbf{n}_\beta \cdot \nabla\tilde{\mathbf{v}}_\beta dA$ indicates that

$$\frac{\mu_\beta}{V_\beta}\int\limits_{A_{\beta\sigma}+A_{\beta\gamma}} \mathbf{n}_\beta \cdot \nabla\tilde{\mathbf{v}}_\beta dA = \mathbf{O}\left(\frac{\mu_\beta\langle\mathbf{v}_\beta\rangle^\beta}{l_\beta}a\right) \tag{36}$$

Because of the no slip boundary condition at the fluid-solid interface $A_{\beta\sigma}$, we have used

$$\tilde{\mathbf{v}}_\beta = \mathbf{O}\left(\langle\mathbf{v}_\beta\rangle^\beta\right) \tag{37}$$

in this estimate and we have designated by a the interfacial area per unit volume $\frac{A_{\beta\sigma}+A_{\beta\gamma}}{V_\beta}$. Providing a precise estimation of this last quantity is a difficult task. However, a lower bound of a, given by $\frac{A_{\beta\gamma}}{V_\beta}$, can be reasonably estimated to be on the order of $1/l_\beta$ leading to

$$\frac{\mu_\beta}{V_\beta}\int\limits_{A_{\beta\sigma}+A_{\beta\gamma}} \mathbf{n}_\beta \cdot \nabla\tilde{\mathbf{v}}_\beta dA = \mathbf{O}\left(\frac{\mu_\beta\langle\mathbf{v}_\beta\rangle^\beta}{l_\beta^2}\right) \tag{38}$$

i.e.

$$\varepsilon_\beta^{-1}\mu_\beta\nabla^2\langle\mathbf{v}_\beta\rangle \ll \frac{\mu_\beta}{V_\beta}\int\limits_{A_{\beta\sigma}+A_{\beta\gamma}} \mathbf{n}_\beta \cdot \nabla\tilde{\mathbf{v}}_\beta dA \tag{39}$$

and

$$\mu_\beta\varepsilon_\beta^{-1}\nabla\varepsilon_\beta \cdot \nabla\langle\mathbf{v}_\beta\rangle^\beta \ll \frac{\mu_\beta}{V_\beta}\int\limits_{A_{\beta\sigma}+A_{\beta\gamma}} \mathbf{n}_\beta \cdot \nabla\tilde{\mathbf{v}}_\beta dA \tag{40}$$

This indicates that Brinkman correction terms are unimportant in the macroscopic momentum equation and can be disregarded in the averaged form that can be written as

$$\begin{aligned}\rho_\beta\frac{\partial\langle\mathbf{v}_\beta\rangle^\beta}{\partial t} + \rho_\beta\langle\mathbf{v}_\beta\rangle^\beta \cdot \nabla\langle\mathbf{v}_\beta\rangle^\beta + \rho_\beta\varepsilon_\beta^{-1}\nabla \cdot \langle\tilde{\mathbf{v}}_\beta\tilde{\mathbf{v}}_\beta\rangle \\ = -\nabla\langle p_\beta\rangle^\beta + \rho_\beta\mathbf{g} \\ +\frac{1}{V_\beta}\int\limits_{A_{\beta\sigma}+A_{\beta\gamma}} \mathbf{n}_\beta \cdot (-\mathbf{I}\tilde{p}_\beta + \mu_\beta\nabla\tilde{\mathbf{v}}_\beta)dA\end{aligned} \tag{41}$$

For completeness, we simply list the analogue result in the γ-phase as

$$\begin{aligned}\rho_\gamma\frac{\partial\langle\mathbf{v}_\gamma\rangle^\gamma}{\partial t} + \rho_\gamma\langle\mathbf{v}_\gamma\rangle^\gamma \cdot \nabla\langle\mathbf{v}_\gamma\rangle^\gamma + \rho_\gamma\varepsilon_\gamma^{-1}\nabla \cdot \langle\tilde{\mathbf{v}}_\gamma\tilde{\mathbf{v}}_\gamma\rangle \\ = -\nabla\langle p_\gamma\rangle^\gamma + \rho_\gamma\mathbf{g} \\ +\frac{1}{V_\gamma}\int\limits_{A_{\gamma\sigma}+A_{\beta\gamma}} \mathbf{n}_\gamma \cdot (-\mathbf{I}\tilde{p}_\gamma + \mu_\gamma\nabla\tilde{\mathbf{v}}_\gamma)dA\end{aligned} \tag{42}$$

At this stage of the development, the averaged momentum equation does not represent a closed form since velocity and pressure deviations having microscopic length-scale of variation are still present. Using this averaged form, we now need to derive the closure problem and this is detailed in the following section.

4 Closure

The objective of this section is to develop the relationships between spatial deviations and average quantities in order to close the macroscopic model.

4.1 Continuity equation

To derive the spatial deviation form of the continuity equation, we recall the point and average mass balance equations, namely

$$\nabla \cdot \mathbf{v}_\beta = 0 \tag{43}$$

and

$$\frac{\partial \varepsilon_\beta}{\partial t} + \nabla \cdot \langle \mathbf{v}_\beta \rangle = 0 \tag{44}$$

or an equivalent version

$$\nabla \cdot \langle \mathbf{v}_\beta \rangle^\beta = -\varepsilon_\beta^{-1} \left[\frac{\partial \varepsilon_\beta}{\partial t} + \langle \mathbf{v}_\beta \rangle^\beta \cdot \nabla \varepsilon_\beta \right] \tag{45}$$

Subtracting the latter from the former leads to

$$\nabla \cdot \tilde{\mathbf{v}}_\beta = \varepsilon_\beta^{-1} \left[\frac{\partial \varepsilon_\beta}{\partial t} + \langle \mathbf{v}_\beta \rangle^\beta \cdot \nabla \varepsilon_\beta \right] \tag{46}$$

The right hand side of this equation involves terms varying at the scale L and lead to a non-homogeneous deviation continuity equation. As a consequence, they can be considered as *source terms* for $\tilde{\mathbf{v}}_\beta$ and we shall analyse the contribution of these two sources using order of magnitude arguments. On the basis of the length-scale constraint expressed by equation (13), it is clear that

$$\varepsilon_\beta^{-1} \langle \mathbf{v}_\beta \rangle^\beta \cdot \nabla \varepsilon_\beta \ll \nabla \cdot \tilde{\mathbf{v}}_\beta \tag{47}$$

when ε_β does not exhibit significant variations on a length scale shorter than L. Moreover, when the flow process is observed at times t^* much larger than the characteristic time-scale of phase displacement at the pore-scale, namely under the time-scale constraint

$$t^* \gg \max_{\alpha=\beta,\,\gamma} \left(\frac{l_\alpha}{\| \langle \mathbf{v}_\alpha \rangle^\alpha \|} \right) \tag{48}$$

we also have

$$\varepsilon_\beta^{-1} \frac{\partial \varepsilon_\beta}{\partial t} \ll \nabla \cdot \tilde{\mathbf{v}}_\beta \tag{49}$$

Under these circumstances, the two source terms in equation (46) are negligible leading to the closure equation for the continuity

$$\nabla \cdot \tilde{\mathbf{v}}_\beta = 0 \tag{50}$$

and its analogue in the γ-phase

$$\nabla \cdot \tilde{\mathbf{v}}_\gamma = 0 \tag{51}$$

4.2 Momentum equation

In order to develop the governing differential equations on $\tilde{p}_\beta$ and $\tilde{\mathbf{v}}_\beta$, (as well as their analogue on $\tilde{p}_\gamma$, and $\tilde{\mathbf{v}}_\gamma$) we recall the point and averaged momentum equations under their forms of equations (2a) and (41) respectively given by

$$\rho_\beta(\frac{\partial \mathbf{v}_\beta}{\partial t} + \mathbf{v}_\beta \cdot \nabla \mathbf{v}_\beta) = -\nabla p_\beta + \rho_\beta \mathbf{g} + \mu_\beta \nabla^2 \mathbf{v}_\beta \tag{52}$$

and

$$\begin{aligned} \rho_\beta \frac{\partial \langle \mathbf{v}_\beta \rangle^\beta}{\partial t} + \rho_\beta \langle \mathbf{v}_\beta \rangle^\beta \cdot \nabla \langle \mathbf{v}_\beta \rangle^\beta + \rho_\beta \varepsilon_\beta^{-1} \nabla \cdot \langle \tilde{\mathbf{v}}_\beta \tilde{\mathbf{v}}_\beta \rangle \\ = -\nabla \langle p_\beta \rangle^\beta + \rho_\beta \mathbf{g} \\ + \frac{1}{V_\beta} \int\limits_{A_{\beta\sigma}+A_{\beta\gamma}} \mathbf{n}_\beta \cdot (-\mathbf{I}\tilde{p}_\beta + \mu_\beta \nabla \tilde{\mathbf{v}}_\beta) dA \end{aligned} \tag{53}$$

Subtracting the latter from the former provides the spatial deviations momentum equation that takes the form

$$\begin{aligned} \rho_\beta \frac{\partial \tilde{\mathbf{v}}_\beta}{\partial t} + \rho_\beta \mathbf{v}_\beta \cdot \nabla \mathbf{v}_\beta \\ -\rho_\beta \langle \mathbf{v}_\beta \rangle^\beta \cdot \nabla \langle \mathbf{v}_\beta \rangle^\beta - \rho_\beta \varepsilon_\beta^{-1} \nabla \cdot \langle \tilde{\mathbf{v}}_\beta \tilde{\mathbf{v}}_\beta \rangle \\ = -\nabla \tilde{p}_\beta + \mu_\beta \nabla^2 \tilde{\mathbf{v}}_\beta + \mu_\beta \nabla^2 \langle \mathbf{v}_\beta \rangle^\beta \\ - \frac{1}{V_\beta} \int\limits_{A_{\beta\sigma}+A_{\beta\gamma}} \mathbf{n}_\beta \cdot (-\mathbf{I}\tilde{p}_\beta + \mu_\beta \nabla \tilde{\mathbf{v}}_\beta) dA \end{aligned} \tag{54}$$

Given the orders of magnitude

$$\mu_\beta \nabla^2 \tilde{\mathbf{v}}_\beta = \mathbf{O}\left(\frac{\mu_\beta \langle \mathbf{v}_\beta \rangle^\beta}{l_\beta^2}\right) \tag{55}$$

and

$$\mu_\beta \nabla^2 \langle \mathbf{v}_\beta \rangle^\beta = \mathbf{O}\left(\frac{\mu_\beta \langle \mathbf{v}_\beta \rangle^\beta}{L^2}\right) \tag{56}$$

it is clear that this later term can be discarded from equation (54). Moreover, by introducing the velocity spatial decomposition, the microscopic and the first of the two macroscopic inertial convective terms can be rearranged in the following way

$$\begin{aligned} \rho_\beta \mathbf{v}_\beta \cdot \nabla \mathbf{v}_\beta - \rho_\beta \langle \mathbf{v}_\beta \rangle^\beta \cdot \nabla \langle \mathbf{v}_\beta \rangle^\beta \\ = \rho_\beta \left(\mathbf{v}_\beta \cdot \nabla \tilde{\mathbf{v}}_\beta + \mathbf{v}_\beta \cdot \nabla \langle \mathbf{v}_\beta \rangle^\beta - \langle \mathbf{v}_\beta \rangle^\beta \cdot \nabla \langle \mathbf{v}_\beta \rangle^\beta \right) \\ = \rho_\beta \left(\mathbf{v}_\beta \cdot \nabla \tilde{\mathbf{v}}_\beta + \tilde{\mathbf{v}}_\beta \cdot \nabla \langle \mathbf{v}_\beta \rangle^\beta \right) \end{aligned} \tag{57}$$

leading to the following momentum equation

$$\rho_\beta \frac{\partial \tilde{\mathbf{v}}_\beta}{\partial t} + \rho_\beta \mathbf{v}_\beta \cdot \nabla \tilde{\mathbf{v}}_\beta$$
$$+\rho_\beta \tilde{\mathbf{v}}_\beta \cdot \nabla \langle \mathbf{v}_\beta \rangle^\beta - \rho_\beta \varepsilon_\beta^{-1} \nabla \cdot \langle \tilde{\mathbf{v}}_\beta \tilde{\mathbf{v}}_\beta \rangle$$
$$= -\nabla \tilde{p}_\beta + \mu_\beta \nabla^2 \tilde{\mathbf{v}}_\beta$$
$$-\frac{1}{V_\beta} \int\limits_{A_{\beta\sigma}+A_{\beta\gamma}} \mathbf{n}_\beta \cdot (-\mathbf{I}\tilde{p}_\beta + \mu_\beta \nabla \tilde{\mathbf{v}}_\beta) dA \tag{58}$$

This form can be significantly simplified when the following order of magnitude estimates, based on equation (37), are taken into account

$$\mathbf{v}_\beta \cdot \nabla \tilde{\mathbf{v}}_\beta = \mathbf{O}\left(\frac{\left\| \langle \mathbf{v}_\beta \rangle^\beta \right\|^2}{l_\beta} \right) \tag{59}$$

$$\tilde{\mathbf{v}}_\beta \cdot \nabla \langle \mathbf{v}_\beta \rangle^\beta = \mathbf{O}\left(\frac{\left\| \langle \mathbf{v}_\beta \rangle^\beta \right\|^2}{L} \right) \tag{60}$$

$$\varepsilon_\beta^{-1} \nabla \cdot \langle \tilde{\mathbf{v}}_\beta \tilde{\mathbf{v}}_\beta \rangle = \mathbf{O}\left(\frac{\left\| \langle \mathbf{v}_\beta \rangle^\beta \right\|^2}{L} \right) \tag{61}$$

Here, we have used the fact that $\mathbf{v}_\beta$ and $\tilde{\mathbf{v}}_\beta$ are of the same order of magnitude, namely $\mathbf{O}\left(\langle \mathbf{v}_\beta \rangle^\beta\right)$, and this can be immediately inferred from equations (20) and (37). On the basis of the length-scale constraint, this yields

$$\rho_\beta \mathbf{v}_\beta \cdot \nabla \tilde{\mathbf{v}}_\beta \gg \rho_\beta \tilde{\mathbf{v}}_\beta \cdot \nabla \langle \mathbf{v}_\beta \rangle^\beta \tag{62}$$

$$\rho_\beta \mathbf{v}_\beta \cdot \nabla \tilde{\mathbf{v}}_\beta \gg \rho_\beta \varepsilon_\beta^{-1} \nabla \cdot \langle \tilde{\mathbf{v}}_\beta \tilde{\mathbf{v}}_\beta \rangle \tag{63}$$

As a consequence, the momentum spatial deviation equation takes the form

$$\rho_\beta \frac{\partial \tilde{\mathbf{v}}_\beta}{\partial t} + \rho_\beta \mathbf{v}_\beta \cdot \nabla \tilde{\mathbf{v}}_\beta$$
$$= -\nabla \tilde{p}_\beta + \mu_\beta \nabla^2 \tilde{\mathbf{v}}_\beta$$
$$-\frac{1}{V_\beta} \int\limits_{A_{\beta\sigma}+A_{\beta\gamma}} \mathbf{n}_\beta \cdot (-\mathbf{I}\tilde{p}_\beta + \mu_\beta \nabla \tilde{\mathbf{v}}_\beta) dA \tag{64}$$

At this point, the closure problem remains non-steady and our interest is to provide a constraint for the explicit time dependent term to be negligible. This constraint can be easily formulated if we require the flow process to be observed at times t^* much larger than the characteristic time of viscous relaxation at the pore scale[1], i.e.

$$t^* \gg \max_{\alpha=\beta,\,\gamma} \left(\frac{\rho_\alpha l_\alpha^2}{\mu_\alpha} \right) \tag{65}$$

Under these circumstances, since

[1] The consequence of this time-scale constraint is that i) the acceleration term could have been neglected in comparison to the viscous term in the point momentum balance equations, and ii) the non-stationnary term in the macrosocpic momentum balance equations will be negligible as will be seen later on.

$$\rho_\beta \frac{\partial \tilde{\mathbf{v}}_\beta}{\partial t} = \mathbf{O}\left(\frac{\rho_\beta \langle \mathbf{v}_\beta \rangle^\beta}{t^*}\right) \tag{66}$$

it can be easily seen from equation (55) that

$$\rho_\beta \frac{\partial \tilde{\mathbf{v}}_\beta}{\partial t} \ll \mu_\beta \nabla^2 \tilde{\mathbf{v}}_\beta \tag{67}$$

This leads to a closure equation for the momentum which takes the form

$$\begin{aligned} \rho_\beta \mathbf{v}_\beta \cdot \nabla \tilde{\mathbf{v}}_\beta &= -\nabla \tilde{p}_\beta + \mu_\beta \nabla^2 \tilde{\mathbf{v}}_\beta \\ &\quad -\frac{1}{V_\beta} \int\limits_{A_{\beta\sigma}+A_{\beta\gamma}} \mathbf{n}_\beta \cdot (-\mathbf{I}\tilde{p}_\beta + \mu_\beta \nabla \tilde{\mathbf{v}}_\beta) dA \end{aligned} \tag{68}$$

An equivalent version in the γ-phase is expressed as

$$\begin{aligned} \rho_\gamma \mathbf{v}_\gamma \cdot \nabla \tilde{\mathbf{v}}_\gamma &= -\nabla \tilde{p}_\gamma + \mu_\gamma \nabla^2 \tilde{\mathbf{v}}_\gamma \\ &\quad -\frac{1}{V_\gamma} \int\limits_{A_{\gamma\sigma}+A_{\gamma\beta}} \mathbf{n}_\gamma \cdot (-\mathbf{I}\tilde{p}_\gamma + \mu_\gamma \nabla \tilde{\mathbf{v}}_\gamma) dA \end{aligned} \tag{69}$$

One must keep in mind that these closure equations remain valid under the associated time-scale constraint that can be recalled under the form

$$t^* \gg \max\left(\max_{\alpha=\beta,\,\gamma}\left(\frac{\rho_\alpha l_\alpha^2}{\mu_\alpha}\right),\ \max_{\alpha=\beta,\,\gamma}\left(\frac{l_\alpha}{\|\langle \mathbf{v}_\alpha \rangle^\alpha\|}\right)\right) \tag{70}$$

Since

$$0 \leq l_\alpha \leq l \tag{71}$$

where l designates the mean pore size of the medium, a safe but more useful version of the constraint given by equation (70) can be expressed as[2]

$$t^* \gg l\ \max\left(l \max_{\alpha=\beta,\,\gamma}\left(\frac{\rho_\alpha}{\mu_\alpha}\right),\ \max_{\alpha=\beta,\,\gamma}\left(\frac{\varepsilon_\alpha}{\|\langle \mathbf{v}_\alpha \rangle\|}\right)\right) \tag{72}$$

To complete the closure problem, we now need to construct boundary conditions in order to state the boundary value problem for the pressure and velocity spatial deviations and this is the object of the next paragraph.

[2] A particular situation where this constraint is satisfied is that of an entirely time independent two-phase flow process. It can be envisaged for many problems of practical importance such as the co-injection (co-current or counter-current flow) of two-phases over sufficiently large periods of time, as encountered for instance in packed bed columns of reactors. Note also that, in this particular case, the average mass balance equations simplify to stationary versions $\nabla \cdot \langle \mathbf{v}_\beta \rangle = 0$ and $\nabla \cdot \langle \mathbf{v}_\gamma \rangle = 0$. Again, this situation is only a limit case of processes envisaged here.

4.3 Boundary conditions

By making use of the velocity and pressure decompositions given by equations (20) and (30), along with the analogous ones for the γ-phase, we can express equations (2c) through (2f) as

$$\text{BC1} \qquad \tilde{\mathbf{v}}_\beta = -\langle \mathbf{v}_\beta \rangle^\beta \qquad \text{at } A_{\beta\sigma} \tag{73a}$$

$$\text{BC2} \qquad \tilde{\mathbf{v}}_\beta = \tilde{\mathbf{v}}_\gamma - (\langle \mathbf{v}_\beta \rangle^\beta - \langle \mathbf{v}_\gamma \rangle^\gamma) \qquad \text{at } A_{\beta\gamma} \tag{73b}$$

$$\text{BC3} \qquad -\mathbf{n}_{\beta\gamma}\tilde{p}_\beta = -\mathbf{n}_{\beta\gamma}\tilde{p}_\gamma + \mathbf{n}_{\beta\gamma}(\langle p_\beta \rangle^\beta - \langle p_\gamma \rangle^\gamma)$$

$$-\mathbf{n}_{\beta\gamma} \cdot \left[\mu_\beta(\nabla\tilde{\mathbf{v}}_\beta + \nabla\tilde{\mathbf{v}}_\beta^T) - \mu_\gamma(\nabla\tilde{\mathbf{v}}_\gamma + \nabla\tilde{\mathbf{v}}_\gamma^T)\right] + 2\sigma H \mathbf{n}_{\beta\gamma} \qquad \text{at } A_{\beta\gamma} \tag{73c}$$

$$\text{BC4} \qquad \tilde{\mathbf{v}}_\gamma = -\langle \mathbf{v}_\gamma \rangle^\gamma \qquad \text{at } A_{\gamma\sigma} \tag{73d}$$

In deriving equation (73c) we have used the representation of the viscous stress tensors, Υ_β and Υ_γ, according to equation (4). Moreover, we have discarded the macroscopic viscous part of these two tensors. This is a straightforward consequence of the scale hierarchy described by equation (13) considering the fact that the characteristic length-scale of the gradient is l_β or l_γ when operating on the velocity deviation and L when operating on the average part of the velocity.

Under this form, many source terms appear in the set of boundary conditions, namely $\langle \mathbf{v}_\beta \rangle^\beta$, $\langle \mathbf{v}_\gamma \rangle^\gamma$, $\langle p_\beta \rangle^\beta - \langle p_\gamma \rangle^\gamma$ and $2\sigma H$ leading to an excessively complex closure. This issue was discussed thoroughly in the derivation of macroscopic models for two-phase creeping flow in porous media (Whitaker, 1986b; Torres, 1987; Whitaker, 1994) involving exactly the same boundary conditions. To achieve necessary simplifications, it is convenient to begin with the surface average over $A_{\beta\gamma}$ of the projection of equation (73c) onto the normal $\mathbf{n}_{\beta\gamma}$. The result can be listed as (Whitaker, 1994)

$$\begin{aligned} -(\langle p_\beta \rangle^\beta - \langle p_\gamma \rangle^\gamma) &= 2\sigma \langle H \rangle_{\beta\gamma} + \langle \tilde{p}_\beta - \tilde{p}_\gamma \rangle_{\beta\gamma} \\ &\quad - \left\langle \mathbf{n}_{\beta\gamma} \cdot \left[\mu_\beta(\nabla\tilde{\mathbf{v}}_\beta + \nabla\tilde{\mathbf{v}}_\beta^T) - \mu_\gamma(\nabla\tilde{\mathbf{v}}_\gamma + \nabla\tilde{\mathbf{v}}_\gamma^T)\right] \cdot \mathbf{n}_{\beta\gamma} \right\rangle_{\beta\gamma} \end{aligned} \tag{74}$$

where the area average is denoted by $\langle \rangle_{\beta\gamma}$ and where we have considered $\langle p_\beta \rangle^\beta - \langle p_\gamma \rangle^\gamma$ as a constant with respect to that averaging process following arguments similar to those leading to equation (21). If the pressure, viscous and inertial forces are of comparable magnitude it can be deduced from equation (68) that

$$\tilde{p}_\alpha = O\left(\frac{\mu_\alpha \|\tilde{\mathbf{v}}_\alpha\|}{l_\alpha}\right) + O\left(\rho_\alpha \|\tilde{\mathbf{v}}_\alpha\|^2\right), \qquad \alpha = \beta,\, \gamma \tag{75}$$

Using this allows to write

$$-(\langle p_\beta \rangle^\beta - \langle p_\gamma \rangle^\gamma) = 2\sigma \langle H \rangle_{\beta\gamma} + \max_{\alpha=\beta,\,\gamma} \left(O\langle \mu_\alpha \nabla\tilde{\mathbf{v}}_\alpha \rangle_{\beta\gamma} + O\langle l_\alpha \mathbf{v}_\alpha \cdot \nabla\tilde{\mathbf{v}}_\alpha \rangle_{\beta\gamma} \right) \tag{76}$$

or

$$-(\langle p_\beta \rangle^\beta - \langle p_\gamma \rangle^\gamma) = 2\sigma \langle H \rangle_{\beta\gamma} \left(1 + \max_{\alpha=\beta,\,\gamma} \left(O\left(\frac{\langle \nabla\tilde{\mathbf{v}}_\alpha \rangle_{\beta\gamma}}{\langle H \rangle_{\beta\gamma}\, v}\right) Ca + O\left(\frac{\langle \mathbf{v}_\alpha \cdot \nabla\tilde{\mathbf{v}}_\alpha \rangle_{\beta\gamma}}{\langle H \rangle_{\beta\gamma}\, v^2}\right) We \right)\right) \tag{77}$$

In this last equation, Ca and We are the capillary number and Weber number respectively defined as

$$Ca = \max_{\alpha=\beta,\,\gamma} (\mu_\alpha) \frac{v}{\sigma} \tag{78}$$

and

$$We = \max_{\alpha=\beta,\,\gamma} (\rho_\alpha)\, \frac{v^2 l}{\sigma} \tag{79}$$

Here we have used l to represent the mean pore size and v to represent the order of magnitude common to all the velocities $\langle \mathbf{v}_\alpha \rangle^\alpha$ and $\tilde{\mathbf{v}}_\alpha$ ($\alpha = \beta, \gamma$) due to the no slip boundary condition at the solid-fluid interfaces along with the continuity of velocities at the fluid-fluid interface. We now impose the restrictions

$$\left(\frac{\langle \nabla \tilde{\mathbf{v}}_\alpha \rangle_{\beta\gamma}}{\langle H \rangle_{\beta\gamma}\, v} \right) Ca \ll 1 \tag{80}$$

and

$$\left(\frac{\langle \mathbf{v}_\alpha \cdot \nabla \tilde{\mathbf{v}}_\alpha \rangle_{\beta\gamma}}{\langle H \rangle_{\beta\gamma}\, v^2} \right) We \ll 1 \tag{81}$$

so that we can write equation (77) as

$$-(\langle p_\beta \rangle^\beta - \langle p_\gamma \rangle^\gamma) = 2\sigma \langle H \rangle_{\beta\gamma} \tag{82}$$

which is nothing else than the traditional capillary pressure. If we impose that $\langle H \rangle_{\beta\gamma}$ is at most $O\left(l^{-1}\right)$ which is a reasonable approximation if the solid phase is wetted by one of the two fluid phases, and neither the β- nor the the γ-phase is under the form of ganglia of radius significantly smaller than the mean pore size, then one can reasonably expect

$$\frac{\langle \nabla \tilde{\mathbf{v}}_\alpha \rangle_{\beta\gamma}}{\langle H \rangle_{\beta\gamma}\, v} \ll 1 \tag{83}$$

and

$$\frac{\langle \mathbf{v}_\alpha \cdot \nabla \tilde{\mathbf{v}}_\alpha \rangle_{\beta\gamma}}{\langle H \rangle_{\beta\gamma}\, v^2} \ll 1 \tag{84}$$

This can be readily inferred from the fact that $\langle \nabla \tilde{\mathbf{v}}_\alpha \rangle_{\beta\gamma}$ and $\langle \mathbf{v}_\alpha \cdot \nabla \tilde{\mathbf{v}}_\alpha \rangle_{\beta\gamma}$ are expected to be much smaller in magnitude than $\frac{v}{l}$ and $\frac{v^2}{l}$ respectively. Under these circumstances, one would only require Ca and We be at most of order 1 for the above development to hold. Nevertheless, one must keep in mind that the requirements are those given by equations (80) and (81) and when these constraints are satisfied, the normal stress jump at $A_{\beta\gamma}$ can be written as (Torres, 1987)

$$\begin{aligned} \text{BC3} \qquad -\mathbf{n}_{\beta\gamma}\tilde{p}_\beta \;=\; & -\mathbf{n}_{\beta\gamma}\tilde{p}_\gamma - \mathbf{n}_{\beta\gamma} \cdot \left[\mu_\beta (\nabla \tilde{\mathbf{v}}_\beta + \nabla \tilde{\mathbf{v}}_\beta^T) - \mu_\gamma (\nabla \tilde{\mathbf{v}}_\gamma + \nabla \tilde{\mathbf{v}}_\gamma^T) \right] \\ & + 2\sigma \left(H - \langle H \rangle_{\beta\gamma} \right) \mathbf{n}_{\beta\gamma} \qquad \text{at } A_{\beta\gamma} \end{aligned} \tag{85}$$

At this point, the closure still involves the term of curvature deviation $H - \langle H \rangle_{\beta\gamma}$ in the above boundary condition. Conditions under which this term can exhibit significant variations over the averaging volume are not easy to identify due the diversity of geometrical, wetting and hydrodynamic situations that can be encountered. Clearly, comprehensive numerical experiments of two-phase flow in complex enough configurations would greatly highlight this issue and provide some explicit criteria on the importance of this term. In the absence of more detailed information on that matter, we shall follow some assumption made in previous studies on two-phase creeping flow (Auriault, 1987; Whitaker, 1994) i.e.

$$\text{Hypothesis} \qquad \left(H - \langle H \rangle_{\beta\gamma} \right) \simeq 0 \text{ in } V \tag{86}$$

One of the necessary conditions to put forth such an hypothesis certainly lies in negligible gravity effects over V in comparison to capillary effects, leading to a small pore-scale Bond number compared to unity. It is however highly probable that this is not a sufficient one. In the rest of this work, we keep the hypothesis given in equation (86).

Since the objective is not to solve the boundary value problem for the closure over the entire macroscopic structure, we assume that a representative elementary volume can be exhibited on that structure. This allows to replace the deviation forms of the two boundary conditions expressed in equations (2i) and (2j) by periodic ones leading to a local form of the closure problem that is written as

$$\rho_\beta \mathbf{v}_\beta \cdot \nabla \tilde{\mathbf{v}}_\beta = -\nabla \tilde{p}_\beta + \mu_\beta \nabla^2 \tilde{\mathbf{v}}_\beta$$

$$-\frac{1}{V_\beta} \int_{A_{\beta\sigma}+A_{\beta\gamma}} \mathbf{n}_\beta \cdot (-\tilde{p}_\beta \mathbf{I} + \mu_\beta \nabla \tilde{\mathbf{v}}_\beta) dA \qquad \text{in } V_\beta \tag{87a}$$

$$\nabla \cdot \tilde{\mathbf{v}}_\beta = 0 \qquad \text{in } V_\beta \tag{87b}$$

$$\text{BC1} \qquad \tilde{\mathbf{v}}_\beta = -\langle \mathbf{v}_\beta \rangle^\beta \qquad \text{at } A_{\beta\sigma} \tag{87c}$$

$$\text{BC2} \qquad \tilde{\mathbf{v}}_\beta = \tilde{\mathbf{v}}_\gamma - (\langle \mathbf{v}_\beta \rangle^\beta - \langle \mathbf{v}_\gamma \rangle^\gamma) \qquad \text{at } A_{\beta\gamma} \tag{87d}$$

$$\text{BC3} \qquad -\mathbf{n}_{\beta\gamma} \tilde{p}_\beta = -\mathbf{n}_{\beta\gamma} \tilde{p}_\gamma$$

$$-\mathbf{n}_{\beta\gamma} \cdot \left[\mu_\beta (\nabla \tilde{\mathbf{v}}_\beta + \nabla \tilde{\mathbf{v}}_\beta^T) - \mu_\gamma (\nabla \tilde{\mathbf{v}}_\gamma + \nabla \tilde{\mathbf{v}}_\gamma^T) \right] \qquad \text{at } A_{\beta\gamma} \tag{87e}$$

$$\text{BC4} \qquad \tilde{\mathbf{v}}_\gamma = -\langle \mathbf{v}_\gamma \rangle^\gamma \qquad \text{at } A_{\gamma\sigma} \tag{87f}$$

$$\rho_\gamma \mathbf{v}_\gamma \cdot \nabla \tilde{\mathbf{v}}_\gamma = -\nabla \tilde{p}_\gamma + \mu_\gamma \nabla^2 \tilde{\mathbf{v}}_\gamma$$

$$-\frac{1}{V_\gamma} \int_{A_{\gamma\sigma}+A_{\beta\gamma}} \mathbf{n}_\gamma \cdot (-\tilde{p}_\gamma \mathbf{I} + \mu_\gamma \nabla \tilde{\mathbf{v}}_\gamma) dA \qquad \text{in } V_\gamma \tag{87g}$$

$$\nabla \cdot \tilde{\mathbf{v}}_\gamma = 0 \qquad \text{in } V_\gamma \tag{87h}$$

Periodicity

$$\tilde{\mathbf{v}}_\beta(\mathbf{r}+\mathbf{l}_i) = \tilde{\mathbf{v}}_\beta(\mathbf{r}) \qquad \tilde{\mathbf{v}}_\gamma(\mathbf{r}+\mathbf{l}_i) = \tilde{\mathbf{v}}_\gamma(\mathbf{r}) \qquad i = 1,2,3 \tag{87i}$$

$$\tilde{p}_\beta(\mathbf{r}+\mathbf{l}_i) = \tilde{p}_\beta(\mathbf{r}) \qquad \tilde{p}_\gamma(\mathbf{r}+\mathbf{l}_i) = \tilde{p}_\gamma(\mathbf{r}) \qquad i = 1,2,3 \tag{87j}$$

An equivalent condition to that given in equation (6) would be required to avoid the solution on $\tilde{p}_\beta$ and $\tilde{p}_\gamma$ to within an arbitrary additive constant. This could be obtained by a condition on one of the pressure deviations. However, this condition is of no practical importance since any additive constant in the pressure deviation fields does not affect the macroscopic closed form of the governing equations. For this reason, no such condition will be further considered in our development.

In addition to the time-scale constraint of equation (70) and the hypothesis given by equation (86), this closure was developped with

Average

$$\langle \tilde{\mathbf{v}}_\beta \rangle^\beta = 0 \qquad \langle \tilde{\mathbf{v}}_\gamma \rangle^\gamma = 0 \tag{87k}$$

as a result of the scale hierarchy expressed by equation (13).

Even if no explicit dependence of the curvature appears in the closure problem, one must keep in mind that the interface $A_{\beta\gamma}$ must be located before the resolution of the set of equations (87).

4.4 Closure variables

The local closure problem given by equations (87) is made non-homogeneous because of the presence of the two source terms $\langle \mathbf{v}_\beta \rangle^\beta$ and $\langle \mathbf{v}_\gamma \rangle^\gamma$. For this reason, we want to find a solution of the closure in terms of these sources leading to a representation for the spatial deviation velocities and pressures given by[3]

$$\tilde{\mathbf{v}}_\beta = \mathbf{A}_{\beta\beta} \cdot \langle \mathbf{v}_\beta \rangle^\beta + \mathbf{A}_{\beta\gamma} \cdot \langle \mathbf{v}_\gamma \rangle^\gamma \tag{88}$$

$$\tilde{p}_\beta = \mu_\beta \left[\mathbf{a}_{\beta\beta} \cdot \langle \mathbf{v}_\beta \rangle^\beta + \mathbf{a}_{\beta\gamma} \cdot \langle \mathbf{v}_\gamma \rangle^\gamma \right] \tag{89}$$

$$\tilde{\mathbf{v}}_\gamma = \mathbf{A}_{\gamma\beta} \cdot \langle \mathbf{v}_\beta \rangle^\beta + \mathbf{A}_{\gamma\gamma} \cdot \langle \mathbf{v}_\gamma \rangle^\gamma \tag{90}$$

$$\tilde{p}_\gamma = \mu_\gamma \left[\mathbf{a}_{\gamma\beta} \cdot \langle \mathbf{v}_\beta \rangle^\beta + \mathbf{a}_{\gamma\gamma} \cdot \langle \mathbf{v}_\gamma \rangle^\gamma \right] \tag{91}$$

In this representation $\mathbf{A}_{\alpha\kappa}$ and $\mathbf{a}_{\alpha\kappa}$ are tensors and vectors referred to as closure variables with the nomenclature arranged so that α represents the phase in which the closure variable is defined and κ indicates which velocity is mapped onto the spatial deviation. This representation can now be inserted in the closure problem provided above and we choose to specify the closure variables according to two boundary value problems each one being associated to one of the source terms. For the coefficients associated to $\langle \mathbf{v}_\beta \rangle^\beta$, we obtain

Problem I:

$$(\rho_\beta \mathbf{v}_\beta / \mu_\beta) \cdot \nabla \mathbf{A}_{\beta\beta} = -\nabla \mathbf{a}_{\beta\beta} + \nabla^2 \mathbf{A}_{\beta\beta}$$

$$-\frac{1}{V_\beta} \int\limits_{A_{\beta\sigma}+A_{\beta\gamma}} \mathbf{n}_\beta \cdot (-\mathbf{I}\mathbf{a}_{\beta\beta} + \nabla \mathbf{A}_{\beta\beta}) dA \qquad \text{in } V_\beta \tag{92a}$$

$$\nabla \cdot \mathbf{A}_{\beta\beta} = 0 \qquad \text{in } V_\beta \tag{92b}$$

$$\text{BC1} \quad \mathbf{A}_{\beta\beta} = -\mathbf{I} \qquad \text{at } A_{\beta\sigma} \tag{92c}$$

$$\text{BC2} \quad \mathbf{A}_{\beta\beta} = \mathbf{A}_{\gamma\beta} - \mathbf{I} \qquad \text{at } A_{\beta\gamma} \tag{92d}$$

$$\text{BC3} \quad \mu_\beta \mathbf{n}_{\beta\gamma} \cdot \left[-\mathbf{I}\mathbf{a}_{\beta\beta} + (\nabla \mathbf{A}_{\beta\beta} + \nabla \mathbf{A}_{\beta\beta}^T) \right]$$

$$= \mu_\gamma \mathbf{n}_{\beta\gamma} \cdot \left[-\mathbf{I}\mathbf{a}_{\gamma\beta} + (\nabla \mathbf{A}_{\gamma\beta} + \nabla \mathbf{A}_{\gamma\beta}^T) \right] \qquad \text{at } A_{\beta\gamma} \tag{92e}$$

$$\text{BC4} \quad \mathbf{A}_{\gamma\beta} = 0 \qquad \text{at } A_{\gamma\sigma} \tag{92f}$$

$$(\rho_\gamma \mathbf{v}_\gamma / \mu_\gamma) \cdot \nabla \mathbf{A}_{\gamma\beta} = -\nabla \mathbf{a}_{\gamma\beta} + \nabla^2 \mathbf{A}_{\gamma\beta}$$

$$-\frac{1}{V_\gamma} \int\limits_{A_{\gamma\sigma}+A_{\beta\gamma}} \mathbf{n}_\gamma \cdot (-\mathbf{I}\mathbf{a}_{\gamma\beta} + \nabla \mathbf{A}_{\gamma\beta}) dA \qquad \text{in } V_\gamma \tag{92g}$$

$$\nabla \cdot \mathbf{A}_{\gamma\beta} = 0 \qquad \text{in } V_\gamma \tag{92h}$$

Periodicity

$$\mathbf{a}_{\beta\beta}(\mathbf{r} + \mathbf{l}_i) = \mathbf{a}_{\beta\beta}(\mathbf{r}) \qquad \mathbf{a}_{\gamma\beta}(\mathbf{r} + \mathbf{l}_i) = \mathbf{a}_{\gamma\beta}(\mathbf{r}) \qquad i = 1, 2, 3 \tag{92i}$$

$$\mathbf{A}_{\beta\beta}(\mathbf{r} + \mathbf{l}_i) = \mathbf{A}_{\beta\beta}(\mathbf{r}) \qquad \mathbf{A}_{\gamma\beta}(\mathbf{r} + \mathbf{l}_i) = \mathbf{A}_{\gamma\beta}(\mathbf{r}) \qquad i = 1, 2, 3 \tag{92j}$$

Average

$$\langle \mathbf{A}_{\beta\beta} \rangle^\beta = 0 \qquad \langle \mathbf{A}_{\gamma\beta} \rangle^\gamma = 0 \tag{92k}$$

[3] In this mapping, we have omitted additive scalar and vector fields since it can be proven, following the same development as the one provided for creeping two-phase flow (Whitaker, 1986b), that these fields are either zero or constants of no importance in the macrosocpic governing equations.

The second boundary value problem associated with the coefficient of $\langle \mathbf{v}_\gamma \rangle^\gamma$ takes the analogous form given by

Problem II:

$$(\rho_\beta \mathbf{v}_\beta/\mu_\beta) \cdot \nabla \mathbf{A}_{\beta\gamma} = -\nabla \mathbf{a}_{\beta\gamma} + \nabla^2 \mathbf{A}_{\beta\gamma}$$
$$-\frac{1}{V_\beta} \int\limits_{A_{\beta\sigma}+A_{\beta\gamma}} \mathbf{n}_\beta \cdot (-\mathbf{I}\mathbf{a}_{\beta\gamma} + \nabla \mathbf{A}_{\beta\gamma}) dA \qquad \text{in } V_\beta \tag{93a}$$

$$\nabla \cdot \mathbf{A}_{\beta\gamma} = 0 \qquad \text{in } V_\beta \tag{93b}$$

$$\text{BC1} \qquad \mathbf{A}_{\beta\gamma} = 0 \qquad \text{at } A_{\beta\sigma} \tag{93c}$$

$$\text{BC2} \qquad \mathbf{A}_{\beta\gamma} = \mathbf{A}_{\gamma\gamma} + \mathbf{I} \qquad \text{at } A_{\beta\gamma} \tag{93d}$$

$$\text{BC3} \qquad \mu_\beta \mathbf{n}_{\beta\gamma} \cdot \left[-\mathbf{I}\mathbf{a}_{\beta\gamma} + (\nabla \mathbf{A}_{\beta\gamma} + \nabla \mathbf{A}_{\beta\gamma}^T)\right]$$
$$= \mu_\gamma \mathbf{n}_{\beta\gamma} \cdot \left[-\mathbf{I}\mathbf{a}_{\gamma\gamma} + (\nabla \mathbf{A}_{\gamma\gamma} + \nabla \mathbf{A}_{\gamma\gamma}^T)\right] \qquad \text{at } A_{\beta\gamma} \tag{93e}$$

$$\text{BC4} \qquad \mathbf{A}_{\gamma\gamma} = -\mathbf{I} \qquad \text{at } A_{\gamma\sigma} \tag{93f}$$

$$(\rho_\gamma \mathbf{v}_\gamma/\mu_\gamma) \cdot \nabla \mathbf{A}_{\gamma\gamma} = -\nabla \mathbf{a}_{\gamma\gamma} + \nabla^2 \mathbf{A}_{\gamma\gamma}$$
$$-\frac{1}{V_\gamma} \int\limits_{A_{\gamma\sigma}+A_{\beta\gamma}} \mathbf{n}_\gamma \cdot (-\mathbf{I}\mathbf{a}_{\gamma\gamma} + \nabla \mathbf{A}_{\gamma\gamma}) dA \qquad \text{in } V_\gamma \tag{93g}$$

$$\nabla \cdot \mathbf{A}_{\gamma\gamma} = 0 \qquad \text{in } V_\gamma \tag{93h}$$

Periodicity

$$\mathbf{a}_{\beta\gamma}(\mathbf{r} + \mathbf{l}_i) = \mathbf{a}_{\beta\gamma}(\mathbf{r}) \qquad \mathbf{a}_{\gamma\gamma}(\mathbf{r} + \mathbf{l}_i) = \mathbf{a}_{\gamma\gamma}(\mathbf{r}) \qquad i = 1, 2, 3 \tag{93i}$$

$$\mathbf{A}_{\beta\gamma}(\mathbf{r} + \mathbf{l}_i) = \mathbf{A}_{\beta\gamma}(\mathbf{r}) \qquad \mathbf{A}_{\gamma\gamma}(\mathbf{r} + \mathbf{l}_i) = \mathbf{A}_{\gamma\gamma}(\mathbf{r}) \qquad i = 1, 2, 3 \tag{93j}$$

Average

$$\langle \mathbf{A}_{\beta\gamma} \rangle^\beta = 0 \qquad \langle \mathbf{A}_{\gamma\gamma} \rangle^\gamma = 0 \tag{93k}$$

4.5 Decomposition of the closure problems

We shall progress towards some more tractable versions of the above two boundary value problems by using a convenient decomposition with the idea that this decomposition will lead to a macroscopic model containing the classical Darcy part and a remaining part lumping the inertial effects. To accomplish this, we decompose the four tensors and four vectors defined in equations (88) through (91) according to

$$\mathbf{A}_{\beta\beta} = \mathbf{A}_{\beta\beta 1} + \mathbf{A}_{\beta\beta 2} \tag{94}$$
$$\mathbf{a}_{\beta\beta} = \mathbf{a}_{\beta\beta 1} + \mathbf{a}_{\beta\beta 2} \tag{95}$$
$$\mathbf{A}_{\beta\gamma} = \mathbf{A}_{\beta\gamma 1} + \mathbf{A}_{\beta\gamma 2} \tag{96}$$
$$\mathbf{a}_{\beta\gamma} = \mathbf{a}_{\beta\gamma 1} + \mathbf{a}_{\beta\gamma 2} \tag{97}$$

$$\mathbf{A}_{\gamma\gamma} = \mathbf{A}_{\gamma\gamma 1} + \mathbf{A}_{\gamma\gamma 2} \tag{98}$$
$$\mathbf{a}_{\gamma\gamma} = \mathbf{a}_{\gamma\gamma 1} + \mathbf{a}_{\gamma\gamma 2} \tag{99}$$
$$\mathbf{A}_{\gamma\beta} = \mathbf{A}_{\gamma\beta 1} + \mathbf{A}_{\gamma\beta 2} \tag{100}$$
$$\mathbf{a}_{\gamma\beta} = \mathbf{a}_{\gamma\beta 1} + \mathbf{a}_{\gamma\beta 2} \tag{101}$$

and we choose to specify the tensors and vectors $\mathbf{A}_{\beta\beta 1}$, $\mathbf{a}_{\beta\beta 1}$, $\mathbf{A}_{\gamma\beta 1}$ and $\mathbf{a}_{\gamma\beta 1}$ by the following problem

Problem I1

$$-\nabla \mathbf{a}_{\beta\beta 1} + \nabla^2 \mathbf{A}_{\beta\beta 1} = -\varepsilon_\beta \mathbf{K}_\beta^{-1} \qquad \text{in } V_\beta \tag{102a}$$

$$\nabla \cdot \mathbf{A}_{\beta\beta 1} = 0 \qquad \text{in } V_\beta \tag{102b}$$

$$\text{BC1} \quad \mathbf{A}_{\beta\beta 1} = -\mathbf{I} \qquad \text{at } A_{\beta\sigma} \tag{102c}$$

$$\text{BC2} \quad \mathbf{A}_{\beta\beta 1} = \mathbf{A}_{\gamma\beta 1} - \mathbf{I} \qquad \text{at } A_{\beta\gamma} \tag{102d}$$

$$\text{BC3} \quad \mu_\beta \mathbf{n}_{\beta\gamma} \cdot \left[-\mathbf{I}\mathbf{a}_{\beta\beta} + (\nabla \mathbf{A}_{\beta\beta 1} + \nabla \mathbf{A}_{\beta\beta 1}^T)\right]$$
$$= \mu_\gamma \mathbf{n}_{\beta\gamma} \cdot \left[-\mathbf{I}\mathbf{a}_{\gamma\beta} + (\nabla \mathbf{A}_{\gamma\beta 1} + \nabla \mathbf{A}_{\gamma\beta 1}^T)\right] \qquad \text{at } A_{\beta\gamma} \tag{102e}$$

$$\text{BC4} \quad \mathbf{A}_{\gamma\beta 1} = 0 \qquad \text{at } A_{\gamma\sigma} \tag{102f}$$

$$-\nabla \mathbf{a}_{\gamma\beta 1} + \nabla^2 \mathbf{A}_{\gamma\beta 1} = \varepsilon_\beta \mathbf{K}_\gamma^{-1} \cdot \mathbf{K}_{\gamma\beta} \qquad \text{in } V_\gamma \tag{102g}$$

$$\nabla \cdot \mathbf{A}_{\gamma\beta 1} = 0 \qquad \text{in } V_\gamma \tag{102h}$$

Periodicity

$$\mathbf{a}_{\beta\beta 1}(\mathbf{r} + \mathbf{l}_i) = \mathbf{a}_{\beta\beta 1}(\mathbf{r}) \qquad \mathbf{a}_{\gamma\beta 1}(\mathbf{r} + \mathbf{l}_i) = \mathbf{a}_{\gamma\beta 1}(\mathbf{r}) \qquad i = 1, 2, 3 \tag{102i}$$

$$\mathbf{A}_{\beta\beta 1}(\mathbf{r} + \mathbf{l}_i) = \mathbf{A}_{\beta\beta 1}(\mathbf{r}) \qquad \mathbf{A}_{\gamma\beta 1}(\mathbf{r} + \mathbf{l}_i) = \mathbf{A}_{\gamma\beta 1}(\mathbf{r}) \qquad i = 1, 2, 3 \tag{102j}$$

Average

$$\langle \mathbf{A}_{\beta\beta 1} \rangle^\beta = 0 \qquad \langle \mathbf{A}_{\gamma\beta 1} \rangle^\gamma = 0 \tag{102k}$$

Similarly, we specify the tensors and vectors $\mathbf{A}_{\beta\gamma 1}$, $\mathbf{a}_{\beta\gamma 1}$, $\mathbf{A}_{\gamma\gamma 1}$ and $\mathbf{a}_{\gamma\gamma 1}$ by the following problem

Problem II1

$$-\nabla \mathbf{a}_{\beta\gamma 1} + \nabla^2 \mathbf{A}_{\beta\gamma 1} = \varepsilon_\gamma \mathbf{K}_\beta^{-1} \cdot \mathbf{K}_{\beta\gamma} \qquad \text{in } V_\beta \tag{103a}$$

$$\nabla \cdot \mathbf{A}_{\beta\gamma 1} = 0 \qquad \text{in } V_\beta \tag{103b}$$

$$\text{BC1} \quad \mathbf{A}_{\beta\gamma 1} = 0 \qquad \text{at } A_{\beta\sigma} \tag{103c}$$

$$\text{BC2} \quad \mathbf{A}_{\beta\gamma 1} = \mathbf{A}_{\gamma\gamma 1} + \mathbf{I} \qquad \text{at } A_{\beta\gamma} \tag{103d}$$

$$\text{BC3} \quad \mu_\beta \mathbf{n}_{\beta\gamma} \cdot \left[-\mathbf{I}\mathbf{a}_{\beta\gamma} + (\nabla \mathbf{A}_{\beta\gamma 1} + \nabla \mathbf{A}_{\beta\gamma 1}^T)\right]$$
$$= \mu_\gamma \mathbf{n}_{\beta\gamma} \cdot \left[-\mathbf{I}\mathbf{a}_{\gamma\gamma} + (\nabla \mathbf{A}_{\gamma\gamma 1} + \nabla \mathbf{A}_{\gamma\gamma 1}^T)\right] \qquad \text{at } A_{\beta\gamma} \tag{103e}$$

$$\text{BC4} \quad \mathbf{A}_{\gamma\gamma 1} = -\mathbf{I} \qquad \text{at } A_{\gamma\sigma} \tag{103f}$$

$$-\nabla \mathbf{a}_{\gamma\gamma 1} + \nabla^2 \mathbf{A}_{\gamma\gamma 1} = -\varepsilon_\gamma \mathbf{K}_\gamma^{-1} \qquad \text{in } V_\gamma \tag{103g}$$

$$\nabla \cdot \mathbf{A}_{\gamma\gamma 1} = 0 \qquad \text{in } V_\gamma \tag{103h}$$

Periodicity

$$\mathbf{a}_{\beta\gamma 1}(\mathbf{r} + \mathbf{l}_i) = \mathbf{a}_{\beta\gamma 1}(\mathbf{r}) \qquad \mathbf{a}_{\gamma\gamma 1}(\mathbf{r} + \mathbf{l}_i) = \mathbf{a}_{\gamma\gamma 1}(\mathbf{r}) \qquad i = 1, 2, 3 \tag{103i}$$

$$\mathbf{A}_{\beta\gamma 1}(\mathbf{r} + \mathbf{l}_i) = \mathbf{A}_{\beta\gamma 1}(\mathbf{r}) \qquad \mathbf{A}_{\gamma\gamma 1}(\mathbf{r} + \mathbf{l}_i) = \mathbf{A}_{\gamma\gamma 1}(\mathbf{r}) \qquad i = 1, 2, 3 \tag{103j}$$

Average

$$\langle \mathbf{A}_{\beta\gamma 1} \rangle^\beta = 0 \qquad \langle \mathbf{A}_{\gamma\gamma 1} \rangle^\gamma = 0 \tag{103k}$$

While writing equations (102a), (102g), (103a) and (103g) we have used the following definitions

$$\frac{1}{V_\beta}\int\limits_{A_{\beta\sigma}+A_{\beta\gamma}} \mathbf{n}_\beta\cdot(-\mathbf{I}\mathbf{a}_{\beta\beta 1}+\nabla\mathbf{A}_{\beta\beta 1})dA=-\varepsilon_\beta\mathbf{K}_\beta^{-1} \tag{104}$$

$$\frac{1}{V_\gamma}\int\limits_{A_{\gamma\sigma}+A_{\beta\gamma}} \mathbf{n}_\gamma\cdot(-\mathbf{I}\mathbf{a}_{\gamma\beta 1}+\nabla\mathbf{A}_{\gamma\beta 1})dA=\varepsilon_\beta\mathbf{K}_\gamma^{-1}\cdot\mathbf{K}_{\gamma\beta} \tag{105}$$

$$\frac{1}{V_\beta}\int\limits_{A_{\beta\sigma}+A_{\beta\gamma}} \mathbf{n}_\beta\cdot(-\mathbf{I}\mathbf{a}_{\beta\gamma 1}+\nabla\mathbf{A}_{\beta\gamma 1})dA=\varepsilon_\gamma\mathbf{K}_\beta^{-1}\cdot\mathbf{K}_{\beta\gamma} \tag{106}$$

$$\frac{1}{V_\gamma}\int\limits_{A_{\gamma\sigma}+A_{\beta\gamma}} \mathbf{n}_\gamma\cdot(-\mathbf{I}\mathbf{a}_{\gamma\gamma 1}+\nabla\mathbf{A}_{\gamma\gamma 1})dA=-\varepsilon_\gamma\mathbf{K}_\gamma^{-1} \tag{107}$$

where $\mathbf{K}_\alpha$ and $\mathbf{K}_{\alpha\kappa}$ are the permeability and viscous drag tensors as used in the derivation of the macroscopic two-phase flow model in the creeping regime (Whitaker, 1986b; Whitaker, 1994; Lasseux et al., 1996). The closure problem must now be completed with the two following boundary value problems defining the four tensors $\mathbf{A}_{\beta\beta 2}$, $\mathbf{A}_{\gamma\beta 2}$, $\mathbf{A}_{\beta\gamma 2}$ and $\mathbf{A}_{\gamma\gamma 2}$ and the four vectors $\mathbf{a}_{\beta\beta 2}$, $\mathbf{a}_{\gamma\beta 2}$, $\mathbf{a}_{\beta\gamma 2}$ and $\mathbf{a}_{\gamma\gamma 2}$

Problem I2

$$\begin{aligned}&(\rho_\beta\mathbf{v}_\beta/\mu_\beta)\cdot\nabla\mathbf{A}_{\beta\beta 1}+(\rho_\beta\mathbf{v}_\beta/\mu_\beta)\cdot\nabla\mathbf{A}_{\beta\beta 2}\\ &=-\nabla\mathbf{a}_{\beta\beta 2}+\nabla^2\mathbf{A}_{\beta\beta 2}+\varepsilon_\beta\mathbf{K}_\beta^{-1}\cdot\mathbf{F}_\beta \qquad \text{in } V_\beta\end{aligned} \tag{108a}$$

$$\nabla\cdot\mathbf{A}_{\beta\beta 2}=0 \qquad \text{in } V_\beta \tag{108b}$$

$$\text{BC1} \quad \mathbf{A}_{\beta\beta 2}=0 \qquad \text{at } A_{\beta\sigma} \tag{108c}$$

$$\text{BC2} \quad \mathbf{A}_{\beta\beta 2}=\mathbf{A}_{\gamma\beta 2} \qquad \text{at } A_{\beta\gamma} \tag{108d}$$

$$\begin{aligned}&\text{BC3} \quad \mu_\beta\mathbf{n}_{\beta\gamma}\cdot(\nabla\mathbf{A}_{\beta\beta 2}+\nabla\mathbf{A}_{\beta\beta 2}^T)\\ &=\mu_\gamma\mathbf{n}_{\beta\gamma}\cdot(\nabla\mathbf{A}_{\gamma\beta 2}+\nabla\mathbf{A}_{\gamma\beta 2}^T) \qquad \text{at } A_{\beta\gamma}\end{aligned} \tag{108e}$$

$$\text{BC4} \quad \mathbf{A}_{\gamma\beta 2}=0 \qquad \text{at } A_{\gamma\sigma} \tag{108f}$$

$$\begin{aligned}&(\rho_\gamma\mathbf{v}_\gamma/\mu_\gamma)\cdot\nabla\mathbf{A}_{\gamma\beta 1}+(\rho_\gamma\mathbf{v}_\gamma/\mu_\gamma)\cdot\nabla\mathbf{A}_{\gamma\beta 2}\\ &=-\nabla\mathbf{a}_{\gamma\beta 2}+\nabla^2\mathbf{A}_{\gamma\beta 2}+\varepsilon_\beta\mathbf{K}_\gamma^{-1}\cdot\mathbf{F}_{\gamma\beta} \qquad \text{in } V_\gamma\end{aligned} \tag{108g}$$

$$\nabla\cdot\mathbf{A}_{\gamma\beta 2}=0 \qquad \text{in } V_\gamma \tag{108h}$$

Periodicity

$$\mathbf{A}_{\beta\beta 2}(\mathbf{r}+\mathbf{l}_i) = \mathbf{A}_{\beta\beta 2}(\mathbf{r}) \qquad \mathbf{A}_{\gamma\beta 2}(\mathbf{r}+\mathbf{l}_i)=\mathbf{A}_{\gamma\beta 2}(\mathbf{r}) \qquad i=1,2,3 \tag{108i}$$

$$\mathbf{a}_{\beta\beta 2}(\mathbf{r}+\mathbf{l}_i) = \mathbf{a}_{\beta\beta 2}(\mathbf{r}) \qquad \mathbf{a}_{\gamma\beta 2}(\mathbf{r}+\mathbf{l}_i)=\mathbf{a}_{\gamma\beta 2}(\mathbf{r}) \qquad i=1,2,3 \tag{108j}$$

Average

$$\langle\mathbf{A}_{\beta\beta 2}\rangle^\beta=0 \qquad \langle\mathbf{A}_{\gamma\beta 2}\rangle^\gamma=0 \tag{108k}$$

Problem II2

$$
\begin{aligned}
&(\rho_\beta \mathbf{v}_\beta/\mu_\beta)\cdot\nabla\mathbf{A}_{\beta\gamma 1} + (\rho_\beta \mathbf{v}_\beta/\mu_\beta)\cdot\nabla\mathbf{A}_{\beta\gamma 2} \\
&= -\nabla\mathbf{a}_{\beta\gamma 2} + \nabla^2\mathbf{A}_{\beta\gamma 2} + \varepsilon_\gamma \mathbf{K}_\beta^{-1}\cdot\mathbf{F}_{\beta\gamma} \qquad \text{in } V_\beta && \text{(109a)}\\
&\nabla\cdot\mathbf{A}_{\beta\gamma 2} = 0 \qquad \text{in } V_\beta && \text{(109b)}\\
&\text{BC1} \quad \mathbf{A}_{\beta\gamma 2} = 0 \qquad \text{at } A_{\beta\sigma} && \text{(109c)}\\
&\text{BC2} \quad \mathbf{A}_{\beta\gamma 2} = \mathbf{A}_{\gamma\gamma 2} \qquad \text{at } A_{\beta\gamma} && \text{(109d)}\\
&\text{BC3} \quad \mu_\beta \mathbf{n}_{\beta\gamma}\cdot(\nabla\mathbf{A}_{\beta\gamma 2} + \nabla\mathbf{A}_{\beta\gamma 2}^T) \\
&= \mu_\gamma \mathbf{n}_{\beta\gamma}\cdot(\nabla\mathbf{A}_{\gamma\gamma 2} + \nabla\mathbf{A}_{\gamma\gamma 2}^T) \qquad \text{at } A_{\beta\gamma} && \text{(109e)}\\
&\text{BC4} \quad \mathbf{A}_{\gamma\gamma 2} = 0 \qquad \text{at } A_{\gamma\sigma} && \text{(109f)}\\
&(\rho_\gamma \mathbf{v}_\gamma/\mu_\gamma)\cdot\nabla\mathbf{A}_{\gamma\gamma 1} + (\rho_\gamma \mathbf{v}_\gamma/\mu_\gamma)\cdot\nabla\mathbf{A}_{\gamma\gamma 2} \\
&= -\nabla\mathbf{a}_{\gamma\gamma 2} + \nabla^2\mathbf{A}_{\gamma\gamma 2} + \varepsilon_\gamma \mathbf{K}_\gamma^{-1}\cdot\mathbf{F}_\gamma \qquad \text{in } V_\gamma && \text{(109g)}\\
&\nabla\cdot\mathbf{A}_{\gamma\gamma 2} = 0 \qquad \text{in } V_\gamma && \text{(109h)}
\end{aligned}
$$

Periodicity

$$
\begin{aligned}
\mathbf{A}_{\beta\gamma 2}(\mathbf{r}+\mathbf{l}_i) &= \mathbf{A}_{\beta\gamma 2}(\mathbf{r}) \quad \mathbf{A}_{\gamma\gamma 2}(\mathbf{r}+\mathbf{l}_i) = \mathbf{A}_{\gamma\gamma 2}(\mathbf{r}) \quad i=1,2,3 && \text{(109i)}\\
\mathbf{a}_{\beta\gamma 2}(\mathbf{r}+\mathbf{l}_i) &= \mathbf{a}_{\beta\gamma 2}(\mathbf{r}) \quad \mathbf{a}_{\gamma\gamma 2}(\mathbf{r}+\mathbf{l}_i) = \mathbf{a}_{\gamma\gamma 2}(\mathbf{r}) \quad i=1,2,3 && \text{(109j)}
\end{aligned}
$$

Average

$$
\langle \mathbf{A}_{\beta\gamma 2}\rangle^\beta = 0 \qquad \langle \mathbf{A}_{\gamma\gamma 2}\rangle^\gamma = 0 \tag{109k}
$$

In writing the momentum equations (108a) and (109g), we have used the definitions of the *inertial correction tensors* $\mathbf{F}_\beta$ and $\mathbf{F}_\gamma$ in the β and γ phase respectively given by

$$
\frac{1}{V_\beta}\int\limits_{A_{\beta\sigma}+A_{\beta\gamma}} \mathbf{n}_\beta\cdot(-\mathbf{I}\mathbf{a}_{\beta\beta 2} + \nabla\mathbf{A}_{\beta\beta 2})\,dA = -\varepsilon_\beta \mathbf{K}_\beta^{-1}\cdot\mathbf{F}_\beta \tag{110}
$$

and

$$
\frac{1}{V_\gamma}\int\limits_{A_{\gamma\sigma}+A_{\beta\gamma}} \mathbf{n}_\gamma\cdot(-\mathbf{I}\mathbf{a}_{\gamma\gamma 2} + \nabla\mathbf{A}_{\gamma\gamma 2})\,dA = -\varepsilon_\gamma \mathbf{K}_\gamma^{-1}\cdot\mathbf{F}_\gamma \tag{111}
$$

Similarily, in equations (108g) and (109a), we have used the *coupling inertial correction tensors* $\mathbf{F}_{\gamma\beta}$ and $\mathbf{F}_{\beta\gamma}$ given by

$$
\frac{1}{V_\gamma}\int\limits_{A_{\gamma\sigma}+A_{\beta\gamma}} \mathbf{n}_\gamma\cdot(-\mathbf{I}\mathbf{a}_{\gamma\beta 2} + \nabla\mathbf{A}_{\gamma\beta 2})\,dA = -\varepsilon_\beta \mathbf{K}_\gamma^{-1}\cdot\mathbf{F}_{\gamma\beta} \tag{112}
$$

and

$$
\frac{1}{V_\beta}\int\limits_{A_{\beta\sigma}+A_{\beta\gamma}} \mathbf{n}_\beta\cdot(-\mathbf{I}\mathbf{a}_{\beta\gamma 2} + \nabla\mathbf{A}_{\beta\gamma 2})\,dA = -\varepsilon_\gamma \mathbf{K}_\beta^{-1}\cdot\mathbf{F}_{\beta\gamma} \tag{113}
$$

It shall be noted that the resolution of the microscopic flow problem is required prior to that of the four boundary value problems described above and allowing the determination of the eight permeability

and inertial correction tensors. On the one hand, the solution of the microscopic flow provides the location of the $A_{\beta\gamma}$ interface necessary to solve the four problems I1, II1, I2 and II2, noting that problems I1 and II1 are purely geometrical ones. On the other hand, it provides the microscopic velocity fields $\mathbf{v}_\beta$ and $\mathbf{v}_\gamma$ necessary to solve problems I2 and II2.

At this point, we are in position to move on to the macroscopic closed form of the inertial two-phase flow process under consideration.

5 Macroscopic equations

Before introducing the representations of the deviations as functions of the average velocities in the average momentum equations, macroscopic acceleration and convective inertial terms in these last equations need to be reinspected. This is motivated by the time-scale constraint introduced in equation (70) as a requirement to simplify the closure problem. In addition, our interest is to examine the conditions under which macroscopic inertial terms are significant. To do so, we recall the average momentum equation in its last version of equation (41) as

$$\begin{aligned}\rho_\beta \frac{\partial \langle \mathbf{v}_\beta \rangle^\beta}{\partial t} + \rho_\beta \langle \mathbf{v}_\beta \rangle^\beta \cdot \nabla \langle \mathbf{v}_\beta \rangle^\beta + \rho_\beta \varepsilon_\beta^{-1} \nabla \cdot \langle \tilde{\mathbf{v}}_\beta \tilde{\mathbf{v}}_\beta \rangle \\ = -\nabla \langle p_\beta \rangle^\beta + \rho_\beta \mathbf{g} \\ + \frac{1}{V_\beta} \int\limits_{A_{\beta\sigma}+A_{\beta\gamma}} \mathbf{n}_\beta \cdot (-\mathbf{I}\tilde{p}_\beta + \mu_\beta \nabla \tilde{\mathbf{v}}_\beta) dA \end{aligned} \tag{114}$$

The order of magnitude of the two macroscopic inertial terms is the same and, on the basis of equation (37), is given by

$$\rho_\beta \langle \mathbf{v}_\beta \rangle^\beta \cdot \nabla \langle \mathbf{v}_\beta \rangle^\beta = O\left(\frac{\rho_\beta \left\| \langle \mathbf{v}_\beta \rangle^\beta \right\|^2}{L} \right) \tag{115}$$

$$\rho_\beta \varepsilon_\beta^{-1} \nabla \cdot \langle \tilde{\mathbf{v}}_\beta \tilde{\mathbf{v}}_\beta \rangle = O\left(\frac{\rho_\beta \left\| \langle \mathbf{v}_\beta \rangle^\beta \right\|^2}{L} \right) \tag{116}$$

Recalling equation (38), the order of magintude of the interfacial normal viscous stress term is

$$\frac{\mu_\beta}{V_\beta} \int\limits_{A_{\beta\sigma}+A_{\beta\gamma}} \mathbf{n}_\beta \cdot \nabla \tilde{\mathbf{v}}_\beta dA = \mathbf{O}\left(\frac{\mu_\beta \langle \mathbf{v}_\beta \rangle^\beta}{l_\beta^2} \right) \tag{117}$$

Clearly, the two macroscopic inertial terms are negligible in comparison to this last integral term in the averaged momentum equations when the following constraint is satisfied

$$\max_{\alpha=\beta,\ \gamma} \left(\frac{\rho_\alpha \left\| \langle \mathbf{v}_\alpha \rangle^\alpha \right\| l_\alpha}{\mu_\alpha} \frac{l_\alpha}{L} \right) \ll 1 \tag{118}$$

From a practical point of view, a safe constraint would be

$$\frac{l}{L} \max_{\alpha=\beta,\ \gamma} \left(\frac{\mathrm{Re}_\alpha}{\varepsilon_\alpha} \right) \ll 1 \tag{119}$$

where Re_α is a Reynolds number based on the mean pore-size l, associated to the α-phase and defined by

$$\mathrm{Re}_\alpha = \frac{\rho_\alpha \left\| \langle \mathbf{v}_\alpha \rangle \right\| l}{\mu_\alpha} \tag{120}$$

Under this constraint, the macroscopic momentum balance equation can be written as

$$\rho_\beta \frac{\partial \langle \mathbf{v}_\beta \rangle^\beta}{\partial t} = -\nabla \langle p_\beta \rangle^\beta + \rho_\beta \mathbf{g} + \frac{1}{V_\beta} \int\limits_{A_{\beta\sigma}+A_{\beta\gamma}} \mathbf{n}_\beta \cdot (-\mathbf{I}\tilde{p}_\beta + \mu_\beta \nabla \tilde{\mathbf{v}}_\beta) dA \tag{121}$$

We now turn our attention to the acceleration term and consider its order of magnitude which is given by

$$\rho_\beta \frac{\partial \langle \mathbf{v}_\beta \rangle^\beta}{\partial t} = \mathbf{O}\left(\frac{\rho_\beta \langle \mathbf{v}_\beta \rangle^\beta}{t^*} \right) \tag{122}$$

Under the constraint already indicated by equation (65), i.e.

$$t^* \gg \max_{\alpha=\beta,\ \gamma} \left(\frac{\rho_\alpha l_\alpha^2}{\mu_\alpha} \right) \tag{123}$$

it can be clearly seen that

$$\rho_\beta \frac{\partial \langle \mathbf{v}_\beta \rangle^\beta}{\partial t} \ll \frac{\mu_\beta}{V_\beta} \int\limits_{A_{\beta\sigma}+A_{\beta\gamma}} \mathbf{n}_\beta \cdot \nabla \tilde{\mathbf{v}}_\beta dA \tag{124}$$

so that the average momentum equation is finally

$$0 = -\nabla \langle p_\beta \rangle^\beta + \rho_\beta \mathbf{g} + \frac{1}{V_\beta} \int\limits_{A_{\beta\sigma}+A_{\beta\gamma}} \mathbf{n}_\beta \cdot (-\mathbf{I}\tilde{p}_\beta + \mu_\beta \nabla \tilde{\mathbf{v}}_\beta) dA \tag{125}$$

We are now ready to obtain the closed form by introducing the representations of the deviations detailed above in this last equation. This yields

$$\begin{aligned} 0 = &-\nabla \langle p_\beta \rangle^\beta + \rho_\beta \mathbf{g} \\ &+\mu_\beta \left\{ \frac{1}{V_\beta} \int\limits_{A_{\beta\sigma}+A_{\beta\gamma}} \mathbf{n}_\beta \cdot (-\mathbf{I}\mathbf{a}_{\beta\beta 1} + \nabla \mathbf{A}_{\beta\beta 1}) dA \right\} \cdot \langle \mathbf{v}_\beta \rangle^\beta \\ &+\mu_\beta \left\{ \frac{1}{V_\beta} \int\limits_{A_{\beta\sigma}+A_{\beta\gamma}} \mathbf{n}_\beta \cdot (-\mathbf{I}\mathbf{a}_{\beta\beta 2} + \nabla \mathbf{A}_{\beta\beta 2})\, dA \right\} \cdot \langle \mathbf{v}_\beta \rangle^\beta \\ &+\mu_\beta \left\{ \frac{1}{V_\beta} \int\limits_{A_{\beta\sigma}+A_{\beta\gamma}} \mathbf{n}_\beta \cdot (-\mathbf{I}\mathbf{a}_{\beta\gamma 1} + \nabla \mathbf{A}_{\beta\gamma 1}) dA \right\} \cdot \langle \mathbf{v}_\gamma \rangle^\gamma \\ &+\mu_\beta \left\{ \frac{1}{V_\beta} \int\limits_{A_{\beta\sigma}+A_{\beta\gamma}} \mathbf{n}_\beta \cdot (-\mathbf{I}\mathbf{a}_{\beta\gamma 2} + \nabla \mathbf{A}_{\beta\gamma 2})\, dA \right\} \cdot \langle \mathbf{v}_\gamma \rangle^\gamma \end{aligned} \tag{126}$$

where all the area integrals can be identified from the definitions of the permeability, viscous drag and inertial correction tensors. Using the relationships (104) through (107) and (110) through (113), we can write

$$\begin{aligned} 0 \quad = \quad & -\nabla\langle p_\beta\rangle^\beta + \rho_\beta \mathbf{g} \\ & -\mu_\beta \mathbf{K}_\beta^{-1}\cdot\langle \mathbf{v}_\beta\rangle - \mu_\beta \mathbf{K}_\beta^{-1}\cdot\mathbf{F}_\beta\cdot\langle \mathbf{v}_\beta\rangle \\ & +\mu_\beta \mathbf{K}_\beta^{-1}\cdot\mathbf{K}_{\beta\gamma}\cdot\langle \mathbf{v}_\gamma\rangle - \mu_\beta \mathbf{K}_\beta^{-1}\cdot\mathbf{F}_{\beta\gamma}\cdot\langle \mathbf{v}_\gamma\rangle \end{aligned} \tag{127}$$

Rearranging, this gives

$$\langle \mathbf{v}_\beta\rangle = -\frac{\mathbf{K}_\beta}{\mu_\beta}\cdot\left(\nabla\langle p_\beta\rangle^\beta - \rho_\beta\mathbf{g}\right) - \mathbf{F}_\beta\cdot\langle \mathbf{v}_\beta\rangle + \mathbf{K}_{\beta\gamma}\cdot\langle \mathbf{v}_\gamma\rangle - \mathbf{F}_{\beta\gamma}\cdot\langle \mathbf{v}_\gamma\rangle \tag{128}$$

which represents our final macroscopic momentum balance equation for two-phase inertial flow in homogeneous porous media under all the constraints detailed in the course of the development. The analogue form in the γ-phase is

$$\langle \mathbf{v}_\gamma\rangle = -\frac{\mathbf{K}_\gamma}{\mu_\gamma}\cdot\left(\nabla\langle p_\gamma\rangle^\gamma - \rho_\gamma\mathbf{g}\right) - \mathbf{F}_\gamma\cdot\langle \mathbf{v}_\gamma\rangle + \mathbf{K}_{\gamma\beta}\cdot\langle \mathbf{v}_\beta\rangle - \mathbf{F}_{\gamma\beta}\cdot\langle \mathbf{v}_\beta\rangle \tag{129}$$

If inertial effects are absent, these equations have the same form as those obtained for two-phase creeping flow in homogeneous porous madia, i.e. (Whitaker, 1994)

$$\langle \mathbf{v}_\alpha\rangle = -\frac{\mathbf{K}_\alpha}{\mu_\alpha}\cdot\left(\nabla\langle p_\alpha\rangle^\alpha - \rho_\alpha\mathbf{g}\right) + \mathbf{K}_{\alpha\kappa}\cdot\langle \mathbf{v}_\kappa\rangle \qquad \alpha,\,\kappa=\beta,\,\gamma \qquad \alpha\neq\kappa \tag{130}$$

The importance of the viscous coupling present in such a model has been the subject of active work (Kalaydjian, 1990; Rose, 1989; Zarcone, 1994) and an order of magnitude was developed in Whitaker (1994) leading to $\mathbf{K}_{\beta\gamma}\cdot\mathbf{K}_{\gamma\beta} = \mathbf{O}(\mathbf{I})$. Later, Lasseux et al. (1996) derived an exact relationship between these two tensors given by

$$\mu_\beta \mathbf{K}_{\beta\gamma}\cdot\mathbf{K}_\gamma = \mu_\gamma \mathbf{K}_\beta\cdot\mathbf{K}_{\gamma\beta}^T \tag{131}$$

In the same reference, it was shown that a more convenient form than that of equation (130) is

$$\langle \mathbf{v}_\alpha\rangle = -\frac{\mathbf{K}^*_{\alpha\alpha}}{\mu_\alpha}\cdot\left(\nabla\langle p_\alpha\rangle^\alpha - \rho_\alpha\mathbf{g}\right) - \mathbf{K}^*_{\alpha\kappa}\cdot\left(\nabla\langle p_\kappa\rangle^\kappa - \rho_\kappa\mathbf{g}\right) \qquad \alpha,\,\kappa=\beta,\,\gamma \qquad \alpha\neq\kappa \tag{132}$$

in accordance with a result obtained by the homogenization technique (Auriault, 1987). The dominant and coupling permeability tensors $\mathbf{K}^*_{\alpha\alpha}$ and $\mathbf{K}^*_{\alpha\kappa}$ ($\alpha,\,\kappa=\beta,\,\gamma;\ \alpha\neq\kappa$) appearing in this last equation are related to the tensors of equation (130) by

$$\mathbf{K}^*_{\alpha\alpha} = \left(\mathbf{I} - \mathbf{K}_{\alpha\kappa}\cdot\mathbf{K}_{\kappa\alpha}\right)^{-1}\cdot\mathbf{K}_\alpha \qquad \alpha,\,\kappa=\beta,\,\gamma \qquad \alpha\neq\kappa \tag{133}$$

$$\mathbf{K}^*_{\alpha\kappa} = \left(\mathbf{I} - \mathbf{K}_{\alpha\kappa}\cdot\mathbf{K}_{\kappa\alpha}\right)^{-1}\cdot\left(\mathbf{K}_{\alpha\kappa}\cdot\mathbf{K}_\kappa\right) \qquad \alpha,\,\kappa=\beta,\,\gamma \qquad \alpha\neq\kappa \tag{134}$$

and are given by closure problems that are recalled in appendix 2 of this paper. These closure problems are rearranged versions of problems I1 and II1 given by equations (102) and (103). Following the same lines, we shall prefer the following macroscopic momentum equation in the case under study in the present work

$$\begin{aligned}\langle \mathbf{v}_\beta \rangle &= -\frac{\mathbf{K}^*_{\beta\beta}}{\mu_\beta}(\nabla \langle p_\beta \rangle^\beta - \rho_\beta \mathbf{g}) - \mathbf{F}_\beta \cdot \langle \mathbf{v}_\beta \rangle \\ &\quad -\frac{\mathbf{K}^*_{\beta\gamma}}{\mu_\gamma}(\nabla \langle p_\gamma \rangle^\gamma - \rho_\gamma \mathbf{g}) - \mathbf{F}_{\beta\gamma} \cdot \langle \mathbf{v}_\gamma \rangle \end{aligned} \tag{135}$$

and its equivalent in the γ-phase

$$\begin{aligned}\langle \mathbf{v}_\gamma \rangle &= -\frac{\mathbf{K}^*_{\gamma\gamma}}{\mu_\gamma}(\nabla \langle p_\gamma \rangle^\gamma - \rho_\gamma \mathbf{g}) - \mathbf{F}_\gamma \cdot \langle \mathbf{v}_\gamma \rangle \\ &\quad -\frac{\mathbf{K}^*_{\gamma\beta}}{\mu_\beta}(\nabla \langle p_\beta \rangle^\beta - \rho_\beta \mathbf{g}) - \mathbf{F}_{\gamma\beta} \cdot \langle \mathbf{v}_\beta \rangle \end{aligned} \tag{136}$$

In the next section, we provide alternate versions of the closure problems the solutions of which are required to find the inertial correction tensors.

6 Obtention procedure of the F tensors

In this section we present a more tractable form of the boundary value problems that are to be solved to determine the four inertial tensors $\mathbf{F}_\beta$, $\mathbf{F}_\gamma$, $\mathbf{F}_{\beta\gamma}$ and $\mathbf{F}_{\gamma\beta}$. Rather than starting from the closure problems I2 and II2 given by equations (108) and (109), it is more convenient to start from the forms I and II of equations (92) and (93) and we recall them as

Problem I

$$(\rho_\beta \mathbf{v}_\beta/\mu_\beta) \cdot \nabla \mathbf{A}_{\beta\beta} = -\nabla \mathbf{a}_{\beta\beta} + \nabla^2 \mathbf{A}_{\beta\beta} + \varepsilon_\beta \mathbf{H}_\beta^{-1} \qquad \text{in } V_\beta \tag{137a}$$

$$\nabla \cdot \mathbf{A}_{\beta\beta} = 0 \qquad \text{in } V_\beta \tag{137b}$$

$$\text{BC1} \quad \mathbf{A}_{\beta\beta} = -\mathbf{I} \qquad \text{at } A_{\beta\sigma} \tag{137c}$$

$$\text{BC2} \quad \mathbf{A}_{\beta\beta} = \mathbf{A}_{\gamma\beta} - \mathbf{I} \qquad \text{at } A_{\beta\gamma} \tag{137d}$$

$$\begin{aligned}&\text{BC3} \quad \mu_\beta \mathbf{n}_{\beta\gamma} \cdot \left[-\mathbf{I}\mathbf{a}_{\beta\beta} + (\nabla \mathbf{A}_{\beta\beta} + \nabla \mathbf{A}_{\beta\beta}^T)\right] \\ &= \mu_\gamma \mathbf{n}_{\beta\gamma} \cdot \left[-\mathbf{I}\mathbf{a}_{\gamma\beta} + (\nabla \mathbf{A}_{\gamma\beta} + \nabla \mathbf{A}_{\gamma\beta}^T)\right] \qquad \text{at } A_{\beta\gamma}\end{aligned} \tag{137e}$$

$$\text{BC4} \quad \mathbf{A}_{\gamma\beta} = 0 \qquad \text{at } A_{\gamma\sigma} \tag{137f}$$

$$(\rho_\gamma \mathbf{v}_\gamma/\mu_\gamma) \cdot \nabla \mathbf{A}_{\gamma\beta} = -\nabla \mathbf{a}_{\gamma\beta} + \nabla^2 \mathbf{A}_{\gamma\beta} - \varepsilon_\beta \mathbf{K}_\gamma^{-1} \cdot \mathbf{H}_{\gamma\beta} \qquad \text{in } V_\gamma \tag{137g}$$

$$\nabla \cdot \mathbf{A}_{\gamma\beta} = 0 \qquad \text{in } V_\gamma \tag{137h}$$

Periodicity

$$\mathbf{a}_{\beta\beta}(\mathbf{r} + \mathbf{l}_i) = \mathbf{a}_{\beta\beta}(\mathbf{r}) \qquad \mathbf{a}_{\gamma\beta}(\mathbf{r} + \mathbf{l}_i) = \mathbf{a}_{\gamma\beta}(\mathbf{r}) \qquad i = 1, 2, 3 \tag{137i}$$

$$\mathbf{A}_{\beta\beta}(\mathbf{r} + \mathbf{l}_i) = \mathbf{A}_{\beta\beta}(\mathbf{r}) \qquad \mathbf{A}_{\gamma\beta}(\mathbf{r} + \mathbf{l}_i) = \mathbf{A}_{\gamma\beta}(\mathbf{r}) \qquad i = 1, 2, 3 \tag{137j}$$

Average

$$\langle \mathbf{A}_{\beta\beta} \rangle^\beta = 0 \qquad \langle \mathbf{A}_{\gamma\beta} \rangle^\gamma = 0 \tag{137k}$$

Problem II

$$(\rho_\beta \mathbf{v}_\beta/\mu_\beta)\cdot\nabla\mathbf{A}_{\beta\gamma} = -\nabla\mathbf{a}_{\beta\gamma} + \nabla^2\mathbf{A}_{\beta\gamma} - \varepsilon_\gamma\mathbf{K}_\beta^{-1}\cdot\mathbf{H}_{\beta\gamma} \qquad \text{in } V_\beta \tag{138a}$$

$$\nabla\cdot\mathbf{A}_{\beta\gamma} = 0 \qquad \text{in } V_\beta \tag{138b}$$

$$\text{BC1} \quad \mathbf{A}_{\beta\gamma} = 0 \qquad \text{at } A_{\beta\sigma} \tag{138c}$$

$$\text{BC2} \quad \mathbf{A}_{\beta\gamma} = \mathbf{A}_{\gamma\gamma} + \mathbf{I} \qquad \text{at } A_{\beta\gamma} \tag{138d}$$

$$\text{BC3} \quad \mu_\beta \mathbf{n}_{\beta\gamma}\cdot\left[-\mathbf{I}a_{\beta\gamma} + (\nabla\mathbf{A}_{\beta\gamma} + \nabla\mathbf{A}_{\beta\gamma}^T)\right]$$
$$= \mu_\gamma \mathbf{n}_{\beta\gamma}\cdot\left[-\mathbf{I}a_{\gamma\gamma} + (\nabla\mathbf{A}_{\gamma\gamma} + \nabla\mathbf{A}_{\gamma\gamma}^T)\right] \qquad \text{at } A_{\beta\gamma} \tag{138e}$$

$$\text{BC4} \quad \mathbf{A}_{\gamma\gamma} = -\mathbf{I} \qquad \text{at } A_{\gamma\sigma} \tag{138f}$$

$$(\rho_\gamma \mathbf{v}_\gamma/\mu_\gamma)\cdot\nabla\mathbf{A}_{\gamma\gamma} = -\nabla\mathbf{a}_{\gamma\gamma} + \nabla^2\mathbf{A}_{\gamma\gamma} + \varepsilon_\gamma\mathbf{H}_\gamma^{-1} \qquad \text{in } V_\gamma \tag{138g}$$

$$\nabla\cdot\mathbf{A}_{\gamma\gamma} = 0 \qquad \text{in } V_\gamma \tag{138h}$$

Periodicity

$$\mathbf{a}_{\beta\gamma}(\mathbf{r}+\mathbf{l}_i) = \mathbf{a}_{\beta\gamma}(\mathbf{r}) \qquad \mathbf{a}_{\gamma\gamma}(\mathbf{r}+\mathbf{l}_i) = \mathbf{a}_{\gamma\gamma}(\mathbf{r}) \qquad i = 1,2,3 \tag{138i}$$

$$\mathbf{A}_{\beta\gamma}(\mathbf{r}+\mathbf{l}_i) = \mathbf{A}_{\beta\gamma}(\mathbf{r}) \qquad \mathbf{A}_{\gamma\gamma}(\mathbf{r}+\mathbf{l}_i) = \mathbf{A}_{\gamma\gamma}(\mathbf{r}) \qquad i = 1,2,3 \tag{138j}$$

Average

$$\langle\mathbf{A}_{\beta\gamma}\rangle^\beta = 0 \qquad \langle\mathbf{A}_{\gamma\gamma}\rangle^\gamma = 0 \tag{138k}$$

Here, we have used the tensors $\mathbf{H}_\beta$, $\mathbf{H}_{\gamma\beta}$, $\mathbf{H}_\gamma$, and $\mathbf{H}_{\beta\gamma}$ defined by

$$\varepsilon_\beta\mathbf{H}_\beta^{-1} = -\frac{1}{V_\beta}\int\limits_{A_{\beta\sigma}+A_{\beta\gamma}} \mathbf{n}_\beta\cdot(-\mathbf{I}a_{\beta\beta} + \nabla\mathbf{A}_{\beta\beta})dA \tag{139}$$

$$\varepsilon_\beta\mathbf{K}_\gamma^{-1}\cdot\mathbf{H}_{\gamma\beta} = \frac{1}{V_\gamma}\int\limits_{A_{\gamma\sigma}+A_{\beta\gamma}} \mathbf{n}_\gamma\cdot(-\mathbf{I}a_{\gamma\beta} + \nabla\mathbf{A}_{\gamma\beta})dA \tag{140}$$

$$\varepsilon_\gamma\mathbf{K}_\beta^{-1}\cdot\mathbf{H}_{\beta\gamma} = \frac{1}{V_\beta}\int\limits_{A_{\beta\sigma}+A_{\beta\gamma}} \mathbf{n}_\beta\cdot(-\mathbf{I}a_{\beta\gamma} + \nabla\mathbf{A}_{\beta\gamma})dA \tag{141}$$

$$\varepsilon_\gamma\mathbf{H}_\gamma^{-1} = -\frac{1}{V_\gamma}\int\limits_{A_{\gamma\sigma}+A_{\beta\gamma}} \mathbf{n}_\gamma\cdot(-\mathbf{I}a_{\gamma\gamma} + \nabla\mathbf{A}_{\gamma\gamma})dA \tag{142}$$

and it shall be noted that

$$\mathbf{H}_\beta^{-1} = \mathbf{K}_\beta^{-1}\cdot(\mathbf{I}+\mathbf{F}_\beta) \tag{143}$$

$$\mathbf{H}_{\gamma\beta} = \mathbf{K}_{\gamma\beta} - \mathbf{F}_{\gamma\beta} \tag{144}$$

$$\mathbf{H}_{\beta\gamma} = \mathbf{K}_{\beta\gamma} - \mathbf{F}_{\beta\gamma} \tag{145}$$

$$\mathbf{H}_\gamma^{-1} = \mathbf{K}_\gamma^{-1}\cdot(\mathbf{I}+\mathbf{F}_\gamma) \tag{146}$$

Under their initial forms, these two problems are integro-differential ones and simpler versions are desirable for tractable resolution. This can be performed by setting

$$\mathbf{A}_{\beta\beta} = -\mathbf{I} - \varepsilon_\beta \left[\mathbf{A}^{\mathbf{0}}_{\beta\beta} \cdot \mathbf{H}_\beta^{-1} - \mathbf{A}^{\mathbf{0}}_{\beta\gamma} \cdot \left(\mathbf{K}_\gamma^{-1} \cdot \mathbf{H}_{\gamma\beta} \right) \right] \tag{147}$$

$$\mathbf{a}_{\beta\beta} = -\varepsilon_\beta \left[\mathbf{a}^{\mathbf{0}}_{\beta\beta} \cdot \mathbf{H}_\beta^{-1} - \mathbf{a}^{\mathbf{0}}_{\beta\gamma} \cdot \left(\mathbf{K}_\gamma^{-1} \cdot \mathbf{H}_{\gamma\beta} \right) \right] \tag{148}$$

$$\mathbf{A}_{\gamma\beta} = -\varepsilon_\beta \left[\mathbf{A}^{\mathbf{0}}_{\gamma\beta} \cdot \mathbf{H}_\beta^{-1} - \mathbf{A}^{\mathbf{0}}_{\gamma\gamma} \cdot \left(\mathbf{K}_\gamma^{-1} \cdot \mathbf{H}_{\gamma\beta} \right) \right] \tag{149}$$

$$\mathbf{a}_{\gamma\beta} = -\varepsilon_\beta \left[\mathbf{a}^{\mathbf{0}}_{\gamma\beta} \cdot \mathbf{H}_\beta^{-1} - \mathbf{a}^{\mathbf{0}}_{\gamma\gamma} \cdot \left(\mathbf{K}_\gamma^{-1} \cdot \mathbf{H}_{\gamma\beta} \right) \right] \tag{150}$$

and

$$\mathbf{A}_{\gamma\gamma} = -\mathbf{I} - \varepsilon_\gamma \left[\mathbf{A}^{\mathbf{0}}_{\gamma\gamma} \cdot \mathbf{H}_\gamma^{-1} - \mathbf{A}^{\mathbf{0}}_{\gamma\beta} \cdot \left(\mathbf{K}_\beta^{-1} \cdot \mathbf{H}_{\beta\gamma} \right) \right] \tag{151}$$

$$\mathbf{a}_{\gamma\gamma} = -\varepsilon_\gamma \left[\mathbf{a}^{\mathbf{0}}_{\gamma\gamma} \cdot \mathbf{H}_\gamma^{-1} - \mathbf{A}^{\mathbf{0}}_{\gamma\beta} \cdot \left(\mathbf{K}_\beta^{-1} \cdot \mathbf{H}_{\beta\gamma} \right) \right] \tag{152}$$

$$\mathbf{A}_{\beta\gamma} = -\varepsilon_\gamma \left[\mathbf{A}^{\mathbf{0}}_{\beta\gamma} \cdot \mathbf{H}_\gamma^{-1} - \mathbf{A}^{\mathbf{0}}_{\beta\beta} \cdot \left(\mathbf{K}_\beta^{-1} \cdot \mathbf{H}_{\beta\gamma} \right) \right] \tag{153}$$

$$\mathbf{a}_{\beta\gamma} = -\varepsilon_\gamma \left[\mathbf{a}^{\mathbf{0}}_{\beta\gamma} \cdot \mathbf{H}_\gamma^{-1} - \mathbf{a}^{\mathbf{0}}_{\beta\beta} \cdot \left(\mathbf{K}_\beta^{-1} \cdot \mathbf{H}_{\beta\gamma} \right) \right] \tag{154}$$

When these decompositions are replaced in the above problems I and II, and because of the absence of the curvature in the normal stress jump boundary condition at $A_{\beta\gamma}$, the two following forms of the closure problems can be used to compute the inertial correction tensors

Problem I(a)

$$(\rho_\beta \mathbf{v}_\beta / \mu_\beta) \cdot \nabla \mathbf{A}^0_{\beta\beta} = -\nabla \mathbf{a}^0_{\beta\beta} + \nabla^2 \mathbf{A}^0_{\beta\beta} - \mathbf{I} \qquad \text{in } V_\beta \tag{155a}$$

$$\nabla \cdot \mathbf{A}^0_{\beta\beta} = 0 \qquad \text{in } V_\beta \tag{155b}$$

$$\text{BC1} \qquad \mathbf{A}^0_{\beta\beta} = 0 \qquad \text{at } A_{\beta\sigma} \tag{155c}$$

$$\text{BC2} \qquad \mathbf{A}^0_{\beta\beta} = \mathbf{A}^0_{\gamma\beta} \qquad \text{at } A_{\beta\gamma} \tag{155d}$$

$$\text{BC3} \qquad \mu_\beta \mathbf{n}_{\beta\gamma} \cdot \left[-\mathbf{I}\mathbf{a}^0_{\beta\beta} + (\nabla \mathbf{A}^0_{\beta\beta} + \nabla \mathbf{A}^{0T}_{\beta\beta}) \right]$$
$$= \mu_\gamma \mathbf{n}_{\beta\gamma} \cdot \left[-\mathbf{I}\mathbf{a}^0_{\gamma\beta} + (\nabla \mathbf{A}^0_{\gamma\beta} + \nabla \mathbf{A}^{0T}_{\gamma\beta}) \right] \qquad \text{at } A_{\beta\gamma} \tag{155e}$$

$$\text{BC4} \qquad \mathbf{A}^0_{\gamma\beta} = 0 \qquad \text{at } A_{\gamma\sigma} \tag{155f}$$

$$(\rho_\gamma \mathbf{v}_\gamma / \mu_\gamma) \cdot \nabla \mathbf{A}^0_{\gamma\beta} = -\nabla \mathbf{a}^0_{\gamma\beta} + \nabla^2 \mathbf{A}^0_{\gamma\beta} \qquad \text{in } V_\gamma \tag{155g}$$

$$\nabla \cdot \mathbf{A}^0_{\gamma\beta} = 0 \qquad \text{in } V_\gamma \tag{155h}$$

Periodicity

$$\mathbf{a}^0_{\beta\beta}(\mathbf{r} + \mathbf{l}_i) = \mathbf{a}^0_{\beta\beta}(\mathbf{r}) \qquad \mathbf{a}^0_{\gamma\beta}(\mathbf{r} + \mathbf{l}_i) = \mathbf{a}^0_{\gamma\beta}(\mathbf{r}) \qquad i = 1, 2, 3 \tag{155i}$$

$$\mathbf{A}^0_{\beta\beta}(\mathbf{r} + \mathbf{l}_i) = \mathbf{A}^0_{\beta\beta}(\mathbf{r}) \qquad \mathbf{A}^0_{\gamma\beta}(\mathbf{r} + \mathbf{l}_i) = \mathbf{A}^0_{\gamma\beta}(\mathbf{r}) \qquad i = 1, 2, 3 \tag{155j}$$

Problem II(a)

$$(\rho_\beta \mathbf{v}_\beta/\mu_\beta)\cdot\nabla\mathbf{A}^0_{\beta\gamma} = -\nabla\mathbf{a}^0_{\beta\gamma} + \nabla^2\mathbf{A}^0_{\beta\gamma} \qquad \text{in } V_\beta \tag{156a}$$

$$\nabla\cdot\mathbf{A}^0_{\beta\gamma} = 0 \qquad \text{in } V_\beta \tag{156b}$$

$$\text{BC1} \qquad \mathbf{A}^0_{\beta\gamma} = 0 \qquad \text{at } A_{\beta\sigma} \tag{156c}$$

$$\text{BC2} \qquad \mathbf{A}^0_{\beta\gamma} = \mathbf{A}^0_{\gamma\gamma} \qquad \text{at } A_{\beta\gamma} \tag{156d}$$

$$\text{BC3} \qquad \mu_\beta \mathbf{n}_{\beta\gamma}\cdot\left[-\mathbf{I}\mathbf{a}^0_{\beta\gamma} + (\nabla\mathbf{A}^0_{\beta\gamma} + \nabla\mathbf{A}^{0T}_{\beta\gamma})\right]$$

$$= \mu_\gamma \mathbf{n}_{\beta\gamma}\cdot\left[-\mathbf{I}\mathbf{a}^0_{\gamma\gamma} + (\nabla\mathbf{A}^0_{\gamma\gamma} + \nabla\mathbf{A}^{0T}_{\gamma\gamma})\right] \qquad \text{at } A_{\beta\gamma} \tag{156e}$$

$$\text{BC4} \qquad \mathbf{A}^0_{\gamma\gamma} = 0 \qquad \text{at } A_{\gamma\sigma} \tag{156f}$$

$$(\rho_\gamma \mathbf{v}_\gamma/\mu_\gamma)\cdot\nabla\mathbf{A}^0_{\gamma\gamma} = -\nabla\mathbf{a}^0_{\gamma\gamma} + \nabla^2\mathbf{A}^0_{\gamma\gamma} - \mathbf{I} \qquad \text{in } V_\gamma \tag{156g}$$

$$\nabla\cdot\mathbf{A}^0_{\gamma\gamma} = 0 \qquad \text{in } V_\gamma \tag{156h}$$

Periodicity

$$\mathbf{a}^0_{\beta\gamma}(\mathbf{r}+\mathbf{l}_i) = \mathbf{a}^0_{\beta\gamma}(\mathbf{r}) \qquad \mathbf{a}^0_{\gamma\gamma}(\mathbf{r}+\mathbf{l}_i) = \mathbf{a}^0_{\gamma\gamma}(\mathbf{r}) \qquad i = 1,2,3 \tag{156i}$$

$$\mathbf{A}^0_{\beta\gamma}(\mathbf{r}+\mathbf{l}_i) = \mathbf{A}^0_{\beta\gamma}(\mathbf{r}) \qquad \mathbf{A}^0_{\gamma\gamma}(\mathbf{r}+\mathbf{l}_i) = \mathbf{A}^0_{\gamma\gamma}(\mathbf{r}) \qquad i = 1,2,3 \tag{156j}$$

Averages

$$\mathbf{H}_\beta = \varepsilon_\beta\left(\left\langle\mathbf{A}^0_{\beta\gamma}\right\rangle^\beta\cdot\left\langle\mathbf{A}^0_{\gamma\gamma}\right\rangle^{\gamma^{-1}}\cdot\left\langle\mathbf{A}^0_{\gamma\beta}\right\rangle^\gamma - \left\langle\mathbf{A}^0_{\beta\beta}\right\rangle^\beta\right) \tag{157}$$

$$\mathbf{H}_{\gamma\beta} = \mathbf{K}_\gamma\cdot\left\langle\mathbf{A}^0_{\gamma\gamma}\right\rangle^{\gamma^{-1}}\cdot\left\langle\mathbf{A}^0_{\gamma\beta}\right\rangle^\gamma\cdot\mathbf{H}_\beta^{-1} \tag{158}$$

$$\mathbf{H}_\gamma = \varepsilon_\gamma\left(\left\langle\mathbf{A}^0_{\gamma\beta}\right\rangle^\gamma\cdot\left\langle\mathbf{A}^0_{\beta\beta}\right\rangle^{\beta^{-1}}\cdot\left\langle\mathbf{A}^0_{\beta\gamma}\right\rangle^\beta - \left\langle\mathbf{A}^0_{\gamma\gamma}\right\rangle^\gamma\right) \tag{159}$$

$$\mathbf{H}_{\beta\gamma} = \mathbf{K}_\beta\cdot\left\langle\mathbf{A}^0_{\beta\beta}\right\rangle^{\beta^{-1}}\cdot\left\langle\mathbf{A}^0_{\beta\gamma}\right\rangle^\beta\cdot\mathbf{H}_\gamma^{-1} \tag{160}$$

Each of these two problems has basically a structure equivalent to that of an incompressible Navier-Stokes two-phase flow without any dependence on the curvature of the fluid-fluid interface. When a solver is available to compute the initial microscopic physical flow problem, the solution of which includes the location of the interface as well as the determination of $\mathbf{v}_\beta$ and $\mathbf{v}_\gamma$, the same solver can be used to solve problems I(a) and II(a) of equations (155) and (156) and determine the four tensors $\mathbf{H}_\beta$, $\mathbf{H}_{\gamma\beta}$, $\mathbf{H}_\gamma$ and $\mathbf{H}_{\beta\gamma}$. Note that the computation of these four tensors requires $\mathbf{K}_\beta$ and $\mathbf{K}_\gamma$ that can be obtained according to the procedure provided in appendix 2 of this paper. Finally, the inertial correction tensors are obtained by making use of the relations (143) through (146), i.e.

$$\mathbf{F}_\beta = \mathbf{K}_\beta\cdot\mathbf{H}_\beta^{-1} - \mathbf{I} \tag{161}$$

$$\mathbf{F}_{\gamma\beta} = \mathbf{K}_{\gamma\beta} - \mathbf{H}_{\gamma\beta} \tag{162}$$

$$\mathbf{F}_\gamma = \mathbf{K}_\gamma\cdot\mathbf{H}_\gamma^{-1} - \mathbf{I} \tag{163}$$

$$\mathbf{F}_{\beta\gamma} = \mathbf{K}_{\beta\gamma} - \mathbf{H}_{\beta\gamma} \tag{164}$$

In these last relationships, $\mathbf{K}_{\gamma\beta}$ and $\mathbf{K}_{\beta\gamma}$ are the two viscous drag tensors obtained from the solution of the boundary value problems also given in appendix 2.

7 Conclusions

In this work, we have derived the macroscopic model for inertial two-phase, incompressible, Newtonian fluid flow through homogenous porous media. The validity of this model is subject to constraints on the length-scales and time-scales as well as on quantities involving the capillary, Reynolds and Weber numbers and assumes that fluctuations of the curvature of the fluid-flluid interface are unimportant over the unit cell representing the porous medium. The averaged continuity equation takes the same form as that obtained when inertia is negligible. The averaged momentum balance equations are those obtained without inertia corrected by two inertial terms. Each of these terms involves an inertial correction tensor. The two pairs of boundary value problems yielding the permeability and inertial correction tensors have been provided in simple enough versions for their solutions to be tractable using a two-phase Navier-Stokes solver. Numerical results are necessary to estimate each of the inertial correction terms and in particular the contribution of the coupling inertial correction term.

Appendix 1

The objective of this appendix is to provide a special form of the general transport theorem as given by equation (12)

$$\frac{\partial}{\partial t}\int\limits_{\mathcal{V}(t)} \psi_\alpha \, dV = \int\limits_{\mathcal{V}(t)} \frac{\partial \psi_\alpha}{\partial t} \, dV + \int\limits_{A(t)} \psi_\alpha \, \mathbf{n}.\mathbf{w} \, dA \tag{1}$$

that can be used in the case of immiscible two-phase flow in a rigid porous medium.

In equation (1), $A(t)$ is the surface enclosing $\mathcal{V}(t)$, $\mathbf{w}$ the velocity of a material point attached to $A(t)$ and $\mathbf{n}$ the unit vector normal to $A(t)$ pointing outside $\mathcal{V}(t)$. Without introducing any particularity, our result is derived by considering a quantity ψ_β defined in $V_\beta(t)$ included at time t in the arbitrary averaging volume V.

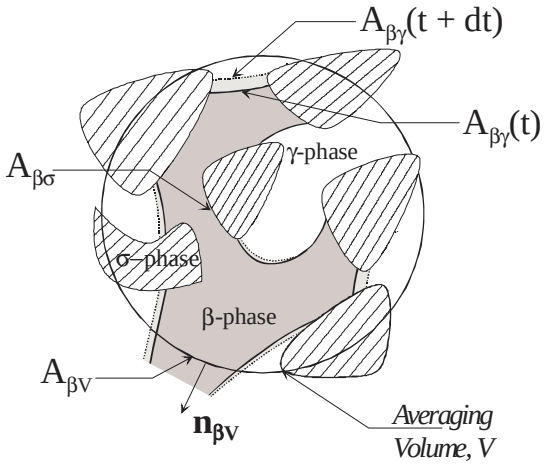

Figure 1: The averaging volume V containing the evolving volume $V_\beta(t)$ enclosed at t by the surfaces $A_{\beta\sigma}(t)$, $A_{\beta\gamma}(t)$ and $A_{\beta V}(t)$.

As depicted in figure 1, the volume $V_\beta(t)$ is enclosed at t by the material surfaces $A_{\beta\sigma}(t)$ and $A_{\beta\gamma}(t)$ and by the arbitrary surface $A_{\beta V}(t)$, the latter representing the portion of the surface enclosing the averaging volume V included in $V_\beta(t)$. Applying the theorem of equation (1) on ψ_β with $\mathcal{V}(t) = V_\beta(t)$ yields

$$\frac{\partial}{\partial t}\int\limits_{\mathcal{V}_\beta(t)} \psi_\beta \, dV = \int\limits_{\mathcal{V}_\beta(t)} \frac{\partial \psi_\beta}{\partial t} \, dV + \int\limits_{A_{\beta\sigma}(t)+A_{\beta\gamma}(t)+A_{\beta V}(t)} \psi_\beta \, \mathbf{n}_{\boldsymbol{\beta}} \cdot \mathbf{w} \, dA \tag{2}$$

where $\mathbf{n}_{\boldsymbol{\beta}}$ represents either $\mathbf{n}_{\boldsymbol{\beta\sigma}}$, $\mathbf{n}_{\boldsymbol{\beta\gamma}}$ or $\mathbf{n}_{\boldsymbol{\beta V}}$. Because $A_{\beta\sigma}(t)$ and $A_{\beta\gamma}(t)$ are material surfaces and since no phase-change occurs on these surfaces, $\mathbf{w} = \mathbf{v}_\beta$ on $A_{\beta\sigma}(t)$ and $A_{\beta\gamma}(t)$. Moreover, due to the no-slip boundary condition on $A_{\beta\sigma}(t)$, the theorem takes the form

$$\frac{\partial}{\partial t}\int\limits_{\mathcal{V}_\beta(t)} \psi_\beta \, dV = \int\limits_{\mathcal{V}_\beta(t)} \frac{\partial \psi_\beta}{\partial t} \, dV + \int\limits_{A_{\beta\gamma}(t)} \psi_\alpha \, \mathbf{n}_{\boldsymbol{\beta\gamma}} \cdot \mathbf{v}_\beta \, dA + \int\limits_{A_{\beta V}(t)} \psi_\beta \, \mathbf{n}_{\boldsymbol{\beta V}} \cdot \mathbf{w} \, dA \tag{3}$$

In addition, the evolution of $A_{\beta V}$ over dt (see figure 1) occurs with a velocity $\mathbf{w}$ having no normal contribution in the transport theorem so that it can be written as

$$\frac{\partial}{\partial t}\int\limits_{\mathcal{V}_\beta(t)} \psi_\beta \, dV = \int\limits_{\mathcal{V}_\beta(t)} \frac{\partial \psi_\beta}{\partial t} \, dV + \int\limits_{A_{\beta\gamma}(t)} \psi_\beta \, \mathbf{n}_{\boldsymbol{\beta\gamma}} \cdot \mathbf{v}_\beta \, dA \tag{4}$$

When this last form is divided by V which is a fixed volume in time, one finally gets the special form of the transport theorem in the case of two-phase immiscible flow in a rigid porous medium

$$\frac{\partial \left\langle \psi_\beta \right\rangle}{\partial t} = \left\langle \frac{\partial \psi_\beta}{\partial t} \right\rangle + \frac{1}{V}\int\limits_{A_{\beta\gamma}(t)} \psi_\beta \, \mathbf{n}_{\boldsymbol{\beta\gamma}} \cdot \mathbf{v}_\beta \, dA \tag{5}$$

Using a constant for ψ_β provides the following relationship

$$\frac{\partial \epsilon_\beta}{\partial t} = \frac{1}{V}\int\limits_{A_{\beta\gamma}(t)} \mathbf{n}_{\boldsymbol{\beta\gamma}} \cdot \mathbf{v}_\beta \, dA \tag{6}$$

which can be used to express the averaged mass conservation equation (15) in its final form (16).

Similarly, when the vector form is used with $\mathbf{v}_\beta$, one has

$$\left\langle \frac{\partial \mathbf{v}_\beta}{\partial t} \right\rangle = \frac{\partial \left\langle \mathbf{v}_\beta \right\rangle}{\partial t} - \frac{1}{V}\int\limits_{A_{\beta\gamma}(t)} \mathbf{n}_{\boldsymbol{\beta\gamma}} \cdot \mathbf{v}_\beta \, \mathbf{v}_\beta \, dA \tag{7}$$

which can be used to average the acceleration term in the left hand side of the original momentum equation (2a) of the paper to arrive at equation (18).

Appendix 2

In this appendix, we simply list the result on the boundary value problems that must be solved in order to determine the four dominant and coupling permeability tensors $\mathbf{K}^*_{\alpha\alpha}$ and $\mathbf{K}^*_{\alpha\kappa}$ (α, $\kappa = \beta$, γ, $\alpha \neq \kappa$) and we refer the reader to Lasseux et al. (1996) for the details. When the same nomenclature as that employed in this last reference is used, these problems are given by

Problem A-I

$$-\nabla \mathbf{d}^0_{\beta\beta} + \nabla^2 \mathbf{D}^0_{\beta\beta} = \mathbf{I} \quad \text{in } V_\beta \tag{1a}$$

$$\nabla \cdot \mathbf{D}^0_{\beta\beta} = 0 \quad \text{in } V_\beta \tag{1b}$$

$$\text{BC1} \quad \mathbf{D}^0_{\beta\beta} = 0 \quad \text{at } A_{\beta\sigma} \tag{1c}$$

$$\text{BC2} \quad \mathbf{D}^0_{\beta\beta} = \mathbf{D}^0_{\gamma\beta} \quad \text{at } A_{\beta\gamma} \tag{1d}$$

$$\text{BC3} \quad \mu_\beta \mathbf{n}_{\beta\gamma} \cdot \left[-\mathbf{I}\mathbf{d}^0_{\beta\beta} + (\nabla \mathbf{D}^0_{\beta\beta} + \nabla \mathbf{D}^{0T}_{\beta\beta})\right] = \mu_\gamma \mathbf{n}_{\beta\gamma} \cdot \left[-\mathbf{I}\mathbf{d}^0_{\gamma\beta} + (\nabla \mathbf{D}^0_{\gamma\beta} + \nabla \mathbf{D}^{0T}_{\gamma\beta})\right] \quad \text{at } A_{\beta\gamma} \tag{1e}$$

$$\text{BC4} \quad \mathbf{D}^0_{\gamma\beta} = 0 \quad \text{at } A_{\gamma\sigma} \tag{1f}$$

$$-\nabla \mathbf{d}^0_{\gamma\beta} + \nabla^2 \mathbf{D}^0_{\gamma\beta} = 0 \quad \text{in } V_\gamma \tag{1g}$$

$$\nabla \cdot \mathbf{D}^0_{\gamma\beta} = 0 \quad \text{in } V_\gamma \tag{1h}$$

Periodicity:

$$\mathbf{d}^0_{\beta\beta}(\mathbf{r} + \mathbf{l}_i) = \mathbf{d}^0_{\beta\beta}(\mathbf{r}) \quad \mathbf{d}^0_{\gamma\beta}(\mathbf{r} + \mathbf{l}_i) = \mathbf{d}^0_{\gamma\beta}(\mathbf{r}) \quad i = 1, 2, 3 \tag{1i}$$

$$\mathbf{D}^0_{\beta\beta}(\mathbf{r} + \mathbf{l}_i) = \mathbf{D}^0_{\beta\beta}(\mathbf{r}) \quad \mathbf{D}^0_{\gamma\beta}(\mathbf{r} + \mathbf{l}_i) = \mathbf{D}^0_{\gamma\beta}(\mathbf{r}) \quad i = 1, 2, 3 \tag{1j}$$

Average:

$$\langle \mathbf{D}^0_{\beta\beta} \rangle^\beta = -\varepsilon_\beta^{-1} \mathbf{K}^*_{\beta\beta} \quad \langle \mathbf{D}^0_{\gamma\beta} \rangle^\gamma = -\varepsilon_\gamma^{-1} \mathbf{K}^*_{\gamma\beta} \tag{1k}$$

Problem A-II

$$-\nabla \mathbf{d}^0_{\beta\gamma} + \nabla^2 \mathbf{D}^0_{\beta\gamma} = 0 \quad \text{in } V_\beta \tag{2a}$$

$$\nabla \cdot \mathbf{D}^0_{\beta\gamma} = 0 \quad \text{in } V_\beta \tag{2b}$$

$$\text{BC1} \quad \mathbf{D}^0_{\beta\gamma} = 0 \quad \text{at } A_{\beta\sigma} \tag{2c}$$

$$\text{BC2} \quad \mathbf{D}^0_{\beta\gamma} = \mathbf{D}^0_{\gamma\gamma} \quad \text{at } A_{\beta\gamma} \tag{2d}$$

$$\text{BC3} \quad \mu_\beta \mathbf{n}_{\beta\gamma} \cdot \left[-\mathbf{I}\mathbf{d}^0_{\beta\gamma} + (\nabla \mathbf{D}^0_{\beta\gamma} + \nabla \mathbf{D}^{0T}_{\beta\gamma})\right] = \mu_\gamma \mathbf{n}_{\beta\gamma} \cdot \left[-\mathbf{I}\mathbf{d}^0_{\gamma\gamma} + (\nabla \mathbf{D}^0_{\gamma\gamma} + \nabla \mathbf{D}^{0T}_{\gamma\gamma})\right] \quad \text{at } A_{\beta\gamma} \tag{2e}$$

$$\text{BC4} \quad \mathbf{D}^0_{\gamma\gamma} = 0 \quad \text{at } A_{\gamma\sigma} \tag{2f}$$

$$-\nabla \mathbf{d}^0_{\gamma\gamma} + \nabla^2 \mathbf{D}^0_{\beta\gamma} = \mathbf{I} \quad \text{in } V_\gamma \tag{2g}$$

$$\nabla \cdot \mathbf{D}^0_{\gamma\gamma} = 0 \quad \text{in } V_\gamma \tag{2h}$$

Periodicity:

$$\mathbf{d}^1_{\beta\gamma}(\mathbf{r} + \mathbf{l}_i) = \mathbf{d}^1_{\beta\gamma}(r) \quad \mathbf{d}^1_{\gamma\gamma}(\mathbf{r} + \mathbf{l}_i) = \mathbf{d}^1_{\gamma\gamma}(\mathbf{r}) \quad i = 1, 2, 3 \tag{2i}$$

$$\mathbf{D}^1_{\beta\gamma}(\mathbf{r} + \mathbf{l}_i) = \mathbf{D}^1_{\beta\gamma}(r) \quad \mathbf{D}^1_{\gamma\gamma}(\mathbf{r} + \mathbf{l}_i) = \mathbf{D}^1_{\gamma\gamma}(\mathbf{r}) \quad i = 1, 2, 3 \tag{2j}$$

Average:

$$\langle \mathbf{D}^0_{\beta\gamma} \rangle^\beta = -\varepsilon_\beta^{-1} \mathbf{K}^*_{\beta\gamma} \quad \langle \mathbf{D}^0_{\gamma\gamma} \rangle^\gamma = -\varepsilon_\gamma^{-1} \mathbf{K}^*_{\gamma\gamma} \tag{2k}$$

Each of these two problems has basically a structure identical to that of a Stokes two-phase flow without any dependence on the curvature of the fluid-fluid interface. When a solver is available to compute the

initial microscopic physical flow problem and locate the interface, the same solver in which inertial terms are removed can be used to solve problems A-I and A-II and determine the four tensors $\mathbf{K}^*_{\alpha\alpha}$ $\mathbf{K}^*_{\alpha\kappa}$ (α, $\kappa = \beta$, γ, $\alpha \neq \kappa$). When these four tensors are computed, the permeability and viscous drag tensors $\mathbf{K}_\alpha$ and $\mathbf{K}_{\alpha\kappa}$ (α, $\kappa = \beta$, γ, $\alpha \neq \kappa$) can be determined according to

$$\mathbf{K}_\alpha = \mathbf{K}^*_{\alpha\alpha} - \mathbf{K}^*_{\alpha\kappa} \cdot \mathbf{K}^{*^{-1}}_{\kappa\kappa} \cdot \mathbf{K}^*_{\kappa\alpha} \qquad \alpha, \kappa = \beta, \gamma \qquad \alpha \neq \kappa \tag{3}$$

$$\mathbf{K}_{\alpha\kappa} = \mathbf{K}^*_{\alpha\kappa} \cdot \left(\mathbf{I} - \mathbf{K}^{*^{-1}}_{\kappa\kappa} \cdot \mathbf{K}^*_{\kappa\alpha} \cdot \mathbf{K}^{*^{-1}}_{\alpha\alpha} \cdot \mathbf{K}^*_{\alpha\kappa} \right) \cdot \left(\mathbf{K}^*_{\kappa\kappa} - \mathbf{K}^*_{\kappa\alpha} \cdot \mathbf{K}^{*^{-1}}_{\alpha\alpha} \cdot \mathbf{K}^*_{\alpha\kappa} \right)^{-1} \qquad \alpha, \kappa = \beta, \gamma \qquad \alpha \neq \kappa \tag{4}$$

Notations

$\mathbf{a}_{\alpha\kappa}$ a vector that maps $\mu_\alpha \langle \mathbf{v}_\kappa \rangle^\kappa$ onto $\tilde{p}_\alpha$, m^{-1}
$\mathbf{A}_{\alpha\kappa}$ a tensor that maps $\langle \mathbf{v}_\kappa \rangle^\kappa$ onto $\tilde{\mathbf{v}}_\alpha$
$A_{\alpha\kappa}$ area of $\alpha - \kappa$ interface contained in the macroscopic region ($= A_{\kappa\alpha}$), m^2
$A_{\alpha e}$ area of $\alpha-$phase entrances and exits associated with the macroscopic region, m^2
$A_{a\kappa}$ area of $\alpha - \kappa$ interface contained within the averaging volume ($=A_{\kappa\alpha}$), m^2
Ca capillary number ($= \max_{\alpha=\beta,\,\gamma} (\mu_\alpha) \frac{v}{\sigma}$)
$\mathbf{F}_\alpha$ inertial correction tensor for the $\alpha-$phase
$\mathbf{F}_{\alpha\kappa}$ coupling inertial correction tensor that maps $\langle \mathbf{v}_\kappa \rangle$ onto $\langle \mathbf{v}_\alpha \rangle$
$\mathbf{g}$ gravitational acceleration, ms^{-2}
H mean curvature, m^{-1}
$\langle H \rangle_{\beta\gamma}$ area average of the mean curvature, m^{-1}
$\mathbf{I}$ unit tensor
$\mathbf{K}_\alpha$ permeability tensor for the $\alpha-$phase, m^2
$\mathbf{K}_{\alpha\kappa}$ viscous drag tensor that maps $\langle \mathbf{v}_\kappa \rangle$ onto $\langle \mathbf{v}_\alpha \rangle$
$\mathbf{K}^*_{\alpha\alpha}$ dominant permeability tensor that maps $(\nabla \langle p_\alpha \rangle^\alpha - \rho_\alpha \mathbf{g})/\mu_\alpha)$ onto $\langle \mathbf{v}_\alpha \rangle$, m^2
$\mathbf{K}^*_{\alpha\kappa}$ dominant permeability tensor that maps $(\nabla \langle p_\kappa \rangle^\kappa - \rho_\kappa \mathbf{g})/\mu_\kappa)$ onto $\langle \mathbf{v}_\alpha \rangle$, m^2
l_α characteristic length for the $\alpha-$phase, m
$\mathbf{l}_i$ $i = 1, 2, 3$, lattice vectors, m
l small length scale representation of the mean pore diameter, m
L characteristic length associated with volume averaged quantities, m
$\mathbf{n}_{\alpha\kappa}$ unit normal vector pointing from the $\alpha-$phase toward the $\kappa-$phase ($= -\mathbf{n}_{\kappa\alpha}$)
$\mathbf{n}_\beta$ unit normal vector representing both $\mathbf{n}_{\beta\gamma}$ and $\mathbf{n}_{\beta\sigma}$
$\mathbf{n}_\gamma$ unit normal vector representing both $\mathbf{n}_{\gamma\beta}$ and $\mathbf{n}_{\gamma\sigma}$
p_α pressure in the $\alpha-$phase, Pa
$\langle p_\alpha \rangle$ superficial average pressure in the $\alpha-$phase, Pa
$\langle p_\alpha \rangle^\alpha$ intrinsic average pressure in the $\alpha-$phase, Pa
$\widetilde{p}_\alpha$ pressure deviation in the $\alpha-$phase ($= p_\alpha - \langle p_\alpha \rangle^\alpha$), Pa
p^0_α reference pressure in the $\alpha-$phase, Pa
r_0 radius of the averaging volume V, m
$\mathbf{r}$ position vector, m
Re_α Reynolds number associated to the $\alpha-$phase, ($= \frac{\rho_\alpha \| \langle \mathbf{v}_\alpha \rangle \| l}{\mu_\alpha}$)
t time, s
t^* characteristic process time, s
v velocity order of magnitude common to all the velocities , m/s
$\mathbf{v}_\alpha$ velocity in the $\alpha-$phase, m/s
$\langle \mathbf{v}_\alpha \rangle$ superficial average velocity in the $\alpha-$phase, m/s
$\langle \mathbf{v}_\alpha \rangle^\alpha$ intrinsic average velocity in the $\alpha-$phase, m/s
$\tilde{\mathbf{v}}_\alpha$ velocity deviation in the $\alpha-$phase ($= \mathbf{v}_\alpha - \langle \mathbf{v}_\alpha \rangle^\alpha$), m/s
V_α volume of the $\alpha-$phase, contained within the averaging volume, m^3
V averaging volume, m^3

We Weber number ($= \max_{\alpha=\beta,\,\gamma} (\rho_\alpha) \frac{v^2 l}{\sigma}$)

Greek letters

ε_α volume fraction of the $\alpha-$phase, $(= V_\alpha/V)$
μ_α viscosity of the $\alpha-$phase, $Pa.s$
ρ_α density of the $\alpha-$phase, kg/m^3
σ interfacial tension between the β- and γ-phase
Υ_α viscous stress tensor in the α-phase, Pa

References

Ahmed, N. and Sunada, D. K.: 1969, Nonlinear flow in porous media, *J. Hydr. Div ASCE* **95**(HY6), 1847–1857.

Amaral Souto, H. and Moyne, C.: 1997, Dispersion in two-dimensional periodic porous media, Part I: Hydrodynamics, *Phys Fluids* **9**(8), 2243–2252.

Auriault, J. L.: 1987, Nonsaturated deformable porous media: Quasistatics, *Transport in Porous Media* **2**(1), 45–64.

Bear, J.: 1972, *Dynamics of Fluids in Porous Media*, Dover, New York.

Beavers, G. S. and Sparrow, E. M.: 1969, Non-Darcy flow through fibrous porous media, *J. Appl. Mech. Trans. ASME* **December**, 711–714.

Blick, E. F.: 1966, Capillary orifice model for high speed flow through porous media, *I and EC, Process Design and Development* **5**, 90–94.

Buchlin, J. and Stubos, A.: 1987, Phase change phenomena at liquid saturated self heated particulate beds, *Application of Transport in Porous media, Von Karman Institute for Fluid Dynamics, Rhode-Sainte-Genèse, Belgium* **4**, 221–276.

Carbonell, R. G. and Whitaker, S.: 1984, *Fundamentals of Transport Phenomena in Porous Media*, Martinus Nijhoff Publishers, Dordrecht, chapter Heat and Mass Transfer in Porous Media, pp. 121–198.

Chen, Z., Lyons, S. L. and Qin, G.: 2001, Derivation of the Forchheimer law via homogenization, *Transport in Porous Media* **44**(2), 325–335.

Coulaud, O., Morel, P. and Caltagirone, J. P.: 1988, Numerical modeling of non-linear effects in laminar flow through a porous medium, *J. Fluid. Mech.* **190**, 393–407.

Cvetkovic, V. D.: 1986, A continuum approach to high velocity flow in a porous medium, *Transport in Porous Media* **1**(1), 63–97.

Darcy, H.: 1856, Les fontaines publiques de la ville de Dijon, *Librairie des corps impériaux des ponts et chaussées et des mines, Paris* .

Dullien, A. L. and Azzam, M. I. S.: 1973, Flow rate-pressure gradient measurement in periodically nonuniform capillary tube, *AIChE J.* **19**, 222–229.

Ergun, S.: 1952, Fluid flow through packed columns, *Chem. Eng. Prog.* **48**, 89–94.

Evans, E. V. and Evans, R. D.: 1988, Influence of an immobile or mobile saturation on non-Darcy compressible flow of real gases in propped fractures, *J. Petrol. Technol* **40**(10), 1343–1351.

Evans, R. D., Hudson, C. S. and Greenlee, J. E.: 1987, The effect of an immobile liquid saturation on the non-Darcy flow coefficient in porous media, *J. SPE Prod. Engng Trans. AIME* **283**, 331–338.

Firdaouss, M. and Guermond, J. L.: 1995, Sur l'homogénéisation des équations de Navier-Stokes à faible nombre de Reynolds, *C. R. Acad. Sci. Paris, Série I* **320**, 245–251.

Firdaouss, M., Guermond, J. L. and Le Quéré, P.: 1997, Nonlinear corrections to Darcy's law at low Reynolds numbers, *J. Fluid Mech.* **343**, 331–350.

Firoozabadi, A. and Katz, D. L.: 1979, An analysis of high-velocity gas flow through porous media, *Journal of Petroleum Technology* **February 1979**, 211–216.

Firoozabadi, A., Thomas, L. K. and Todd, B.: 1995, High-velocity flow in porous media, *SPE Reservoir Engineering* **10**, 149–152.

Forchheimer, P.: 1901, Wasserbewgung durch boden, *Z. Ver. Deutsch. Ing.* **XXXXV**(45), 1782–1788.

Fourar, M. and Lenormand, R.: 2000, Inertial effects in two-phase flow through fractures, *Oil and Gas Science and Technology - Rev. IFP* **55**(3), 259–268.

Geertsma, J.: 1974, Estimating the coefficient of inertial resistance in fluid flow through porous media, *Society of Petroleum Engineers Journal* **October 1974.**, 445–450.

Giorgi, T.: 1997, Derivation of the Forchheimer law via matched asymptotic expansions, *Transport in Porous Media* **29**(2), 191–206.

Gray, W. G.: 1975, A derivation of the equations for multi-phase transport, *Chem. Eng. sci.* **30**, 229–233.

Howes, F. and Whitaker, S.: 1985, The spatial averaging theorem revisited, *Chem. Eng. Sci.* **40**, 1387–1392.

Irmay, S.: 1958, On the theoretical derivation of Darcy and Forchheimer formulas, *J. Geophys. Res.* **39**, 702–707.

Kalaydjian, F.: 1990, Origin and quantification of coupling between relative permeabilities for two-phase flows in porous media, *Transport in Porous Media* **5**(3), 215–229.

Koch, J. B. and Ladd, A. J. C.: 1997, Moderate Reynolds number flows through periodic and random arrays of aligned cylinders, *J. Fluid Mech.* **349**, 31–66.

Lasseux, D., Whitaker, S. and Quintard, M.: 1996, Determination of permeability tensors for two-phase flow in homogeneous porous media: Theory, *Transport in Porous Media* **24**(1), 107–137.

Lipinski, R. J.: 1980, A particle bed dryout model with upwind and downward boiling, *Trans. Am. Nucl. Soc.* **35**, 350–358.

Lipinski, T. J.: 1982, A model for boiling and dryout in particle beds., *Report SAND 82-0756 (NUREG/CR-2646), Sandia Labs* .

Liu, X., Civan, F. and Evans, R. D.: 1995, Correlations of the non-Darcy flow coefficient, *J. Canad. Petrol. Technol.* **34**(10), 50–54.

Lockhart, R. and Martinelli, R.: 1949, Proposed correlation of data for isorthermal two-phase two-component flow in pipes, *Chem. Eng. Prog.* **45**, 39.

Ma, H. and Ruth, D. W.: 1993, The microscopic analysis of high Forchheimer number flow in porous media, *Transport in Porous Media* **13**(2), 139–160.

MacDonald, I. F., El-Sayed, M. S., Mow, K. and Dullien, F. A. L.: 1979, Flow through porous media, the Ergun equation revisited, *Ind. Eng. Chem. Fundm* **18**(3), 199–208.

Mei, C. C. and Auriault, J. L.: 1991, The effect of weak inertia on flow through a porous medium, *J. Fluid Mech.* **222**, 647–663.

Muskat, M.: 1937, *The flow of homogeneous fluids through porous media*, International Human Resources Development Corporation (reprint from McGraw-Hill, 1982), Boston.

Papathanasiou, T. D., Markicevic, B. and Dendy, E. D.: 2001, A computational evaluation of the Ergun and Forchheimer equations for fibrous porous media, *Phys. Fluids* **13**(10), 2795–2804.

Quintard, M. and Whitaker, S.: 1994, Transport in ordered and disordered porous media II: Generalized volume averaging, *Transport in Porous Media* **14**(2), 179–206.

Raats, D. A. C. and Klute, A.: 1968, Transport in soils: The balance of momentum, *Soil. Sci. Soc. Amer. Proc.* **32**, 161–166.

Rasoloarijaona, M. and Auriault, J. L.: 1994, Nonlinear seepage flow through a rigid porous medium, *Eur. J. Mech. B/Fluids* **13**(2), 177–195.

Rojas, S. and Koplik, J.: 1998, Nonlinear flow in porous media, *Phys. Rev. E* **58(4)**, 4476–4782.

Rose, W.: 1989, Data interpretation problems to be expected in the study of coupled fluid flow in porous media, *Transport in Porous Media* **4**(2), 185–189.

Ruth, D. and Ma, H.: 1993, Numerical analysis of the viscous incompressible flow in a diverging-converging RUC, *Transport in Porous Media* **13**(2), 161–177.

Scheidegger, A. E.: 1974, *The Physics of Flow Through Porous Media*, University of Toronto Press, Toronto, Canada.

Skjetne, E. and Auriault, J. L.: 1999, High-velocity laminar and turbulent flow in porous media, *Transport in Porous Media* **36**, 131–147.

Skjetne, E., Hansen, A. and Gudmundsson, J. S.: 1999, High velocity flow in a rough fracture, *J. Fluid Mech.* **383**, 1–28.

Slattery, J. C.: 1990, *Interfacial Transport Phenomena*, Springer, New York.

Thauvin, F. and Mohanty, K. K.: 1998, Network modeling of non-Darcy flow through porous media, *Transport in Porous Media* **31**(1), 19–37.

Torres, F. E.: 1987, Closure of the governing equations for immiscible two-phase flow: A research comment, *Transport in Porous Media* **2**(4), 383–393.

Truesdell, C. and Toupin, R.: 1960, *The Classical Field Theories*, Springer-Verlag, New-York.

Ward, J. C.: 1964, Turbulent flow in porous media, *J. Hydr. Div., ASCE* **90**(HY5), 1–12.

Whitaker, S.: 1986a, Flow in porous media I: A theoretical derivation of Darcy's law, *Transport in Porous Media* **1**(1), 3–25.

Whitaker, S.: 1986b, Flow in porous media II: The governing equation for immiscible two-phase flow, *Transport in Porous Media* **1**(1), 105–125.

Whitaker, S.: 1994, The closure problem for two-phase flow in homogeneous porous media, *Chem. Eng. Sci.* **49**, 765–780.

Whitaker, S.: 1996, The Forchheimer equation: A theoretical development, *Transport in Porous Media* **25**(1), 27–61.

Whitaker, S.: 1999, *The Method of Volume Averaging*, Theory and Applications of Transport in Porous Media, Kluwer Academic, Dordrecht, The Netherlands.

Wodie, J. C. and Levy, T.: 1991, Correction non linéaire de la loi de Darcy, *C. R Acad. Sci. Paris II* pp. 157–161.

Zarcone, C.: 1994, *Etude du couplage visqueux en milieu poreux : Mesure des perméabilités relatives croisées*, PhD thesis, INP Toulouse.

Chapitre 4

Numerical simulation of two-phase inertial flow in heterogeneous porous media

Numerical simulation of two-phase inertial flow in heterogeneous porous media

Abstract

In this work, we present the development of a 3D numerical tool for non-Darcy two-phase incompressible flow simulation in heterogeneous porous media. The physical model selected is the generalized Darcy-Forchheimer model. A validation is performed first by comparing numerical results with a semi-analytical solution of the Buckley-Leverett type. Secondly, we highlight the importance of the inertial terms as a function of a suitable Reynolds number and numerical results obtained on 1D and 2D heterogeneous configurations are presented.

Résumé

Dans ce travail, nous présentons la mise en place d'un outil numérique 3D de simulation d'écoulement diphasique incompressible hors régime de Darcy. Le modèle retenu est celui de Darcy-Forchheimer généralisé. Après avoir validé l'outil sur la base d'une solution semi analytique 1D de type Buckley-Leverett, on présente des résultats dans différentes configurations hétérogènes et on met en évidence l'importance des termes inertiels en fonction d'un nombre de Reynolds de l'écoulement convenablement défini.

1 Introduction

Under certain conditions such as the near-wellbore region and/or in very permeable reservoirs, hydrocarbon recovery by water flooding or gas injection can lead to high flow rates for which the classical description of two-phase flow in porous media by the generalized Darcy's law is no longer valid (Tek et al., 1962; Scheidegger, 1972; Katz and Lee, 1990; Kalaydjian et al., 1996). This type of flow is also under concern in chemical engineering applications during two-phase flow in packed-bed reactors for instance. It is therefore necessary to call upon a more complete flow model in which inertial effects are taken into account by introducing an additional term in the momentum balance equations. In this work, two-phase, incompressible, non-stationary flow in porous media is considered with Reynolds numbers high enough to justify the use of a model including inertial terms. The physical model used is the generalized Darcy-Forchheimer model (Schulenberg and Muller, 1987; Wang et al., 1999). Heterogeneous media composed of several homogeneous regions each having isotropic transport properties at the Darcy scale will be studied. The wetting and nonwetting phases will be distinguished by the indices "w" and "o" (for water and oil) respectively. Without imposing any restrictions in the numerical approach, our work will focus on imbibition only.

2 Governing equations

The most widely used momentum conservation equation at the Darcy scale is Darcy's law (Darcy, 1856). Although Darcy's experiment dealt only with one dimensional creeping flow of water through various porous media, he established the basic relationship between the flow rate and the pressure gradient which can be modified in various ways to model a wide variety of flows in different regimes. Later, this empirical model was confirmed on a theoretical basis (Ene and Sanchez-Palencia, 1975; Whitaker, 1986a; Auriault, 1987). The steady-state one-phase flow problem at sufficiently small Reynolds number can be written as

$$\nabla \cdot \mathbf{u} = 0 \tag{1}$$

$$\mathbf{u} = -\frac{\mathbf{K}}{\mu} \cdot (\nabla p - \rho \mathbf{g}) \tag{2}$$

along with adequate boundary conditions. In the three dimensional form of Darcy's law (Eq. 2), $\mathbf{K}$, $\mathbf{u}$, p, μ, ρ and $\mathbf{g}$ are respectively the intrinsic permeability tensor, the Darcy or seepage velocity, the fluid pressure, the fluid dynamic viscosity, the fluid density and the gravity acceleration. The intrinsic permeability, $\mathbf{K}$, has the dimension of length squared and depends mainly on the geometrical structure of the porous medium.

Modelling of two-phase flow in porous media is based on the generalization of the single phase flow equations. At very low Reynolds number, the physical flow model most largely admitted (Muskat, 1937) and justified theoretically (Raats and Klute, 1968; Whitaker, 1986b; Auriault, 1987) is that of generalized Darcy's law, given by ($\alpha = o,\, w$)

$$\varepsilon \frac{\partial}{\partial t} S_\alpha + \nabla \cdot \mathbf{u}_\alpha = 0 \tag{3}$$

$$\mathbf{u}_\alpha = -\mathbf{M}_\alpha \cdot (\nabla p_\alpha - \rho_\alpha \mathbf{g}) \tag{4}$$

$$p_c = p_o - p_w \tag{5}$$

$$S_w + S_o = 1 \tag{6}$$

In Eqs. (3) and (4), S_α is the α-phase saturation defined as:

$$S_\alpha = \frac{V_\alpha}{V} \tag{7}$$

in which V_α is the volume of the α-phase contained within a representative elementary volume V of the porous medium. When one phase is displaced by another phase in a saturated porous medium, the totality of the fluid in place cannot be removed because of trapping mechanisms resulting from capillary forces at the pore scale. Thus, concerning two-phase flow of water and oil in porous media, two specific quantities are defined: the irreducible water saturation (S_{wi}) and residual oil saturation (S_{or}). These two saturations allow to define the higher and lower limits of water and oil saturations as:

$$S_{wi} \leq S_w \leq 1 - S_{or} \tag{8}$$

$$S_{or} \leq S_o \leq 1 - S_{wi} \tag{9}$$

In the generalized Darcy's law (Eq. 4), $\mathbf{M}_\alpha$ ($\alpha = o,\, w$) is the α-phase mobility defined as

$$\mathbf{M}_\alpha = \frac{\mathbf{K}_\alpha}{\mu_\alpha} \tag{10}$$

in which $\mathbf{K}_\alpha$ is the α-phase effective permeability. It is related to the intrinsic permeability $\mathbf{K}$ by the following relation

$$\mathbf{K}_\alpha = \mathbf{K}\mathbf{k}_{r\alpha} \tag{11}$$

In this relation $\mathbf{k}_{r\alpha}$ is the $\alpha-$phase relative permeability. The relative permeability concept indicates the fact that each fluid influences the flow of the other fluid through the reduction of the flow section and thus the reduction in the effective permeability $\mathbf{K}_\alpha$ of a fluid due to the presence of the other fluid. In this work, in addition to scalar intrinsic permeabilities due to isotropy ($\mathbf{K} = k\mathbf{I}$), scalar relative permeabilities will also be considered although it might not be adequate in the general case of anisotropic porous media as reported by Bear et al. (1987) and Ahmadi and Quintard (1995) where the use of tensorial relative permeabilities

was highlighted. Relative permeabilities are functions of several dimensionless groups involving properties of both the fluid and the medium (Marle, 1972). In the viscous-capillary regime, it is generally assumed that relative permeabilities depend on the phase saturation only. They are often given as power functions of fluids saturations (Corey, 1954)

$$k_{rw} = (S^*)^\gamma \tag{12}$$
$$k_{ro} = (1 - S^*)^\theta \tag{13}$$

with

$$S^* = \frac{S - S_{wi}}{1 - S_{wi} - S_{or}} \tag{14}$$

where S^* is the reduced saturation and γ and θ are constant exponents. Following the same idea as for k_r, it is generally admitted that the capillary pressure defined in Eq. (5) only depends on S^*. In this work, we have adopted a correlation of the form:

$$p_c(S_w) = p_{c_0}(1 - S^*)^\xi \tag{15}$$

The parameters ξ and p_{c_0} are constant, the latter representing the capillary pressure value when $S_w = S_{wi}$. The exact form of the relative permeability and capillary pressure functions, generally expressed as a function of S_w and defined between the two end-points (S_{wi} and $1 - S_{or}$), depends on the geometry of the porous medium, its wetting properties and fluids distributions. They are generally obtained experimentally for each particular case (Corey, 1954; Brooks and Corey, 1966; Honarpour et al., 1986; Abdobal, 2002).

2.1 Non-Darcy flow regime

When the flow-rate of fluids is relatively high, Darcy's law does not describe correctly the momentum conservation, due to the appearance of significant inertial effects. These can be taken into account by adding a corrective term to Darcy's equation. Various modifications were made to this law in order to take into account these important inertial effects (Ergun, 1952; Hubbert, 1956). Even for single-phase flow, the problem arising from the presence of significant inertial effects is complex from the point of view of scaling and some attempts on the formalization of macroscopic models were undertaken (Mei and Auriault, 1991; Whitaker, 1996; Skjetne and Auriault, 1999). For the two-phase flow case, a complete theoretical formalization of a model at the Darcy scale is still lacking. In a largely empirical way, the generalized Darcy-Forchheimer equation is classically used. It is based on the one hand on the empirical Darcy-Forchheimer model for single-phase flow (Forchheimer, 1901) and on the other hand on a generalization of this model to the two-phase flow case in a similar way to that originally followed for flow in the Darcy regime. The resulting momentum balance equation involves a quadratic correction of the velocity and is written as ($\alpha = o,\, w$):

$$-(\nabla p_\alpha - \rho_\alpha \mathbf{g}) = \mu_\alpha \mathbf{K}_\alpha^{-1} \cdot \mathbf{u}_\alpha + \rho_\alpha \left\|\mathbf{u}_\alpha\right\| \boldsymbol{\beta}_\alpha \cdot \mathbf{u}_\alpha \tag{16}$$

In this relation $\boldsymbol{\beta}_\alpha$ is a coefficient (having a priori a tensorial form) generally called the effective inertial resistance factor or high-velocity flow coefficient or non-Darcy flow coefficient (Geertsma, 1974; Liu et al., 1995). The inertial term in Eq. (16) may also be expressed in terms of the passability factor, $\boldsymbol{\eta}_\alpha$, (Lipinski, 1980; Buchlin and Stubos, 1987) defined as

$$\boldsymbol{\beta}_\alpha = \boldsymbol{\eta}_\alpha^{-1} \quad (\alpha = o,\, w) \tag{17}$$

classically used in nuclear safety applications. The additional pressure drop resulting from non-Darcy effects due to high flow velocity is described by the second term ($\rho_\alpha \left|\mathbf{u}_\alpha\right| \boldsymbol{\beta}_\alpha \cdot \mathbf{u}_\alpha$) on the right-hand side of equation (16). Whatever the form of this term, it accounts for the extra friction due to inertial effects (Katz and Lee, 1990).

In a traditional way, taking into account isotropy of the medium, one can write $\boldsymbol{\beta}_\alpha = \beta_\alpha \mathbf{I} = \beta\beta_{r\alpha}\mathbf{I}$, in which β is the intrinsic inertial resistance factor of the medium and $\beta_{r\alpha}$ is the relative inertial resistance factor to the $\alpha-$phase, a nonlinear function of the saturation. Empirical relations correlating β_α with porosity and effective permeability were proposed in the literature (Geertsma, 1974; Evans et al., 1987; Evans and Evans, 1988; Liu et al., 1995).

2.2 Non-Darcy flow coefficient

There is a great diversity in the correlations proposed in the literature for the expression of the non-Darcy flow coefficients (see Li and Engler (2001) for a review). This diversity of the empirical correlations can be attributed to the difference in lithology, in pore geometry of the formation and therefore in the flow patterns on the one hand and on the different number of parameters used in the literature for the correlations on the other hand. The major parameters considered are the permeability (k), the porosity (ε) and the tortuosity (τ), the three being related to each other (Li and Engler, 2001).

One of the most commonly used correlations was obtained from experimental data and dimensional analysis by Geertsma (1974) for single phase inertial flow in porous media:

$$\beta = \frac{0.005}{k^{0.5}\varepsilon^{5.5}} \tag{18}$$

In this correlation, the permeability is expressed in cm^2 and β in cm^{-1}. In the same reference, Geertsma (1974) was also the first to propose an expression of the inertial coefficient for two-phase flow, by replacing the permeability in Eq. (18) by the effective permeability ($K_\alpha = kkr_\alpha$) and the porosity by the void fraction occupied by the corresponding fluid ($\varepsilon\ S_\alpha$), thus giving

$$\beta_\alpha = \frac{0.005}{K_\alpha^{0.5}(\varepsilon\ S_\alpha)^{5.5}} \tag{19}$$

More recently, the importance of including tortuosity τ in the correlation has been pointed out by Liu et al. (1995). In order to test Geertsma's proposition and to develop a general correlation for the non-Darcy flow coefficient, a large variety of single and two-phase flow data were collected by these authors. In their work, data was gathered from various sources (Cornell and Katz, 1953; Geertsma, 1974; Evans et al., 1987; Evans and Evans, 1988; Whitney, 1988) including studies on consolidated and unconsolidated porous media as well as an analysis of the effect of immobile liquid saturation. Since in most experimental studies, there was a lack of information on the tortuosity, a value of 1.414, in accordance with Carman (1937), was used for the tortuosity in those works. On this basis, Liu et al. (1995) found a more satisfactory correlation by including the tortuosity factor in the expression of the inertial coefficient and this correlation is given by:

$$\beta_\alpha = \frac{8.91\ 10^8\tau}{\varepsilon K_\alpha} \tag{20}$$

In this relation, β_α and K_α are expressed in ft^{-1} and md respectively.

In the computations carried out in this work, the non-Darcy coefficient given in Eq. (20) was used for each phase with a tortuosity value of 1.9 (Wahyudi et al., 2000). Using the expression of K_α in Eq. (20) and identifying β as $\frac{8.91\ 10^8\tau}{\varepsilon k}$ leads to:

$$\beta_{r\alpha} = k_{r\alpha}^{-1} \tag{21}$$

This form corresponds to that suggested by many other authors (Lipinski, 1982; Lee and Catton, 1984; Saez and Carbonnell, 1985). However, it must be noted that β_α is a user-fixed function and its choice has no influence on the numerical approach developed here. A more thorough discussion of these correlations is beyond the scope of this paper.

2.3 Reformulation of the problem

The Darcy-Forchheimer equation (16) may be written in the form ($\alpha = o,\, w$):

$$\mathbf{u}_\alpha = -\left[\frac{\mu_\alpha}{l}(l\mathbf{K}_\alpha^{-1} + \boldsymbol{\beta}_\alpha \,\mathrm{Re}_\alpha)\right]^{-1} \cdot (\nabla p_\alpha - \rho_\alpha \mathbf{g}) \tag{22}$$

with the Reynolds number, Re_α, associated with the $\alpha-$phase defined as

$$\mathrm{Re}_\alpha = \frac{\rho_\alpha \,\|\mathbf{u}_\alpha\|\, l}{\mu_\alpha} \tag{23}$$

In this relationship l represents a characteristic length-scale of the problem. In the literature, this length is generally associated to the pore-scale and is typically taken equal to the size of the solid grains ((Muskat, 1937)). In that case, this quantity can be estimated by using relations between intrinsic permeability and porosity of the Kozeny-Carman type (Koederitz et al., 1989). In the present work, a more suitable choice of this characteristic length-scale allowing a better quantification of the inertial effects is proposed.

As suggested by Eq. (22), introducing a new expression of the mobility given by

$$\mathbf{M}_\alpha = \left[\frac{\mu_\alpha}{l}(l\mathbf{K}_\alpha^{-1} + \boldsymbol{\beta}_\alpha \,\mathrm{Re}_\alpha)\right]^{-1} \tag{24}$$

leads to a form of this equation similar to generalized Darcy's law (3). The latter is obtained if the term $\boldsymbol{\beta}_\alpha \,\mathrm{Re}_\alpha$ is negligible in comparison with $l\mathbf{K}_\alpha^{-1}$. For our particular case of isotropic porous medium ($\mathbf{M}_\alpha = M_\alpha \mathbf{I}$,) the expression of the mobility given by Eq. (24) can be written as

$$M_\alpha = \left[\frac{\mu_\alpha}{K_\alpha}(1 + \frac{K_\alpha \beta_\alpha}{l}\,\mathrm{Re}_\alpha)\right]^{-1} \tag{25}$$

This expression suggests that a relevant choice of the characteristic length is $l = k\beta$ giving the following expression of the Reynolds number

$$\mathrm{Re}_\alpha = \frac{\rho_\alpha \,\|\mathbf{u}_\alpha\|\, k\beta}{\mu_\alpha} \tag{26}$$

With this definition, the $\alpha-$phase mobility can be written as

$$M_\alpha = \left[\frac{\mu_\alpha}{K_\alpha}(1 + k_{r\alpha}\beta_{r\alpha}\,\mathrm{Re}_\alpha)\right]^{-1} \tag{27}$$

In this manner, comparing Re_α to unity gives a precise idea on the importance of inertial effects with respect to a Darcy regime behavior. Moreover, this definition has the advantages of i) involving macroscopic quantities k and β available from experiments ii) avoid the introduction of a microscopic quantity (typically the grain size) that is most of the time unknown a priori and difficult to estimate precisely because of the absence of a universal relationship between macroscopic and microscopic characteristic lengths. An essential difference between the inertial problem we are dealing with and the classical Darcy's problem is the treatment of the nonlinearity associated to the special definition of the mobilities in our case. Indeed, in addition to "classical" nonlinearity functions of the saturation, mobilities are here non-linear functions of the Reynolds number therefore of the velocity.

To the momentum conservation equations (22), it is necessary to associate the mass conservation equations

$$\frac{\partial}{\partial t}(\varepsilon S_\alpha) + \nabla \cdot \mathbf{u}_\alpha = 0 \quad (\alpha = o,\, w) \tag{28}$$

which remains unmodified in comparison to the Darcy regime. Closing the problem with the saturations and capillary pressure relationships leads to the following boundary value problem:

$$\left\{\begin{array}{l} \frac{\partial}{\partial t}(\varepsilon S_w) + \nabla \cdot [-\mathbf{M}_w(\nabla p_w - \rho_w \mathbf{g})] = 0 \\ \frac{\partial}{\partial t}(\varepsilon S_o) + \nabla \cdot [-\mathbf{M}_o(\nabla p_o - \rho_o \mathbf{g})] = 0 \\ S_w + S_o = 1 \\ p_c = p_c(S_w) \end{array}\right. \tag{29}$$

along with the required boundary and initial conditions. Taking S_w and p_o as unknowns, the problem is reformulated in terms of the total velocity $\mathbf{u}_t$ and the total mobility $\mathbf{M}$ defined as:

$$\mathbf{u}_t = \mathbf{u}_w + \mathbf{u}_o \tag{30}$$

$$\mathbf{M} = \mathbf{M}_w + \mathbf{M}_o \tag{31}$$

This reformulation, based upon incompressibility of the two fluids has the advantage of simplifying the numerical scheme by introducing the divergence free total velocity. Other formulations are proposed in the literature (Aziz and Settari, 1979; Chavent, 1976). With this choice, the problem can therefore be written as:

$$\left\{\begin{array}{l} \nabla \cdot (\mathbf{u}_t) = 0 \\ \mathbf{u}_t = -\mathbf{M}\nabla p_o + \mathbf{M}_w \nabla p_c + [\mathbf{M}_w \rho_w + \mathbf{M}_o \rho_o]\,\mathbf{g} \\ \varepsilon \frac{\partial S_w}{\partial t} + \nabla \cdot \{-\mathbf{M}_w\,[\nabla p_o - \nabla p_c - \rho_w \mathbf{g}]\} = 0 \end{array}\right. \tag{32}$$

with initial and boundary conditions discussed below.

2.4 Boundary and interface conditions

Interface conditions

Necessary initial and boundary conditions include conditions at the interface, $\Gamma_{\omega\eta}$, between two different homogeneous regions ω and η when considering a heterogeneous porous medium. At $\Gamma_{\omega\eta}$, it is necessary to ensure flux and pressure continuity for each phase. These conditions, with our particular formulation, can be written as:

$$\begin{array}{l} \mathbf{u}_t^{\eta} \cdot \mathbf{n}_{\omega\eta} = \mathbf{u}_t^{\omega}.\mathbf{n}_{\omega\eta} \quad at \;\; \Gamma_{\omega\eta} \\ \mathbf{u}_w^{\eta} \cdot \mathbf{n}_{\omega\eta} = \mathbf{u}_w^{\omega}.\mathbf{n}_{\omega\eta} \quad at \;\; \Gamma_{\omega\eta} \\ p_c^{\omega} = p_c^{\eta} \quad at \;\; \Gamma_{\omega\eta} \end{array} \tag{33}$$

where $\mathbf{n}_{\omega\eta}$ is the unit vector normal to $\Gamma_{\omega\eta}$ and directed from the $\omega-$region towards the $\eta-$region.

Boundary conditions

Several types of boundary conditions are possible for this kind of problem. The conditions classically employed are of the imposed pressure type, imposed flow rate type or impermeable boundaries. In the following, we consider a given domain delimited by an inlet, an outlet and lateral surfaces. Thus the system to be solved is:

$$\left\{\begin{array}{l} \nabla \cdot (\mathbf{u}_t) = 0 \\ \mathbf{u}_t = -\mathbf{M}\nabla p_o + \mathbf{M}_w \nabla p_c + [\mathbf{M}_w \rho_w + \mathbf{M}_o \rho_o]\,\mathbf{g} \\ \varepsilon \frac{\partial S_w}{\partial t} + \nabla \cdot \{-\mathbf{M}_w\,[\nabla p_o - \nabla p_c - \rho_w \mathbf{g}]\} = 0 \\ \text{At the inlet:} \quad \mathbf{u}_w \cdot \mathbf{n}_i = u_{imposed} \text{ or } p_o = p_{imposed};\; S_w = 1 - S_{or} \\ \text{On the lateral surfaces} \quad \mathbf{u}_t \cdot \mathbf{n}_l = 0 \\ \text{At the outlet:} \\ \left\{\begin{array}{c} p_o = p_{atm} \\ \text{As long as } S_w(\mathbf{r}_e, t) < 1 - S_{or};\; \mathbf{u}_w \cdot \mathbf{n}_e = 0 \\ \text{When } S_w(\mathbf{r}_e, t) = 1 - S_{or};\; \text{simulation end} \end{array}\right. \\ \text{Initial conditions:} \\ p_o(\mathbf{r}, t=0) = p_0(\mathbf{r}); \quad S_w(\mathbf{r}, t=0) = S_0(\mathbf{r}) \end{array}\right. \tag{34}$$

where $\mathbf{r}$ and t are respectively the position vector and time variable, $\mathbf{r}_e$ the position vector corresponding the outlet face. We have denoted by $\mathbf{n}_i$, $\mathbf{n}_e$ and $\mathbf{n}_l$ respectively the unit vectors normal to the inlet face, the exit face and the lateral surfaces that are supposed to be impervious. Since our study focuses on imbibition, the inlet face is assumed to be in contact with water and therefore at a saturation of $1 - S_{or}$. Either imposed pressure or imposed flow-rate conditions at the inlet of the medium are considered in this work. When flow-rate is imposed, taking into account Eq. (26), a suitable choice of a general Reynolds number, Re, for our problem is

$$\mathrm{Re} = k\beta \left\|\mathbf{u}_t\right\| \max_{\alpha} \left(\frac{\rho_\alpha}{\mu_\alpha}\right) \tag{35}$$

For an imposed pressure condition, the Reynolds number as defined above varies as a function of time. For this case, an upper bound of the Reynolds number can be defined as follows

$$\mathrm{Re} = \max_{\kappa,\alpha}\left(\frac{k_\kappa \beta_\kappa \rho_\alpha u_{\kappa,\alpha}}{\mu_\alpha}\right) \tag{36}$$

in which κ designates homogeneous regions composing the medium, while $\alpha = o, w$. In this equation, an estimation of the velocity, $u_{\kappa,\alpha}$, obtained on the basis of the Forchheimer equation for one-dimensional single-phase flow of the $\alpha-$phase in the $\kappa-$region is given by

$$u_{\kappa,\alpha} = \frac{1}{2\rho_\alpha \beta_\kappa}\left(-\frac{\mu_\alpha}{k_\kappa} + \sqrt{\frac{\mu_\alpha^2}{k_\kappa^2} + 4\rho_\alpha \beta_\kappa \frac{\triangle p_\alpha}{L}}\right) \tag{37}$$

in which $\triangle p_\alpha$ corresponds to the pressure difference between the inlet and the outlet faces i.e. over the total length of the medium L. With this estimation of the velocity, the Reynolds number can be written as

$$\mathrm{Re} = \frac{1}{2}\max_{\kappa,\alpha}\left(-1 + \sqrt{1 + \frac{4\rho_\alpha \beta_\kappa k_\kappa^2}{\mu_\alpha^2}\frac{\triangle p_\alpha}{L}}\right) \tag{38}$$

While the pressure boundary condition at the outlet face corresponds to the fact that oil leaves the porous medium at atmospheric pressure, the choice of the saturation boundary condition is rather delicate. The boundary condition proposed in Eq. (34) mimics a classical "end effect" (Marle, 1972). Indeed, when simulating imbibition, the medium is initially saturated with oil and water is injected. The fluid which thus primarily leaves the porous medium at the outlet face is oil. Water is accumulated at the outlet ($\mathbf{u}_w \cdot \mathbf{n}_e = 0$) as long as the saturation is below $1 - S_{or}$ and is allowed to break through only when the maximum water saturation is reached, which means that the front has entirely swept the medium. This boundary condition leads to exaggerated end effects under certain conditions. For this reason, an alternative outlet condition has also been considered. It consists in violating the capillary pressure relationship at the outlet face by letting water leave the medium without imposing any special conditions.

3 Discretization and numerical modelling

In order to discretize the system of equations in space, we use a finite volume method over a staggered grid and a first order upwind scheme to estimate mobilities. The scheme in time, identical to that used for traditional two-phase flow in Darcy's regime, is of type IMPES in which the oil pressure is determined implicitly and water saturation is calculated in an explicit manner (Aziz and Settari, 1979; Chen et al., 2004). This scheme decouples the pressure and saturation equations, thus reducing the computational effort required for their solution. This method is efficient and simple and requires less computer memory compared to other methods such as simultaneous solution (SS) methods or fully implicit ones (sequential solution method SEQ). However, the IMPES method requires more restrictive time steps than implicit algorithms on the basis of a stability criterion associated to the explicit part of the scheme.

3.1 Stability

There are two stability limits which can be studied independently (Aziz and Settari, 1979). The first concerns the explicit treatment of the capillary pressure and depends on the magnitude of $\frac{dp_c}{dS_w}$. The second is related to the explicit treatment of the mobilities. For two-phase flow in Darcy's regime, the first limit being rather complex, a physical criterion based on the second limit is generally imposed in industrial codes. This criterion stipulates that during a time step, each grid-block cannot be flooded by a volume of fluid larger than the pore-volume it contains, i.e.

$$\Delta t \leq \Delta t_{\text{lim}} = \frac{\delta \varepsilon \Delta x \Delta y \Delta z}{u_{tx} \Delta y \Delta z + u_{ty} \Delta z \Delta x + u_{tz} \Delta x \Delta y} \tag{39}$$

where Δx, Δy and Δz are the grid-sizes in the three directions of space, u_{tx}, u_{ty}, and u_{tz} are the three components of the total velocity, $\mathbf{u}_t$, and δ is a selected security coefficient less than 1. Since the first stability limit is ignored, the use of this criterion, even in Darcy's regime, does not guarantee the stability of the IMPES method. In this work, without performing a detailed stability analysis, the criterion imposed by Eq. 39 was used. A 3D numerical tool was developed to solve inertial two-phase flow in heterogeneous porous media based on the physical model described above and having the features briefly detailed below.

3.2 Algorithm

On the basis of the initial imposed saturation field, relative permeabilities, capillary pressure and relative inertial coefficients are calculated at each point at the initial time $t = 0$. As discussed above, these parameters can be obtained from laboratory experiments and/or correlations established in the literature and are considered known for our simulation. This allows the computation of the oil pressure at each node at $t = \Delta t$ implicitly by solving the discretized version of the first relation in Eq. (34) in which the total velocity has been substitued from the second relation. In this resolution, saturations in the capillary pressure and in the mobilities are taken at the previous time step (initial condition for the first time step). The treatment of the velocity in the mobilities is performed using three different schemes and will be discussed later. The symmetric linear system corresponding to the implicit treatment of the oil pressure is solved by a Conjugate Gradient method. Using the third relation in Eq. (34), the water saturation at the same time step is computed in an explicit manner. Then p_w, $\mathbf{u}_o$ and $\mathbf{u}_w$ and therefore the total velocity, $\mathbf{u}_t$, are computed. Before proceeding to the next time step, the corresponding Δt is determined based on Eq. (39).

3.3 Treatment of non-linearities

As mentioned above, in order to compute the oil pressure at the time step $n+1$, saturations are evaluated at the previous time step n as stipulated by the explicit scheme. However, another important issue is the choice of the position for the estimation of the mobilities when evaluating velocities at the interface between two nodes. Indeed, velocities, and therefore pressure gradients are evaluated at the interface between two grid-blocks, while saturations, and thus mobilities, are evaluated at the center of grid-blocks. To circumvent this difficulty, an upwind scheme classically used in petroleum engineering is employed. It consists in estimating mobilities using the value of saturation on the node located upwind to the flow with regards to the interface which ensures physical results.

As already mentioned, the main difficulty lies in the correct estimation of the mobilities. For this reason, special care must be taken in treating these terms. In this work, three different methods are proposed: the fixed point iteration method, the purely explicit scheme or the Adams-Bashford method.

Fixed point iteration method

To take into account the nonlinear dependence of the Darcy-Forchheimer equation on velocity, a classical fixed point iteration method can be used for the computation of the oil pressure p_o. This iterative process starts with the initialization of the velocity of each phase at zero. These velocity fields are used to evaluate mobilities and the resulting oil pressure field is used to calculate a new value of the

flow velocity field (1st iteration). The fixed point iterations are repeated, without any time iterations, until two successive velocity fields are sufficiently close:

$$\frac{\left|\left\|\left(\mathbf{u}_\alpha^{n+1}\right)^{k+1}\right\| - \left\|\left(\mathbf{u}_\alpha^{n+1}\right)^{k}\right\|\right|}{\left\|\left(\mathbf{u}_\alpha^{n+1}\right)^{k}\right\|} \leq \varepsilon_r \qquad (\alpha = o,\ w) \tag{40}$$

The index k corresponds to the fixed point iteration, $n+1$ to the time iterations and ε_r is a user-fixed tolerance error. For the next time-steps, the last computed velocity fields are used to initialize the fixed point iterations.

Purely explicit method

The second scheme used is purely explicit. It consists in using the velocity fields of the preceding time-step, $\mathbf{u}_\alpha^n$, in the expression of the mobility (Eq. 27) for calculating oil pressure at time $t = (n+1)\,\Delta t$.

Adams-Bashford method

Finally the third scheme is an Adams-Bashford method. It consists of a time extrapolation of the velocity fields from two previous time steps in order to evaluate the Reynolds number intervening in the mobility. Since $\|\mathbf{u}_\alpha\|$ is to be estimated at $t = (n+1)\,\Delta t$, this scheme can be written as

$$\left\|\mathbf{u}_\alpha^{n+1}\right\| = \left(\frac{\Delta t_{_{n-1,n}} + \Delta t_{_{n-2,n-1}}}{\Delta t_{_{n-2,n-1}}}\right)\left\|\mathbf{u}_\alpha^{n-1}\right\| - \left(\frac{\Delta t_{_{n-1,n}}}{\Delta t_{_{n-2,n-1}}}\right)\left\|\mathbf{u}_\alpha^{n-2}\right\| \qquad (\alpha = o,\ w) \tag{41}$$

in which $\Delta t_{_{n-1,n}}$ is the time step between the two instants t_{n-1} and t_n, different from $\Delta t_{_{n-2,n-1}}$ in the general case. In the particular case of constant time step, the velocity in Eq. (27) is taken equal to $2\left\|\mathbf{u}_\alpha^n\right\| - \left\|\mathbf{u}_\alpha^{n-1}\right\|$.

4 Validation and tests on the schemes

In order to validate our numerical tool, its results have been compared to those obtained using a semi-analytical solution of "Buckley-Leverett" type. On the basis of a the fractional flow theory, Buckley and Leverett (1942) proposed an analytical solution for one-dimensional flow of two incompressible, immiscible fluids in homogeneous porous media under negligible capillary pressure assumption and in the Darcy regime.

4.1 Analytical solution for inertial flow

The analytical resolution of the system of equations describing the inertial two-phase incompressible, immiscible flow in one-dimensional homogeneous porous media, under negligible capillary pressure assumption, leads to a traditional frontal displacement similar to that obtained for Darcy's regime (Wu, 2001).

In the case of one-dimensional inertial flow in the x-direction in a semi-infinite homogeneous porous medium of constant section A, the mass and momentum conservation equations presented above (Eqs. (28) and (16)) can be written as follows ($\alpha = o, w$):

$$-\frac{\partial u_\alpha}{\partial x} = \varepsilon \frac{\partial S_\alpha}{\partial t} \tag{42}$$

$$-\frac{\partial p_\alpha}{\partial x} = \frac{\mu_\alpha}{K_\alpha} u_\alpha + \beta_\alpha \rho_\alpha u_\alpha^2 \tag{43}$$

where u_α is the Darcy's velocity for the α-phase. To achieve the mathematical description of the physical problem, initial and boundary conditions must be indicated:

$$S_w(x, t=0) = S_{wi} \tag{44}$$

Since water is injected continuously with a known flow rate, $q(t)$, at the inlet face of the porous medium ($x = 0$), the associated boundary conditions are:

$$u_w(x=0,t) = q(t)/A \tag{45}$$

$$u_o(x=0,t) = 0 \tag{46}$$

According to the work of Wu (2001), the concept of fractional flow is employed to simplify the governing equation (42) in terms of saturations only. The fractional flow of the $\alpha-$phase is defined as:

$$f_\alpha = \frac{u_\alpha}{u_t} \qquad (\alpha = o, w) \tag{47}$$

with the evident relationship:

$$f_w + f_o = 1 \tag{48}$$

Introduction of f_w and f_o in the momentum balance equations leads to the following analytical expression of the fractional flow for the water-phase:

$$f_w = \frac{\left[-a + \left(a^2 + 4u_t b\left(\frac{\mu_o}{K_o} + \rho_o\beta_o u_t\right)\right)^{1/2}\right]}{2bu_t} \tag{49}$$

where

$$a = \frac{\mu_o}{K_o} + \frac{\mu_w}{K_w} + 2\rho_o\beta_o u_t \tag{50}$$

$$b = \rho_w\beta_w - \rho_o\beta_o \tag{51}$$

Equation (49) indicates that, for given injection rate and fluid properties, f_w is only a function of water saturation. The mass balance equation (42) can therefore be written in terms of the fractional flow:

$$\frac{\partial S_w}{\partial t} + W(S_w)\frac{\partial S_w}{\partial x} = 0 \tag{52}$$

where

$$W(S_w) = -\frac{dx}{dt} = \frac{q(t)}{\varepsilon A}\left(\frac{\partial f_w}{\partial S_w}\right)_t \tag{53}$$

Equation (52) is the frontal equation for non-Darcy immiscible two-phase displacement and has the same form as the Buckley-Leverett equation. The expression (53) shows that for a given time and injection flow rate each value of the saturation, S_w, is propagated in homogeneous porous media at a constant velocity $W(S_w)$. Actually, Eq. (52) is a hyperbolic transport equation which is solved classically using the method of characteristics. The Welge tangent method is used to determine a constant front (or shock) saturation, S_f, ahead of a smoothly varying saturation (Marle, 1972). This is required to keep a physically meaningful saturation profile.

4.2 Comparison with numerical simulations - validation

In this section, supposing negligible capillary effects, the system of equations is solved numerically for a 1D homogeneous porous medium. Results are compared to those obtained analytically using the Buckley-Leverett approach presented in the previous paragraph. Simulations were performed with the fixed point iteration scheme (see discussion below on the comparison of the three different schemes). This comparison was carried out with the physical parameters of Table 1. It must be noted that for the effective inertial coefficient, β, the correlation given in Eq. 20 is used with the necessary modification in the constant

($A = 2.923\ 10^{-6} m$) in order to give all properties in SI units. For the case considered in this section, Re is equal to 0.69 which is the same order of magnitude as unity. A more detailed discussion of the importance of inertial effects versus Reynolds number is proposed in the next section.

$k\ [m^2]$	1.10^{-11}	ε	0.4
k_{rw}	$S_w^{*\,2}$	τ	1.9
k_{ro}	$(1 - S_w^*)^2$	$\beta[m^{-1}]$	$\frac{A\tau}{\varepsilon k}$
$\rho_w[kgm^{-3}]$	1000	$\beta_{r\alpha}$	$k_{r\alpha}^{-1}$
$\rho_o[kgm^{-3}]$	900	S_{wi}	0.1
$\mu_w[Pa.s]$	10^{-3}	S_{or}	0.1
$\mu_o[Pa.s]$	$5\ 10^{-3}$		

Table 1: Numerical data for one-dimensional flow in homogeneous porous media

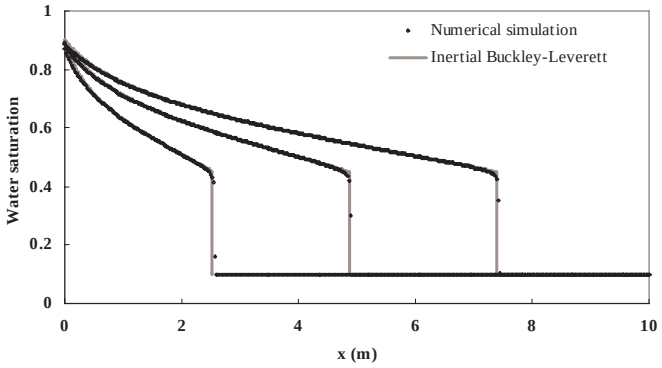

Figure 1: Comparison of saturation profiles for various times (t=10.4s, 20s and 30.4s) obtained by the numerical code with those resulting from the semi-analytical resolution of the Buckly-Leverett type, number of grid-blocks N=400.

The evolution of the water saturation profile $S_w(x,t)$ in the medium obtained by direct simulation on the one hand (using a one-dimensional version of the code with imposed flow rate at the inlet face) and by the quasi analytical resolution of the Buckley-Leverett type of equation on the other hand, shows a very good agreement as indicated in Fig. (1). This result validates our numerical tool in the particular case of one-dimensional two-phase flow in homogeneous porous media without capillary pressure.

4.3 Comparison of the three different schemes for treating nonlinearity

In this section, computations are performed on a one-dimensional homogeneous porous medium of length $10m$ with the characteristics indicated in Table 1. The capillary pressure is neglected in order to allow comparisons with the semi-analytical result described above. A velocity of $5\ 10^{-2} m s^{-1}$ is imposed at the inlet face corresponding to a Reynolds number defined by Eq. (35) equal to 0.69. The water saturation profiles are compared using the three different schemes mentioned above for the treatment of the nonlinearity resulting from the inertial term in the momentum balance equation. For these comparisons, identical grid sizes and time-steps are used.

For 50 grid blocks, the three schemes provide identical fields for a time step Δt equal to Δt_{lim} of Eq. (39) with a value of $\delta = 0.1$, leading to a time step of 0.16s (Fig. 2). In comparison to the semi-analytical

results, there is considerable numerical diffusion for all three schemes. With the same number of grid blocks ($N = 50$), but higher values of δ, the three schemes have a rather different behavior (Figs. 3 and 4). The Adams-Bashford method features instability behind the saturation front. Indeed, this method called extrapolation method by Aziz and Settari (1979) is known to introduce additional stability limitations. We can therefore affirm that, at least in the homogeneous case studied here, the most satisfactory result considering both the rarefaction zone and the front is obtained by the fixed point iteration method, which is adopted for all simulations performed in this paper.

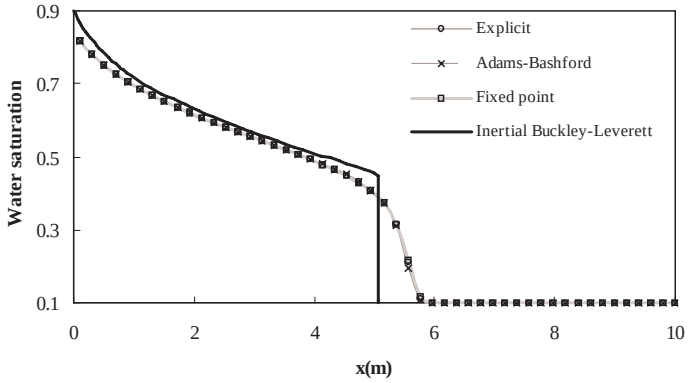

Figure 2: Comparison of saturation fields for a 1D homogeneous porous medium with negligible capillary pressure obtained with the three schemes, δ =0.1, time step $\Delta t = 0.16s$, number of grid blocks $N = 50$.

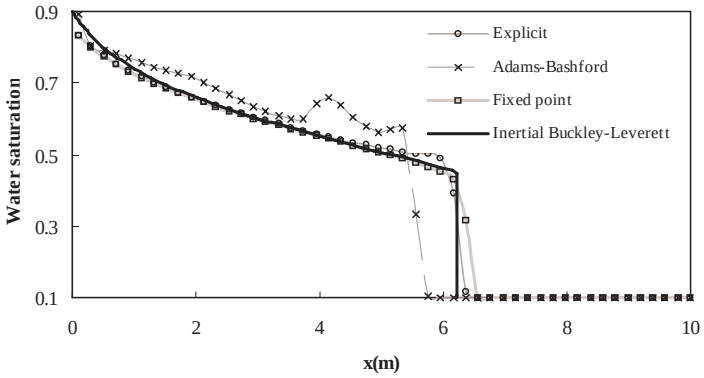

Figure 3: Comparison of saturation fields for a 1D homogeneous porous medium with negligible capillary pressure obtained with the three schemes, δ =0.4, time step $\Delta t = 0.64s$, number of grid blocks $N = 50$.

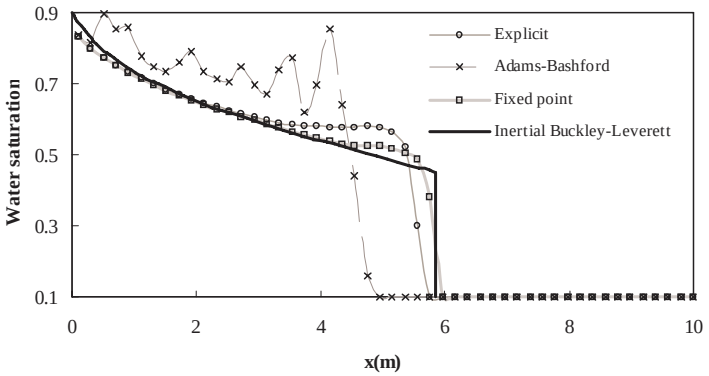

Figure 4: Comparison of saturation fields for a 1D homogeneous porous medium with negligible capillary pressure obtained with the three schemes, δ =0.5, time step $\Delta t = 0.8s$, number of grid blocks $N = 50$.

For 300 grid blocks and $\delta = 0.1$ leading to a time-step of $0.026s$, the three schemes provide identical fields close to the semi-analytical result (Fig. 5).

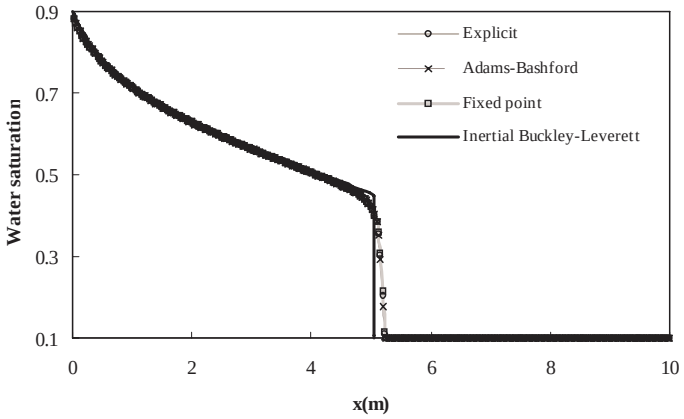

Figure 5: Comparison of saturation fields for a 1D homogeneous porous medium with negligible capillary pressure obtained with the three schemes, δ =0.1, time step $\Delta t = 0.026s$, number of grid blocks $N = 300$.

Finally, it must be noted that the explicit scheme is definitely more powerful in terms of computing time than the fixed point method and is less expensive in memory capacity than the Adams-Bashford scheme. It can give similar results as the two other methods for a small δ, therefore a small Δt. It gives satisfactory results for a large number of grid blocks and a small Δt. This conclusion however needs to be examined more thoroughly before generalizing to a heterogeneous medium.

5 Numerical experiments

In this section, we present numerical simualtions performed in different situations including homogeneous and heterogeneous media with capillary pressure. The objective is to highlight from comparison with

results obtained with the classical Darcy model the impact of inertial terms on the structure and kinetics of the saturation profiles

5.1 Comparison of Darcy and non-Darcy (Forchheimer) flow regimes

In this paragraph, we highlight the influence of the inertial terms on the saturation profiles (Figs. 6 to 8) for different Reynolds numbers, Re, defined in Eq. (35) in the case of 1D flows in homogeneous porous media. For a given Re, saturation profiles are obtained by solving the boundary value problem corresponding to two-phase flow in the Darcy regime. These profiles are compared to those obtained by the resolution of the boundary value problem (Eq. 34) taking into account the additional Forchheimer term corresponding to inertial effects. In these simulations, the flow rate is imposed at the inlet face. Saturation profiles are presented at two different times (see Figures 6 to 8). Three different velocities $u_w = u_t = 10^{-3}ms^{-1}, 10^{-2}ms^{-1}$ and $10^{-1}ms^{-1}$ corresponding to Reynolds number equal to 0.014, 0.14 and 1.4 respectively were considered. Although using Re defined by Eq. (35) allows a discussion of the inertial effects by a simple comparison of the Reynolds number with unity, we also indicate the corresponding values of a "classical Reynolds number" defined as $\mathrm{Re}_{cl} = \max_{\alpha}(\rho_\alpha/\mu_\alpha)\,\|\mathbf{u}_t\|\,d$ for completeness. As mentioned previously, d is the grain size obtained from the Kozeny-Carman relationship ($d = 10^{-4}m$). The corresponding values of Re_{cl} for the three cases under consideration are respectively 0.1, 1 and 10. The homogeneous medium for which the properties are reported in 1 is $10m$ long and its capillary pressure is taken as

$$p_c(S_w) = 500(1 - S^*)^2 \quad \text{Pa} \tag{54}$$

While inertial effects are negligible for a Re below 0.014, they become significant beyond this value. As expected, due to additional friction, the displacement of the saturation front is inhibited by inertial effects. Ignoring these effects for Reynolds numbers roughly larger than 0.01 may therefore lead to significant errors in watercut curves and a noticeable underestimation of the breakthrough time.

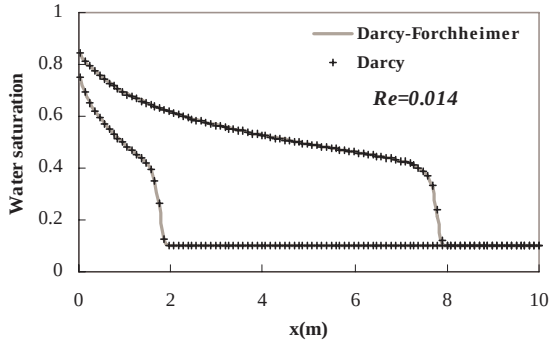

Figure 6: Water saturation profiles along the medium for $t = 300s$ and $1400s$ for a Reynolds number of 0.014.

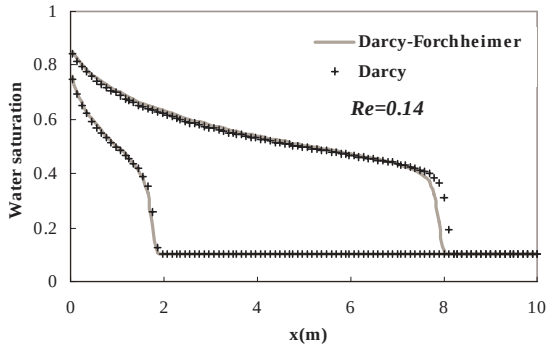

Figure 7: Water saturation profiles along the medium for $t = 30s$ and $145s$ for a Reynolds number of 0.14.

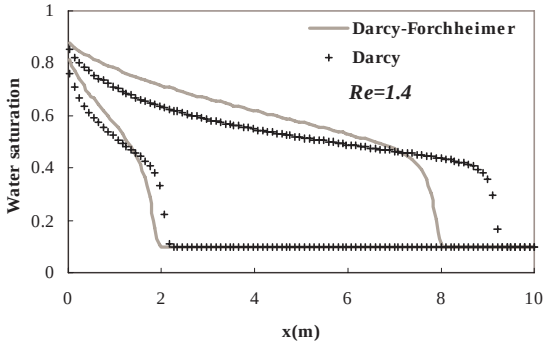

Figure 8: Water saturation profiles along the medium for $t = 3.5s$ and $16.5s$ for a Reynolds number of 1.4.

5.2 One-dimensional heterogeneous porous media

In this part of the work, results of simulations carried out on heterogeneous media comprising two regions (η and ω) in a one-dimensional configuration are presented. The flow is perpendicular to two layers of length $5m$ and of properties indicated in Table 2. Moreover, β, $\beta_{r\alpha}$, ρ_w, ρ_o, μ_w and μ_o were taken equal to those given in Table 1.

	$\eta - region$	$\omega - region$
$k(m^2)$	10^{-10}	10^{-11}
k_{rw}	S^{*3}	S^{*2}
k_{ro}	$(1 - S^*)^3$	$(1 - S^*)^2$
ε	0.436	0.225
S_{wi}	0.385	0.295
S_{or}	0.185	0.178
$p_c(Pa)$	$500\ (1 - S_w^*)^2$	$5000\ (1 - S_w^*)^2$

Table 2: Numerical data for the two regions for simulations of inertial flow in heterogeneous porous media

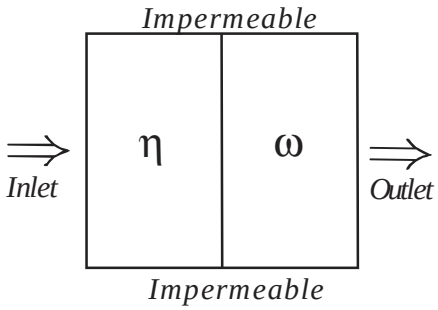

Figure 9: Two-layer medium with flow perpendicular to the strata.

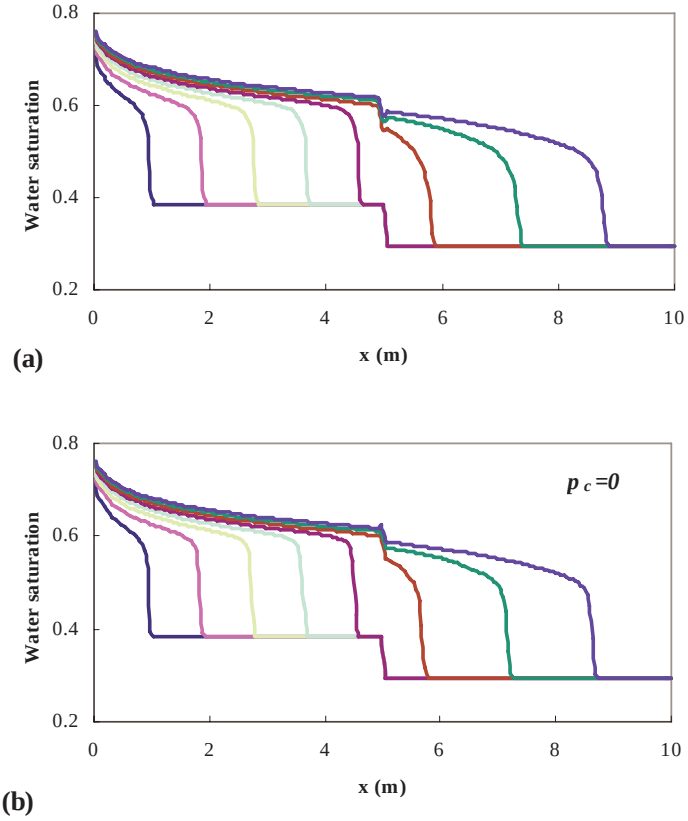

Figure 10: Saturation profiles along the medium for various times ($10^3 s$, $2.10^3 s$, $3.10^3 s$, $4.10^3 s$, $5.10^3 s$, $6.10^3 s$, $7.10^3 s$ and $8.10^3 s$) for one-dimensional flow in a heterogeneous porous medium (flow rate imposed at the inlet face); Reynold numbers: $\mathrm{Re}_\eta = 10^{-3}$, $\mathrm{Re}_\omega = 2.10^{-3}$; (a) with capillary pressure, (b) without capillary pressure.

The configuration presented in Fig. (9) is studied for different values of injection flow rates leading to different Reynolds numbers (Re_η and Re_ω) in the two regions. A first test case consists in injecting water into the more permeable zone (η). For a displacement in the Darcy regime, i.e. at very low injection rate, the influence of capillary pressure is examined. The capillary pressure effects are small in the case

studied here and do not cause significant modifications in the saturation profiles (Fig. 10). These effects become even more negligible as the flow rate increases. While for Reynolds numbers, Re_η and Re_ω, equal to 0.09 and 0.17 respectively, the saturation profiles are only slightly modified in comparison to the Darcy regime profiles (Fig. 11), further increase of the flow rate leads to significant modifications in the saturation profiles (Fig. 12). In fact, it can be seen in this last case that the saturation jump at the $\eta\omega$ interface is reversed when compared to the saturation profiles obtained at lower velocities and reported in figures 10 and 11. Note that this effect results from inertial effects only and is not due to capillary forces. As expected, oil is evacuated from the medium in a more efficient manner for higher Reynolds numbers ($\mathrm{Re}_\eta = 1.27$ and $\mathrm{Re}_\omega = 2.46$). For this last case, a numerical simulation using the Darcy model leads to very different and therefore erroneous results (Fig. 12).

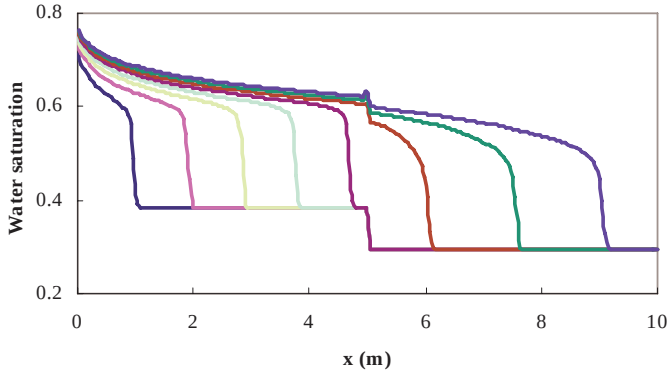

Figure 11: Saturation profiles along the medium for various times ($15s$, $30s$, $45s$, $60s$, $75s$, $90s$, $105s$ and $120s$) for one-dimensional flow in a heterogeneous porous medium (flow rate imposed at the inlet face); Reynold numbers: $\mathrm{Re}_\eta = 0.09$, $\mathrm{Re}_\omega = 0.17$.

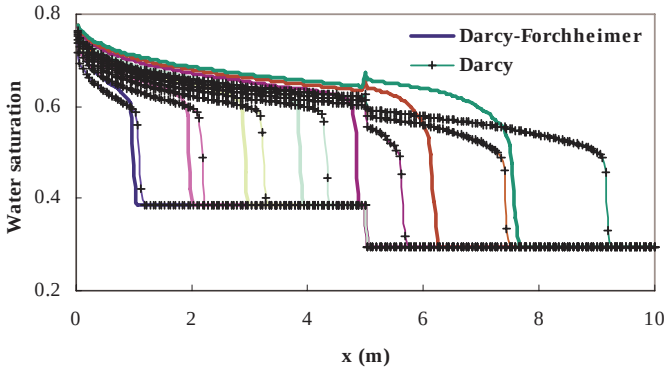

Figure 12: Saturation profiles along the medium for various times ($1.2s$, $2.4s$, $3.6s$, $4.8s$, $6s$, $7.2s$ and $8.4s$) for one-dimensional flow in a heterogeneous porous medium (flow rate imposed at the inlet face); Reynold numbers: $\mathrm{Re}_\eta = 1.27$, $\mathrm{Re}_\omega = 2.46$.

For high Reynolds numbers ($\mathrm{Re}_\eta = 1.27$ and $\mathrm{Re}_\omega = 2.46$), water has been injected into the low

permeability zone (ω). The corresponding water-saturation profiles are illustrated in Fig. (13). There is a significant difference between the saturation fields obtained using the Darcy-Forchheimer model and those obtained using the Darcy model.

For all cases, the saturation-jump at the interface between the two regions is well reproduced. It is important to note that this jump is not a numerical artefact and is simply related to the pressure continuity for both phases and therefore capillary pressure continuity at the interface between the two regions inducing saturation discontinuity.

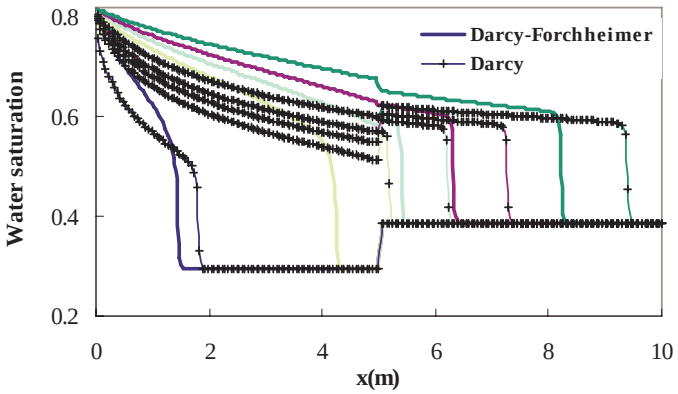

Figure 13: Saturation profiles along the medium for various times ($1.2s$, $2.4s$, $3.6s$, $4.8s$, $6s$, $7.2s$ and $8.4s$) for one-dimensional flow in a heterogeneous porous medium (flow rate imposed at the inlet face); water injected into the less permeable region; Reynold numbers: $\mathrm{Re}_\eta = 1.27$, $\mathrm{Re}_\omega = 2.46$.

5.3 Two-dimensional heterogeneous porous media

In this paragraph, results of simulations carried out on heterogeneous media comprising two regions (η and ω) in two-dimensional configurations are presented. These simulations are performed with the parameters of Table (2). The values of β, $\beta_{r\alpha}$, ρ_w, ρ_o, μ_w, and μ_o are taken equal to those given in Table (1). Two cases are considered:

- Stratified case corresponding to a two-layer medium with flow parallel to the layers of thickness $0.5m$ and of length $1m$. (Fig.14).

- Nodular case corresponding to a heterogeneous medium composed of a block of η-region with dimensions $1m \times 1m$, with a centered inclusion of ω-region of size $0.25m \times 0.25m$. (Fig. 15).

For the cases studied here, oil-pressure is imposed at the inlet face. The Reynolds number given here is therefore given by Eq. (38).

Stratified case

Saturation fields obtained for a low Reynolds number ($\mathrm{Re} = 6.3\ 10^{-3}$) with and without capillary pressure are first compared (Figs. 16 and 17). The pressures imposed at the inlet and outlet faces are respectively $1.05\ 10^5 Pa$ and $10^5 Pa$. In this particular case of low pressure gradient in the medium, capillary pressure and capillary pressure gradient contrast in the two layers lead to perturbations at the interface between the two layers. As it can be seen from figure 18, a simulation with the same boundary conditions but with p_{c_0} (see Eq. (15)) for the η-region equal to $4000Pa$ leads to a smooth saturation front.

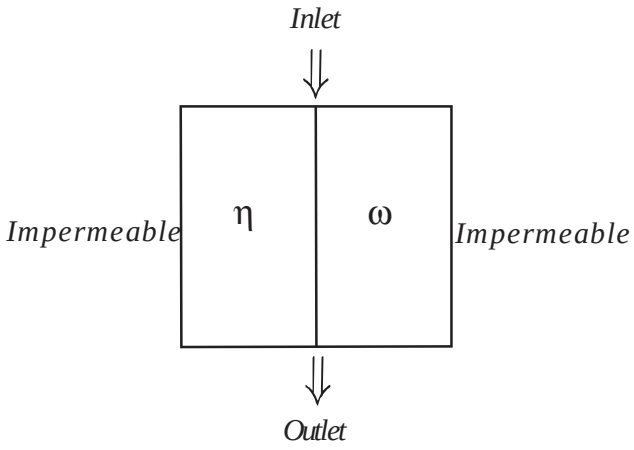

Figure 14: Stratified medium with flow parallel to the layers.

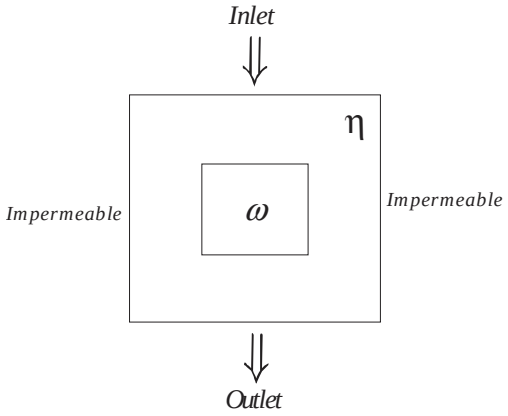

Figure 15: Geometrical configuration for 2D heterogeneous porous medium with inclusion.

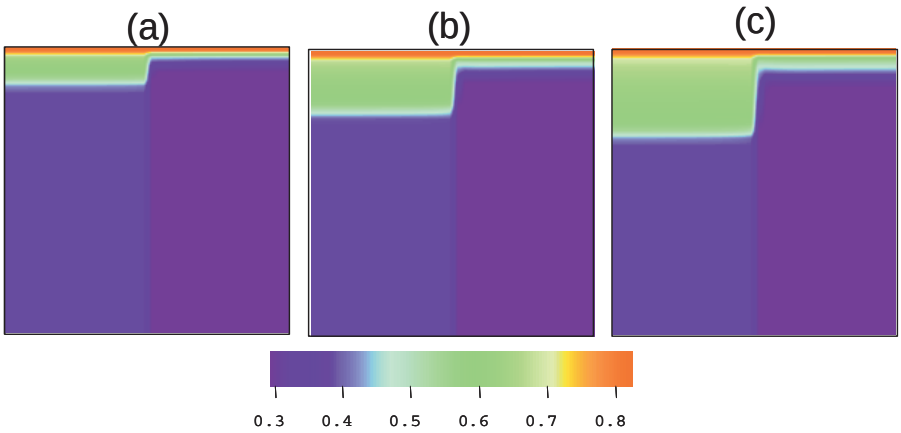

Figure 17: Evolution of the saturation fields at three given times (a) t=100s, (b) t=200s, (c) t=300s for two dimensional flow in a two-layer medium. The Darcy-Forchheimer model is used with imposed pressure at the inlet and zero capillary pressure.

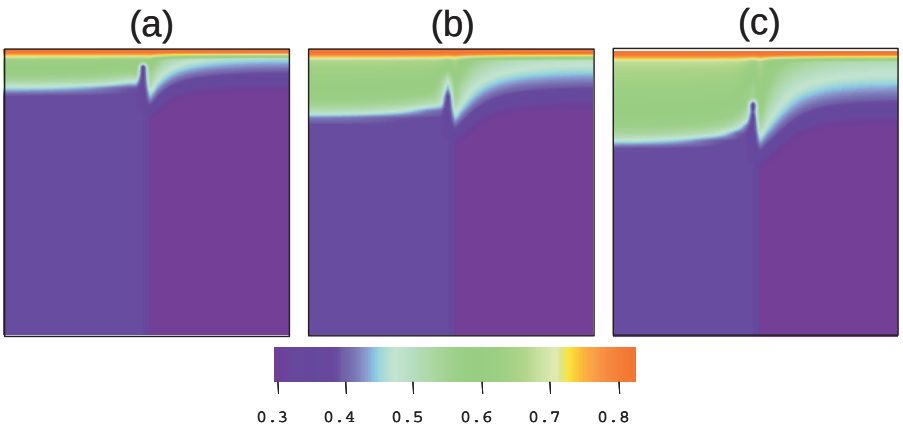

Figure 16: Evolution of the saturation fields at three given times (a) t=100s, (b) t=200s, (c) t=300s for two dimensional flow in a two-layer medium. The Darcy-Forchheimer model is used with imposed pressure at the inlet.

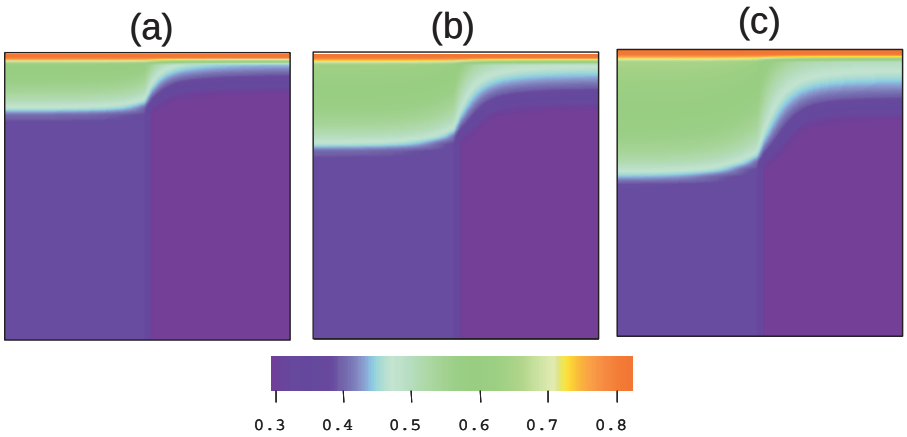

Figure 18: Evolution of the saturation fields at three given times (a) $t = 100s$, (b) $t = 200s$, (c) $t = 300s$ for two dimensional flow in a two-layer medium. The Darcy-Forchheimer model is used with imposed pressure at the inlet and with p_{c0} in the $\eta-$region equal to $4000Pa$.

For a high value of the Reynolds number (Re = 3.1), corresponding to imposed inlet and outlet pressures of $10^7 Pa$ and $10^5 Pa$ respectively, the capillary pressure has no influence on the saturation profiles as it can be seen by comparing fields obtained with and without capillary pressure (Figs. 19 and 20).

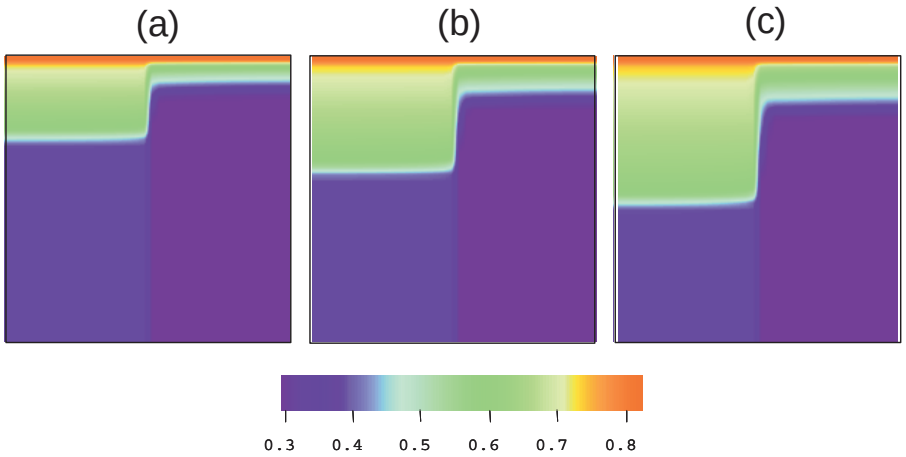

Figure 19: Evolution of the saturation fields at three given times (a) t=0.22s, (b) t=0.33s, (c) t=0.44s for two dimensional flow in a two-layer medium. The Darcy-Forchheimer model is used with imposed pressure at the inlet.

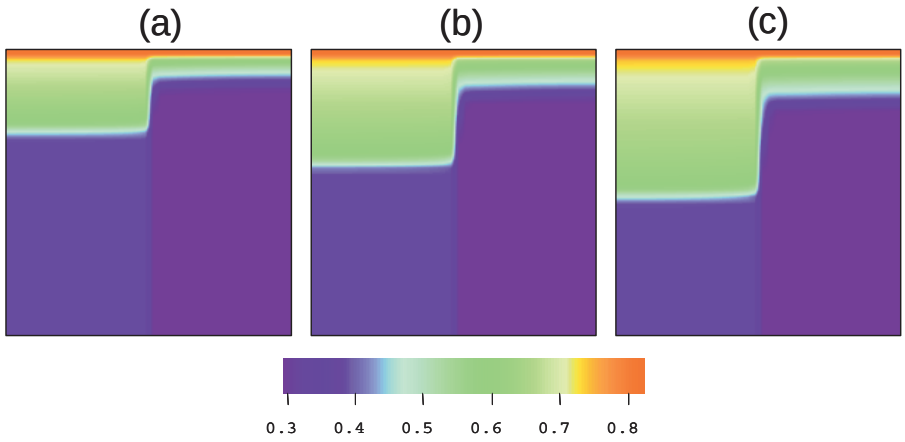

Figure 20: Evolution of the saturation fields at three given times (a) t=0.22s, (b) t=0.33s, (c) t=0.44s for two dimensional flow in a two-layer medium. The Darcy-Forchheimer model is used with imposed pressure at the inlet and zero capillary pressure.

Finally, for a Reynolds number equal to 3.1, the saturation fields obtained using the Darcy-Forchheimer model presented in Fig. (19) are compared to those obtained for the same times using the Darcy model (Fig. 21). The latter show a much faster propagation of the front in the more permeable η-region while, there is no significant difference in the front displacement in the less permeable ω-region. We note here that Reynolds number as defined in Eq. (38) is mainly representative of the behavior in the more permeable zone, since the maximal value in this relation is obtained for the β-phase in the η-region.

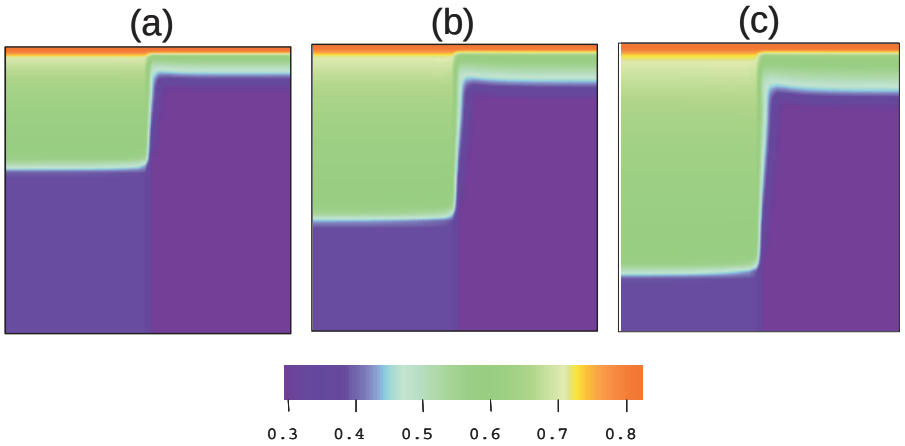

Figure 21: Evolution of the saturation fields at three given times (a) t=0.22s, (b) t=0.33s, (c) t=0.44s for two dimensional flow in a two-layer medium. The Darcy model is used with imposed pressure at the inlet.

Nodular case

For a small Reynolds number ($\mathrm{Re} = 6.3\ 10^{-3}$), corresponding to imposed inlet and outlet pressures of $1.05\ 10^5 Pa$ and $10^5 Pa$ respectively, the influence of capillary pressure has first been investigated. In this case of an inclusion of a less permeable zone in a more permeable one, capillary effects have significant influence on the saturation fields (see Figs. 22 and 24). As already discussed for the stratified case, our choice of capillary pressure curves leads to a perpurbed saturation front at the interface between

the two media. Decreasing the capillary pressure contrast (p_{c_0} equal to 4000 Pa and 5000 Pa for η-region and ω-region respectively) leads to more spread and less perturbed fronts (Fig. 23). For higher Reynolds number, capillary effects are negligible as can be seen by comparing figures 25 and 26. The last comparison is performed between the fields obtained using the Darcy-Forchheimer model (Fig. 25), with those obtained using the Darcy model (Fig. 27) for a Reynolds number equal to 3.1. Again, for a given time, the saturation front has propagated much further in the more permeable matrix when the Darcy model is used, while there is no significant difference of the saturation field in the less permeable inclusion.

It should be noted that, for both 2D configurations presented here, the saturation jump between the two homogeneous regions is well reproduced.

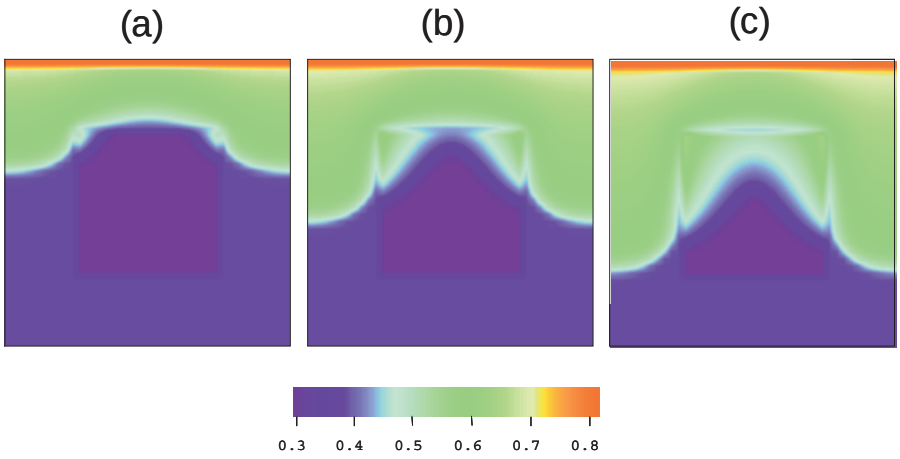

Figure 22: Evolution of the saturation fields at three given times (a) $t = 400s$, (b) $t = 600s$, (c) $t = 800s$ for two dimensional flow in a nodular medium with Re $= 6.4\ 10^{-3}$: simulaton with capillary pressure and imposed pressure at the inlet.

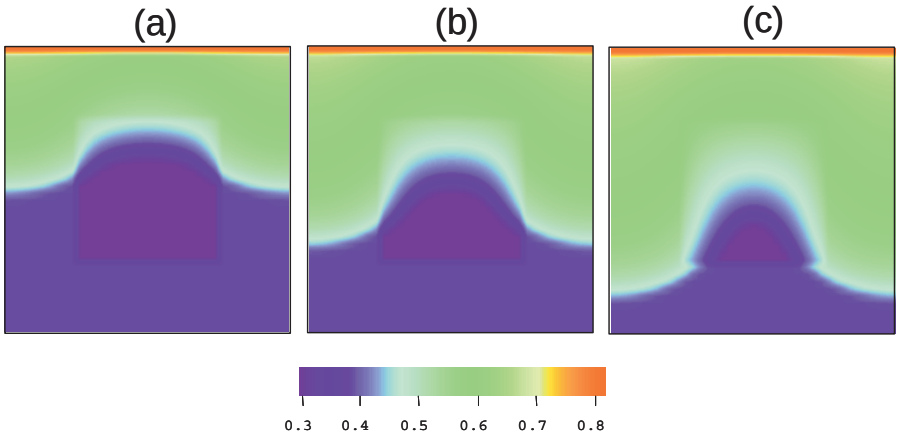

Figure 23: Saturation field at (a) $t = 400s$ (b) $t = 600s$ and (c) $t = 800s$ for two dimensional flow in a nodular medium with Re $= 6.4\ 10^{-3}$: simulaton with p_{c_0} in $\eta-$region equal to $4000Pa$ and imposed pressure at the inlet.

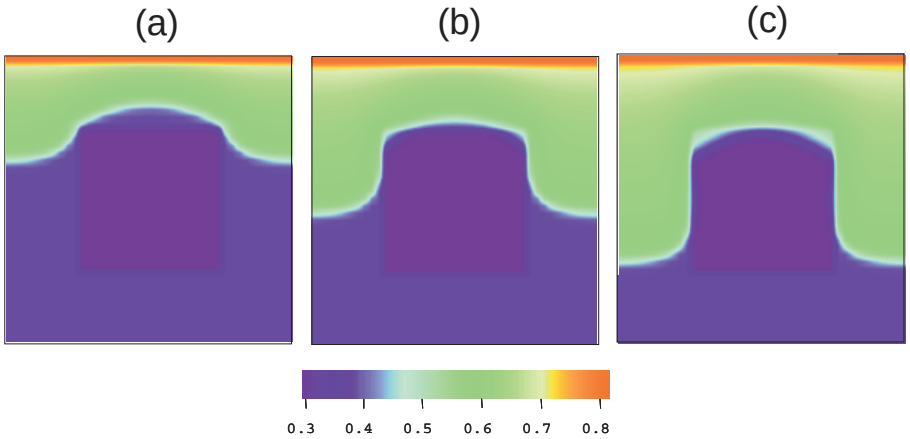

Figure 24: Evolution of the saturation fields at three given times (a) $t = 400s$, (b) $t = 600s$, (c) $t = 800s$ for two dimensional flow in a nodular medium with Re $= 6.4\ 10^{-3}$: simulaton with no capillary pressure and imposed pressure at the inlet.

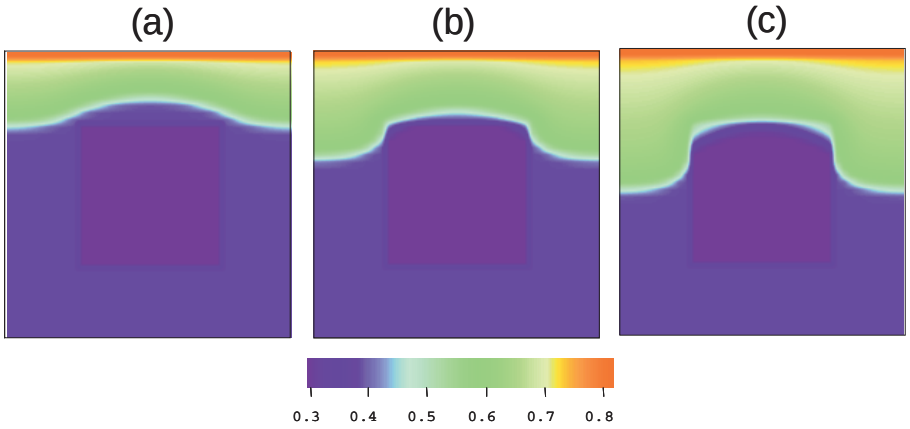

Figure 25: Evolution of the saturation fields at three given times (a) $t = 0.22s$, (b) $t = 0.33s$, (c) $t = 0.44s$ for two dimensional flow in a nodular medium with Re $= 12.6$. The Darcy-Forchheimer model is used with imposed pressure at the inlet.

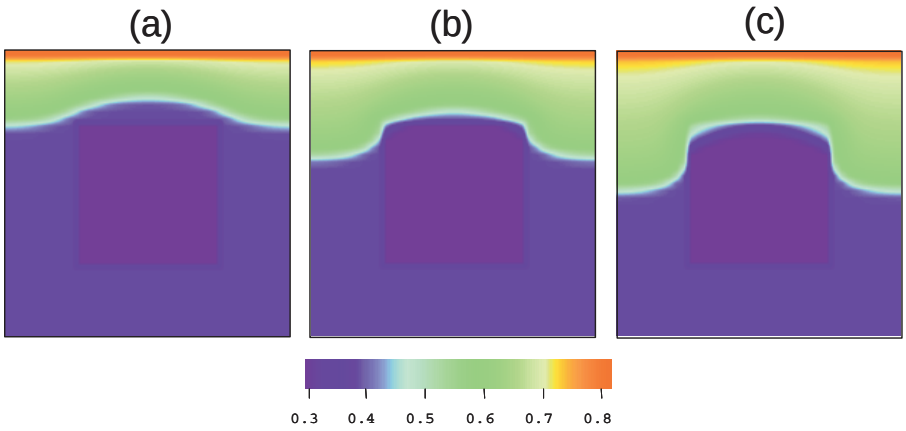

Figure 26: Evolution of the saturation fields at three given times (a) $t = 0.22s$, (b) $t = 0.33s$, (c) $t = 0.44s$ for two dimensional flow in a nodular medium with Re = 3.1. The Darcy-Forchheimer model is used without capillary pressure and imposed pressure at the inlet.

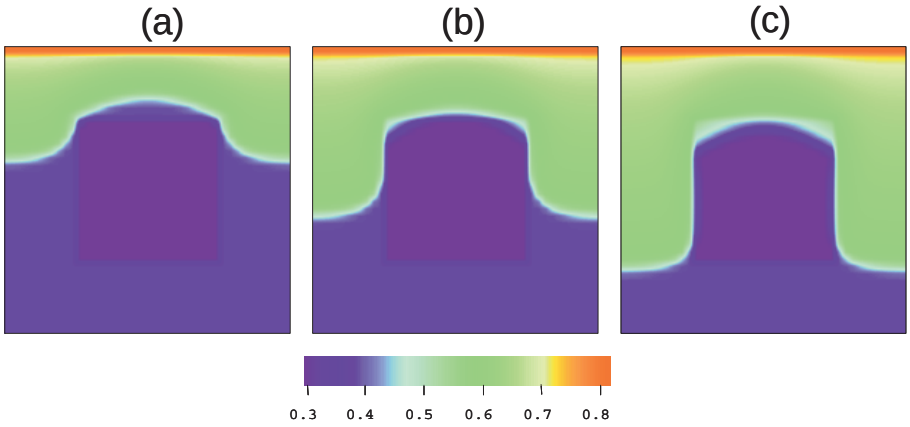

Figure 27: Evolution of the saturation fields at three given times (a) $t = 0.22s$, (b) $t = 0.33s$, (c) $t = 0.44s$ for two dimensional flow in a nodular medium with Re = 12.6. The Darcy model is used with imposed pressure at the inlet.

6 Conclusion

On the basis of the generalized Darcy-Forchheimer model, a numerical tool has been developed for simulating two-phase inertial immiscible and incompressible flow in three-dimensional heterogeneous porous media. A new definition of Reynolds number (Re) allowing the quantification of inertial effects by comparing Re with unity has been proposed. For one dimensional flow in homogeneous porous media, under negligible capillary pressure assumption, the numerical tool has been validated by comparing the results to those obtained using a semi-analytical solution of the Buckley-Leverett type. The importance of inertial effects on the transport of the saturation front has been first analyzed through 1D simulations of flow in homogeneous porous media.

Simulations have been carried out on a few test cases including one and two-dimensional heterogeneous porous media. The behavior of the saturation fields and particularly the jump at the interface between two regions of contrasted properties (permeability, capillary pressure, ...) is restored in a very satisfactory manner. For negligible Reynolds numbers, the importance of capillary effects is investigated. For high Reynolds numbers, capillary effects are shown to be negligible. For a given sufficiently high Reynolds number, saturation fronts obtained by taking into account the quadratic correction are compared to fronts obtained when the correction is neglected for homogeneous and 1D and 2D heterogeneous configurations showing very significant modifications in saturation fields. Although the differences observed are dependent on the choice of the inertial coefficient (chosen here in agreement with experimental correlations provided in the literature), it is shown that breakthrough curves are underestimated when inertial effects are neglected. This work provides a useful tool for future analysis and comprehension of macroscopic inertial two-phase flow in heterogeneous porous media.

References

Abdobal, S.: 2002, *Ecoulements Diphasiques En Milieux Poreux: Etude Expérimental Des Écoulements Liquide-Gaz et Liquide-Liquide À Forts Débits*, PhD thesis, Institut National Polytechnique de Lorraine.

Ahmadi, A. and Quintard, M.: 1995, Calculation of large-scale properties for multiphase flow in random porous media, *Iranian Journal of Science and Technology* **9, No. 1 Transaction A**, 11–37.

Auriault, J. L.: 1987, Nonsaturated deformable porous media: Quasisatics, *Transport in Porous Media* **2**(1), 45–64.

Aziz, K. and Settari, A.: 1979, *Petroleum Reservoir Simulation*, Elsevier Applied Science Publishers, London.

Bear, J., Braester, C. and Menier, P. C.: 1987, Effective and relative permeabilities of anisotropic porous media, *Transport in Porous Media* **2 (3)**, 301–316.

Brooks, R. H. and Corey, A. T.: 1966, Properties of porous media affecting fluid flow, *J. Irrig. and Drain. Div. (Proc ASCE) IR 2* **92**, 61–88.

Buchlin, J. M. and Stubos, A.: 1987, Phase change phenomena at liquid saturated self heated particulate beds, *in Bear, J. Buchlin, J.M. (Eds.), Modeling and Applications of Transport Phenomena, Vol. 4, Kluwer Academic Publishing, Dordrecht, The Netherlands* pp. 221–276.

Buckley, S. E. and Leverett, M. C.: 1942, Mechanism of fluid displacement in sands, *Trans. Am. Inst. Min. Metall. Pet. Eng.* **146**, 107–116.

Carman, P. C.: 1937, Fluid flow through a granular bed, *Trans. Inst. Chem. Eng.* **15**, 150–166.

Chavent, G.: 1976, A new formulation of diphasic incompressible flows in porous media, *Lecture note in Math. 503, Springer-Verlag* pp. 258–270.

Chen, Z., Huan, G. and Li, B.: 2004, An improved IMPES method for two-phase flow in porous media, *Transport in Porous Media* **54**, 361–376.

Corey, A. T.: 1954, The interrelation between gas and oil relative permeabilities, *Prod Mon.* **19**(1), 38–41.

Cornell, D. and Katz, D. L.: 1953, Flow of gases through consolidated porous media, *Indus. and Eng. Chem.* **45**, 2145–2152.

Darcy, H.: 1856, Fontaines publiques de la ville de Dijon, *Librairie des corps impériaux des ponts et chaussées et des mines, Paris* .

Ene, H. I. and Sanchez-Palencia, E.: 1975, Equations et phénomènes de surface pour l'écoulement dans un modèle de milieu poreux, *Journal de Mécanique* **14, 1**, 73–108.

Ergun, S.: 1952, Fluid flow through packed columns, *Chem. Eng. Prog.* **48**, 89–94.

Evans, E. V. and Evans, R. D.: 1988, Influence of an immobile or mobile saturation on non-darcy compressible flow of real gases in propped fractures, *J. Petrol. Technol* **40**(10), 1343–1351.

Evans, R. D., Hudson, C. S. and Greenlee, J. E.: 1987, The effect of an immobile liquid saturation on the non-Darcy flow coefficient in porous media, *J. SPE Prod. Engng Trans. AIME* **283**, 331–338.

Forchheimer, P.: 1901, Wasserbewegung durch boden. z., *Vereines deutscher ingnieure* **XXXXV**(49), 1781–1788.

Geertsma, J.: 1974, Estimating the coefficient of inertial resistant in fluid flow through porous media, *Society of Petroleum Engineers Journal* **October**, 445–450.

Honarpour, M., Koederitz, L. and Harvey, A. H.: 1986, *Relative Permeability of Petroleum Reservoirs*, CRC Press, Inc., Boca Raton, Florida.

Hubbert, M. K.: 1956, Darcy's law and the field equation of the flow of underground fluids, *Trans. SPE of AIME* **207**, 222– 239. (JPT).

Kalaydjian, F., Bourbiaux, J. M. and Lombard, J. M.: 1996, Predicting gas-condensate reservoir performance: How flow parameters are altered when approaching producing wells, *SPE 36715* **Proc.**, The APE Annual Technical Conference and Exhibition, Denver, Oct. 6–9.

Katz, D. L. and Lee, R. L.: 1990, *Natural Gas Engineering, Production and Storage, Chemical Engineering Series*, McGraw-Hill, New York.

Koederitz, L. F., Harvey, A. H. and Honarpour, M.: 1989, *Introduction to Petroleum Reservoir Analysis*, Gulf Publishing Company, Houston.

Lee, H. S. and Catton, I.: 1984, Two-phase flow in stratified porous media, *6th Information Exchange Meeting on Debris Coolability, Los Angeles* .

Li, D. and Engler, T. W.: 2001, Literature review on correlation of the non-Darcy coefficient, SPE Proc., SPE Permian Basin Oil and Gas Recovery Conference , Society of Petroleum Engineers, Richardson, TX. paper SPE 70015.

Lipinski, R. J.: 1980, A particle bed dryout model with upward and downward boiling, *Trans. Am. Nucl. Soc.* **35**, 350–358.

Lipinski, R. J.: 1982, A model for boiling and dryout in particle beds, *Report SAND 82-0756 (NUREG/CR-2646) Sandia Labs* .

Liu, X., Civan, F. and Evans, R. D.: 1995, Correlations of the non-Darcy flow coefficient, *J. Canad. Petrol. Technol.* **34**(10), 50–54.

Marle, C. M.: 1972, *Cours de Production, Tome IV, Les Écoulements Polyphasiques En Milieu Poreux*, Editions Technip, Paris.

Mei, C. C. and Auriault, J. L.: 1991, The effect of weak inertia on flow through a porous medium, *J. Fluid Mech* **222**, 647–663.

Muskat, M.: 1937, *Flow of Homogeneous Fluid Through Porous Media*, McGraw-Hill, New York.

Raats, A. A. C. and Klute, A.: 1968, Transport in soil: The balance of momentum, *Soil. Sci. Soc. Amer. Proc.* **32**, 161–166.

Saez, A. E. and Carbonnell, R. G.: 1985, Hydrodynamic parameters for gas-liquid co-current flow in packed beds, *AIChE* **31**, 52–62.

Scheidegger, A. E.: 1972, *The Physics of Flow Through Porous Media*, University of Toronto Press, Toronto, Canada.

Schulenberg, T. and Muller, V.: 1987, An improved model for two-phase flow through beds of coarse particles, *International Journal of Multiphase Flow* **13**, 87–97.

Skjetne, E. and Auriault, J. L.: 1999, High-velocity laminar and turbulent flow in porous media, *Transport in Porous Media* **36**(2), 131–147.

Tek, M. R., Coats, K. H. and Katz, D. L.: 1962, The effect of turbulence on flow of natural gas through porous reservoirs, *J. Petrol. Technol. Trans. AIME* **222**, 799–806.

Wahyudi, I., Montillet, A. and Khalifa, A. O. A.: 2000, Darcy and post-Darcy flows within different sands, *Journal of Hydraulic Research* **40(4)**, 519–525.

Wang, X., Thauvin, F. and Mohanty, K. K.: 1999, Non-Darcy flow through anisotropic porous media, *Chemical Engineering Science* **54**, 1859–1869.

Whitaker, S.: 1986a, Flow in porous media i: A theoretical derivation of Darcy's law, *Transport in Porous Media* **1**(1), 3–25.

Whitaker, S.: 1986b, Flow in porous media II: The governing equation for immiscible two-phase flow, *Transport in Porous Media* **1**(1), 105–125.

Whitaker, S.: 1996, The Forchheimer equation: A theoretical development, *Transport in Porous Media* **25**(1), 27–61.

Whitney, D. D.: 1988, *Characterization of the non-Darcy flow coefficient in propped hydraulic fractures*, Master's thesis, University of Oklahoma.

Wu, Y. S.: 2001, Non-darcy displacement of immiscible fluids in porous media, *Water Resources Research* **37**(12), 2943–2950.

Chapitre 5

Conclusions générales

Conclusions générales

Dans ce travail nous nous sommes intéressés aux écoulements mono- et diphasiques inertiels en milieux poreux homogènes et hétérogènes, et nous avons suivi simultanément deux approches, l'une à caractère théorique, l'autre à caractère numérique.

La première partie du travail qui repose sur une étude théorique du changement d'échelle par la méthode de prise de moyenne volumique des écoulements inertiels incompressibles monophasiques (Whitaker, 1996). En partant de l'équation de Navier-Stokes à l'échelle du pore, cette prise de moyenne fournit les équations macroscopiques exactes, ainsi que les problèmes de fermeture permettant de déterminer les propriétés macroscopiques pour ce type d'écoulement. Ce changement d'échelle conduit en particulier à un modèle plus général que le modèle classique de Forchheimer qui fait intervenir un coefficient de résistance inertiel scalaire. Il introduit une correction vectorielle à la loi de Darcy et un tenseur de correction inertiel $\mathbf{F}$. A partir de la résolution numérique du problème de fermeture et de l'écoulement, le comportement du tenseur de correction à la loi de Darcy en fonction du nombre de Reynolds, de l'orientation du gradient de pression, du désordre dans la structure et de la porosité a été étudié. Un grand nombre de simulations numériques effectués sur des milieux modèles bidimensionnels ont permis d'analyser les différents régimes d'écoulement en fonction du nombre de Reynolds. Ces régimes ont été étudié à partir d'une forme adimensionnelle de la force macroscopique supplémentaire exercée sur la structure et due aux effets inertiels en comparaison à celle exercée en régime de Darcy. Les conclusions suivantes peuvent être formulées :

- Pour des structures ordonnées, en général, le tenseur de correction $\mathbf{F}$ est un tenseur plein non-symetrique même pour une structure géométriquement isotrope. Ceci est en accord avec le fait que la force exercée n'est pas une traînée pure. Plus précisément cette force n'est pas alignée avec la vitesse moyenne. Le cas d'un gradient de pression appliqué selon un axe de symétrie d'une cellule représentative est une exception. Pour des milieux désordonnés isotropes, le tenseur $\mathbf{F}$ est diagonal quand il estimé sur un Volume Elémentaire Représentatif du milieu dont la taille augmente avec le nombre de Reynolds.

- L'intensité des effets inertiels augmente avec le nombre de Reynolds dans tous les cas. Il a été montré, cependant, que la définition du nombre de Reynolds joue un rôle essentiel dans la représentation et l'interprétation des résultats. Pour un milieu isotrope ordonné, à une valeur de Reynolds donnée, l'intensité des effets inertiels est une fonction décroissante de la porosité lorsque le nombre de Reynolds est défini à l'aide de la racine carrée de la perméabilité. Le comportement inverse est observé lorsque la dimension caractéristique pour la définition du nombre de Reynolds est la taille de grain.

- En accord avec la théorie, dans tous les cas étudiés ici, un régime d'inertie faible, caractérisé par une dépendance de la correction en la carré du Re, c'est-à-dire en puissance cubique de la vitesse est retrouvé. Dans la plupart des cas étudiés, l'intensité de la correction dans ce régime reste très faible, sauf pour les milieux ordonnés pour certaines orientations du gradient de pression.

- Pour des Re plus grand, le régime de forte inertie où la correction est supposée suivre une dépendance linéaire en Re (dépendance quadratique en vitesse) est généralement une approximation pertinente. Ce régime correspond à un intervalle de nombre de Reynolds d'extension variable centrée sur un point l'inflexion de la correction en fonction de Re. De plus, puisqu'il n'est pas purement quadratique, il conduit à l'introduction de "la perméabilité de Forchheimer" différente de la perméabilité intrinsèque si une correction de type Forchheimer est adoptée.

- Le comportement de la correction dans la zone de transition entre les régimes d'inertie faible et forte n'a pas été détaillé. En revanche, un Reynolds de transition minimisant l'écart entre les modèles proposés pour chaque régime est estimé. Lorsque Re est défini avec la racine carrée de la perméabilité, ce Reynolds

de transition est une fonction croissante de la porosité, alors que le comportement inverse est observé pour un Re défini avec la taille de grain comme dimension caractéristique. A porosité et perméabilité égales, ce Reynolds de transition décroît fortement lorsque du désordre structurel est introduit. L'étendue de la zone de transition n'est pas affectée sensiblement par le désordre structurel.

- Sur des structures désordonnées, la dépendance quadratique en vitesse de la correction à la loi de Darcy semble être une approximation robuste pour un large intervalle de nombre de Reynolds. De plus, le Reynolds de transition et le module de la correction en régime d'inertie faible restent petits, fournissant par là-même une explication au fait que ce régime est la plupart du temps ignoré lors des expériences de laboratoire.

- Malgré le caractère bidimensionnel de notre étude sur les milieux désordonnés, les résultats obtenus laissent à penser que les conclusions peuvent être étendues aux milieux réels 3D.

La deuxième partie du travail est consacrée à une étude théorique du changement d'échelle des écoulements diphasiques inertiels en milieu poreux homogène. La méthode de prise de moyenne volumique est appliquée aux équations de Navier-Stokes dans chaque phase. Le développement théorique est détaillé et l'ensemble des contraintes nécessaires à l'obtention d'une forme macroscopique des équations sont précisées. Ces contraintes correspondent à la séparation des échelles, à des contraintes d'échelle de temps, ainsi que sur des quantités faisant intervenir le nombre capillaire et le nombre de Weber.

L'équation de quantité de mouvement macroscopique obtenue pour chaque phase admet des termes de Darcy incluant un tenseur de perméabilité de couplage et des termes inertiels faisant intervenir un tenseur de correction inertiel et un tenseur de correction inertiel de couplage. Le développement conduit également à des problèmes de fermeture permettant une détermination explicite des tenseurs macroscopiques à partir des propriétés microscopiques.

Dans la dernière partie, nous avons mis en place un outil de simulation numérique 3D des écoulements diphasiques en milieu poreux hétérogène en régime inertiel basé sur un modèle de Darcy-Forchheimer généralisé. La méthode des volumes finis et un schéma IMPES ont été utilisés. La non-linéarité en vitesse associée au terme de Forchheimer a été traitée à l'aide de trois schémas différents. Dans le cas 1D homogène, sous l'hypothèse d'un gradient de pression capillaire nul, nous avons pu valider le code à l'aide d'une solution semi-analytique de type Buckley-Leverett.

Une première analyse en milieu homogène 1D de l'impact des effets inertiels sur le transport du front de saturation en fonction d'un nombre de Reynolds de l'écoulement convenablement choisi et justifié a été effectuée. Nous avons montré qu'à partir d'un nombre de Reynolds de l'ordre de 0.1, les effets inertiels deviennent significatifs et s'amplifient au delà de cette valeur.

Nous avons également illustré le cas d'écoulements de ce type sur des structures hétérogènes à l'aide de simulations effectuées sur des milieux comportant deux régions en configuration 1D et 2D. Dans le cas 1D, les deux strates sont orthogonales à l'écoulement tandis que les cas 2D correspondent aux milieux stratifiés avec écoulement parallèle aux strates. Nous avons également abordé le cas d'un milieu nodulaire. Nous avons montré que pour des valeurs élevées du nombre de Reynolds, les effets capillaires sont négligeables. En effet, les champs de saturation sont fortement modifiés lorsque les effets inertiels sont pris en compte. Dans ces conditions, l'utilisation d'un modèle de Darcy généralisé conduirait à une sous-estimation du temps de percée. Par ailleurs, ces simulations en milieu hétérogène 1D et 2D restituent de manière très satisfaisante le comportement de la saturation à l'interface entre deux régions de perméabilités fortement contrastées. Ce travail fournit donc un outil précieux pour l'analyse future des écoulements mutiphasiques inertiels en milieu poreux hétérogène.

Annexe 1

0.1 Modèle Numérique et Discrétisation

Dans cette annexe, on reprend le système d'équations d'écoulement diphasique inertiel en milieu poreux présenté au chapitre 4 :

$$div(\mathbf{u}_t) = 0 \tag{1a}$$

$$\mathbf{u}_t = -\mathbf{M}\nabla p_o + \mathbf{M}_w \nabla p_c + [\mathbf{M}_w \rho_w + \mathbf{M}_o \rho_o]\,\mathbf{g} \tag{1b}$$

$$\varepsilon \frac{\partial S_w}{\partial t} + \nabla \cdot \{-\mathbf{M}_w\,[\nabla p_o - \nabla p_c - \rho_w \mathbf{g}]\} = 0 \tag{1c}$$

$$p_o(\mathbf{r}_e, t) = p_{imp} \text{ ou } \mathbf{u}_w \cdot \mathbf{n}_e = 0 \quad \text{sur la face d'entrée} \tag{1d}$$

$$S_w(\mathbf{r}_e, t) = 1 - S_{o_r} \quad \text{sur la face d'entrée} \tag{1e}$$

$$\mathbf{u}_t \cdot \mathbf{n}_l = 0 \quad \text{sur les surfaces latérales}$$

$$\text{Sur la face de sortie} \begin{cases} p_o = p_{atm} \\ \text{Tant que } S_w(\mathbf{r}_s, t) < 1 - S_{or};\ \mathbf{u}_w \cdot \mathbf{n}_s = 0 \\ \text{Lorsque } S_w(\mathbf{r}_s, t) = 1 - S_{or};\ \text{fin de la simulation} \end{cases} \tag{1f}$$

$$p_o(\mathbf{r}, 0) = p_0(\mathbf{r}) \quad sur \quad V \tag{1g}$$

$$S_w(\mathbf{r}, 0) = S_0(\mathbf{r}) \quad sur \quad V \tag{1h}$$

Dans ce système les variables S_w et p_o considérées comme les inconnues correspondent à la saturation en eau et la pression en huile et $\mathbf{u}_t$ est la vitesse totale. Les variables $\mathbf{r}$, $\mathbf{r}_e$ et $\mathbf{r}_s$ symbolisent respectivement les vecteurs position dans le milieu et sur les faces d'entrée et de sortie. Les vecteurs $\mathbf{n}_e$, $\mathbf{n}_s$ et $\mathbf{n}_l$ correspondent aux vecteurs normaux sortant de la face d'entrée, de la face de sortie et de la surface latérale respectivement. Les tenseurs $\mathbf{M}$, $\mathbf{M}_w$ et $\mathbf{M}_o$ sont les mobilités totales, de la phase eau et de la phase huile respectivement. Ce sont des fonctions non-linéaires de la saturation en eau et de la vitesse. Dans le cas d'imbibition, sur la face d'entrée, l'eau est toujours présente ($S_w(\mathbf{r}_e, t) = 1 - S_{o_r}$) et ou bien la pression dans la phase huile est imposée ou bien la vitesse l'eau a l'entrée du milieu est imposée. La condition à la limite en pression, sur la face de sortie traduit le fait que l'huile sort à pression atmosphérique.

A ce stade, nous appliquons la méthode des volumes finis, comme méthode de discrétisation, au système d'équations ci-dessus. En raisonnant sur des bilan de flux, cette méthode permet de rester proche de la physique du problème et donc de mieux comprendre les phénomènes et leur interprétation.

Les relations complémentaires de pression capillaire et de saturation permettent de déterminer la saturation en huile, S_o et la pression en eau p_w :

$$p_c(S_w) = p_o - p_w \tag{2}$$

$$S_w + S_o = 1 \tag{3}$$

0.1.1 Ecoulement Monodimensionnel

On discrétise le milieu continu en mailles centrées sur les noeuds de calcul. On se basera sur le schéma de la Figure (1) pour appuyer notre raisonnement. Cette représentation est significative du cas bidimensionnel et tridimensionnel.

Les deux faces Γ_1 et Γ_3 sont les faces d'entrée/sortie de la maille, tandis que les faces Γ_2 et Γ_4 correspondent aux surfaces latérales imperméables. On applique la méthode de volumes finis, qui consiste à intégrer les équations de conservation précédentes sur les mailles.

On choisit d'évaluer les pressions et saturations au centre des mailles, ce qui impose l'écriture des vitesses et des gradients de pression sur les faces des mailles.

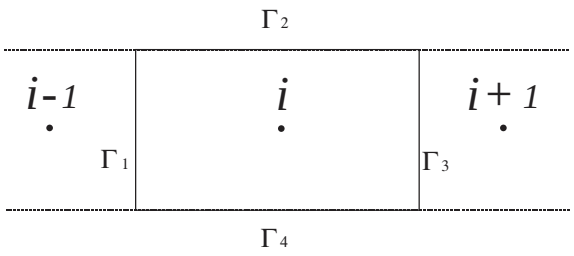

Figure 1: Représentation d'une maille pour l'écoulement monodimensionnel en milieux poreux

Les mobilités seront évaluées à l'aide de la saturation au noeud en amont de l'écoulement, ce qui correspond au schéma amont des pétroliers. Quant au schéma en temps, la méthode d'IMPES, Implicite en Pression et Explicite en Saturation est adoptée.

Equation en pression

Pour discrétiser l'équation de pression en huile, l'équation (1a) est intégrée sur le volume de contrôle V_c :

$$\int_{\Gamma} (\nabla \cdot \mathbf{u}_t) dV = 0 \tag{4}$$

Grâce au théorème de la divergence, on obtient :

$$\int_{V_c} (\nabla \cdot \mathbf{u}_t) dV = \int_{\Gamma} \mathbf{u}_t \cdot \mathbf{n} d\Gamma = 0 \tag{5}$$

$$\int_{\Gamma_1} \mathbf{u}_t \cdot \mathbf{n}_1 d\Gamma + \int_{\Gamma_2} \mathbf{u}_t \cdot \mathbf{n}_2 d\Gamma + \int_{\Gamma_3} \mathbf{u}_t \cdot \mathbf{n}_3 d\Gamma + \int_{\Gamma_4} \mathbf{u}_t \cdot \mathbf{n}_4 d\Gamma = 0 \tag{6}$$

où Γ est la surface extérieure du volume V composée de 4 faces Γ_i de vecteur unitaire normal sortant $\mathbf{n}_i$. A titre d'exemple, le calcul de l'intégrale sur la surface Γ_1 est décrit ci-dessous.

$$\begin{aligned} \int_{\Gamma_1} \mathbf{u}_t \cdot \mathbf{n}_1 d\Gamma &= -\int_{\Gamma_1} M(S_w, u_w, u_o) \nabla p_o \cdot \mathbf{n}_1 d\Gamma_1 + \int_{\Gamma_1} M_w(S_w, u_w) \nabla p_c \cdot \mathbf{n}_1 d\Gamma_1 \\ &\quad + \int_{\Gamma_1} M_w(S_w, u_w) \rho_w \mathbf{g} \cdot \mathbf{n}_1 d\Gamma_1 + \int_{\Gamma_1} M_o(S_w, u_o) \rho_o \mathbf{g} \cdot \mathbf{n}_1 d\Gamma_1 \end{aligned} \tag{7}$$

Dans le cas 1D, cela conduit à :

$$\begin{aligned} \int_{\Gamma_1} \mathbf{u}_t \cdot \mathbf{n}_1 d\Gamma &= \int_{\Gamma_1} M(S_w, u_w, u_o) \frac{\partial p_o}{\partial x} d\Gamma_1 - \int_{\Gamma_1} M_w(S_w, u_w) \frac{\partial p_c}{\partial x} d\Gamma_1 \\ &\quad - \int_{\Gamma_1} M_w(S_w, u_w) \rho_w g_x d\Gamma_1 - \int_{\Gamma_1} M_o(S_w, u_o) \rho_o g_x d\Gamma_1 \end{aligned} \tag{8}$$

avec g_x la composante de $\mathbf{g}$ selon la direction d'écoulement x. Le gradient de pression et les mobilités étant considérés constants sur les faces d'entrée et de sortie de la maille du fait que celles-ci sont petites, on a :

$$\int_{\Gamma_1} \mathbf{u}_t \cdot \mathbf{n}_1 d\Gamma = \left[M(S_w,u_w,u_o)\frac{\partial p_o}{\partial x}\right]_{\Gamma_1}\Gamma_1 - \left[M_w(S_w,u_w)\frac{\partial p_c}{\partial x}\right]_{\Gamma_1}\Gamma_1 - [\rho_w g_x M_w(S_w,u_w)]_{\Gamma_1}\Gamma_1 - [\rho_o g_x M_o(S_w,u_o)]_{\Gamma_1}\Gamma_1 \quad (9)$$

On a de même sur Γ_3 :

$$\int_{\Gamma_1} \mathbf{u}_t \cdot \mathbf{n}_3 d\Gamma = \left[-M(S_w,u_w,u_o)\frac{\partial p_o}{\partial x}\right]_{\Gamma_3}\Gamma_3 + \left[M_w(S_w,u_w)\frac{\partial p_c}{\partial x}\right]_{\Gamma_3}\Gamma_3 + [\rho_w g_x M_w(S_w,u_w)]_{\Gamma_3}\Gamma_3 + [\rho_o g_x M_o(S_w,u_o)]_{\Gamma_3}\Gamma_3 \quad (10)$$

La condition d'imperméabilité conduit aux flux nuls sur les surfaces latérales, Γ_2 et Γ_4. Ce qui conduit à l'équation complète suivante :

$$\left[M(S_w,u_w,u_o)\frac{\partial p_o}{\partial x}\right]_{\Gamma_1}\Gamma_1 - \left[M_w(S_w,u_w)\frac{\partial p_c}{\partial x}\right]_{\Gamma_1}\Gamma_1 - [\rho_w g_x M_w(S_w,u_w)]_{\Gamma_1}\Gamma_1 - [\rho_o g_x M_o(S_w,u_o)]_{\Gamma_1}\Gamma_1 - \left[M(S_w,u_w,u_o)\frac{\partial p_o}{\partial x}\right]_{\Gamma_3} + \left[M_w(S_w,u_w)\frac{\partial p_c}{\partial x}\right]_{\Gamma_3}\Gamma_3 + [\rho_w g_x M_w(S_w,u_w)]_{\Gamma_3}\Gamma_3 + [\rho_o g_x M_o(S_w,u_o)]_{\Gamma_3}\Gamma_3 = 0 \quad (11)$$

Dans le cas monodimensionnel $\Gamma_1 = \Gamma_3 = \Delta y\ \Delta z = 1$ et on obtient donc finalement :

$$\left[M(S_w,u_w,u_o)\frac{\partial p_o}{\partial x}\right]_{\Gamma_1} - \left[M_w(S_w,u_w)\frac{\partial p_c}{\partial x}\right]_{\Gamma_1} - [\rho_w g_x M_w(S_w,u_w)]_{\Gamma_1} - [\rho_o g_x M_o(S_w,u_o)]_{\Gamma_1} - \left[M(S_w,u_w,u_o)\frac{\partial p_o}{\partial x}\right]_{\Gamma_3} - M(S_w,u_w,u_o)\frac{\partial p_o}{\partial x}_{\Gamma_3} + \left[M_w(S_w,u_w)\frac{\partial p_c}{\partial x}\right]_{\Gamma_3} + [\rho_w g_x M_w(S_w,u_w)]_{\Gamma_3} + [\rho_o g_x M_o(S_w,u_o)]_{\Gamma_3} = 0 \quad (12)$$

Avec le schéma amont en considérant l'écoulement dans le sens $i \rightarrow i+1$, ainsi que le schéma IMPES (IMplicite en Pression et Explicite en Saturation), on écrit :

$$M(S^n_{w_{i-1}},u^k_w,u^k_o)\frac{p^{n+1}_{o_i} - p^{n+1}_{o_{i-1}}}{\Delta x} - M_w(S^n_{w_{i-1}},u^k_w)\frac{p^n_{c_i} - p^n_{c_{i-1}}}{\Delta x} - \rho_w g_x M_w(S^n_{w_{i-1}},u^k_w) - \rho_o g_x M_o(S^n_{w_{i-1}},u^k_o) - M(S^n_{w_i},u^k_w,u^k_o)\frac{p^{n+1}_{o_{i+1}} - p^{n+1}_{o_i}}{\Delta x} + M_w(S^n_{w_i},u^k_w)\frac{p^n_{c_{i+1}} - p^n_{c_i}}{\Delta x} + \rho_w g_x M_w(S^n_{w_i},u^k_w) + \rho_o g_x M_o(S^n_{w_i},u^k_o) = 0 \quad (13)$$

Les exposants k, n et $n+1$ correspondent au pas de temps. Le choix de l'exposant k associé au schéma choisi pour le traitement de la non-linéarité liée à la vitesse est discuté au chapitre 4 et ne sera pas répété ici. En ce qui concerne la position pour ces vitesses, aucun indice n'est mis car celles-ci sont calculées à l'interface entre les mailles et leur estimation ne pose donc aucun problème. A titre d'exemple en adoptant le schéma explicite pour le traitement des vitesses dans les mobilités, on obtient finalement :

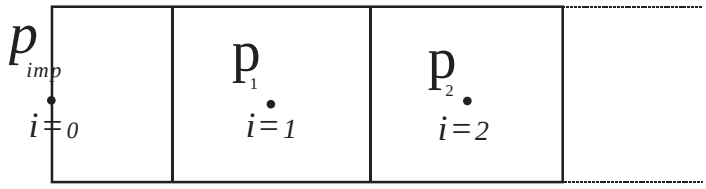

Figure 2: Représentation de la première demi maille considérée dans le cas de condition de pression imposé à l'entrée du milieu pour écoulement monodimensionnel

$$
\begin{aligned}
&p_{o_i}^{n+1}\left[\frac{M(S_{w_{i-1}}^n,u_w^n,u_o^n)}{\Delta x}+\frac{M(S_{w_i}^n,u_w^n,u_o^n)}{\Delta x}\right]+p_{o_{i-1}}^{n+1}\left[-\frac{M(S_{w_{i-1}}^n,u_w^n,u_o^n)}{\Delta x}\right]\\
&+p_{o_{i+1}}^{n+1}\left[-\frac{M(S_{w_i}^n,u_w^n,u_o^n)}{\Delta x}\right]+p_{c_i}^{n}\left[-\frac{M_w(S_{w_{i-1}}^n,u_w^n)}{\Delta x}-\frac{M_w(S_{w_i}^n,u_w^n)}{\Delta x}\right]\\
&+p_{c_{i-1}}^{n}\left[\frac{M_w(S_{w_{i-1}}^n,u_w^n)}{\Delta x}\right]+p_{c_{i+1}}^{n}\left[\frac{M_w(S_{w_i}^n,u_w^n)}{\Delta x}\right]\\
&+\left[M_w(S_{w_i}^n,u_w^n)-M_w(S_{w_{i-1}}^n,u_w^n)\right]+\rho_o g_x\left[M_o(S_{w_i}^n,u_o^n)-M_o(S_{w_{i-1}}^n,u_o^n)\right]=0
\end{aligned}
\tag{14}
$$

Traitement des conditions aux limites

Plusieurs types de conditions aux limites sont envisageables pour ce genre de problème. Les conditions classiquement employées sont les conditions de type pression imposée, débit imposé (ou vitesse imposée) ou bien surfaces imperméables.

Conditions aux limites sur la face d'entrée

Sur la face d'entrée, dans le cas d'une condition de type pression imposée, une demi maille est considérée (Figure 2) plaçant donc un noeud à pression connue à la frontière du milieu. A ce noeud, l'eau est toujours présente ($S_w^n = 1 - S_{or}$) avec la pression en huile égal à p_{imp} et en conséquence

$$
\begin{aligned}
p_{o0}^{n+1} &= p_{imp} && \text{(15a)}\\
p_{c0}^{n} &= p_c^n(S_w^n = 1 - S_{or}) && \text{(15b)}
\end{aligned}
$$

et pour la mobilité, à l'interface des mailles 0 et 1, en considérant l'écoulement de 0 vers 1, le schéma conduit à

$$
\begin{aligned}
M(S_{w_0}^n,u_w^k,u_o^k) &= M(S_w = 1 - S_{or},u_w^k,u_o^k) = M_0 && \text{(16a)}\\
M_w(S_{w_0}^n,u_w^k) &= M_w(S_w = 1 - S_{or},u_w^k) = M_{w0} && \text{(16b)}\\
M_o(S_{w_0}^n,u_o^k) &= M_o(S_w = 1 - S_{or},u_o^k) = 0 && \text{(16c)}
\end{aligned}
$$

En remplaçant cette valeur dans l'équation (13) on obtient pour le noeud 1

$$
\begin{aligned}
&M_0\frac{p_{o_1}^{n+1}-p_{imp}}{\Delta x}-M_{w0}\frac{p_{c_1}^n-p_{c0}^n}{\Delta x}-\rho_w g_x M_{w0}\\
&-M(S_{w_1}^n,u_w^k,u_o^k)\frac{p_{o_2}^{n+1}-p_{o_1}^{n+1}}{\Delta x}+M_w(S_{w_1}^n,u_w^k)\frac{p_{c_2}^n-p_{c_1}^n}{\Delta x}\\
&+\rho_w g_x M_w(S_{w_1}^n,u_w^k)+\rho_o g_x M_o(S_{w_1}^n,u_o^k)=0
\end{aligned}
\tag{17}
$$

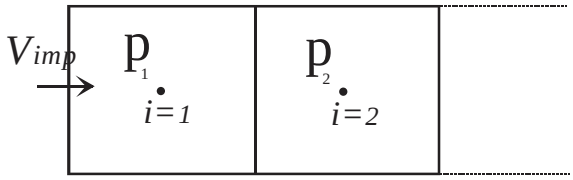

Figure 3: Représentation de la première maille pour la condition de type vitesse imposée en écoulement monodimensionnel

et finalement pour le schéma explicite pour le traitement des vitesses dans les mobilités, on obtient

$$\begin{aligned} p_{o_1}^{n+1}\left[\frac{M_0}{\Delta x}+\frac{M(S_{w_1}^n,u_w^n,u_o^n)}{\Delta x}\right]+p_{imp}\left[-\frac{M_0}{\Delta x}\right]+p_{o_2}^{n+1}\left[-\frac{M(S_{w_1}^n,u_w^n,u_o^n)}{\Delta x}\right] \\ +p_{c_1}^n\left[-\frac{M_{w0}}{\Delta x}-\frac{M_w(S_{w_1}^n,u_w^n)}{\Delta x}\right]+p_{c_0}^n\left[\frac{M_{w0}}{\Delta x}\right]+p_{c_2}^n\left[\frac{M_w(S_{w_1}^n,u_w^n)}{\Delta x}\right] \\ +\rho_w g_x\left[M_w(S_{w_1}^n,u_w^n)-M_{w0}\right]+\rho_o g_x\left[M_o(S_{w_1}^n,u_o^n)\right]=0 \end{aligned} \tag{18}$$

Une autre possibilité pour la condition à l'entrée est d'imposer la vitesse. Dans ce cas, l'eau est toujours présente à l'entrée avec une vitesse imposée égale à V_{imp} (Figure 3) et en conséquence l'intégrale sur la face d'entrée est simplifiée :

$$\int_{\Gamma_1}\mathbf{u}_t\cdot\mathbf{n}_1 d\Gamma=\int_{\Gamma_1}V_{imp}\cdot\mathbf{n}_1 d\Gamma_1=-V_{imp}dA=-V_{imp} \tag{19}$$

Remplaçant cette relation dans l'équation (13) en considérant un écoulement de 1 vers 2, conduit à

$$\begin{aligned} V_{imp}-M(S_{w_1}^n,u_w^k,u_o^k)\frac{p_{o_2}^{n+1}-p_{o_1}^{n+1}}{\Delta x}+M_w(S_{w_1}^n,u_w^k)\frac{p_{c_2}^n-p_{c_1}^n}{\Delta x} \\ +\rho_w g_x M_w(S_{w_1}^n,u_w^k)+\rho_o g_x M_o(S_{w_1}^n,u_o^k)=0 \end{aligned} \tag{20}$$

et finalement (avec le schéma explicite pour les vitesses)

$$\begin{aligned} V_{imp}+p_{o_1}^{n+1}\left[\frac{M(S_{w_1}^n,u_w^n,u_o^n)}{\Delta x}\right]+p_{o_2}^{n+1}\left[-\frac{M(S_{w_1}^n,u_w^n,u_o^n)}{\Delta x}\right] \\ +p_{c_1}^n\left[-\frac{M_w(S_{w_1}^n,u_w^n)}{\Delta x}\right]+p_{c_2}^n\left[\frac{M_w(S_{w_1}^n,u_w^n)}{\Delta x}\right] \\ +\rho_w g_x\left[M_w(S_{w_1}^n,u_w^n)\right]+\rho_o g_x\left[M_o(S_{w_1}^n,u_o^n)\right]=0 \end{aligned} \tag{21}$$

Conditions aux limites sur la face de sortie
Sur la face de sortie, la pression est toujours égale à la pression atmosphérique, (Figure 4), et donc

$$p_{o_{N+1}}^{n+1}=p_s$$

En remplaçant cette valeur dans l'équation (13), on obtient l'équation discrétisée suivante pour le noeud N :

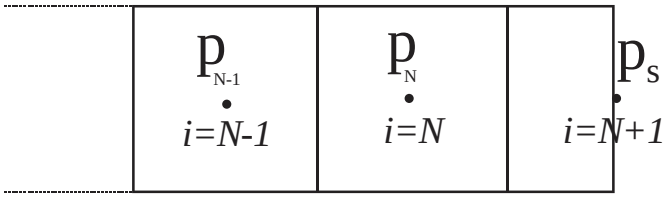

Figure 4: Représentation de la dernière maille avec une demi maille en pression (pression atmosphérique imposée à la sortie)

$$\begin{aligned} M(S^n_{w_{N-1}}, u^k_w, u^k_o)\frac{p^{n+1}_{o_N} - p^{n+1}_{o_{N-1}}}{\Delta x} - M_w(S^n_{w_{N-1}}, u^k_w)\frac{p^n_{c_N} - p^n_{c_{N-1}}}{\Delta x} \\ -\rho_w g_x M_w(S^n_{w_{N-1}}, u^k_w) - \rho_o g_x M_o(S^n_{w_{N-1}}, u^k_o) \\ -M(S^n_{w_N}, u^k_w, u^k_o)\frac{p_s - p^{n+1}_{o_N}}{\Delta x} + M_w(S^n_{w_N}, u^k_w)\frac{p^n_{c_{N+1}} - p^n_{c_N}}{\Delta x} \\ +\rho_w g_x M_w(S^n_{w_N}, u^k_w) + \rho_o g_x M_o(S^n_{w_N}, u^k_o) = 0 \end{aligned} \tag{22}$$

Mise sous forme matricielle

L'équation en pression en huile du système précédent, une fois discrétisée, en tenant compte des conditions aux limites et initiale, se met sous forme matricielle. L'équation (14) peut s'écrire de la manière suivante :

$$a_i p^{n+1}_{o_i} + b_i p^{n+1}_{o_{i-1}} + c_i p^{n+1}_{o_{i+1}} = d_i \tag{23}$$

avec pour les noeuds internes du milieu :

$$a_i = \left[\frac{M(S^n_{w_{i-1}}, u^n_w, u^n_o)}{\Delta x} + \frac{M(S^n_{w_i}, u^n_w, u^n_o)}{\Delta x}\right] \tag{24a}$$

$$b_i = \left[-\frac{M(S^n_{w_{i-1}}, u^n_w, u^n_o)}{\Delta x}\right] \tag{24b}$$

$$c_i = \left[-\frac{M(S^n_{w_i}, u^n_w, u^n_o)}{\Delta x}\right] \tag{24c}$$

$$d_i = -\left(\begin{array}{c} p^n_{c_i}\left[-\frac{M_w(S^n_{w_{i-1}}, u^n_w)}{\Delta x} - \frac{M_w(S^n_{w_i}, u^n_w)}{\Delta x}\right] + p^n_{c_{i-1}}\left[\frac{M_w(S^n_{w_{i-1}}, u^n_w)}{\Delta x}\right] \\ +p^n_{c_{i+1}}\left[\frac{M_w(S^n_{w_i}, u^n_w)}{\Delta x}\right] + \rho_w g_x\left[M_w(S^n_{w_i}, u^n_w) - M_w(S^n_{w_{i-1}}, u^n_w)\right] \\ +\rho_o g_x\left[M_o(S^n_{w_i}, u^n_o) - M_o(S^n_{w_{i-1}}, u^n_o)\right] \end{array}\right) \tag{24d}$$

La matrice est tridiagonale et symétrique, et les coefficients de celle-ci sont fonction des mobilités en eau et en huile qui dépendent elle-même, de manière non-linéaire, de la saturation en eau et de la vitesse. Le second membre est fonction des mobilités et de la pression capillaire.

Equation en Saturation L'équation discrétisée en saturation en eau s'écrit à partir de l'équation de conservation de la masse (1c) appliquée à la phase w:

$$\varepsilon\frac{\partial S_w}{\partial t} + \nabla\cdot\{-M_w(S_w,u_w)\left[\nabla p_o - \nabla p_c - \rho_w\mathbf{g}\right]\} = 0 \tag{25}$$

$$\int_{V_c}\varepsilon\frac{\partial S_w}{\partial t}dV + \int_{V_c}\nabla\cdot\{-M_w(S_w,u_w)(\nabla p_o - \nabla p_c - \rho_w\mathbf{g})\}\,dV = 0 \tag{26}$$

$$\varepsilon\int_{V_c}\frac{\partial S_w}{\partial t}dV + \int_{\Gamma}\{-M_w(S_w,u_w)\left[\nabla p_o - \nabla p_c - \rho_w\mathbf{g}\right]\}\cdot\mathbf{n}d\Gamma = 0 \tag{27}$$

Après simplifications, en 1D, en appliquant les mêmes hypothèses que précédemment, le gradient de pression et les mobilités étant considérés constants sur les faces d'entrée et sortie de la maille, on calcule la saturation de manière explicite (pour le schéma explicite pour la vitesse intervenant dan la mobilité) :

$$S_{w_i}^{n+1} = S_{w_i}^n - \frac{\Delta t}{\varepsilon\Delta x}\left\{\begin{array}{l} M_w(S_{w_{i-1}}^n,u_w^n)\left[\frac{(p_{o_i}^{n+1}-p_{o_{i-1}}^{n+1})}{\Delta x} - \frac{(p_{c_i}^{n}-p_{c_{i-1}}^{n})}{\Delta x} - \rho_w g_x\right] \\ -M_w(S_{w_i}^n,u_w^n)\left[\frac{(p_{o_{i+1}}^{n+1}-p_{o_i}^{n+1})}{\Delta x} - \frac{(p_{c_{i+1}}^{n}-p_{c_i}^{n})}{\Delta x} - \rho_w g_x\right] \end{array}\right\} \tag{28}$$

0.1.2 Ecoulement Bidimensionnel et Tridimensionnel

En écoulement bidimensionnel (ou tridimensionnel), la méthode est identique à celle du cas monodimensionnel. Les écoulements pourront s'effectuer dans deux (ou trois) directions au lieu d'une, compte tenu des hétérogénéités.

On évalue les pressions, saturations, mobilités de la manière définie en section précédente. En particulier, pour le calcul des mobilités on utilise toujours le schéma amont et on prend la valeur de la saturation à l'instant précédent celui pour lequel on est en train de faire le calcul.

Nous avons supposé que les tenseurs $\mathbf{K}_\alpha$ et $\boldsymbol{\beta}_\alpha$ sont sphériques, conduisant à des tenseurs de mobilité sphériques.

Discrétisation de l'équation en pression

$$\int_{V_c}(\nabla\cdot\mathbf{u}_t)dV = 0 \tag{29}$$

Grâce au théorème de la divergence, on obtient :

$$\int_{V_c}(\nabla\cdot\mathbf{u}_t)dV = \int_{\Gamma}\mathbf{u}_t\cdot\mathbf{n}d\Gamma = 0 \tag{30}$$

conduisant à la forme suivante pour une cellule parallélépipédique ayant six faces notées Γ_i $(i=1,..,6)$:

$$\int_{\Gamma_1}\mathbf{u}_t\cdot\mathbf{n}_1d\Gamma + \int_{\Gamma_2}\mathbf{u}_t\cdot\mathbf{n}_2d\Gamma + \int_{\Gamma_3}\mathbf{u}_t\cdot\mathbf{n}_3d\Gamma + \int_{\Gamma_4}\mathbf{u}_t\cdot\mathbf{n}_4d\Gamma + \int_{\Gamma_5}\mathbf{u}_t\cdot\mathbf{n}_5d\Gamma + \int_{\Gamma_6}\mathbf{u}_t\cdot\mathbf{n}_6d\Gamma = 0 \tag{31}$$

La méthode étant strictement identique à ce qui a été présenté pour le cas monodimensionnel, nous donnons simplement le résultant pour un sens d'écoulement dans la direction $i\rightarrow i+1$, $j\rightarrow j+1$, $k\rightarrow k+1$:

$$
\begin{aligned}
&- \left[\begin{array}{c} -M_{i-1,j,k} \frac{p^{n+1}_{o_{i,j,k}} - p^{n+1}_{o_{i-1,j,k}}}{\Delta x} + M_{w_{i-1,j,k}} \frac{p^{n}_{c_{i,j,k}} - p^{n}_{c_{i-1,j,k}}}{\Delta x} \\ +(M_{w_{i-1,j,k}}\rho_w + M_{o_{i-1,j,k}}\rho_o) g_x \end{array} \right] dA_x \\
&+ \left[\begin{array}{c} -M_{i,j,k} \frac{p^{n+1}_{o_{i+1,j,k}} - p^{n+1}_{o_{i,j,k}}}{\Delta x} + M_{w_{i,j,k}} \frac{p^{n}_{c_{i+1,j,k}} - p^{n}_{c_{i,j,k}}}{\Delta x} \\ +(M_{w_{i,j,k}}\rho_w + M_{o_{i,j,k}}\rho_o) g_x \end{array} \right] dA_x \\
&- \left[\begin{array}{c} -M_{i,j-1,k} \frac{p^{n+1}_{o_{i,j,k}} - p^{n+1}_{o_{i,j-1,k}}}{\Delta y} + M_{w_{i,j-1,k}} \frac{p^{n}_{c_{i,j,k}} - p^{n}_{c_{i,j-1,k}}}{\Delta y} \\ +(M_{w_{i,j-1,k}}\rho_w + \rho_o M_{o_{i,j-1,k}}) g_y \end{array} \right] dA_y \\
&+ \left[\begin{array}{c} -M_{i,j,k} \frac{p^{n+1}_{o_{i,j+1,k}} - p^{n+1}_{o_{i,j,k}}}{\Delta y} + M_{w_{i,j,k}} \frac{p^{n}_{c_{i,j+1,k}} - p^{n}_{c_{i,j,k}}}{\Delta y} \\ +(M_{w_{i,j,k}}\rho_w + \rho_o M_{o_{i,j,k}}) g_y \end{array} \right] dA_y \\
&- \left[\begin{array}{c} -M_{i,j,k-1} \frac{p^{n+1}_{o_{i,j,k}} - p^{n+1}_{o_{i,j,k-1}}}{\Delta z} + M_{w_{i,j,k-1}} \frac{p^{n}_{c_{i,j,k}} - p^{n}_{c_{i,j,k-1}}}{\Delta z} \\ +(M_{w_{i,j,k-1}}\rho_w + \rho_o M_{o_{i,j,k-1}}) g_z \end{array} \right] dA_z \\
&+ \left[\begin{array}{c} -M_{i,j,k} \frac{p^{n+1}_{o_{i,j,k+1}} - p^{n+1}_{o_{i,j,k}}}{\Delta z} + M_{w_{i,j,k}} \frac{p^{n}_{c_{i,j,k+1}} - p^{n}_{c_{i,j,k}}}{\Delta z} \\ +(M_{w_{i,j,k}}\rho_w + \rho_o M_{o_{i,j,k}}) g_z \end{array} \right] dA_z = 0
\end{aligned} \tag{32}
$$

avec $M_{i,j,k}$ et $M_{\alpha_{i,j,k}}$ $(\alpha = w, o)$ égaux respectivement à $M(S^n_{w_{i,j,k}}, u^k_w, u^k_o)$ et $M_\alpha(S^n_{w_{i,j,k}}, u^k_w)$ et

$$
dA_x = \Delta y \, \Delta z \tag{33a}
$$

$$
dA_y = \Delta z \, \Delta x \tag{33b}
$$

$$
dA_z = \Delta x \, \Delta y \tag{33c}
$$

Ceci conduit à :

$$
\begin{aligned}
&\left[\begin{array}{c} (M_{i-1,j,k} + M_{i,j,k}) \frac{dA_x}{\Delta x} + (M_{i,j-1,k} + M_{i,j,k}) \frac{dA_y}{\Delta y} \\ +(M_{i,j,k-1} + M_{i,j,k}) \frac{dA_z}{\Delta z} \end{array} \right] p^{n+1}_{o_{i,j,k}} \\
&\quad + \left[-M_{i-1,j,k} \frac{dA_x}{\Delta x} \right] p^{n+1}_{o_{i-1,j,k}} + \left[-M_{i,j,k} \frac{dA_x}{\Delta x} \right] p^{n+1}_{o_{i+1,j,k}} \\
&\quad + \left[-M_{i,j-1,k} \frac{dA_y}{\Delta y} \right] p^{n+1}_{o_{i,j-1,k}} + \left[-M_{i,j,k} \frac{dA_y}{\Delta y} \right] p^{n+1}_{o_{i,j+1,k}} \\
&\quad + \left[-M_{i,j,k-1} \frac{dA_z}{\Delta z} \right] p^{n+1}_{o_{i,j,k-1}} + \left[-M_{i,j,k} \frac{dA_z}{\Delta z} \right] p^{n+1}_{o_{i,j,k+1}} \\
&- \left[M_{w_{i-1,j,k}} \frac{p^n_{c_{i,j,k}} - p^n_{c_{i-1,j,k}}}{\Delta x} + (M_{w_{i-1,j,k}}\rho_w + M_{o_{i-1,j,k}}\rho_o) g_x \right] dA_x \\
&\quad + \left[M_{w_{i,j,k}} \frac{p^n_{c_{i+1,j,k}} - p^n_{c_{i,j,k}}}{\Delta x} + (M_{w_{i,j,k}}\rho_w + M_{o_{i,j,k}}\rho_o) g_x \right] dA_x \\
&- \left[M_{w_{i,j-1,k}} \frac{p^n_{c_{i,j,k}} - p^n_{c_{i,j-1,k}}}{\Delta y} + (M_{w_{i,j-1,k}}\rho_w + \rho_o M_{o_{i,j-1,k}}) g_y \right] dA_y \\
&\quad + \left[M_{w_{i,j,k}} \frac{p^n_{c_{i,j+1,k}} - p^n_{c_{i,j,k}}}{\Delta y} + (M_{w_{i,j,k}}\rho_w + \rho_o M_{o_{i,j,k}}) g_y \right] dA_y \\
&- \left[M_{w_{i,j,k-1}} \frac{p^n_{c_{i,j,k}} - p^n_{c_{i,j,k-1}}}{\Delta z} + (M_{w_{i,j,k-1}}\rho_w + \rho_o M_{o_{i,j,k-1}}) g_z \right] dA_z \\
&\quad + \left[M_{w_{i,j,k}} \frac{p^n_{c_{i,j,k+1}} - p^n_{c_{i,j,k}}}{\Delta z} + (M_{w_{i,j,k}}\rho_w + \rho_o M_{o_{i,j,k}}) g_z \right] dA_z = 0
\end{aligned} \tag{34}
$$

A titre d'exemple, l'équation précédente peut s'écrire sous la forme :

$$\begin{aligned} & Z_{i,j,k}p^{n+1}_{o_{i,j,k-1}} + G_{i,j,k}p^{n+1}_{o_{i,j-1,k}} + C_{i,j,k}p^{n+1}_{o_{i-1,j,k}} + A_{i,j,k}p^{n+1}_{o_{i,j,k}} \\ & +B_{i,j,k}p^{n+1}_{o_{i+1,j,k}} + F_{i,j,k}p^{n+1}_{o_{i,j+1,k}} + S_{i,j,k}p^{n+1}_{o_{i,j,k+1}} \\ = \quad & D_{i,j,k} \end{aligned} \tag{35}$$

avec

$$Z_{i,j,k} = \left[-M_{i,j,k-1}\frac{dA_z}{\Delta z}\right] \tag{36a}$$

$$G_{i,j,k} = \left[-M_{i,j-1,k}\frac{dA_y}{\Delta y}\right] \tag{36b}$$

$$C_{i,j,k} = \left[-M_{i-1,j,k}\frac{dA_x}{\Delta x}\right] \tag{36c}$$

$$A_{i,j,k} = \left[\begin{array}{c}(M_{i-1,j,k}+M_{i,j,k})\frac{dA_x}{\Delta x} + (M_{i,j-1,k}+M_{i,j,k})\frac{dA_y}{\Delta y} \\ +(M_{i,j,k-1}+M_{i,j,k})\frac{dA_z}{\Delta z}\end{array}\right] \tag{36d}$$

$$B_{i,j,k} = \left[-M_{i,j,k}\frac{dA_x}{\Delta x}\right] \tag{36e}$$

$$F_{i,j,k} = \left[-M_{i,j,k}\frac{dA_y}{\Delta y}\right] \tag{36f}$$

$$S_{i,j,k} = \left[-M_{i,j,k}\frac{dA_z}{\Delta z}\right] \tag{36g}$$

et

$$\begin{aligned} D_{i,j,k} = \quad & \left[M_{w_{i-1,j,k}}\frac{p^n_{c_{i,j,k}} - p^n_{c_{i-1,j,k}}}{\Delta x} + (M_{w_{i-1,j,k}}\rho_w + M_{o_{i-1,j,k}}\rho_o)g_x\right]dA_x \\ & - \left[M_{w_{i,j,k}}\frac{p^n_{c_{i+1,j,k}} - p^n_{c_{i,j,k}}}{\Delta x} + (M_{w_{i,j,k}}\rho_w + M_{o_{i,j,k}}\rho_o)g_x\right]dA_x \\ & + \left[M_{w_{i,j-1,k}}\frac{p^n_{c_{i,j,k}} - p^n_{c_{i,j-1,k}}}{\Delta y} + (M_{w_{i,j-1,k}}\rho_w + \rho_o M_{o_{i,j-1,k}})g_y\right]dA_y \\ & - \left[M_{w_{i,j,k}}\frac{p^n_{c_{i,j+1,k}} - p^n_{c_{i,j,k}}}{\Delta y} + (M_{w_{i,j,k}}\rho_w + \rho_o M_{o_{i,j,k}})g_y\right]dA_y \\ & + \left[M_{w_{i,j,k-1}}\frac{p^n_{c_{i,j,k}} - p^n_{c_{i,j,k-1}}}{\Delta z} + (M_{w_{i,j,k-1}}\rho_w + \rho_o M_{o_{i,j,k-1}})g_z\right]dA_z \\ & - \left[M_{w_{i,j,k}}\frac{p^n_{c_{i,j,k+1}} - p^n_{c_{i,j,k}}}{\Delta z} + (M_{w_{i,j,k}}\rho_w + \rho_o M_{o_{i,j,k}})g_z\right]dA_z \end{aligned} \tag{37}$$

Le second membre fait intervenir les pressions capillaires et les mobilités, les conditions aux limites en pression sont prises en compte dans le second membre comme il a été fait dans le cas monodimensionnel.

L'équation en p_o, une fois discrétisée, en tenant compte des conditions aux limites et initiale, se met sous forme matricielle. Le système linéaire obtenu est symétrique et résolu à l'aide de la méthode de Gradient Conjugué. En écoulement tri dimensionnel (ou bidimensionnel), la matrice est sept diagonal (ou penta diagonale).

Equation en Saturation

$$\varepsilon\frac{\partial S_w}{\partial t} + \nabla\cdot\{-M_w(S_w,u_w)\left[\nabla p_o - \nabla p_c - \rho_w\mathbf{g}\right]\} = 0 \tag{38}$$

Si l'écoulement est selon $i \to i+1$, $j \to j+1$, $k \to k+1$ et en considérant le schéma explicite pour la prise en compte de la vitesse dans la mobilité, on obtient :

$$S^{n+1}_{w_{i,j,k}} = S^n_{w_{i,j,k}} - \frac{\Delta t}{\varepsilon \Delta V} \left\{ \begin{array}{l} M_w(S^n_{w_{i-1,j,k}}, u^n_w) \left[\begin{array}{l} \frac{(p^{n+1}_{o_{i,j,k}} - p^{n+1}_{o_{i-1,j,k}})}{\Delta x} \\ -\frac{(p^n_{c_{i,j,k}} - p^n_{c_{i-1,j,k}})}{\Delta x} - \rho_w g_x \end{array} \right] dA_x \\ -M_w(S^n_{w_{i,j,k}}, u^n_w) \left[\begin{array}{l} \frac{(p^{n+1}_{o_{i+1,j,k}} - p^{n+1}_{o_{i,j,k}})}{\Delta x} \\ -\frac{(p^n_{c_{i+1,j,k}} - p^n_{c_{i,j,k}})}{\Delta x} - \rho_w g_x \end{array} \right] dA_x \\ M_w(S^n_{w_{i,j-1,k}}, u^n_w) \left[\begin{array}{l} \frac{(p^{n+1}_{o_{i,j,k}} - p^{n+1}_{o_{i,j-1,k}})}{\Delta y} \\ -\frac{(p^n_{c_{i,j,k}} - p^n_{c_{i,j-1,k}})}{\Delta y} - \rho_w g_y \end{array} \right] dA_y \\ -M_w(S^n_{w_{i,j,k}}, u^n_w) \left[\begin{array}{l} \frac{(p^{n+1}_{o_{i,j+1,k}} - p^{n+1}_{o_{i,j,k}})}{\Delta y} \\ -\frac{(p^n_{c_{i,j+1,k}} - p^n_{c_{i,j,k}})}{\Delta y} - \rho_w g_y \end{array} \right] dA_y \\ M_w(S^n_{w_{i,j,k-1}}, u^n_w) \left[\begin{array}{l} \frac{(p^{n+1}_{o_{i,j,k}} - p^{n+1}_{o_{i,j,k-1}})}{\Delta z} \\ -\frac{(p^n_{c_{i,j,k}} - p^n_{c_{i,j,k-1}})}{\Delta z} - \rho_w g_x \end{array} \right] dA_z \\ -M_w(S^n_{w_{i,j,k}}, u^n_w) \left[\begin{array}{l} \frac{(p^{n+1}_{o_{i,j,k+1}} - p^{n+1}_{o_{i,j,k}})}{\Delta z} \\ -\frac{(p^n_{c_{i,j,k+1}} - p^n_{c_{i,j,k}})}{\Delta z} - \rho_w g_z \end{array} \right] dA_z \end{array} \right\} \tag{39}$$

Où

$$\Delta V = \Delta x \ \Delta y \ \Delta z \tag{40}$$

Ainsi, ayant calculé le champ de pression en huile pour le pas de temps $n+1$, et connaissant les autres variables au pas de temps précédent la saturation en tout point est calculée.

Traitement des Conditions à l'interface entre deux milieux Lorsqu'on considère un milieu poreux hétérogène, à l'interface entre deux milieux différents, il est nécessaire d'assurer la continuité des vitesses de chaque phase ainsi que la continuité des pressions

$$\mathbf{u}^\eta_o \cdot \mathbf{n}_{\omega\eta} = \mathbf{u}^\omega_o . \mathbf{n}_{\omega\eta} \quad sur \ \ \Gamma_{\omega\eta} \tag{41}$$

et

$$\mathbf{u}^\eta_w \cdot \mathbf{n}_{\omega\eta} = \mathbf{u}^\omega_w . \mathbf{n}_{\omega\eta} \quad sur \ \ \Gamma_{\omega\eta} \tag{42}$$

De plus :

$$p^\omega_o = p^\eta_o \quad sur \ \ \Gamma_{\omega\eta} \tag{43a}$$
$$p^\omega_w = p^\eta_w \quad sur \ \ \Gamma_{\omega\eta} \tag{43b}$$

et par conséquent

$$p^\omega_c = p^\eta_c \quad sur \ \ \Gamma_{\omega\eta} \tag{44}$$

où $\Gamma_{\omega\eta}$ est l'interface entre deux milieux, η et ω, et $\mathbf{n}_{\omega\eta}$ le vecteur unitaire normal à $\Gamma_{\omega\eta}$ orientée du milieu ω vers le milieu η.

On considère le cas 1D présenté sur la Figure (5). Afin de satisfaire ces conditions, à un point, x, sur l'interface, on peut écrire pour chaque phase

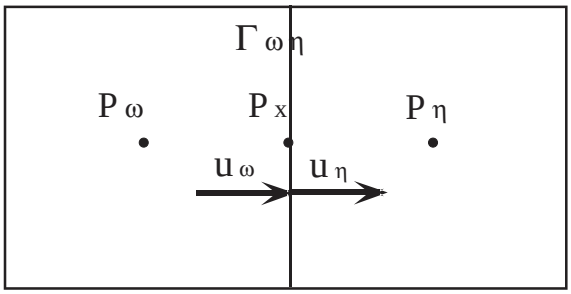

Figure 5: L'interface d'un milieu poreux hétérogène à deux types de roche

$$u_\omega = -M_\omega \frac{p_x - p_\omega}{\Delta x/2} \tag{45}$$

$$u_\eta = -M_\eta \frac{p_\eta - p_x}{\Delta x/2} \tag{46}$$

la continuité des vitesses à l'interface conduit à

$$u_\omega = u_\eta \tag{47}$$

$$-M_\omega \frac{p_x - p_\omega}{\Delta x/2} = -M_\eta \frac{p_\eta - p_x}{\Delta x/2} \tag{48}$$

Cette égalité permet de calculer la pression à l'interface

$$p_x = \frac{M_\omega p_\omega + M_\eta p_\eta}{M_\omega + M_\eta} \tag{49}$$

Maintenant on peut calculer la vitesse à l'interface en fonction des pressions aux noeuds de chaque côté

$$u_\omega = u_\eta = -\frac{2M_\omega M_\eta}{(M_\omega + M_\eta)} \frac{p_\eta - p_\omega}{\Delta x} \tag{50}$$

Ce résultat nous montre clairement que pour avoir la continuité des vitesses ainsi que la continuité de la pression, il suffit de prendre des moyennes harmoniques des mobilités des deux milieux à l'interface. Dans l'expression de la mobilité à l'interface, nous avons considéré le schéma amont pour la partie dépendante de la saturation.